STOCHASTIC MODEL FOR EARTHQUAKE GROUND MOTION USING WAVELET PACKETS

A DISSERTATION
SUBMITTED TO THE DEPARTMENT OF CIVIL AND ENVIRONMENTAL ENGINEERING
AND THE COMMITTEE ON GRADUATE STUDIES
OF STANFORD UNIVERSITY
IN PARTIAL FULFILLMENT OF THE REQUIREMENTS
FOR THE DEGREE OF
DOCTOR OF PHILOSOPHY

Yoshifumi Yamamoto

April 2011

This dissertation is online at: http://purl.stanford.edu/kj426ng0836

I certify that I have read this dissertation and that, in my opinion, it is fully adequate in scope and quality as a dissertation for the degree of Doctor of Philosophy.

Jack Baker, Primary Adviser

I certify that I have read this dissertation and that, in my opinion, it is fully adequate in scope and quality as a dissertation for the degree of Doctor of Philosophy.

Anne Kiremidjian

I certify that I have read this dissertation and that, in my opinion, it is fully adequate in scope and quality as a dissertation for the degree of Doctor of Philosophy.

Eduardo Miranda

Approved for the Stanford University Committee on Graduate Studies.

Patricia J. Gumport, Vice Provost Graduate Education

This signature page was generated electronically upon submission of this dissertation in electronic format. An original signed hard copy of the signature page is on file in University Archives.

Abstract

For performance-based design, nonlinear dynamic structural analysis for various types of input ground motions is required. Stochastic (simulated) ground motions are sometimes useful as input motions, because unlike recorded motions they are not limited in number and because their properties can be varied systematically to study the impact of ground motion properties on structural response. This dissertation describes an approach by which the wavelet packet transform can be used to characterize complex time-varying earthquake ground motions, and it illustrates the potential benefits of such an approach in a variety of earthquake engineering applications. The proposed model is based on Thráinsson and Kiremidjian (2002), which use Fourier amplitudes and phase differences to simulate ground motions and attenuation models to their model parameters. We extend their model using wavelet packet transform since it can control the time and frequency characteristic of time series. The time- and frequency-varying properties of real ground motions can be captured using wavelet packets, so a model is developed that requires only 13 parameters to describe a given ground motion. These 13 parameters are then related to seismological variables such as earthquake magnitude, distance, and site condition, through regression analysis that captures trends in mean values, standard deviations and correlations of these parameters observed in a large database of recorded strong ground motions. The resulting regression equations then form a model that can be used to predict ground motions for a future earthquake scenario; this model is analogous to widely used empirical ground motion prediction models (formerly called "attenuation models") except that this model predicts entire time series rather than only response spectra. The ground motions produced using this predictive model are explored in detail, and are shown to have elastic response spectra, inelastic response spectra, durations, mean periods, etc., that are consistent in both

mean and variability to existing published predictive models for those properties. That consistency allows the proposed model to be used in place of existing models for probabilistic seismic hazard analysis (PSHA) calculations. This new way to calculate PSHA is termed "simulation-based probabilistic seismic hazard analysis" and it allows a deeper understanding of ground motion hazard and hazard deaggregation than is possible with traditional PSHA because it produces a suite of potential ground motion time histories rather than simply a distribution of response spectra. The potential benefits of this approach are demonstrated and explored in detail. Taking this analysis even further, this suite of time histories can be used as input for nonlinear dynamic analysis of structures, to perform a risk analysis (i.e., "probabilistic seismic demand analysis") that allows computation of the probability of the structure exceeding some level of response in a future earthquake. These risk calculations are often performed today using small sets of scaled recorded ground motions, but that approach requires a variety of assumptions regarding important properties of ground motions, the impacts of ground motion scaling, etc. The approach proposed here facilitates examination of those assumptions, and provides a variety of other relevant information not obtainable by that traditional approach.

Acknowledgements

I would like to express my gratitude to my advisor, Professor Jack W. Baker, for his support, patience, and encouragement throughout my graduate studies. I was very lucky to find an advisor who always finds the time for listening to and discussing the little problems and roadblocks that unavoidably crop up in the course of performing research. His technical and editorial advice was essential to the completion of this dissertation.

My thanks also go to my reading committee, Professor Anne Kiremidjian and Professor Eduardo Miranda, for reading previous drafts of this dissertation and providing many valuable comments that improved the contents of this dissertation. I would like to thank the members of my defense committee, Professor Greg Deierlein and Professor Eric Dunham for their helpful feedback regarding this work. I also wish to thank to Professor Curt Haselton for providing the building models and the matlab scripts to compute structural responses. Thanks to all of the students, staff and faculty associated with the John A. Blume Earthquake Engineering Center.

This material is based in part upon work supported by the National Science Foundation under NSF grant number CMMI 0726684. Any opinions, findings and conclusions or recommendations expressed in this material are those of the author and do not necessarily reflect the views of the National Science Foundation.

During the course of my PhD, I have had research discussions with several students in the Blume Center. In particular, Shrey Shahi, Ting Lin, and Nirmal Jayaram have provided valuable support and feedback on this research. Thanks to my research group mates Andy Seifried, Shrey Shahi, Ting Lin, Lynne Burks, Mahalia Miller, Christophe Loth, and Victor Victorsson for valuable discussions during weekly group meetings and for their friendship.

I also thank to Kajima corporation for giving a opportunity to start this research in

Stanford.

I dedicate this dissertation to my wife, Yoshiko Yamamoto, my two boys, Kazuma Yamamoto and Tomohiro Yamamoto, and my parents who have been very supportive of my decision to pursue PhD in Stanford University and have always encouraged me. I wish to express my gratitude to them for their all supports that always encouraged me.

Contents

List of Tables

List of Figures

Chapter 1

Introduction

1.1 Motivation

Nonlinear dynamic structural analysis generally requires the use of large numbers of input ground motions in order to determine performance of structures in terms of probability distributions of engineering demand parameters, which is used for performance-based design. However, the number of available recorded ground motions is limited and may not be sufficient for characterizing a particular analysis condition.

In order to obtain additional ground motions for a particular analysis condition, ground motion scaling and spectral matching are widely used to adjust recorded ground motions and make them more representative of the target analysis condition. Ground motion scaling modifies the amplitude of a "seed" recorded ground motion by multiplying a constant, in order to to match a target spectral acceleration at a particular target period, or approximately match a spectrum (e.g. a uniform hazard spectrum) over a range of periods. Spectral matching modifies recorded ground motions by adjusting Fourier amplitudes (e.g. Silva and Lee 1987), adding small wavelets (e.g.Hancock et al. 2006, Al Atik and Abrahamson 2010), or adjusting wavelet coefficients (e.g. Mukherjee and Gupta 2002, Suarez and Montejo 2005, Nakamura et al. 2008, Yazdani and Takada 2009, Giaralis and Spanos 2009) to make their spectra reasonably match the target response spectra over a range of periods.

However, these approaches change the relationship between characteristics of recorded ground motions and their associated seismological conditions, so the results of these operations could have characteristics different from those of actual recorded ground motions (Bazzurro and Luco 2006, Luco and Bazzurro 2007). An alternative approach is, therefore, to generate artificial earthquake ground motions whose characteristics are consistent with both the physical condition of interest and the characteristics of the actual recorded ground motions.

1.2 Simulation approaches

Douglas and Aochi (2008) provides a comprehensive review of the many ground motion simulation techniques proposed in the past, including methods to generate time series ground motions as well as ground motion prediction models (GMPMs) for intensity measures. This dissertation focuses on generating ground motion time series for input to nonlinear dynamic structural analysis, thus we will briefly review similar related work.

The three general types of strong ground motion simulation techniques are physics-based simulations, stochastic simulations, and hybrid simulations (which combines the first two). Physics-based simulations generate ground motions by modeling fault rupture and resulting wave propagation using analytical models (e.g. Zerva 1988, Mavroeidis and Papageorgiou 2003), finite element methods (FEM, e.g. Moczo et al. 2007) or finite difference methods (FDM, e.g. Boore 1973, Pitarka et al. 1998, Moczo et al. 2007). Most analytical models are limited to a layered homogeneous medium; however, the results of physics-based simulations naturally include effects of coherency, directivity, site amplification, surface wave, and other physical effects caused by geometric conditions (assuming that those effects are included in the given model's formulation).

Since physics-based simulations require a large number of seismological information about fault rupture (e.g. rise time, stress drop, cut-off frequency, position of asperities, etc.), and the resulting simulated ground motions are sensitive to these parameters, it is difficult to predict appropriate seismological parameters of future earthquake scenarios. Also, since the FEM and FDM simulate wave propagation with precise physical information (e.g. shear wave velocity, Q value, and three-dimensional crustal structure), it is computationally expensive to produce a large number of simulations that cover the range of possible future earthquakes. In addition, the frequencies of ground shaking that can be generated using FEM and FEM are constrained by the spatial resolution of the fault rupture model and crustal structure model. Limitations on measurement of these properties and limitations on computational time required to process high-resolution simulations indicate that current simulations are limited to frequencies below 2Hz, even when petascale computing facilities are used (Cui et al. 2010). Higher-frequency components are important for some structures, however, such as low- and mid-rise buildings, nuclear power plants, and some geotechnical structures.

Other simulations can improve the computational cost and input data requirements described above, for example by using a point-source model but coupling it with a physics-based wave propagation algorithm, or by using only 2D crustal velocity models rather than 3D (e.g. Haase et al. 1996). Those simplifications greatly reduce the computational cost and input data requirements of the simulations, and can produce reasonable results in some cases, but their generality and ability to incorporate the complete physical rupture and wave propagation process is limited.

The above descriptions are also focused on simulation approaches that perform forward simulations of future earthquakes, and which are capable of producing an infinite set of simulations by including randomness in model parameters for future earthquakes (Cui et al. 2010). Many simulations are performed using, for example, a source model obtained from inversion of a past earthquake (e.g. Wald et al. 1991, Pitarka et al. 1998). These simulations overcome some limitations of physics-based models discussed above, because a realistic source description is readily available, but they are not directly applicable for computing reliability of structures subjected to future earthquake ground motions.

Stochastic simulations, in contrast, are empirically calibrated approaches that directly simulate the recorded ground motions using fewer parameters than physics-based simulations. With this approach, it is difficult to consider physical phenomena such as surface waves, directivity, etc., exclusively since there are likely no parameters in the model to control these effects. In addition, it is difficult to consider the effect of three-dimensional crustal structure because in general each stochastic simulation uses only the near surface soil conditions under the station.

Hybrid simulations (e.g., Hartzell et al. 1999, Martin Mai and Beroza 2003, Graves and Pitarka 2010) combine physics-based simulations for low-frequency components and empirical simulations or stochastic simulation for high-frequency components using frequency filters. This overcomes practical limitations of the individual approaches, and is based on the idea that the effects of fault rupture and wave propagation can be considered as stochastic at higher frequencies. Even though hybrid simulations combine the advantages of both physics-based and stochastic simulations, combining the ground motions from the two simulations possess challenges related to tapering one approach's ground motion in and the other's out at the transition frequency. Maintaining appropriate phasing across the two sources can also be problematic. Also the simulation currently used at high frequencies in hybrid simulations is a method of superposing ground motion recordings of small earthquakes (empirical Green's functions, e.g. Hartzell 1978, Irikura 1983) or stochastic simulations from statistical models of source, path, and site amplification (e.g. Papageorgiou and Aki 1983a, 1983b, Boore 1983, 2003), or theoretical Green's functions (e.g. Zeng et al. 1994). These simulations require the same detailed information as physics-based simulations. Therefore, computational cost depends on the type of physics-based simulations.

For performance-based design, where we often need a large number of input ground motions, stochastic simulations may be more practical than physics-based simulations and hybrid simulations. This dissertation focuses on the stochastic simulation approach, so similar previous research will be discussed in more detail.

Research on stochastic simulations has been conducted for more than 50 years by many researchers. There are comprehensive reviews almost every 10 years by authors such as Liu (1970a), Ahmadi (1979), Shinozuka and Deodatis (1988), Kozin (1988), Conte and Peng (1997), and Rezaeian (2010). One important issue raised in these reviews is that of time and frequency nonstationarity, which describes the changing amplitudes of time series (temporal nonstationarity) and changing frequency characteristics (spectral nonstationarity) in time. This nonstationarity is an important factor for affecting nonlinear dynamic response of structures. It can affect the results of nonlinear dynamic structural analysis (Chakravorty and Vanmarck 1973, Yeh and Wen 1990, Conte 1992b, Wang et al. 2002, Spanos et al. 2007), in part because the structure's behavior is also nonstationary as it is driven to nonlinear response and its resulting natural period increases (Papadimitrios 1990) .

Rezaeian (2010) places existing stochastic ground motion models into four categories:

(1) Processes obtained by passing a white noise through a filter, e.g., Bolotin (1960), Shinozuka and Sato (1967), Amin and Ang (1968), Iyengar and Iyengar (1969), Ruiz and Penzien (1971), Alamilla et al. (2001) with subsequent modulation in time for temporal nonstationarity. These processes have constant frequency characteristics along the entire time axis. Rezaeian (2010) developed a fully nonstationary stochastic model that uses a modulated filtered white-noise process in the time domain. Her model has the advantage that the temporal and spectral nonstationarities are separately computed by modulating the response of a linear filter having time-varying characteristics that are applied to a white-noise excitation. However, since these models control frequency nonstationarity from the time domain, it can be difficult to describe the joint time and frequency characteristics of multimodal functions. (2) Processes obtained by passing a train of Poisson pulses through a linear filter, e.g., Cornell (1964), Lin (1965). These processes can generate ground motions with time and frequency nonstationarity Lin (1986) using modulation in time; however, it is difficult to simulate realistic ground motion recordings. (3) Autoregressive moving average (ARMA) models, e.g., Jurkevics and Ulrych (1978), Hoshiya and Hasgur (1978), Polhemus and Cakmak (1981), Kozin (1988), Chang et al. (1982), Conte (1992a), Mobarakeh et al. (2002). These models can simulate ground motions with time and frequency nonstationarity using time-dependent parameters for frequency characteristics, but it is often difficult to link the model parameters to seismological information. This limitation makes it difficult to simulate future ground motions using these models. (4) Various forms of spectral representation, e.g., Saragoni and Hart (1974), Der Kiureghian and Crempien (1989), Conte and Peng (1997), Wen and Gu (2004), Pousse et al. (2006). These models use a short-time Fourier transform or wavelet transform to develop a time-frequency modulating function that matches a particular recorded ground motion. Also, Thráinsson and Kiremidjian (2002) and Montaldo et al. (2003) use phase differences in the ground motion components of various frequencies to generate motions with time-frequency nonstationarity.

The common assumption for all these models is that the simulated motion is a zero-mean Gaussian process. The model proposed in this dissertation characterizes the signal in the time and frequency domain using wavelet transforms, so it fits into the fourth category.

Given that the proposed model uses time and frequency modulation, the followsing paragraphs describe previous research to develop models similar to our proposed stochastic ground motion model.

Page (1952) proposed the instantaneous power spectrum and Priestley (1965) proposed the evolutionary (time-varying) power spectral density (EPSD) to control time and frequency characteristics of nonstationary time series. Liu (1970b) proposed a model based on the instantaneous power spectrum, and Saragoni and Hart (1974) defined the power spectral density for finite time regions. Kameda (1975) and Scherer et al. (1982) both estimated EPSD functions from recorded ground motions using a multifilter technique. Conte and Peng (1997) proposed an extension of Thomson's spectrum estimation method (Thomson 1982) to analyze EPSD functions. More recently, Pousse et al. (2006) used a modified time-dependent ω-square model and two types of modulating functions, which correspond to the P-wave and the S-wave respectively.

Various researchers have used the wavelet transform to characterize ground motions. Among them, Iyama and Kuwamura (1999) demonstrated that the square of an individual wavelet coefficient from the discrete wavelet transform (DWT) is equivalent to the corresponding energy (squared acceleration) in a given time and frequency domain, using energy conservation between wavelets and accelerations in each frequency band. Masuda and Sone (2002) generated artificial ground motions given time and frequency characteristics and response spectra that were comparable to recorded ground motions, using the continuous wavelet transform (CWT) with the time-reversed impulse response function as a wavelet function. These proposed models can characterize time and frequency characteristics of a ground motion, but they only simulate motions based on a target seed ground motion. Sasaki et al. (2003) proposed a model using the DWT to generate artificial ground motions with time and frequency nonstationarity and attenuation models to their model parameters. However, it is difficult to maintain time-frequency characteristics using this approach, because the time resolution of the DWT is very low at low frequencies.

Spanos and Failla (2004) proposed a wavelet-based method to estimate the EPSD of the target ground acceleration record. Spanos and Failla (2004) and Spanos et al. (2007) used CWT instead of the short-time Fourier transform (STFT) in order to achieve an enhanced time resolution for high frequency components. Their implementation was limited, however, to producing simulations that reproduced properties of a "seed" ground motion that was used for calibration, rather than producing simulations for an arbitrary future earthquake scenario.

Nakamura et al. (2008) proposed the model to generate artificial ground motions having a target response spectra by linear combination of wavelet coefficients from large number of recorded ground motions using DWT. The time and frequency characteristics of the simulated motions are taken to match those of a reference recorded ground motion. Amiri et al. (2009, 2011) used the wavelet packet transform (WPT) to generate artificial ground motions compatible with a target pseudo velocity response spectrum and having time and frequency nonstationarity. Their model used a neural network to predict the wavelet packets amplitudes. The simulations from this model are conditional on a target spectrum rather than seismological parameters, however, so it is difficult to generate ground motions that represent the full variability of potential future ground motions.

Several software packages are available to generate artificial ground motions using stochastic models: PSEQGN (Ruiz and Penzien 1969), SIMQKE-I (Vanmarcke et al. 1976) and SIMQKE-II (Vanmarcke et al. 1997). PSEQGN generates ground motions using white noise process with a time-varying modulating function. SIMQKE-I generates ground motions using pseudo-random phasing with a time-varying modulating function. The resulting ground motions have a target spectral shape, which is obtained due to the relationship between the response spectrum values for a given level of damping and the expected Fourier amplitudes of the ground motion (Vanmarcke and Gasparini 1976). The software package SIMQKE-II extends SIMQKE-I to generate ground motions with a specified EPSD and also simulated multiple ground motions at adjacent locations that have appropriate spatial correlation spatial correlation.

The model proposed in this dissertation is based on Thráinsson and Kiremidjian (2002) and we extend their model using WPT since it can fully control the time and frequency characteristic of time series. Here the WPT is employed in order to approximate the EPSD of acceleration time series for stochastic ground motion modeling. The wavelet transform was chosen because it has been noted as an effective tool for producing nonstationary time histories. Among options for wavelet analysis, the CWT is problematic because it is difficult to use to reconstruct time series due to the non-orthogonality of the wavelets at adjacent times and frequencies. At the other extreme, the DWT decomposes time series into wavelet packets in the time and frequency domain without any subjective judgment about window size, however, it has low time-domain resolution at long periods, making it difficult to control long-period properties of the simulations. The WPT is the extended version of DWT. It can have a constant resolution in the time and frequency domain, and its basis functions are orthogonal which allows reconstruction of time series from wavelet packets. Using the WPT, one can maintain temporal and spectral nonstationarities in the time and frequency domain. The stochastic ground motion model proposed here requires 13 model parameters and each parameter has a different role to control the time and frequency characteristics of simulated ground motions. Therefore, one can simulate ground motion with the target time and frequency characteristics.

Another important feature of the proposed stochastic ground motion model is the variability of simulated ground motions, as this affects the variability of structural responses. This is done in the proposed model by calibrating the variability of the predicted model parameters for a given earthquake scenario (e.g. Alamilla et al. 2001, Thráinsson and Kiremidjian 2002, Pousse et al. 2006, and Rezaeian 2010). The model parameters of the proposed stochastic model are predicted through two-stage regression analysis and random generation of these parameters makes simulated ground motions variable. The simulated ground motions from the proposed stochastic model are observed to have similar characteristics to existing ground motion prediction models in terms of the median and variability of spectral acceleration, inelastic response spectra (Bozorgnia and Campbell 2004), Arias intensity (Arias 1970), significant duration (Trifunac and Brady 1975), and mean period (Rathje et al. 2004). Therefore, one can use our simulations for structural design or hazard analysis.

As applications of the proposed model, simulation-based probabilistic seismic hazard analysis (PSHA) and simulation-based probabilistic seismic demand analysis (PSDA) are proposed. These models use simulated ground motions and Monte Carlo simulation to compute the probability that spectral acceleration (S_a) or engineering demand parameter (EDP) is greater than a particular threshold. Simulation-based PSDA in general requires more structural response analyses than current procedures to compute the hazard curves for EDP (Bazzurro 1998, Shome et al. 1998). However, the simulation-based PSDA does not require the use of a ground motion intensity measure, scaling of ground motions, or assumptions regarding functional forms and probability distributions of EDP values. Also, we can perform a deaggregation-like computation to determine the characteristics of the simulated ground motions that produce a given level of EDP, giving insights into ground motion properties that influence structural behavior and thus potentially informing procedures for selecting and scaling recorded ground motions. Thus, despite the procedure's computational expense, it serves as a potentially useful alternate method of evaluating structural reliability.

Further, simulation-based PSDA can be extended to drift hazard analysis that computes the rate of jointly exceeding specified thresholds for two or more EDP parameters–a calculation which is difficult to perform using recorded ground motions. To demonstrate, joint hazard contours (as opposed to hazard curves for a single parameter) of maximum interstory drift ratio (MIDR) and peak floor acceleration (PFA) are produced. Various points on these contours are deaggregated to identify response spectra associated with each, and the relationship between spectral shape, MIDR and PFA are discussed.

1.3 Contributions of this dissertation

1.3.1 Input ground motion of structural analysis

In order to obtain the seismic behavior of structures in terms of the probability distribution of engineering demand parameters, we need to use input ground motions that have appropriate characteristics for possible scenarios for the site of interest. Currently, the shape of spectral acceleration is considered representative of the characteristics of input ground motions; however, other parameters (e.g. duration, dominant period, bandwidth, Arias intensity, etc.) could also be important for structural response. Since the simulated ground motions have characteristics similar to the those observed in recorded ground motions, which are equivalent to the past research regarding median and variability (e.g. Alamilla et al. 2001, Thráinsson and Kiremidjian 2002, Pousse et al. 2006, and Rezaeian 2010), the relationship between the characteristics of ground motion and seismic structural behavior can be determined by using our simulated ground motions. This dissertation also discusses differences in structural responses obtained using our simulated ground motions and selected ground motions scaled to match conditional mean spectra.

1.3.2 Simulation-based Probabilistic Seismic Hazard Analysis and Probabilistic Seismic Demand Analysis

Since stochastic simulation using our stochastic model is computationally inexpensive, Monte Carlo simulations can be run using simulated ground motions to compute a hazard curve for any intensity measure such as S_a or EDPs such as maximum inter-story drift ratio (MIDR), which is difficult to compute from recorded ground motions because of the shortage in number of recorded ground motions for Monte Carlo simulations or the lack of the relationship between scaled ground motions and seismological parameters. Our hazard curves are directly computed from simulated ground motions, and thus don't require assumptions about features such as probability distributions of S_a or EDPs. Also deaggregations are computed for these hazard curves for spectral shapes and several other ground motion parameters. This dissertation discusses the relationship between engineering demand parameters and the characteristics of the simulated ground motions, and also presents studies of the spectral shape associated with ground motions producing a given level of EDPs.

1.4 Organization

This dissertation discusses the proposed stochastic ground motion model and its applications. Chapters 2 and 3 describe the stochastic ground motion model with time and frequency nonstationarity. Chapter 4 discusses the comparisons between the simulated ground motions and Ground Motion Prediction Models (GMPMs). Chapter 5 describes simulation based probabilistic seismic hazard analysis. Chapter 6 examines simulations in terms of the structural responses that they produce and Chapter 7 presents probabilistic seismic demand analysis as an application of simulated ground motions.

Chapter 2 describes the proposed stochastic ground motion model based on wavelet packets. This chapter describes the parameters that determine the time-frequency characteristics of the time series, and describes the structure of our model. It also presents the statistical tests carried out to show the validity of our model structure. Recordings from the 1994 Northridge California earthquake is employed for validation of ground motion simulation by considering the following aspects: spectral acceleration, inelastic spectral displacement, mean time, significant duration, mean frequency, bandwidth, and energy.

Chapter 3 presents the development of a two-stage regression analysis to determine the relationship between our model parameters and seismological information (moment magnitude, source-site distance, and site condition). This chapter explores the characteristics of our database, which is a subset of the NGA database. Then functional forms are fixed and the characteristics of residuals are checked. The relative importance of the model parameters is also discussed in terms of the effect of their uncertainty on the logarithmic standard deviation of the elastic spectral acceleration. Based on these results, we describe the limitations of our model.

Chapter 4 discusses comparisons between our simulations and GMPMs in terms of spectral acceleration, inelastic response spectra, Arias intensity, significant duration, mean period, and the normality and inter-period correlation structure of the prediction errors of spectral acceleration (ε). Based on this comparison, our simulations are judged to be equivalent to GMPMs in terms of the parameters compared in this chapter. These results suggest that the spectral accelerations from the proposed model are compatible with conditional mean spectra.

Chapter 5 computes the hazard curve of spectral acceleration using simulated ground motions and compares it with the comparable hazard curve computed using a GMPM. Since our simulation model is seen to be compatible with GMPMs in Chapter 4, the hazard curves are comparable. This chapter then explores the deaggregation of spectral shape, magnitude, Arias intensity, significant duration, and mean period. The spectral shape is similar to that of conditional mean spectra calculations, and this suggests the validity of conditional mean spectra (at least in cases where the hazard is dominated by a single scenario).

Chapter 6 explores nonlinear dynamic structural analysis using our simulations. Conditional mean spectra are compared with spectral shapes of simulated ground motions conditioned by spectral acceleration at the natural period. The empirical cumulative density function of ductility, maximum inter-story drift ratio, and peak floor acceleration are computed and compared with those from structural analysis using selected ground motion recordings.

Chapter 7 computes the hazard curves of the maximum inter-story drift ratio and peak floor acceleration using simulated ground motions. These hazard curves are currently difficult to compute using actual ground motion recordings because of the limited number of recordings. In addition, this chapter explores the deaggregation of spectral shape, magnitude, Arias intensity, significant duration, and mean period, and discusses the characteristics of this deaggregation.

Finally, Chapter 8 summarizes important findings presented in this dissertation.

Chapter 2

Stochastic ground motion model

2.1 Introduction

A stochastic ground motion model with time and frequency nonstationarity is developed using wavelet packets. The proposed model is based on Thráinsson and Kiremidjian (2002), which use Fourier amplitudes and phase differences to simulate ground motions and attenuation models to their model parameters. We extend their model using the wavelet packet transform, which is an extended version of the discrete wavelet transform. The wavelet packet transform is an operation that decomposes time series data into wavelet packets in the time and frequency domain, and its inverse transform reconstructs a time series from wavelet packets. The characteristics of a nonstationary ground motion can therefore be modeled intuitively by specifying the amplitudes of wavelet packets at each range of time and frequency. In the proposed model, 13 parameters are sufficient to describe the time and frequency characteristics of a ground motion. These parameters can be computed from a specific target ground motion recording, or a ground motion simulation can be produced given the target values of those 13 parameters. In this chapter a background on signal processing using Fourier analysis, wavelet analysis and wavelet packets is provided, in order to illustrate why the wavelet packet transform is an preferred method for analyzing or simulating ground motions. Additionally, a brief background on the physics of wave propagation is provided to motivate some of the parameterization choices used here. The wavelet packets resulting from a ground motion are then summarized using a model requiring 13 parameters, and the estimation of these parameters is discussed.

2.2 Techniques for characterizing time and frequency nonstationarity

Time and frequency nonstationarity describes the changing amplitudes of time series (temporal nonstationarity) and changing frequency characteristics (spectral nonstationarity) in time. Time and frequency nonstationarity can be expressed using the following parameters: 1) group delay time (Cohen 1995), 2) instantaneous frequency (Cohen 1995), 3) spectrogram (running Fourier spectra), and 4) wavelet analysis. These concepts are defined below.

The group delay time (t_g) is computed as follows:

$$t_g = -\frac{d\phi(\omega)}{d\omega} \tag{2.1}$$

$$X(\omega) = \int_{-\infty}^{\infty} x(t)e^{-i\omega t}dt = A(\omega)e^{i\phi(\omega)} \tag{2.2}$$

where $A(\omega)$ and $\phi(\omega)$ are the amplitude and phase angle of $X(\omega)$, respectively, and $X(\omega)$ is a Fourier transform of $x(t)$. The group delay time can express a mean time of each frequency component.

The instantaneous frequency (ω_i) is the same concept as the group delay time, but ω_i is computed using a analytic function $z(t)$ (Cohen 1995) in the time domain instead of $X(\omega)$ in the frequency domain. The analytic function $z(t)$ is a complex function, which is computed by the inverse Fourier transform of $2X(\omega)$ in $\omega \geq 0$.

$$z(t) = \frac{1}{2\pi}\int_{0}^{\infty} 2X(\omega)e^{i\omega t}d\omega \tag{2.3}$$

By definition, the real part of $z(t)$ is $x(t)$. Using the analytic function $z(t)$, ω_i is computed as follows:

$$\omega_i = \frac{d\psi(t)}{dt} \tag{2.4}$$

$$z(t) = a(t)e^{i\psi(t)} \tag{2.5}$$

where $a(t)$ and $\psi(t)$ are the amplitude and phase angle of the analytic function $z(t)$, respectively. The instantaneous frequency can express a mean frequency at each time step. The group delay time can describe the changing frequency characteristics in terms of mean time in each frequency component and the instantaneous frequency can describe the changing frequency characteristics in terms of mean frequency in each time step. However, it is difficult to fully describe the joint time and frequency characteristics by the group delay time or instantaneous frequency (e.g. multimodal functions).

The spectrogram ($P_{SP}(t,\omega)$) is computed by short-time Fourier transform or short-frequency inverse Fourier transform:

$$P_{SP}(t,\omega) = \left| \int_{-\infty}^{\infty} e^{-i\omega\tau} x(\tau) h(\tau - t) d\tau \right|^2 \tag{2.6}$$

$$= \left| \frac{1}{2\pi} \int_{-\infty}^{\infty} e^{i\omega' t} X(\omega') H(\omega - \omega') d\omega' \right|^2 \tag{2.7}$$

where $h(t)$ is a window function, and $H(\omega)$ is a Fourier transform of $h(t)$. The spectrogram describes the distribution of energy in the time and frequency domain for any time series data, and it can be computed very quickly using the Fast Fourier Transform (FFT). Choosing an effective window function is challenging, however, because a short window requires a wide bandwidth and cannot handle low frequency components. On the other hand, a long window produces poor resolution in the time domain. It is also difficult to reconstruct a time series data from the spectrogram.

In contrast, the continuous wavelet transform is defined as (Mallat 1999):

$$C_{s,l} = \int_{-\infty}^{\infty} x(t) \Phi_{s,l}(t) dt = \int_{-\infty}^{\infty} x(t) \frac{1}{\sqrt{s}} \Phi\left(\frac{t-l}{s}\right) \tag{2.8}$$

where $C_{s,l}$ are wavelet coefficients, l is an index associated with time, s is an index associated with frequency, and $\Phi\left(\frac{t-l}{s}\right)$ is the mother wavelet function and its time and frequency coverages are determined automatically. The wavelet packet transform is an modified version of the wavelet transform defined as follows:

$$c^i_{j,k} = \int_{-\infty}^{\infty} x(t) \psi^i_{j,k}(t) dt \tag{2.9}$$

where $x(t)$ is the time series, $c^i_{j,k}$ denotes the ith set of wavelet packets at the jth scale parameter and k is the translation parameter, and $\psi^i_{j,k}(t)$ is the wavelet packet function. Since $\psi^i_{j,k}(t)$ is localized on the time and frequency axes, the wavelet packets can control energy distribution in the time and frequency domain. Also it is possible to reconstruct a time series data from the wavelet packets using the inverse wavelet packet transform as follows:

$$x(t) = \sum_{i=1}^{2^j} \sum_{k=1}^{2^{N-j}} c^i_{j,k} \psi^i_{j,k}(t) \tag{2.10}$$

where 2^N is the number of data in the time series. The wavelet packets can describe the time and frequency characteristics with time and frequency resolutions determined by a selected wavelet function. Ideally the wavelet packet function is preferred with a time resolution as short as possible and with a frequency resolution as narrow as possible; however, because of the uncertainty principle (Mallat 1999), we cannot obtain wavelet packet function in which time and frequency resolutions are both arbitrarily small.

In this dissertation, we employ the wavelet packet transform for stochastic ground motion modeling because it can decompose a time series into wavelet packets in the time and frequency domain and can reconstruct a time series from wavelet packets.

2.3 Wavelet packet transform

The wavelet packet transform and the inverse wavelet packet transform are defined in equations 2.9 and 2.10, respectively. The characteristics of the wavelet packets depend on the characteristics of the wavelet packet function, which has to be orthogonal for the wavelet packet transform. For example, the Haar wavelet (Haar 1910) is a suitable wavelet to analyze the characteristics of time series on the time axis since it has complete compact time support; however, it has long tails on the frequency axis. The Sinc wavelet (Sugihara 1997) is a suitable wavelet to analyze the characteristics of time series on the frequency axis since it has complete compact frequency support; however, it has long tails on the time axis. In this dissertation, the wavelet packet function is computed from the finite-impulse-response-based approximation of the Meyer wavelet (Meyer 1986) because it is orthogonal and it has good localization property on the time axis as well as on the frequency axis. The parameter t_k and f_i are the central time and frequency of each wavelet packet coefficient $c^i_{j,k}$. Since $\psi^i_{j,k}(t)$ is localized around time t_k and frequency f_i, the wavelet packets can control the time and frequency characteristics of $x(t)$. The relationship between the time, frequency, and the wavelet domain of time series data is shown in Figure 2.1.

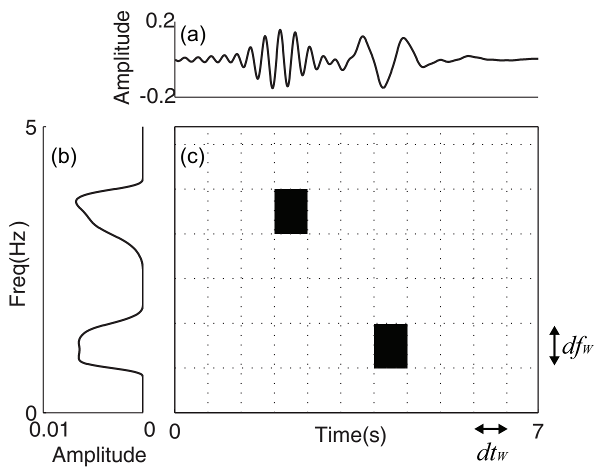

Figure 2.1: The relationship between the time, frequency, and wavelet domain. (a) time series, (b) Fourier spectrum, and (c) wavelet packets.

Figure 2.2 shows acceleration time series data of the 1994 Northridge California earthquake recorded at LABSN Station 00003 Northridge–17645 Saticoy Street (Saticoy St., $R_{hyp} = 18km$, $V_{S30} = 281m/s$) and at CGS–CSMIP Station 25091 Santa Barbara–UCSB Goleta (UCSB Goleta, $R_{hyp} = 123km$, $V_{S30} = 339m/s$) and their wavelet packets. The duration of the Saticoy St. recording is shorter than that of the UCSB Goleta recording, so the wavelet packets are located only at the beginning part of the waveform. The wavelet packets in the UCSB Goleta recording are located over a longer duration of time than those in the Saticoy St. recording. In the UCSB Goleta recording, the wavelet packets with high frequencies have very low amplitudes late in the recording. The reason for this phenomenon is that the high frequency components attenuate more rapidly with distance than the low frequency components and the later waves also include indirect waves that travel longer distances than the direct waves, and thus have lower frequency. This reasonably explains the observation in Figure 2.2 that spectral nonstationarity in the UCSB Goleta recording is stronger than that in the Saticoy St. recording. To describe this time and frequency nonstationarity, we compute the correlation coefficient between the time and frequency of the wavelet packets $\rho(t,f)$ because the mean frequency is changing almost monotonically. For example, $\rho(t,f)$ in the Saticoy St. recording is -0.07, and in the UCSB Goleta recording is -0.34. These both $\rho(t,f)$ are small, however, $\rho(t,f)$ has a relationship with the seismological parameters. Figure 2.3 shows the relationship between $\rho(t,f)$ and hypocentral distance of 153 recorded ground motions of the 1994 Northridge California earthquake. According to the figure, the correlations decrease with larger hypocentral distance, and this trend matches the observations in Figure 2.2. So one can describe the time and frequency nonstationarity by using $\rho(t,f)$.

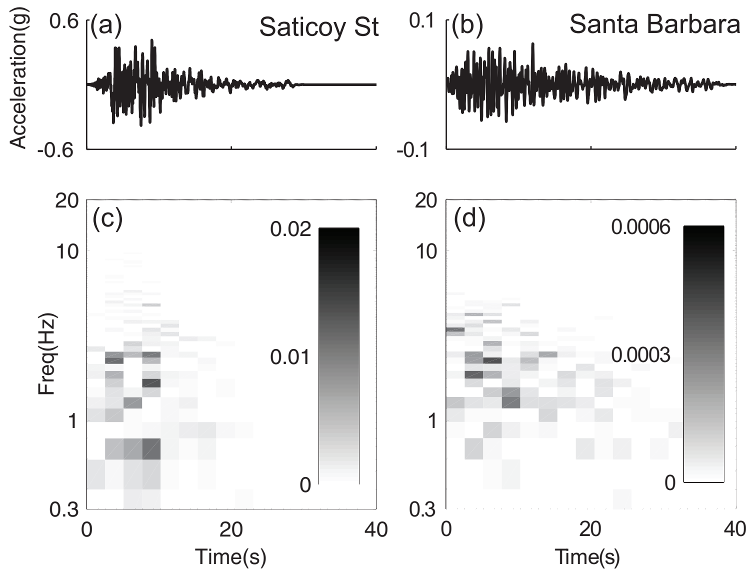

Figure 2.2: Wavelet packets for two example time series from the 1994 Northridge California earthquake. (a) acceleration time series, (c) squared wavelet packet from the Saticoy St. recording, (b) acceleration time series, and (d) squared wavelet packets from the UCSB Goleta recording. The color bars in (c) and (d) indicate the amplitude of the squared wavelet packets.

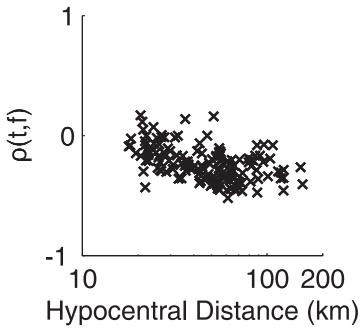

Figure 2.3: The relationship between the correlation and hypocentral distance of the acceleration time series data of the 1994 Northridge California earthquake.

2.4 Wavelet packet transform and EPSD

The evolutionary power spectral density (EPSD) can be estimated using continuous wavelet transform (Spanos and Failla 2004). The continuous wavelet transform provides a more detailed picture of time and frequency characteristics, but unlike the wavelet packet transform, it is difficult to obtain a time series. Here we approximate the EPSD using the wavelet packets. An arbitrary nonstationary process described by the following general form (Priestley 1996)

$$x(t) = \int_{-\infty}^{\infty} A(\omega,t)e^{i\omega t}d\bar{Z}(\omega) \tag{2.11}$$

where $A(\omega,t)$ is the time- and frequency-dependent modulating function, and $\bar{Z}(\omega)$ is a complex random process with orthogonal increments such that

$$E[d\bar{Z}(\omega)d\bar{Z}^*(\omega)'] = \begin{cases} S_{\overline{ff}}(\omega)d\omega & \omega = \omega' \\ 0 & \text{otherwise} \end{cases} \tag{2.12}$$

In equations 2.12, $E[\cdot]$ indicates an expectation; and $S_{\overline{ff}}(\omega)$ indicates the two-sided power spectral density (PSD) for the zero mean stationary process as follows:

$$\bar{x}(t) = \int_{-\infty}^{\infty} e^{i\omega t}d\bar{Z}(\omega) \tag{2.13}$$

Then, the two-sided EPSD of $x(t)$ is then defined as

$$S_{ff}(\omega,t) = |A(\omega,t)|^2 S_{\overline{ff}}(\omega) \tag{2.14}$$

The wavelet packets of the process $x(t)$ at a scale i can then be computed as

$$\begin{aligned} c^i_{j,k} &= \int_{-\infty}^{\infty} x(t)\psi^i_{j,k}(t)dt && (2.15)\\ &= \int_{-\infty}^{\infty} \left\{ \int_{-\infty}^{\infty} A(\omega,t)e^{i\omega t} d\bar{Z}(\omega) \right\} \psi^i_{j,k}(t)dt && (2.16)\\ &= \int_{-\infty}^{\infty} \left\{ \int_{-\infty}^{\infty} A(\omega,t)e^{i\omega t} \psi^i_{j,k}(t)dt \right\} d\bar{Z}(\omega) && (2.17) \end{aligned}$$

Due to the time localization properties of the wavelet $\psi^i_{j,k}(t)$ around the time t_k, it can be assumed that

$$c^i_{j,k} \approx \int_{-\infty}^{\infty} A(\omega,t_k) \left\{ \int_{-\infty}^{\infty} e^{i\omega t} \psi^i_j(t-t_k)dt \right\} d\bar{Z}(\omega) \tag{2.18}$$

Then set $t - t_k = \tau$ in the right-hand side of equation 2.18 to derive

$$\begin{aligned} c^i_{j,k} &\approx \int_{-\infty}^{\infty} A(\omega,t_k) \left\{ \int_{-\infty}^{\infty} e^{i\omega\tau} \psi^i_j(\tau)d\tau \right\} e^{i\omega t_k} d\bar{Z}(\omega) && (2.19)\\ &= \int_{-\infty}^{\infty} A(\omega,t_k)\Psi^i_j(\omega)e^{i\omega t_k} d\bar{Z}(\omega) && (2.20)\\ &= \int_{-\infty}^{\infty} A(\omega,t_k)e^{i\omega t_k} d\bar{Z}'(\omega) && (2.21) \end{aligned}$$

where

$$d\bar{Z}'(\omega) = \Psi^i_j(\omega)d\bar{Z}(\omega) \tag{2.22}$$

Now $\bar{Z}'(\omega)$ in equation 2.22 is a complex random process, that has the orthogonality property of $\bar{Z}(\omega)$. Therefore, it supports the statement that the wavelet packets at scale i, $c^i_{j,k}$ can be considered a nonstationary oscillatory process with respect to the time t_k. Specifically, the two-sided EPSD of $x(t)$ is given by

$$S_{WW}^{c^i_{j,k}} = |A(\omega,t)|^2 |\Psi^i_j(\omega)|^2 S_{\overline{ff}}(\omega) \tag{2.23}$$

Further, an expectation of squared $c^i_{j,k}$ can be defined by the equation

$$E[|c^i_{j,k}|^2] = \int_{\infty}^{\infty} S_{WW}^{c^i_{j,k}} d\omega \tag{2.24}$$

$$= \int_{0}^{\infty} |A(\omega,t)|^2 |\Psi^i_j(\omega)|^2 S_{\overline{ff}}(\omega) d\omega \tag{2.25}$$

Since $\Psi^i_j(\omega)$ is localized around ω_i,

$$E[|c^i_{j,k}|^2] \approx \int_{-\infty}^{\infty} |A(\omega,t)|^2 |\Psi^i_j(\omega)|^2 S_{\overline{ff}}(\omega) d\omega \tag{2.26}$$

Therefore $E[|c^i_{j,k}|^2]$ can be considered to be an approximation of the EPSD, and we can generate the time series data with particular time and frequency characteristics using the wavelet packets.

2.5 Parameters for time and frequency characteristics of time series

To control the time and frequency characteristics of the acceleration time series, we define the following five parameters:

$$E_{acc} = \int_{-\infty}^{\infty} |x(t)|^2 \, dt \tag{2.27}$$

$$E_{th}(t) = \int_{-\infty}^{\infty} t \, |x(t)|^2 \, dt / E_{acc} \tag{2.28}$$

$$\frac{\int_{t_5}^{t_5+t_{95-5}} |x(t)|^2 \, dt}{E_{acc}} = 0.9, \; \frac{\int_0^{t_5} |x(t)|^2 \, dt}{E_{acc}} = 0.05 \tag{2.29}$$

$$E_{th}(f) = \int_{-\infty}^{\infty} f \, |\hat{x}(f)|^2 \, df / E_{acc} \tag{2.30}$$

$$\frac{\int_{f_5}^{f_5+f_{95-5}} |\hat{x}(f)|^2 \, df}{E_{acc}} = 0.9, \; \frac{\int_0^{f_5} |\hat{x}(f)|^2 \, df}{E_{acc}} = 0.05 \tag{2.31}$$

where E_{acc} is the total energy of the acceleration time series, $E_{th}(t)$ is the temporal centroid, which is associated with the arrival time of the main part of the ground motion, t_{95-5} is the $5-95\%$ significant duration that contains 90% of the total energy, $E_{th}(f)$ is the spectral centroid, which is associated with the dominant frequency of the time series, and f_{95-5} is the $5-95\%$ significant bandwidth that contains 90% of the total energy. The total energy of the time series is approximately conserved in wavelet packets because of the orthogonality and the localization property of the wavelet packet function. To capture these parameters using wavelet packets, we employ the following equations:

$$E_{acc} = \sum_i \sum_k |c^i_{j,k}|^2 \tag{2.32}$$

$$E(t) = \sum_i \sum_k t_k \left| c^i_{j,k} \right|^2 / E_{acc} \tag{2.33}$$

$$S^2(t) = \sum_i \sum_k \{t_k - E(t)\}^2 \left| c^i_{j,k} \right|^2 / E_{acc} \tag{2.34}$$

$$E(f) = \sum_i \sum_k f_i \left| c^i_{j,k} \right|^2 / E_{acc} \tag{2.35}$$

$$S^2(f) = \sum_i \sum_k \{f_i - E(f)\}^2 \left|c^i_{j,k}\right|^2 / E_{acc} \tag{2.36}$$

where $E(t)$ is the temporal centroid, $S^2(t)$ is the temporal variance, $E(f)$ is the spectral centroid, and $S^2(f)$ is the spectral variance. These parameters are related to $E_{th}(t)$, t_{95-5}, $E_{th}(f)$, and f_{95-5} respectively, and the correlation of time and frequency of wavelet packets $\rho(t,f)$ as defined by Equation 2.37 is used to control the time and frequency nonstationarity. Figure 2.4 shows the relationship between wavelet packets and these parameters except E_{acc} because E_{acc} is independent of time and frequency.

$$\rho(t,f) = \frac{\sum_i \sum_k [t_k - E(t)][f_i - E(f)] \left|c^i_{j,k}\right|^2}{S(t)S(f)E_{acc}}. \tag{2.37}$$

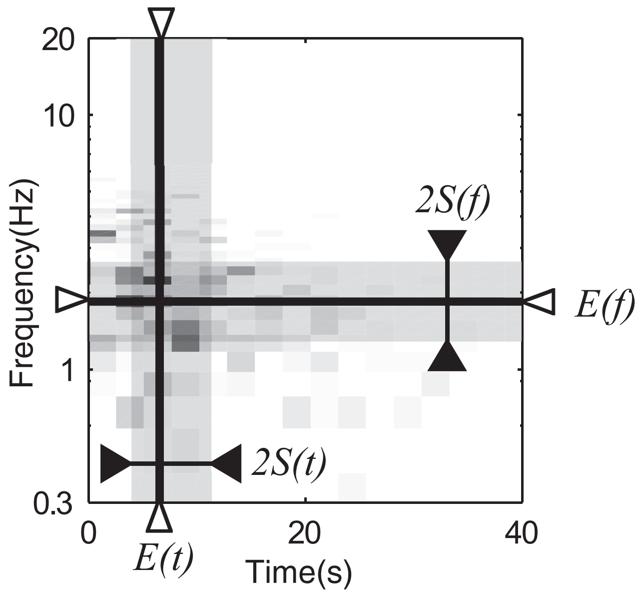

Figure 2.4: Relationship between the parameters($E(t)$, $S(t)$, $E(f)$, and $S(f)$) and the wavelet packets.

Figure 2.5 shows that the target characteristics are estimated well by the parameters of the wavelet packets. By controlling wavelet packets, we therefore can control the time and frequency characteristics of the time series.

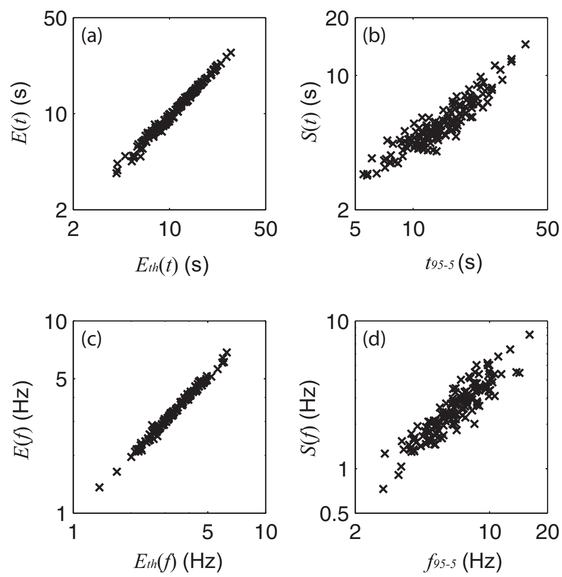

Figure 2.5: Comparison of parameters computed from time series and wavelet packets estimated for a large number of ground motions. (a) temporal centroid, (b) $5-95\%$ significant duration, (c) spectral centroid, and (d) significant bandwidth.

2.6 Stochastic model of ground motion using wavelet packet transform

In order to use the relationships above between time series properties and wavelet packets, our stochastic ground motion model employs two groups of wavelet packets (a major and minor group) because the wavelet packet transform is compressive which results in only a few wavelet packets having large amplitude and the rest having small or zero amplitude. The total wavelet packets are a combination of these two groups as follows:

$$|c^i_{j,k}|^2 = |c^i_{j,k,maj}|^2 + |c^i_{j,k,min}|^2 \tag{2.38}$$

where $c^i_{j,k,maj}$ and $c^i_{j,k,min}$ are the wavelet packets in the major and minor group, respectively.

The major group of wavelet packets are the largest amplitude packets, which together contain 70% of the total energy in the ground motion (typically this is less than 1% of the total number of wavelet packets, which is a number of time step times a number of frequency points). Hence,

$$\frac{\sum_{i,k} |c^i_{j,k,maj}|^2}{\sum_{i,k} |c^i_{j,k}|^2} = 0.7 \tag{2.39}$$

The remaining smaller packets are in the minor group. The ratio of energy in the major group is determined to maximize the difference of the characteristics (duration, bandwidth and mean frequency) of wavelet packets of the major and minor groups. We varied this ratio in increments of 5%, and of all cases considered 70% was observed to produce the best results. The ratio is independent of any seismological parameters in current model because of its simplicity; however further study is expected.

2.6.1 Major group of wavelet packets

The wavelet packets in the major group are strongly random in comparison with those in the minor group, therefore, the squared amplitudes and time-frequency locations of wavelet packets are modeled separately:

$$a_{maj} \sim Exponential[E(|c^i_{j,k,maj}|^2)] \tag{2.40}$$

$$\begin{bmatrix} t_{k,maj} & f_{i,maj} \end{bmatrix} \sim Lognormal[M_{maj}, \Sigma_{maj}] \tag{2.41}$$

where a_{maj} is the squared amplitudes of the wavelet packets in the major group $c^i_{j,k,maj}$, and M_{maj} and Σ_{maj} are defined by

$$M_{maj} = \begin{bmatrix} E(\ln t_{k,maj}) & E(\ln f_{i,maj}) \end{bmatrix} \tag{2.42}$$

$$\Sigma_{maj} = \begin{bmatrix} S^2(\ln t_{k,maj}) & Cov(\ln t_{k,maj}, \ln f_{i,maj}) \\ Cov(\ln t_{k,maj}, \ln f_{i,maj}) & S^2(\ln f_{i,maj}) \end{bmatrix} \tag{2.43}$$

where $t_{k,maj}$ and $f_{i,maj}$ are the center of the time and frequency location of the wavelet coefficients in the major group.

The squared amplitudes of $c^i_{j,k,maj}$ at the time $t_{k,maj}$ and the frequency $f_{i,maj}$ are independent and identically distributed (i.i.d.) exponential random variables with mean $E(|c^i_{j,k}|^2)$, and their time and frequency locations are i.i.d. bivariate lognormal random variables with mean vector and covariance matrix of $t_{k,maj}$ and $f_{i,maj}$. The locations are independent of amplitudes. Figure 2.6 shows normal quantile-quantile plots for $t_{k,maj}$, $f_{i,maj}$, and $a^i_{j,k,maj}$ from the Saticoy St. recording, and the linear trends observed in Figure 2.6. It support the proposed probabilistic rules for the wavelet packets in the major group are appropriate. Figure 2.7 shows the relationship of a_{maj} and $t_{k,maj}$, and a_{maj} and $f_{i,maj}$ for one example ground motion. Based on this figure and many similar calculations for other ground motions, we assume that A_{maj} is independent of $t_{k,maj}$ and $f_{i,maj}$.

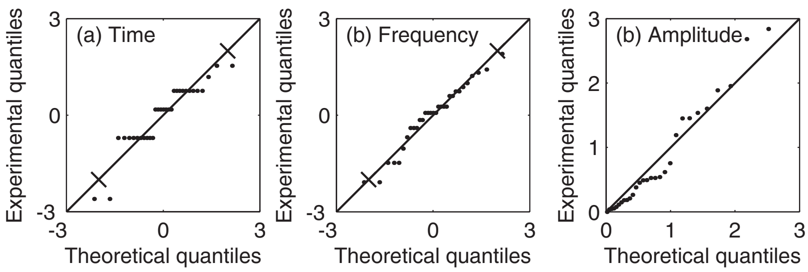

Figure 2.6: Quantile-Quantile plot of the wavelet packets in the major group from the recorded ground motion of the 1994 Northridge California earthquake at LABSN Station 00003 Northridge–17645 Saticoy Street [$R_{hyp} = 18km$, $V_{S30} = 281m/s$] (a) time of major coefficients versus standard normal distribution, (b) frequency of major coefficients versus standard normal distribution, (c) amplitude of major coefficients versus exponential distribution.

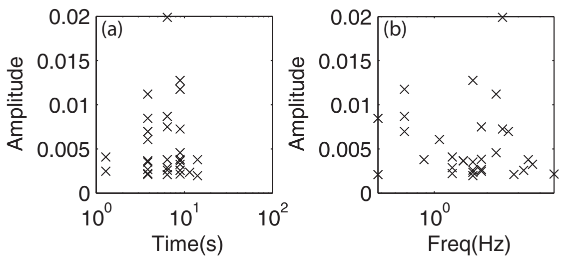

Figure 2.7: Relationship between amplitude and time, and amplitude and frequency of the wavelet packets in the major group from the 1994 Northridge California earthquake recorded at LABSN Station 00003 Northridge–17645 Saticoy Street [$M = 6.7$, $R_{hyp} = 18km$, $V_{S30} = 281m/s$] recorded ground motion (a) amplitudes of major coefficients versus time, (b) amplitudes of major coefficients versus frequency.

2.6.2 Minor group of wavelet packets

The modeling of the Fourier amplitudes are done by the lognormal density function by Sabetta and Pugliese (1996) and Thráinsson and Kiremidjian (2002) to fit the Fourier amplitudes of recorded ground motions. Since the squared wavelet packets in the frequency axis have the characteristics similar to the Fourier amplitudes, it is reasonable to apply the lognormal function to the frequency characteristics of the wavelet packets. Here the wavelet packets distribution in the minor group are estimated by the bivariate lognormal functions of the time and frequency and residuals. The bivariate lognormal function is a simple function and it requires only five parameters to control its characteristics. This function is selected based on the quality to fit the squared amplitudes of the wavelet packets in the minor group.

First, we define X and Y as the natural log of time and frequency.

$$X_k = \ln(t_k), \;\; Y_i = \ln(f_i) \tag{2.44}$$

The bivariate lognormal function to fit $|c^i_{j,k,min}|^2$ is then given by

$$|c^i_{j,k,min}|^2 = \overline{|c^i_{j,k,min}|^2} \times \xi_{k,i} \tag{2.45}$$

where $\overline{|c^i_{j,k,min}|^2}$ is bivariate lognormal function to fit $|c^i_{j,k,min}|^2$, which is defined as follows:

$$\overline{|c^i_{j,k,min}|^2} = \frac{1}{2\pi S(X)S(Y)\sqrt{(1-\rho(X,Y)^2)}} \times \frac{1}{X_k Y_i} \exp\left[-\frac{A^2 - 2R(X,Y)AB + B^2}{2\{1-\rho^2(X,Y)\}}\right] \tag{2.46}$$

where, A and B are defined as:

$$A = \frac{X_k - E(X)}{S(X)}, \; B = \frac{Y_i - E(Y)}{S(Y)} \tag{2.47}$$

where t_k and f_i are the central location of $c^i_{j,k,min}$ in the time and frequency axes, respectively, ρ is the correlation coefficient of $\ln(t_k)$ and $\ln(f_i)$, and $\xi_{k,i}$ are i.i.d. lognormal random variables with median one and logarithmic standard deviation of the residual of the wavelet packets in the minor group computed from the bivariate lognormal function. Figure 2.8 shows fitting lognormal functions to the normalized wavelet packet amplitudes in time axis and frequency axis, and normal quantile-quantile plots for $\xi_{k,i}$ from the Saticoy St. recording. Figure 2.8 supports our assumed bivariate lognormal function for the wavelet packets in the minor group.

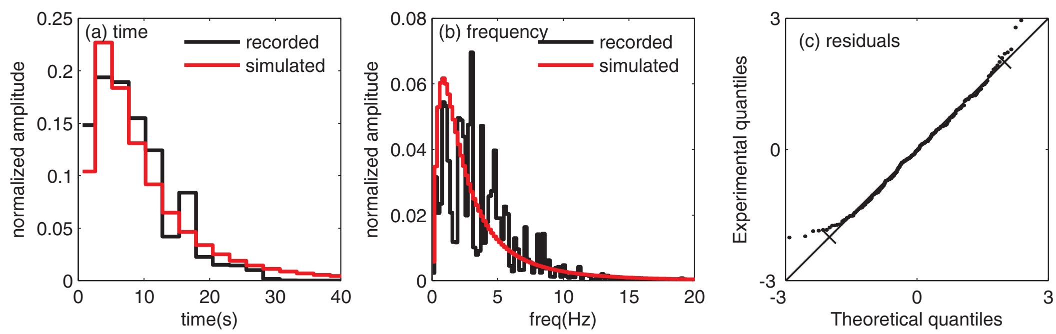

Figure 2.8: Test of modeling of the wavelet packets in the minor group from the recorded ground motion of the 1994 Northridge California earthquake at LABSN Station 00003 Northridge–17645 Saticoy Street [$R_{hyp} = 18km$, $V_{S30} = 281m/s$] (a) fitting of lognormal function in time axis, (b) fitting of lognormal function in frequency axis, (c) Quantile-Quantile plot of the residuals of the wavelet packets.

The time and frequency parameters in the previous section can be computed by combining the parameters of the major and minor group. Therefore, 13 parameters are required in this model: one each of $E(t)$, $S(t)$, $E(f)$, $S(f)$, and $\rho(t,f)$ for both the major and minor groups, $E(a^i_{j,k,maj})$, and E_{acc} for total energy, and the standard deviation of $\xi_{k,i}$. Since the proposed stochastic model provides the squared wavelet packets in the time and frequency domain, the sign of the wavelet packet is also needed to reconstruct the time series data. Here a random sign is applied because a variety of tests suggested that valuation in this choices did not significantly affect ground motion properties of interest (such as spectral acceleration).

2.6.3 Other modeling details

Some minor restrictions on the time and frequency boundaries of recorded ground motions are required, in order to avoid unreasonably prolonged small-amplitude shaking in the time axis and to avoid residual velocity. In the minor group, the stopping time of the wavelet packets at each frequency level i is the temporal centroid $+2S(t)$ given f_i of the minor group. Also the stopping time in the major group is the temporal centroid $+1S(t)$ given f_i of the minor group. Therefore the wavelet packets in the major group are located within the main part of the ground motion.

The approximate time interval (dt_w) and frequency interval (df_w) between the center of adjacent wavelet packets can be defined as follows:

$$dt_w = \frac{2^N dt}{2^{N-j}} = 2^j dt \tag{2.48}$$

$$df_w = \frac{f_N}{2^j} = \frac{1}{2dt}\frac{1}{2^j} \tag{2.49}$$

where 2^N is the number of data in the time series, j is the scale parameter (decomposition level), dt is the time difference of time series, and f_N is the Nyquist frequency. In our model, the maximum wavelet decomposition level is decided by $df_w = 0.1953Hz$ because dt_w is $2.56s$ for this level. Only the lowest frequency level is divided at $0.0977Hz$; therefore, the longest applicable period that can be modeled in the frequency domain is $10.24s$. We decided to use two types of frequency intervals to obtain longer applicable period and to set zeros to the wavelet packets in the lowest frequency level because the wavelets at this level would produce non-zero residual velocities. The number of wavelet packets of the recorded ground motions to estimate the model parameters equals to the number of their time steps. The number of wavelet packets to simulate ground motion can be controlled by the maximum time steps required.

A trigger time correction was necessary when estimating the parameters because some model parameters (e.g. $E(t)$) are specified relative to the starting time of the recording. We defined the trigger time in a recording as the time when the absolute value of the time series crossed 1% of PGA, in order to have a consistent starting time in each recording. The recorded time series used to calibrate the model were truncated by the bandpass filters in the frequency domain to remove noise, and the filtered frequencies differed from ground motion to ground motion, which make it difficult to directly estimate mean frequencies in the motions. To address this problem, we estimated the parameters of the target ground motions using the Maximum Likelihood Method, noting the filter frequencies in the likelihood formulation (appendix B). We assumed that only the wavelet packets in the minor group are bandpass filtered. Therefore, the total energy E_{acc} can vary based on the extrapolation of the wavelet packets in the minor group outside the bandpass filter. However, since this is only for the wavelet packets in the minor group and only for the tail of the lognormal distribution, this difference is very small.

2.7 Simulation of target ground motions

Using our stochastic ground motion model, we considered 153 ground motion recordings from the 1994 Northridge California earthquake ($M = 6.7$). We estimated the 13 model parameters for each of these recordings using the Maximum Likelihood Method (appendix B). We then generated 300 simulated motions for each of the 153 targets and computed the wavelet packets, Fourier spectra, spectral acceleration (S_a), inelastic spectral displacement (S_d), median of $E_{th}(t)$, t_{95-5}, mean period (T_m, Rathje et al. 2004), f_{95-5}, and $\rho(t, f)$, and Arias intensity (I_a, Arias 1970) for each simulated ground motion.

Figures 2.9 and 2.10 show two acceleration time series recorded at near and far distances, respectively, and selected simulated ground motions whose response spectra are the closest to the median of the response spectra of the recorded ground motions. For the recorded ground motions, in the far field, PGA is smaller, $S(t)$ is larger, $\rho(t,f)$ is smaller, and $S(f)$ is smaller than those in the near field. The simulations obtained from the proposed model reflect these characteristics, which are observed empirically and expected theoretically.

Pseudo velocity response spectra of the recorded and simulated ground motions are shown in Figure 2.11 with recorded ground motions. The pseudo velocity response spectra of the simulated ground motions reasonably match those of the recorded ground motions. In the far field, the median of the pseudo velocity response spectra of simulated ground motions is larger than that of the pseudo velocity response spectra from the recorded ground motion at long periods because the recorded ground motion in the far field has been truncated by the high-pass filter at $0.2Hz$ and it does not have any amplitude with a period larger than $5s$. In the proposed model, the wavelet packets are extrapolated beyond the truncation in the frequency domain because the parameters are estimated using the maximum likelihood estimation approach described in appendix B.

Acceleration Fourier spectra of the recorded and simulated ground motions are shown in figures 2.12 and 2.13. Peak frequency, bandwidth, and shape of the Fourier spectra of the simulated ground motion reasonably match those of the recorded ground motions. In the far field, the Fourier amplitudes of the recorded ground motion at low frequencies have a discontinuity around $0.2Hz$ because of high-pass filtering. Therefore the Fourier amplitudes of the simulated ground motion are larger than those of the recorded ground motion at low frequencies in Figure 2.13.

Acceleration, velocity, and displacement time series of the simulated ground motions are shown in figures 2.14 and 2.15 with recorded ground motions. PGA, PGV, PGD, and waveforms of the simulated ground motions reasonably match those of the recorded ground motions. In the far field, the displacements of the simulated ground motion are larger than those of the recorded ground motion because of the recorded motion is missing its low frequencies (which contribute significantly to displacement).

Figures 2.16 and 2.17 compare the median of elastic S_a and inelastic S_d with 5% damping ratio, respectively, of the recordings and associated simulations. For inelastic SDOF system, we employ a non-deteriorating bilinear oscillator with a positive hardening stiffness ratio $\alpha = 0.05$ (Chopra 2007). The SDOF model is controlled by ductility μ, which is the ratio of a maximum displacement to a yield displacement. These figures show that the two match reasonably well except for the PGA, $S_a(0.2s)$ and inelastic $S_d(0.2s)$.

In Figure 2.18, the medians of several other ground motion parameters reasonably match those of their target recordings except for the duration parameter t_{95-5}. The parameter t_{95-5} of the simulations tends to be longer than that of the target recordings in the case of short duration because the stopping time of the recordings as well as the trigger time are unknown and also because we set the time difference between adjacent wavelet packets to $2.56s$ to obtain the frequency resolution less than $0.1Hz$. Additionally, since PGA, S_a and inelastic S_d in short periods are negatively correlated to duration, PGA and S_a in short periods from the simulated ground motions are slightly smaller than those from the target recordings.

To provide further validations, Appendix C provides results similar to those shown in this chapter for recordings from the 1999 Chi-Chi, Taiwan, earthquake. All observations are similar to those observed here from the 1994 Northridge California earthquake recordings.

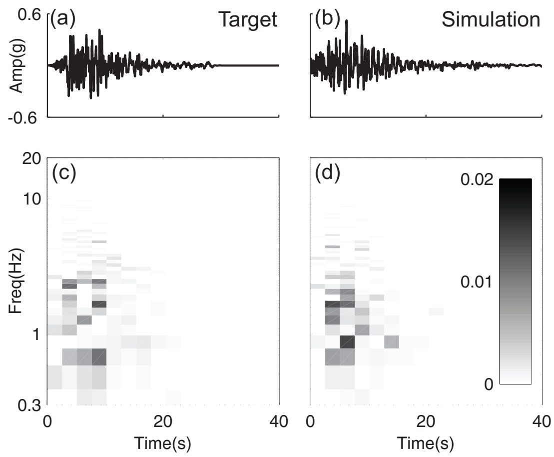

Figure 2.9: Simulation of recorded ground motion from the 1994 Northridge California earthquake at LABSN Station 00003 Northridge–17645 Saticoy Street [$R_{hyp} = 18km$, $V_{S30} = 281m/s$] (a) acceleration time series of recorded ground motion, (b) simulated time series, (c) wavelet packets of recorded ground motion, and (d) wavelet packets of simulated time series.

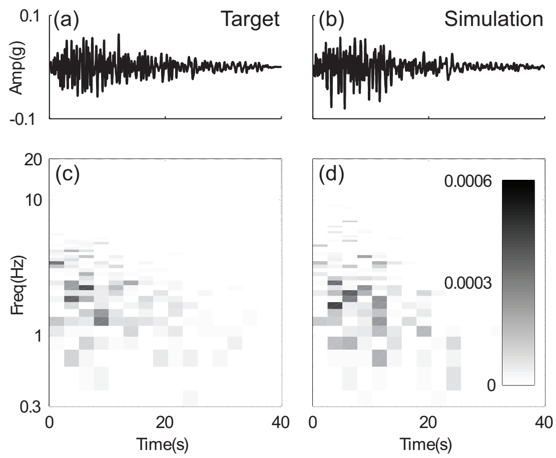

Figure 2.10: Simulation of recorded ground motion from the 1994 Northridge California earthquake at CGS–CSMIP Station 25091 UCSB Goleta–UCSB Goleta [$R_{hyp} = 123km$, $V_{S30} = 339m/s$] (a) acceleration time series of recorded ground motion, (b) simulated time series, (c) wavelet packets of recorded ground motion, and (d) wavelet packets of simulated time series.

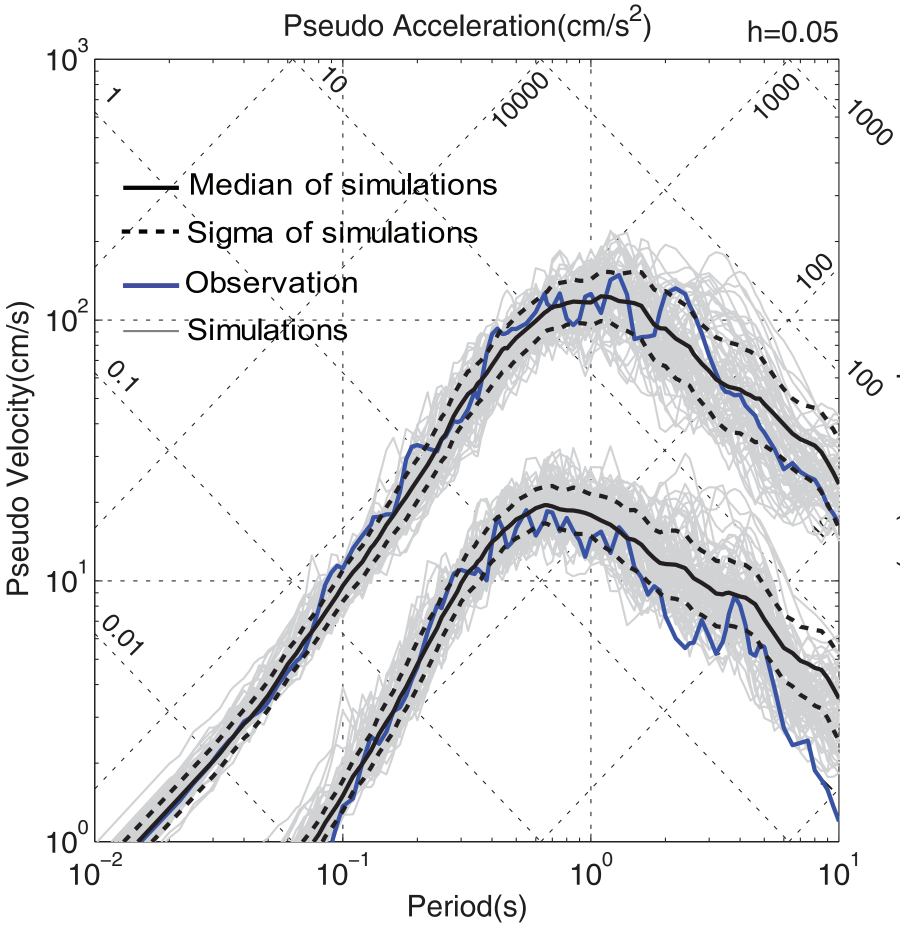

Figure 2.11: Pseudo velocity response spectra of simulated ground motion at near field and far field.

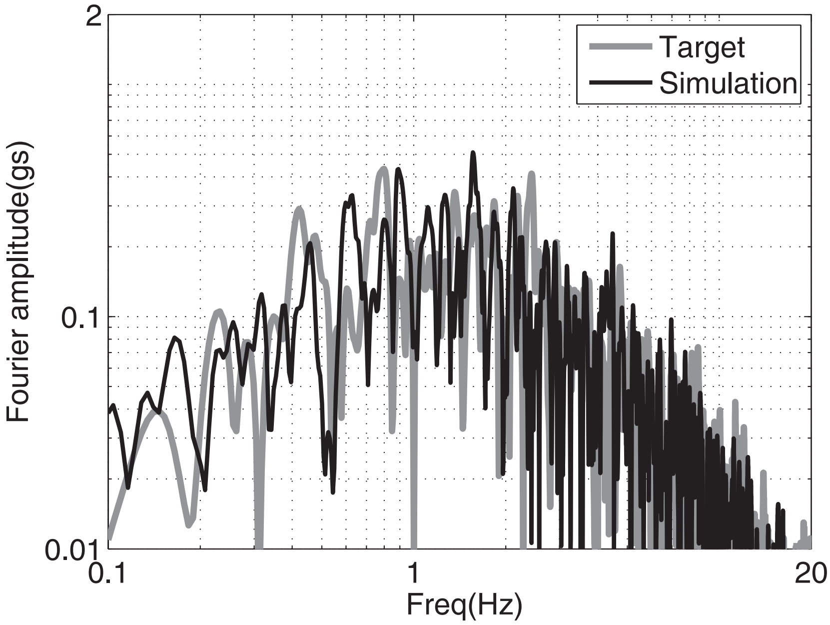

Figure 2.12: Acceleration Fourier spectra of simulated and recorded ground motion of the 1994 Northridge California earthquake at LABSN Station 00003 Northridge–17645 Saticoy Street [$R_{hyp} = 18km, V_{S30} = 281m/s$].

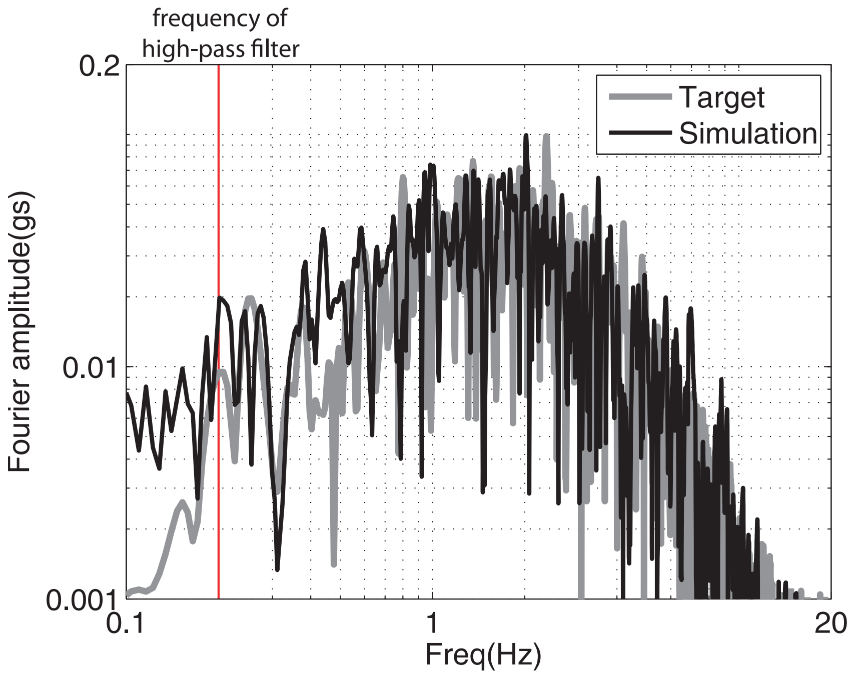

Figure 2.13: Acceleration Fourier spectra of simulated and recorded ground motion of the 1994 Northridge California earthquake at CGS–CSMIP Station 25091 Santa Barbara–UCSB Goleta [$R_{hyp} = 123km, V_{S30} = 339m/s$].

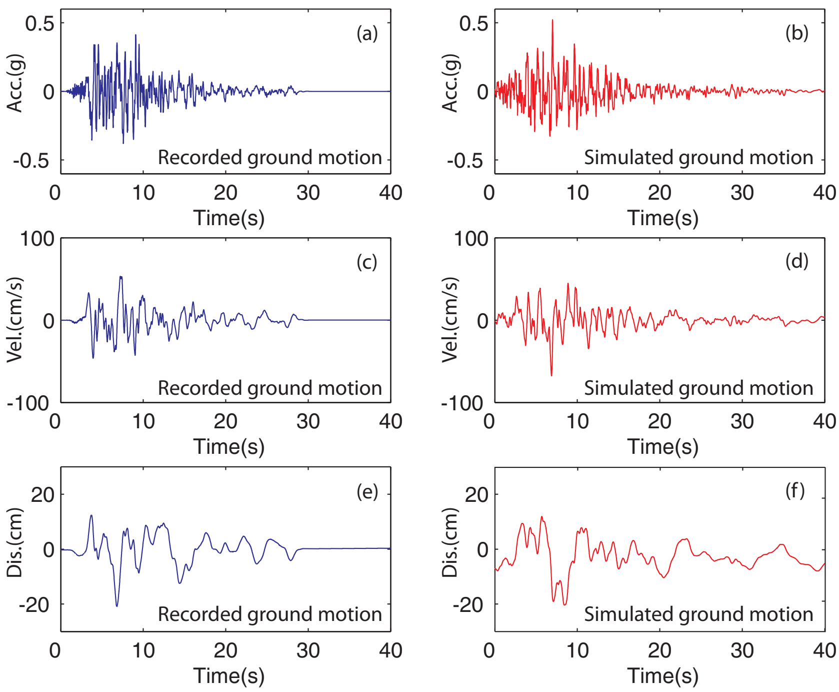

Figure 2.14: Recorded and simulated ground motion of the Northridge California earthquake at LABSN Station 00003 Northridge–17645 Saticoy Street (a) and (b) acceleration(g), (c) and (d) velocity (cm/s), and (e) and (f) displacement (cm) for recorded and simulated ground motion, respectively.

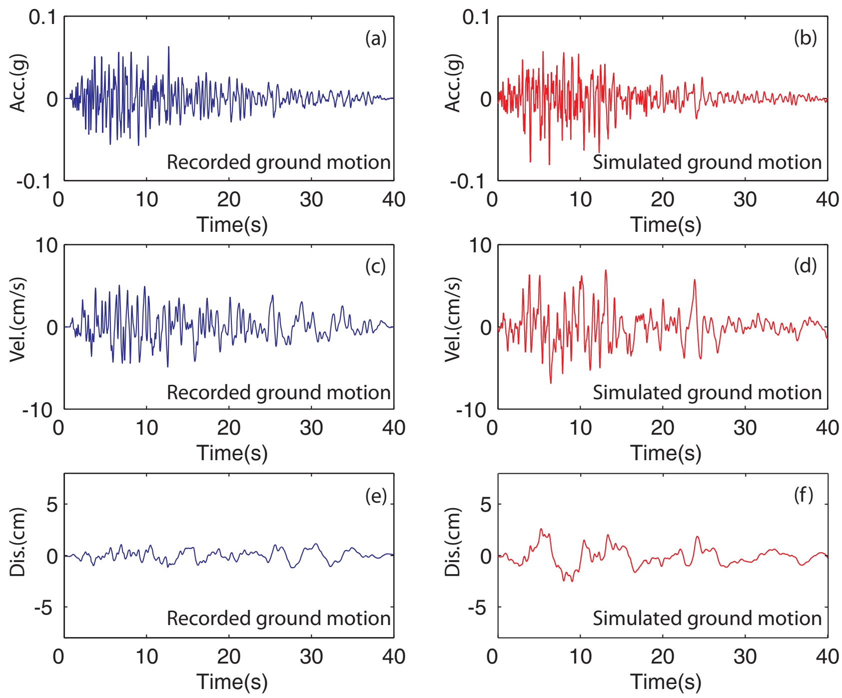

Figure 2.15: Recorded and simulated ground motion of the 1994 Northridge California earthquake at CGS–CSMIP Station 25091 Santa Barbara–UCSB Goleta (a) and (b) acceleration(g), (c) and (d) velocity (cm/s), and (e) and (f) displacement (cm) for recorded and simulated ground motion, respectively.

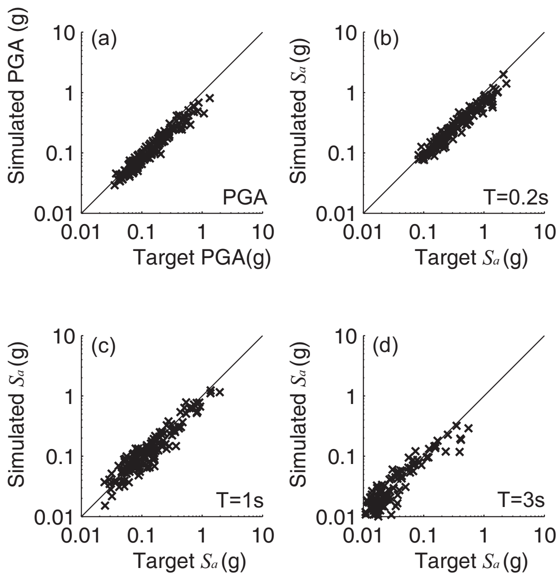

Figure 2.16: PGA and S_a from target time series versus median of corresponding value from simulations. (a) PGA, (b) S_a at $T = 0.2s$, (c) S_a at $T = 1s$, and (d) S_a at $T = 3s$.

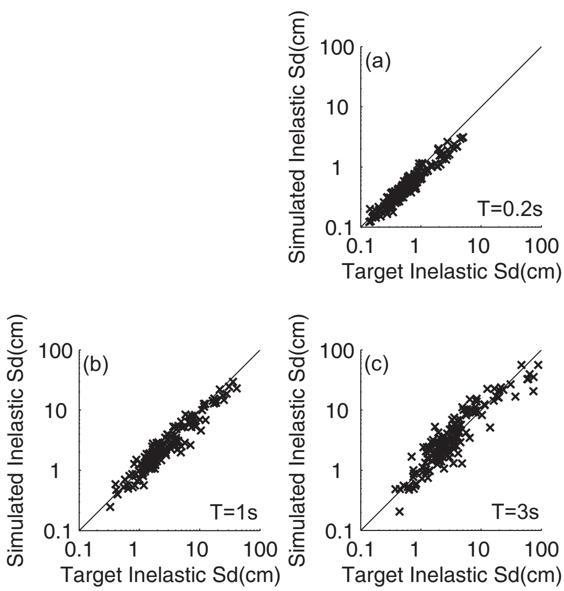

Figure 2.17: Median of inelastic S_d with ductility $\mu = 8$ between target time series and simulations. (a) S_d at $T = 0.2s$, (b) S_d at $T = 1s$, and (c) S_d at $T = 3s$.

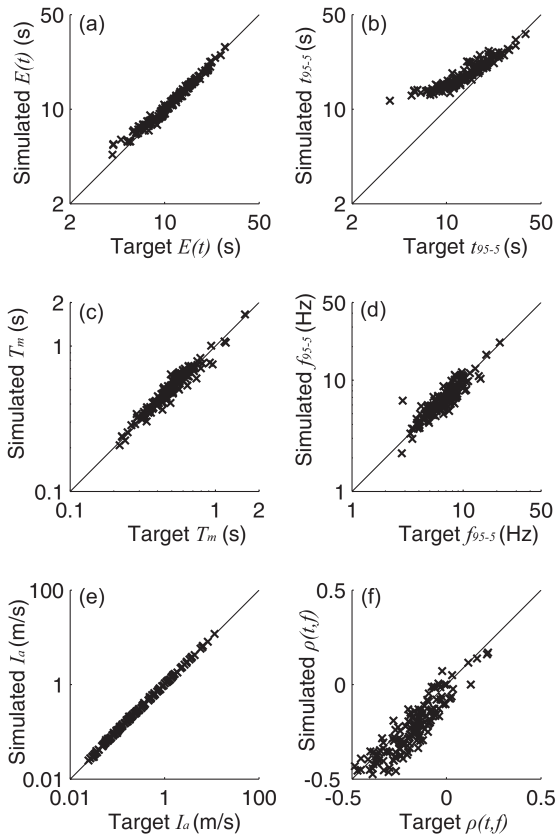

Figure 2.18: Model parameters from the target time series versus the median of the corresponding parameter from 300 simulations. (a) temporal centroid, $E(t)$, (b) significant duration, t_{95-5}, (c) mean period, T_m, (d) significant bandwidth, f_{95-5}, (e) Arias intensity (I_a), and (f) correlation of wavelet packets between time and frequency, $\rho(t,f)$.

2.7.1 Characteristics of median and logarithmic standard deviation of spectral acceleration using simulation from our stochastic model

One important characteristic of simulated ground motions is the logarithmic standard deviation of spectral acceleration ($\sigma_{\ln S_a}$). To examine the characteristics of $\sigma_{\ln S_a}$ of the proposed model, we generated time series data from four types of wavelet packets (Figure 2.19): (A) normal distribution with mean zero and standard deviation one for all time steps and periods, (B) normal distribution with mean zero and standard deviation three around 3s in period and 25s in time, keeping the other wavelet packets are the same as (A), (C) normal distribution with mean zero and standard deviation three around 1s in period and 25s in time, keeping the other wavelet packets are the same as (A), and (D) normal distribution with mean zero and standard deviation three around 0.1s in period and 25s in time, keeping the other wavelet packets are the same as (A). We generated 300 samples for each case and compared the median and logarithmic standard deviation of S_a. Figures 2.20 and 2.21 show S_a and the median and logarithmic standard deviation of S_a of (A) and (B), and (C) and (D), respectively. Figure 2.22 shows the median and logarithmic standard deviation of S_a of all cases. The logarithmic standard deviations, $\sigma_{\ln S_a}$, become larger with increasing period in all cases, and there are also large $\sigma_{\ln S_a}$ for (B), (C), and (D) around periods of large wavelet packets. The $\sigma_{\ln S_a}$ of large wavelet packets decreases with decreasing period. The reason is that a wavelet packet in a long period (low frequency) has larger coverage. Therefore fluctuations of a wavelet packet in long periods can affect spectral acceleration more than fluctuations in short period.

Figure 2.23 shows median and logarithmic standard deviation of S_a of simulated ground motions for four target recorded ground motions with periods normalized by T_m. Two trends appear in these figures. First, $\sigma_{\ln S_a}$ becomes larger in period as shown in the Figure 2.22. Second, $\sigma_{\ln S_a}$ increase significantly around $T/T_m = 1$.

This increase in $\sigma_{\ln S_a}$ arises from the spectral shapes of the transfer functions of a single degree of freedom (SDOF) system. The spectral acceleration at T is affected by long period components more than by short period components because the transfer function of a SDOF system with natural period T has larger amplitudes in periods$> T$ than in periods$< T$.

The peak spectral accelerations are around $T/T_m = 1$. Therefore the spectral accelerations at $T/T_m < 1$ are greatly influenced by the peak Fourier amplitudes, and the $\sigma_{\ln S_a}$s at $T/T_m < 1$ are dominated by $\sigma_{\ln S_a}$s around $T/T_m = 1$ and smaller than those at $T/T_m > 1$.

The median and logarithmic standard deviation of the acceleration Fourier spectra of the recorded ground motions are shown in Figure 2.24. The logarithmic standard deviations of the acceleration Fourier spectra do not increase in period. Therefore the variability of the Fourier amplitude of each frequency is independent of periods and it is different from the variability of the spectral acceleration. Since the characteristics of the wavelet packets in the frequency axis are similar to the characteristics of Fourier amplitudes, we need to study more about the relationship between the variability of Fourier amplitudes and spectral accelerations in order to simulate ground motions with low logarithmic standard deviation of spectral acceleration.

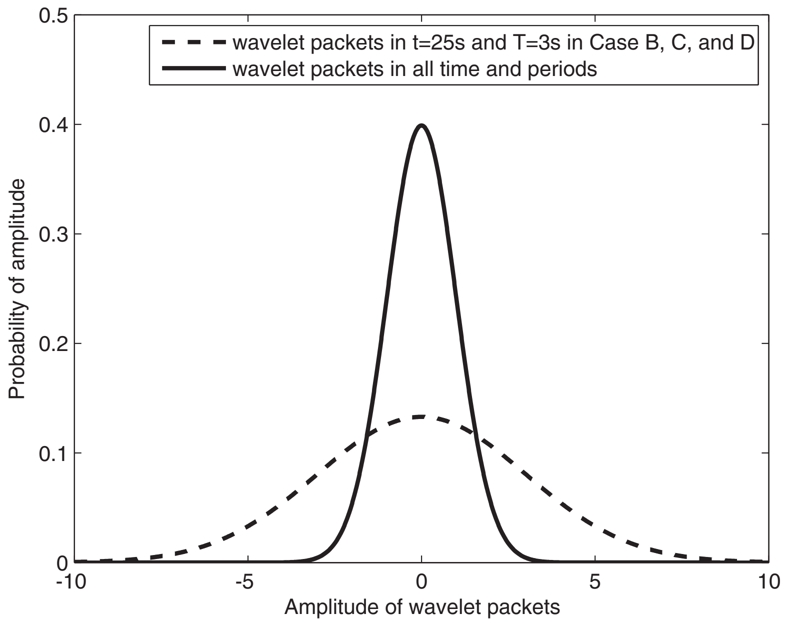

Figure 2.19: Probability density function of amplitudes of wavelet packets.

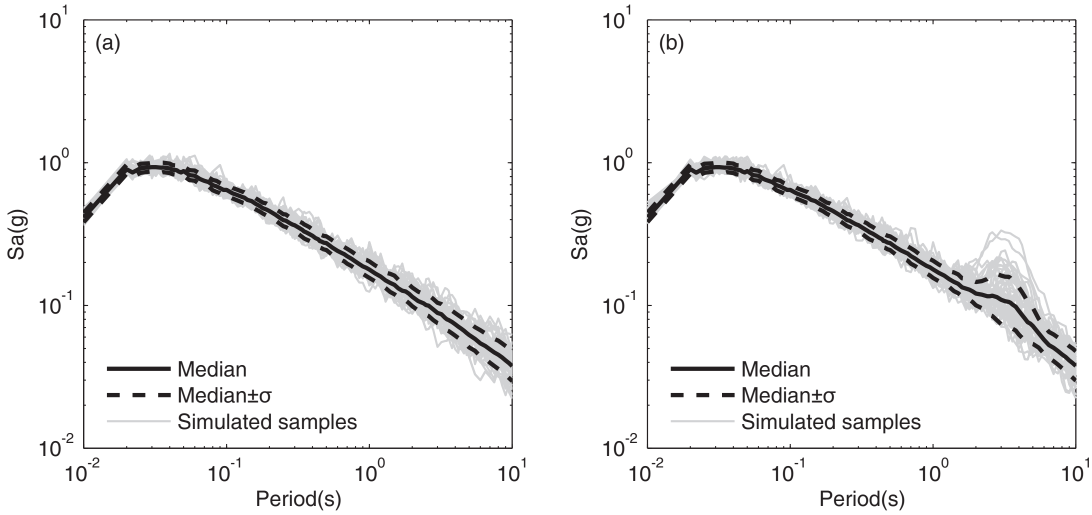

Figure 2.20: S_a of time series data from random wavelet packets (a) random, and (b) add large variability only around time=25s and T=3s.

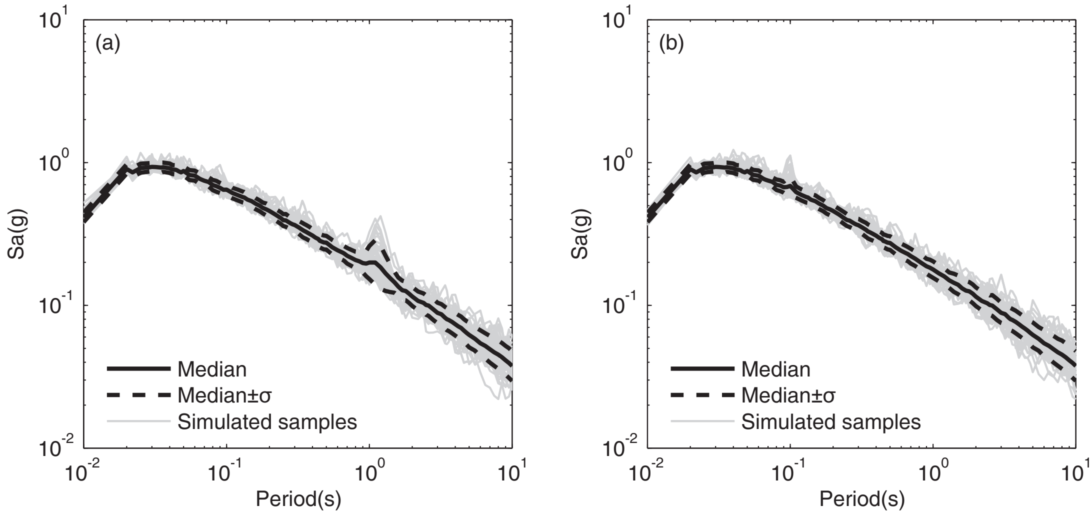

Figure 2.21: S_a of time series data from random wavelet packets (a) add large amplitude only around time=25s and T=1s, and (b) add large amplitude only around time=25s and T=0.1s.

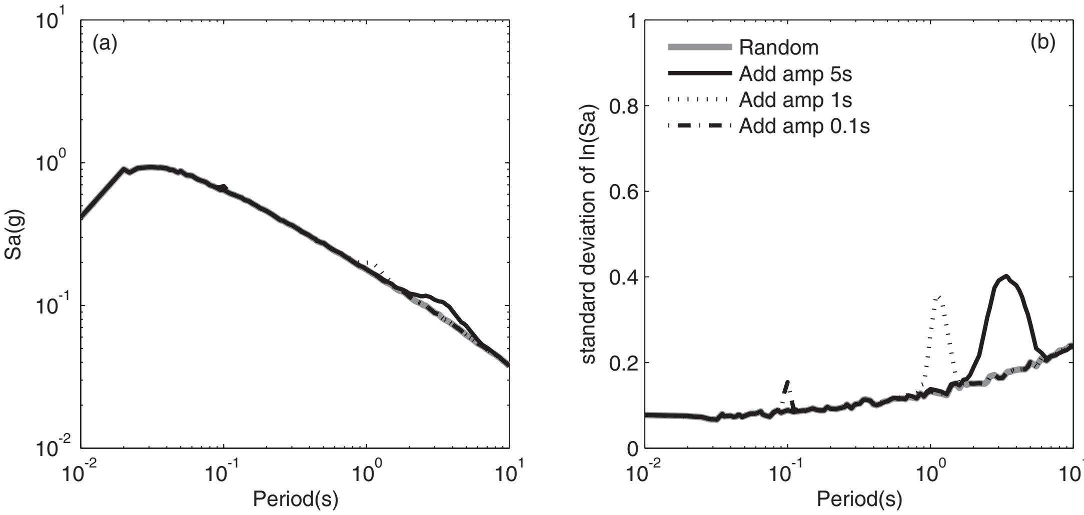

Figure 2.22: S_a of time series data from random wavelet packets (a) median S_a, and (b) logarithmic standard deviation of S_a.

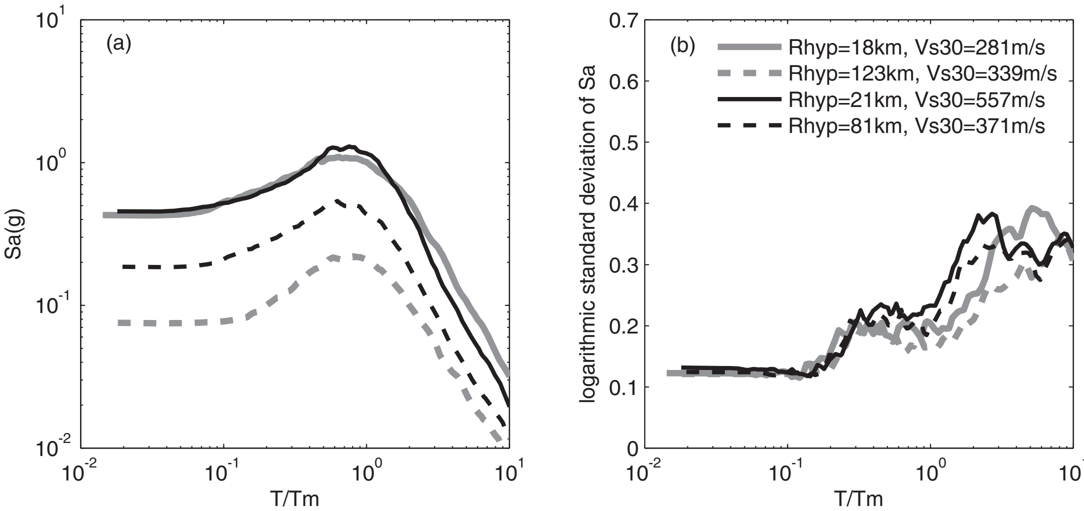

Figure 2.23: Comparison of spectral accelerations from five types of recorded ground motions (a) Median, and (b) logarithmic standard deviation of spectral acceleration.

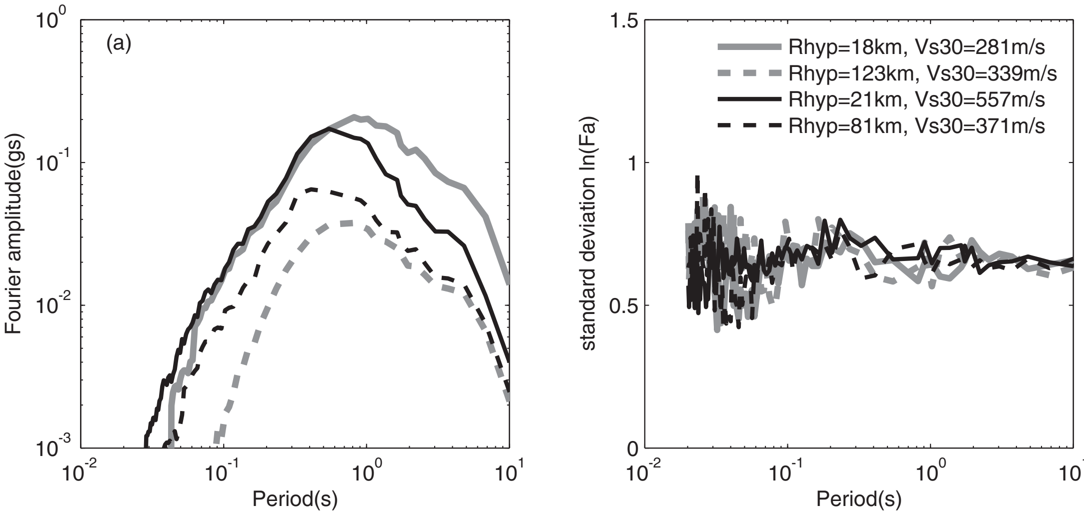

Figure 2.24: Comparison of acceleration Fourier spectra from five types of recorded ground motions (a) Median, and (b) logarithmic standard deviation of acceleration Fourier spectra.

2.7.2 Relative importance of four types of random variables in our stochastic model

The impact of random variables in the proposed model is examined by comparing the simulated ground motions with the ground motion of the 1994 Northridge California earthquake recorded at LABSN Station 00003 Northridge–17645 Saticoy Street. Four types of random variables are included in the proposed model: the residuals of the wavelet packets from bivariate lognormal function in the minor group, the time-frequency location of the wavelet packets in major group, the amplitudes of the wavelet packets in the major group, and the sign of the wavelet packets. Figures 2.25, 2.26, and 2.27 show the S_a from simulated ground motions with one of each type of random variables described above. The random variable of the residuals of the wavelet packets in the minor group affects only S_a with small amplitudes since the amplitudes of the wavelet packets in the minor group are smaller than those in the major group.

The location and amplitudes of the wavelets in the major group, therefore, affect the S_a

around the peak spectral acceleration.

The random sign affects S_a at all periods since it changes the wavelet packets in both the major and the minor group. Based on the logarithmic standard deviation of S_a, the influence of the random sign is the same as that of the other random variables.

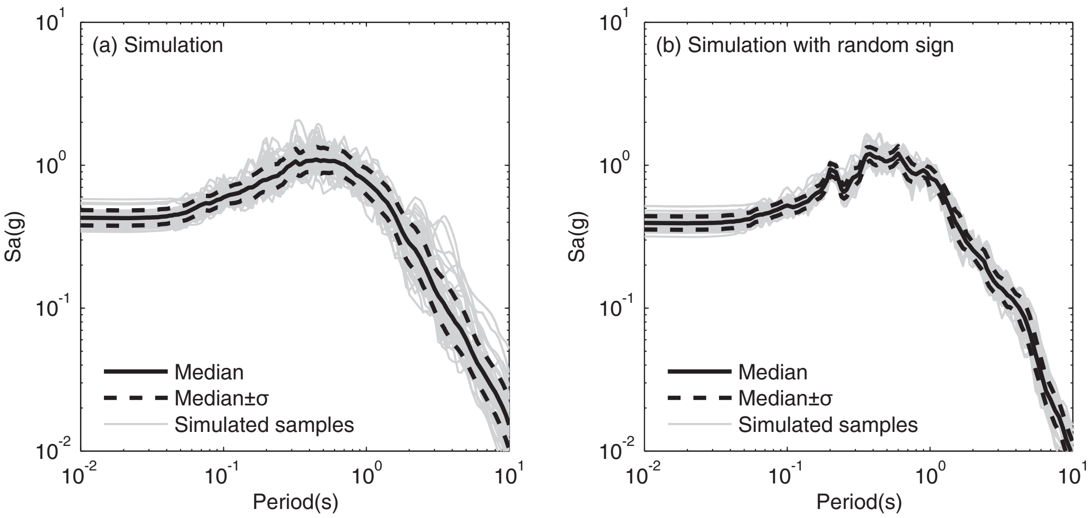

Figure 2.25: spectral acceleration (a) with all randomness, and (b) with only random variables for sign.

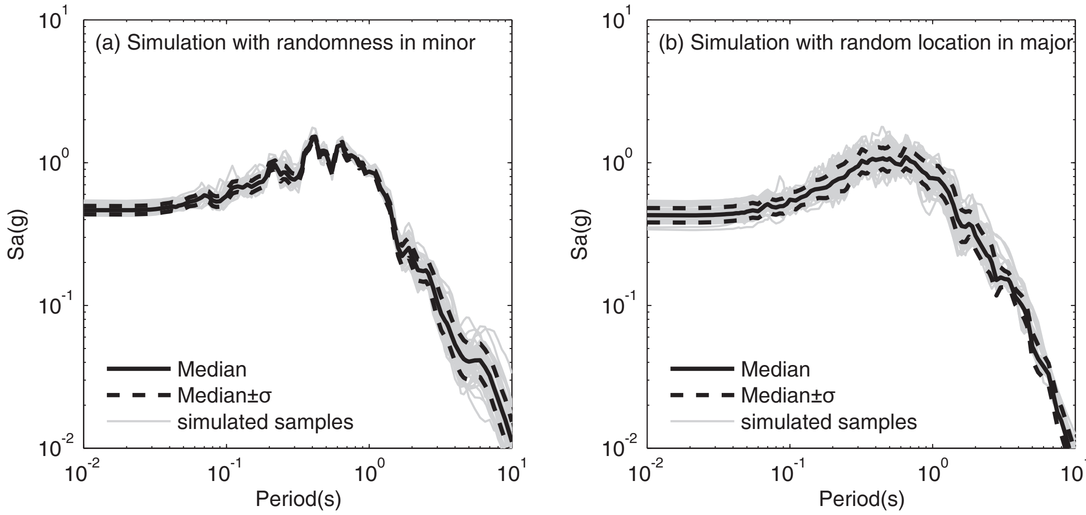

Figure 2.26: spectral acceleration (a) with only random variables for random factor in minor group, and (b) with only random variables for location of wavelets in major group.

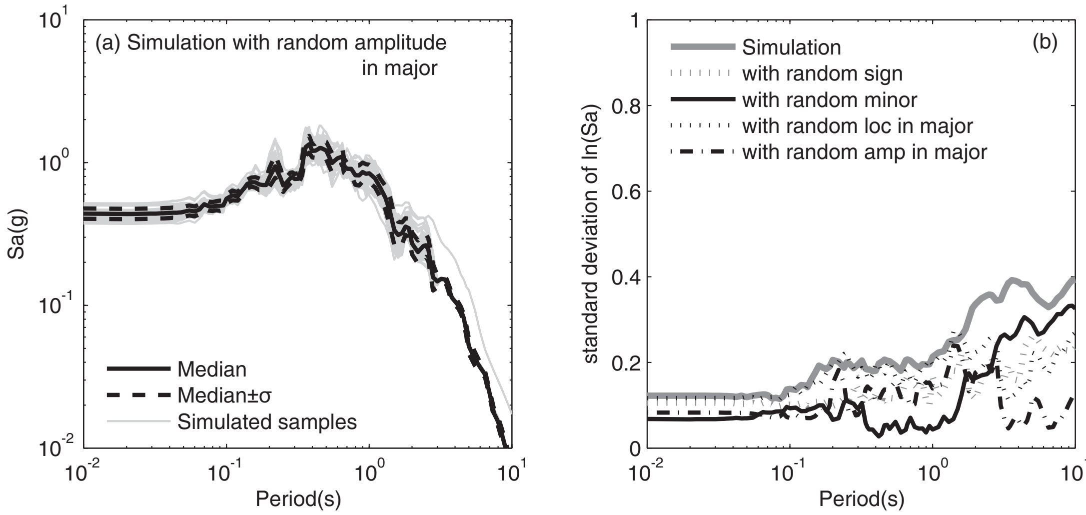

Figure 2.27: spectral acceleration (a) with only random variables for location of wavelets in major group, and (b) logarithmic standard deviation of spectral acceleration of all cases.

2.8 Conclusions

A stochastic model for simulating earthquake ground motions with time and frequency nonstationarity has been developed. The model uses wavelet packets as a method to describe amplitudes of the ground motion as a function of time and frequency; due to these packets having time and frequency localization, they are comparable to an evolutionary power spectral density. This model can simulate ground motion recordings having PGA, significant duration t_{95-5}, mean period T_m, significant bandwidth f_{95-5}, Arias intensity I_a, S_a and inelastic S_d comparable to those same properties observed in recorded ground motions. These results suggest that the synthetic ground motions generated by the proposed model are equivalent to the recorded ground motions in terms of the characteristics that are examined here.

The proposed model has the following desirable features: a) the temporal and the spectral nonstationarity can be controlled by adjusting the parameters describing amplitudes of wavelet packets, b) the model is empirically calibrated and produces motions that are consistent in their important characteristics with observed ground motion recordings, and c) the procedure is computationally inexpensive (1000 simulations can be produced per hour on a standard desktop PC). Obtaining large numbers of ground motions is therefore efficient.

Chapter 3

Regression analysis of model parameters

3.1 Abstract

This chapter describes the calibration needed to use the proposed simulation model to produce a simulated ground motion for a specified earthquake scenario (i.e., magnitude, distance, site condition). This calibration is done by using regression analysis on the observed simulation parameters in a large library of recorded strong ground motions, to identify the relationship between seismological variables such as earthquake magnitude and distance and the 13 parameters of the proposed simulation model. This regression captures relationships in mean values, standard deviations and correlations of these parameters with respect to the seismological variables. The resulting regression equations then form a model that can be used to predict ground motions for a future earthquake scenario. This is analogous to widely used empirical ground motion prediction models (formerly called "attenuation models") except that this model predicts parameters that are then used to generate entire time series rather than only response spectra. This chapter describes the ground motion library used for analysis and the development of appropriate functional forms for the predictive relationships, and it summarizes the final results from the regression models.

3.2 Introduction

The stochastic ground motion model using wavelet packets, which can generate time series with target time and frequency nonstationarities, has been developed for simulating recorded ground motions. The proposed stochastic model requires 13 parameters to describe the time and frequency characteristic of ground motion recordings. In order to simulate ground motions for future earthquakes instead of simulating ground motions similar to past recorded ground motions, the model parameters need to be connected to seismological variables that describe the possible scenarios of future earthquakes.

The model parameters have two types of characteristics: intra- and inter-event characteristics. The intra-event characteristics are the trends within each earthquake, which depend on the geometric relationships between stations and the earthquake as well as on local factors such as basins and near-surface site conditions. The inter-event characteristics are the trends between earthquakes, which depend on the characteristics of the earthquake source. Two types of multivariate regression approaches–mixed effect regression and two-stage regression–are widely used for regression models of observed ground motion intensities, which have intra- and inter-event characteristics. The two-stage regression was proposed by Joyner and Boore (1993) and the mixed effect regression was proposed by Abrahamson and Youngs (1992) for regression models of observed ground motion intensities. Joyner and Boore (1993) compare both types of regression analysis precisely.

In this dissertation, the two-stage regression analysis is employed since we can explore functional forms of intra- and inter-event characteristics separately. The recorded ground motions used in the regression analysis are selected from the database used in Boore and Atkinson (2008) (denoted BA08) for $S_a(1s)$, which is a subset of the Next Generation Attenuation (NGA) database (Chiou et al. 2008). The two-stage regression analysis is conducted for each model parameter using earthquake magnitude, hypocentral distance, rupture distance (closest distance), and V_{S30} as predictors. One additional predictor used here is the difference between hypocentral distances and rupture distances, which captures the geometric relationship between the target location and the earthquake fault. The model parameters are correlated through the correlation matrix of intra- and inter-event residuals.

The results of the regression analysis are reasonable with respect to trends in the scaling of parameters with moment magnitude, hypocentral and rupture distances, and V_{S30}. Also, spectral acceleration and waveform properties change as function of the predictor parameters as expected empirically and theoretically.

3.3 Recorded ground motion database

The recorded ground motions for the regression analysis come from the NGA database (Chiou et al. 2008), which includes 3551 recorded ground motions. In particular, the recorded ground motions are selected from a subset of NGA database that is used in (Boore and Atkinson 2008) for spectral acceleration at $1s$ (the lowest usable frequency is less than or equal to $1Hz$). The exclusion criteria that were applied are listed in Table 2.1 of Boore and Atkinson (2007). One additional criteria hired here is the number of recorded ground motions in each event. In this dissertation, the earthquakes used for the regression analysis contain more than ten recorded ground motions in order to stabilize the regression analysis. The final database consists of fault normal components of 1408 recorded ground motions from 25 earthquakes as summarized in Table 3.1. Figure 3.1 shows the earthquake magnitudes and hypocentral distances of the selected ground motions, and Figure 3.2 shows a histogram of the V_{S30} values of the selected ground motions.

Table 3.1: Selected earthquakes for regression analysis

EQID	Name	Year	M	Mechanism	# of ground motions
30	San Fernando	1971	6.61	Reverse	31
50	Imperial Valley-06	1979	6.53	Strike-Slip	33
68	Irpinia, Italy-01	1980	6.90	Normal	12
76	Coalinga-01	1983	6.36	Reverse	44
90	Morgan Hill	1984	6.19	Strike-Slip	24
101	N. Palm Springs	1986	6.06	Reverse-Oblique	29
113	Whittier Narrows-01	1987	5.99	Reverse-Oblique	101
116	Superstition Hills-02	1987	6.54	Strike-Slip	11
118	Loma Prieta	1989	6.93	Reverse-Oblique	73
125	Landers	1992	7.28	Strike-Slip	67
126	Big Bear-01	1992	6.46	Strike-Slip	39
127	Northridge-01	1994	6.69	Reverse	153
129	Kobe, Japan	1995	6.90	Strike-Slip	12
136	Kocaeli, Turkey	1999	7.51	Strike-Slip	26
137	Chi-Chi, Taiwan	1999	7.62	Reverse-Oblique	380
138	Duzce, Turkey	1999	7.14	Strike-Slip	22
158	Hector Mine	1999	7.13	Strike-Slip	82
160	Yountville	2000	5.00	Strike-Slip	24
161	Big Bear-02	2001	4.53	Strike-Slip	41
163	Anza-02	2001	4.92	Normal-Oblique	71
164	Gulf of California	2001	5.70	Strike-Slip	11
166	Gilroy	2002	4.90	Strike-Slip	33
168	Nenana Mountain, Alaska	2002	6.70	Strike-Slip	33
169	Denali, Alaska	2002	7.90	Strike-Slip	23
170	Big Bear City	2003	4.92	Strike-Slip	33

EQID :NGA database earthquake ID number

M :moment magnitude

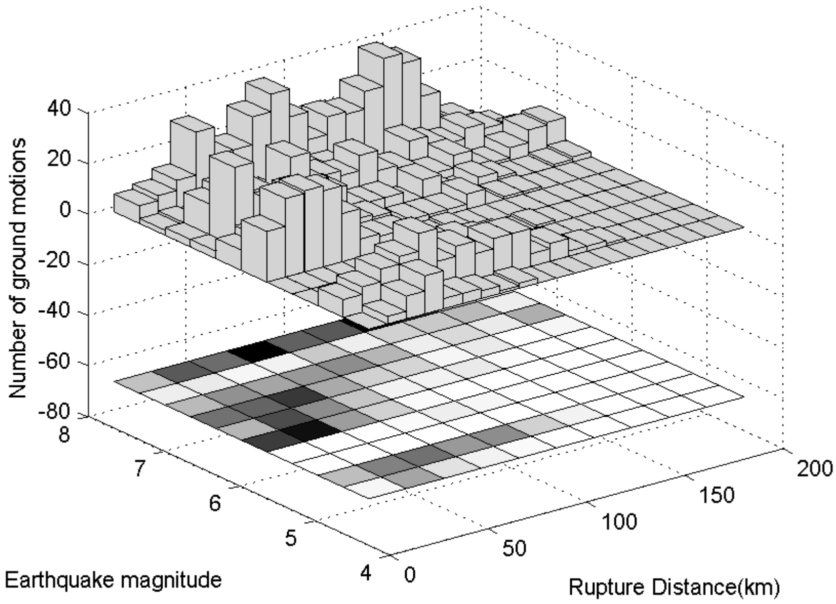

Figure 3.1: Histogram of earthquake magnitudes and hypocentral distances of the selected ground motions.

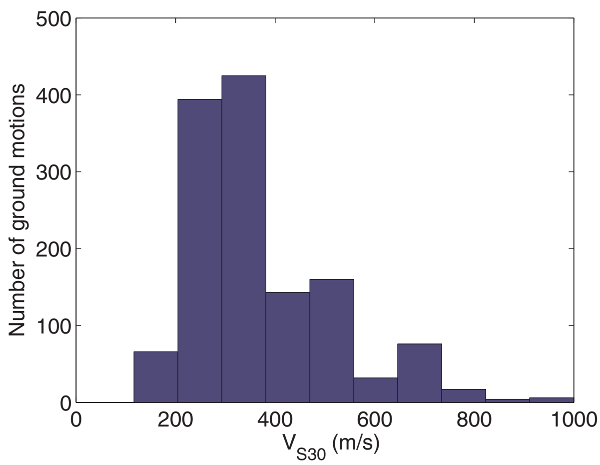

Figure 3.2: Histogram of V_{S30} values of the selected ground motions.

3.4 Two-stage regression analysis

To generate a ground motion from a particular earthquake scenario (i.e., magnitude, distance and site condition), the 13 parameters for our model need to be predicted as a function of those scenario parameters. To build this predictive model, two-stage regression analysis (Joyner and Boore 1993,1994) is employed with moment magnitude (M), hypocentral distance (R_{hyp}), rupture distance (R_{rup}), and average shear wave velocity within 30m depth (V_{S30}) as predictors (Thráinsson and Kiremidjian 2002, Pousse et al. 2006, and Rezaeian 2010).

As response variables, all 13 parameters–mean time $E(t)$, standard deviation of time $S(t)$, mean frequency $E(f)$, standard deviation of frequency $S(f)$, and correlation coefficient of time and frequency $\rho(t,f)$ for both major and minor groups, mean amplitude in the major group $E(|a^i_{j,k,maj}|^2)$, total energy E_{acc}, and the standard deviation of residuals $\xi_{k,i}$–were estimated using the Maximum Likelihood Estimation (Appendix B) and considering the truncation by bandpass filter in the frequency domain for each recorded ground motion after a trigger time correction (Chapter 2.7). The parameters for the minor group are described in Chapter 2 and repeated as follows:

$$|c^i_{j,k}|^2 = |c^i_{j,k,maj}|^2 + |c^i_{j,k,min}|^2 \tag{3.1}$$

$$\frac{\sum_{i,k} |c^i_{j,k,maj}|^2}{\sum_{i,k} |c^i_{j,k}|^2} = 0.7 \tag{3.2}$$

$$E_{acc} = E_{acc,maj} + E_{acc,min} \tag{3.3}$$

$$E_{acc,min} = \sum_i \sum_k |c^i_{j,k,min}|^2 \tag{3.4}$$

$$E(t)_{min} = \sum_i \sum_k t_k \left| c^i_{j,k,min} \right|^2 / E_{acc,min} \tag{3.5}$$

$$S^2(t)_{min} = \sum_i \sum_k \{t_k - E(t)_{min}\}^2 \left|c^i_{j,k,min}\right|^2 / E_{acc,min} \tag{3.6}$$

$$E(f)_{min} = \sum_i \sum_k f_i \left|c^i_{j,k,min}\right|^2 / E_{acc,min} \tag{3.7}$$

$$S^2(f)_{min} = \sum_i \sum_k \{f_i - E(f)_{min}\}^2 \left|c^i_{j,k,min}\right|^2 / E_{acc,min} \tag{3.8}$$

$$\rho(t,f)_{min} = \frac{\sum_i \sum_k \{t_k - E(t)_{min}\}\{f_i - E(f)_{min}\} \left|c^i_{j,k,min}\right|^2}{S(t)_{min} S(f)_{min} E_{acc,min}}, \tag{3.9}$$

where $c^i_{j,k}$ denotes the ith set of wavelet packets at the jth scale parameter and k is the translation parameter, and t_k and f_i are time and frequency of each wavelet packet, respectively.

$$S(\xi_{k,i}) = \frac{1}{N_{min}-1} \sum_i \sum_k \ln |c^i_{j,k,min}|^2 / \overline{|c^i_{j,k,min}|^2} \tag{3.10}$$

where N_{min} is the number of wavelet packets in the minor group and $\overline{|c^i_{j,k,min}|^2}$ is bivariate lognormal function to fit $|c^i_{j,k,min}|^2$, which is defined in Equation 2.46.

The parameters for the major group of packets are described in Chapter 2 and repeated as follows:

$$E_{acc,maj} = \sum_i \sum_k |c^i_{j,k,maj}|^2 \tag{3.11}$$

$$E(t)_{maj} = \sum_{m=1}^{N_{maj}} t_m / N_{maj} \tag{3.12}$$

$$S^2(t)_{maj} = \sum_{m=1}^{N_{maj}} \left\{t_m - E(t)_{maj}\right\}^2 / N_{maj} \tag{3.13}$$

$$E(f)_{maj} = \sum_{m=1}^{N_{maj}} f_m / N_{maj} \tag{3.14}$$

$$S^2(f)_{maj} = \sum_{m=1}^{N_{maj}} \left\{f_m - E(f)_{maj}\right\}^2 / N_{maj} \tag{3.15}$$

$$\rho(t,f)_{maj} = \frac{\sum_{m=1}^{N_{maj}} \left\{t_m - E(t)_{maj}\right\} \left\{f_m - E(f)_{maj}\right\}}{S(t)_{maj} S(f)_{maj}} \tag{3.16}$$

$$E(|a^i_{j,k,maj}|^2) = \sum_{m=1}^{N_{maj}} |a_{m,maj}|^2 / N_{maj}, \tag{3.17}$$

where $c^i_{j,k,maj}$ are wavelet packets in the major group, t_m and f_m are the representative time and frequency of each wavelet packet, and N_{maj} is the number of wavelet packets in the major group.

The correlations of time and frequency in the major and minor group are transformed by the following equation because they are bounded at -1 and 1.

$$\rho' = \Phi^{-1}\left(\frac{\rho+1}{2}\right) \tag{3.18}$$

where Φ is the cumulative density function of the standard normal distribution.

The following equation is a functional form for the model parameters based on the ground motion prediction model (e.g. Boore et al. 1997, Abrahamson and Silva 2008, Boore and Atkinson 2008, Campbell and Bozorgnia 2008, Chiou and Youngs 2008 and

Idriss 2008):

$$
\begin{aligned}
Y &= \alpha+\beta_1 M+\beta_2\ln(M)+\beta_3\exp(M)+\beta_4(R_{hyp}-R_{rup})+\beta_5\ln(R) \\
&\quad +\beta_6\ln(V_{S30})+\eta+\varepsilon && (3.19)\\
R &= \sqrt{R_{RUP}^2+h^2} && (3.20)
\end{aligned}
$$

where Y is the natural log of each model parameter (except for the case of correlation, where $Y=\rho'$), η and ε are intra- and inter-event residuals, respectively, and these residuals for the 13 parameters are correlated. The parameter h is assigned to avoid extremely large values in the near field and is determined by minimizing the mean square error and fitting of the regression predictors (this is consistent with modern ground motion prediction models). Forward stepwise regression analysis is conducted for every parameter in the NGA database, and we selected moment magnitude, rupture distance, and V_{S30} based on their statistical significance as determined from regression p-values.

For magnitude scaling, three types of functional forms of the magnitude are employed in the regression analysis. For the model parameters related to the characteristics in the time domain, $\exp(M)$ is used based on the trends of the target response variables. M is used for the model parameters related to the characteristics in the frequency domain based on the relationship between the magnitude and the corner frequency f_c (Brune 1970), which determines the frequency characteristics of the fault rupture. Also M is used in the regression analysis of $E(a)$ and E_{acc} based on the relationship between magnitude and seismic moment (Kanamori 1977), which is the strength of an earthquake caused by the fault. In addition, $\ln(M)$ is employed for $E(a)$ and E_{acc} since these parameters saturate at large magnitudes.

For distance scaling, two types of distance predictors are employed. The predictor R is employed, which is $\sqrt{R_{RUP}^2+h^2}$ because the size of the fault should be accounted for in the regression analysis to simulate ground motions close to the fault. For example, $S(t)$ cannot be zero and E_{acc} cannot be infinity at rupture distances of zero. To account for the geometric relationship between the target station and the earthquake fault, another predictor, the difference of distances $R_{hyp}-R_{rup}$, is included in the functional forms. The predictor R takes the same values for many sites surrounding the fault; however, simulated ground motions need to have differing characteristics depending on whether the rupture propagates towards or away from the site. Therefore, $R_{hyp} - R_{rup}$ helps to capture that effect.

The uncertainty terms, η and ε, are assumed to be normally distributed, with mean zero and standard deviations of τ and σ, and they are assumed to be independent.

In the two-stage regression analysis, we separate the equation into two regression equations: the first one is associated with intra-event effects with distances and site conditions, and the second one is associated with inter-event effects with the characteristics of the earthquakes (Joyner and Boore 1993,1994).

$$Y = \sum_{i=1}^{N} AI_{EQ} + \beta_4(R_{hyp} - R_{rup}) + \beta_5 \ln(R) + \beta_6 \ln(V_{S30}) + \varepsilon \tag{3.21}$$

$$I_{EQ} = \begin{cases} 1 & \text{for earthquake } i \\ 0 & \text{otherwise} \end{cases} \tag{3.22}$$

$$A = \alpha + \beta_1 M + \beta_2 \ln(M) + \beta_3 \exp(M) + \eta \tag{3.23}$$

where I_{EQ}s are indicator functions for the earthquakes and As are regression coefficients computed from the first regression, and they are response variables of the second regression. The functional form of magnitude in Equation 3.23 is determined by evaluating the p-values for β_1 through β_3. Since each selected earthquake contains more than ten records, equal weights are applied to the second regression, rather than performing a weighted regression.

The resulting regression coefficients are shown in Table 3.2, and the correlation of the intra- and inter-event residuals are shown in tables 3.3 and 3.4, respectively. Regression coefficients that were not statistically significant are set to zeros in Table 3.2. The model parameters are correlated through the intra- and inter-event residuals as well as through the regression coefficients since the model parameters computed from recorded ground motions contain unknown effects that are not considered in the proposed regression model.

Table 3.2: Coefficients of the prediction equation

	α	β_1	β_2	β_3	β_4	β_5	β_6	h	σ	τ
		M	$\ln(M)$	$\exp(M)$	$R_{hyp}-R_{rup}$	$\ln(R)$	$\ln(V_{S30})$			
$E(t)_{min}$	2.64	0	0	0.0004	-0.001	0.22	-0.16	1	0.18	0.21
$S(t)_{min}$	3.06	0	0	0.0004	-0.005	0.11	-0.17	1	0.21	0.23
$E(f)_{min}$	1.29	-0.14	0	0	-0.004	-0.23	0.36	10	0.35	0.26
$S(f)_{min}$	1.48	-0.005	0	0	-0.003	-0.29	0.24	10	0.40	0.29
$R(t,f)_{min}$	-0.36	0.01	0	0	-0.00056	-0.03	0.04	10	0.06	0.03
$E(t)_{maj}$	1.95	0	0	0.0006	-0.002	0.34	-0.20	1	0.27	0.30
$S(t)_{maj}$	1.82	0	0	0.0006	-0.006	0.22	-0.20	1	0.34	0.33
$E(f)_{maj}$	0.81	-0.26	0	0	-0.004	-0.16	0.44	10	0.41	0.26
$S(f)_{maj}$	0.14	-0.12	0	0	-0.002	-0.24	0.39	10	0.56	0.37
$R(t,f)_{maj}$	-0.54	0.01	0	0	-0.00008	-0.08	0.09	10	0.21	0.07
$E(a)_{maj}$	-38.02	-4.52	37.30	0	0	-1.74	-0.94	10	1.13	0.71
E_{acc}	-27.4	-2.58	27.00	0	0	-1.61	-0.88	10	0.85	0.46
$S(\xi_{k,i})$	1.29								0.07	

Table 3.3: Correlation of intra event residuals

	$E(t)_{min}$	$S(t)_{min}$	$E(f)_{min}$	$S(f)_{min}$	$\rho'(t,f)_{min}$	$E(t)_{maj}$	$S(t)_{maj}$	$E(f)_{maj}$	$S(f)_{maj}$	$\rho'(t,f)_{maj}$	$E(a)_{maj}$	E_{acc}
$E(t)_{min}$	1.00	0.79	-0.25	-0.07	-0.41	0.84	0.59	-0.27	-0.11	-0.22	-0.21	-0.05
$S(t)_{min}$	0.79	1.00	-0.18	-0.01	-0.39	0.58	0.63	-0.21	-0.03	-0.23	-0.30	-0.16
$E(f)_{min}$	-0.25	-0.18	1.00	0.83	0.10	-0.12	-0.10	0.86	0.77	0.04	-0.42	-0.27
$S(f)_{min}$	-0.07	-0.01	0.83	1.00	-0.11	0.02	0.06	0.63	0.76	-0.12	-0.51	-0.38
$\rho'(t,f)_{min}$	-0.41	-0.39	0.10	-0.11	1.00	-0.30	-0.29	0.14	-0.09	0.53	0.09	0.01
$E(t)_{maj}$	0.84	0.58	-0.12	0.02	-0.30	1.00	0.63	-0.21	-0.05	-0.23	-0.24	-0.12
$S(t)_{maj}$	0.59	0.63	-0.10	0.06	-0.29	0.63	1.00	-0.20	0.00	-0.21	-0.33	-0.21
$E(f)_{maj}$	-0.27	-0.21	0.86	0.63	0.14	-0.21	-0.20	1.00	0.80	0.08	-0.35	-0.18
$S(f)_{maj}$	-0.11	-0.03	0.77	0.76	-0.09	-0.05	0.00	0.80	1.00	-0.11	-0.53	-0.33
$\rho'(t,f)_{maj}$	-0.22	-0.23	0.04	-0.12	0.53	-0.23	-0.21	0.08	-0.11	1.00	0.12	0.06
$E(a)_{maj}$	-0.21	-0.30	-0.42	-0.51	0.09	-0.24	-0.33	-0.35	-0.53	0.12	1.00	0.89
E_{acc}	-0.05	-0.16	-0.27	-0.38	0.01	-0.12	-0.21	-0.18	-0.33	0.06	0.89	1.00

Table 3.4: Correlation of inter event residuals

	$E(t)_{min}$	$S(t)_{min}$	$E(f)_{min}$	$S(f)_{min}$	$\rho'(t,f)_{min}$	$E(t)_{maj}$	$S(t)_{maj}$	$E(f)_{maj}$	$S(f)_{maj}$	$\rho'(t,f)_{maj}$	$E(a)_{maj}$	E_{acc}
$E(t)_{min}$	1.00	0.91	-0.24	-0.03	-0.55	0.92	0.79	-0.44	-0.17	-0.45	-0.51	-0.31
$S(t)_{min}$	0.91	1.00	-0.16	0.07	-0.58	0.73	0.84	-0.35	-0.05	-0.43	-0.61	-0.35
$E(f)_{min}$	-0.24	-0.16	1.00	0.92	0.38	-0.29	-0.09	0.94	0.96	0.31	-0.25	0.14
$S(f)_{min}$	-0.03	0.07	0.92	1.00	0.28	-0.09	0.10	0.76	0.91	0.24	-0.39	0.02
$\rho'(t,f)_{min}$	-0.55	-0.58	0.38	0.28	1.00	-0.46	-0.52	0.37	0.23	0.78	0.30	0.24
$E(t)_{maj}$	0.92	0.73	-0.29	-0.09	-0.46	1.00	0.75	-0.46	-0.24	-0.48	-0.38	-0.25
$S(t)_{maj}$	0.79	0.84	-0.09	0.10	-0.52	0.75	1.00	-0.24	0.04	-0.61	-0.69	-0.49
$E(f)_{maj}$	-0.44	-0.35	0.94	0.76	0.37	-0.46	-0.24	1.00	0.91	0.29	-0.12	0.19
$S(f)_{maj}$	-0.17	-0.05	0.96	0.91	0.23	-0.24	0.04	0.91	1.00	0.19	-0.38	0.04
$\rho'(t,f)_{maj}$	-0.45	-0.43	0.31	0.24	0.78	-0.48	-0.61	0.29	0.19	1.00	0.25	0.23
$E(a)_{maj}$	-0.51	-0.61	-0.25	-0.39	0.30	-0.38	-0.69	-0.12	-0.38	0.25	1.00	0.80
E_{acc}	-0.31	-0.35	0.14	0.02	0.24	-0.25	-0.49	0.19	0.04	0.23	0.80	1.00

Since there are no statistically significant predictors for $\xi_{k,i}$ in Figure 3.3, it is modeled as a lognormal random variable with a constant logarithmic mean of 1.29 and logarithmic standard deviation of 0.07, which are independent of moment magnitude, hypocentral distance, rupture distance, and V_{S30}.

For the parameters on the time axis, values of β_3 are positive, as seen in Figures 3.7 and 3.17, because earthquakes with large magnitudes have longer durations and thus also later temporal centroids, as seen in Figures 3.5 and 3.15. The median prediction for the first regression analysis of the temporal centroids in both the major and minor groups have large variations in Figures 3.5 and 3.15 since the earthquakes are recorded by different seismograph networks whose thresholds of the trigger time and ending time differ. Although the trigger time is corrected (Section 2.6.3), the regression analysis of $E(t)$s are still less stable than those of the other parameters. Values of β_5 are also positive for those parameters, as seen in Figures 3.4, 3.6, 3.14, and 3.16, because waves propagating over long distances have scattered arrivals and include indirect waves as well as direct waves. The regression coefficients for β_4 are negative because the effect of forward directivity makes $S(t)$ smaller and $E(t)$ earlier. Additionally, negative coefficients for β_6 make $S(t)$ larger and $E(t)$ later because ground motions with long period components amplified by soft soil tend to have longer durations.

For the parameters on the frequency axis, values of β_1 for the parameters $E(f)$ are negative, as seen in Figures 3.9 and 3.19, because earthquakes with large magnitudes have low corner frequencies (Brune 1970). The coefficients β_1 of $S(f)$ are also negative, as seen in Figures 3.11 and 3.21; however, the influence of magnitude for $S(f)$ is smaller than that for $E(f)$.

A long distance of wave propagation makes $E(f)$ lower (i.e. values of β_5 are negative) in Figures 3.8 and 3.18 and makes $S(f)$ narrower in Figures 3.10 and 3.20 because high frequency ground motion components attenuate more quickly with distance than low frequency components. Additionally, a greater difference between hypocentral distance and rupture distance makes $E(f)$ lower because of the forward directivity effect (Boatwright and Boore 1982). The spectral centroid $E(f)$ increases with V_{S30} because the natural frequency of the soil is higher in stiff soil than in soft soil. The spectral standard deviation $S(f)$ also increases with V_{S30} because soft soil plays the role of a band pass filter.

The time and frequency nonstationarity increases (i.e. $\rho'(t,f)$ decreases) with distance in Figures 3.12 and 3.22 because the higher frequency components of ground motions arrive earlier than the lower frequency components, also because the indirect waves recorded in the later part of ground motions have less high frequency components due to the attenuation of high frequency components with distance. The time and frequency nonstationarity slightly increases with magnitude in Figures 3.13 and 3.23 because the ground motions with large magnitude have broader bandwidth and longer duration. In addition, the nonstationarity decreases with V_{S30} because only narrow band components exist in soft soil ground motions.

The mean energy E_{acc} increases with magnitude and saturates at large magnitudes, as seen in Figure 3.27. Also, E_{acc} decreases with distance in Figure 3.26 and increases for small V_{S30} due to site amplification. The trend of $E(a)_{maj}$ is the same as that of E_{acc} in Figures 3.24 and 3.25.

Regarding the normality of the intra- and inter-event residuals, the second regression analysis is less stable than the first regression analysis (as seen in Figures 3.5, 3.7, 3.11, 3.15 and 3.17). Figures 3.5 and 3.7 show large inter-event residuals of $E(t)_{min}$ and $S(t)_{min}$ for recorded ground motions from the 2001 Gulf of California earthquake and the 2002 Denali earthquake since the trigger time and ending time to those recorded ground motions are unstable. Figure 3.11 shows large inter-event residuals of the bandwidth $S(f)_{min}$ for the 1983 Coalinga earthquake and 1997 Kobe earthquake. Also, Figure 3.22 shows skewed intra-event residuals for the time and frequency nonstationarity. However these residuals can still be reasonably assumed to be normally distributed within plus and minus one standard deviation bounds.

More detailed information about the regression model development is available at our website (`www.stanford.edu/~bakerjw/gm_simulation.html`). These regression analyses are also performed using the mixed effect regression, and almost the same coefficients are obtained with that approach. In terms of the logarithmic standard deviation of S_a observed in the simulated ground motions, the analyses are almost identical. The regression model obtained using the Mixed Effect Regression can be found at our website (`www.stanford.edu/~bakerjw/gm_simulation.html`). Therefore, the functional forms of our model parameters can be considered appropriate.

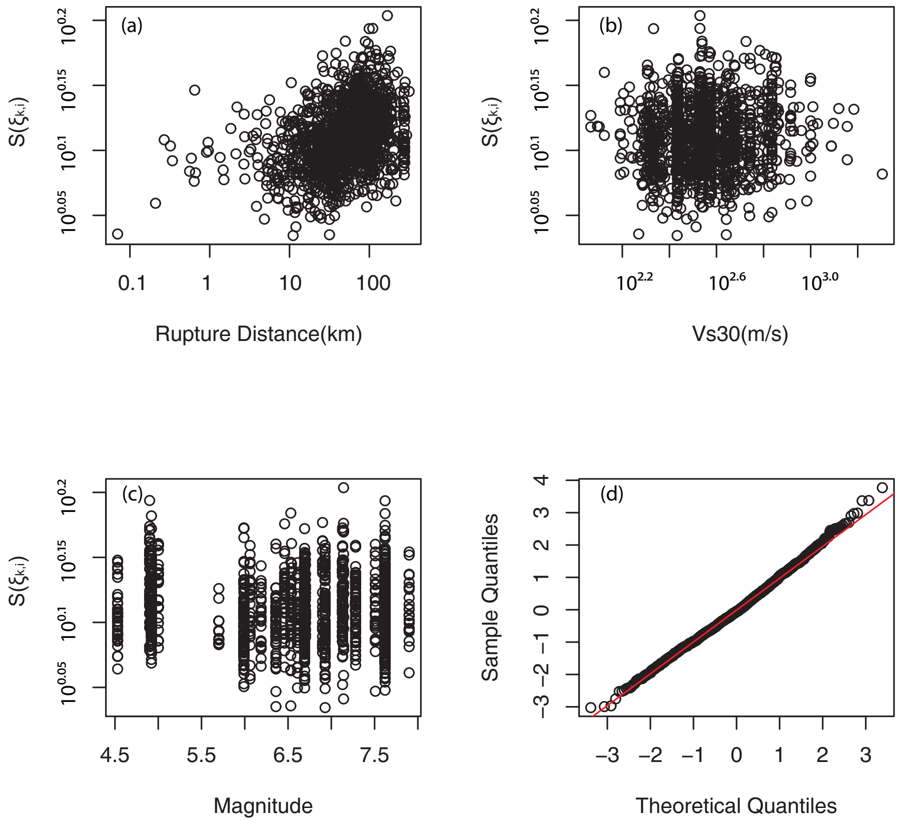

Figure 3.3: Characteristics of logarithmic standard deviation of randomness for wavelet packets in minor group $S(\xi_{k,i})$ (a) $S(\xi_{k,i})$ versus rupture distance, (b) $S(\xi_{k,i})$ versus V_{S30}, (c) $S(\xi_{k,i})$ versus magnitude, and (d) quantile-quantile plot for $S(\xi_{k,i})$.

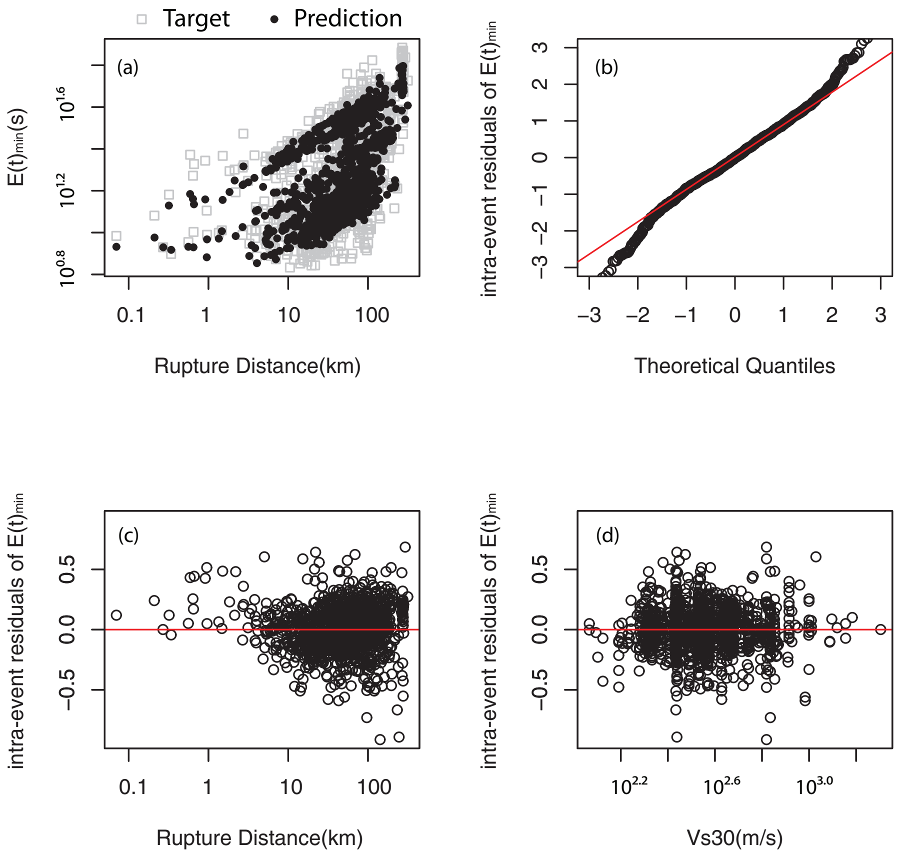

Figure 3.4: First regression analysis of $E(t)$ in minor group (a) median prediction from the first regression, (b) quantile-quantile plot for intra event residuals, (c) intra event residuals versus rupture distance, and (d) intra event residuals versus V_{S30}.

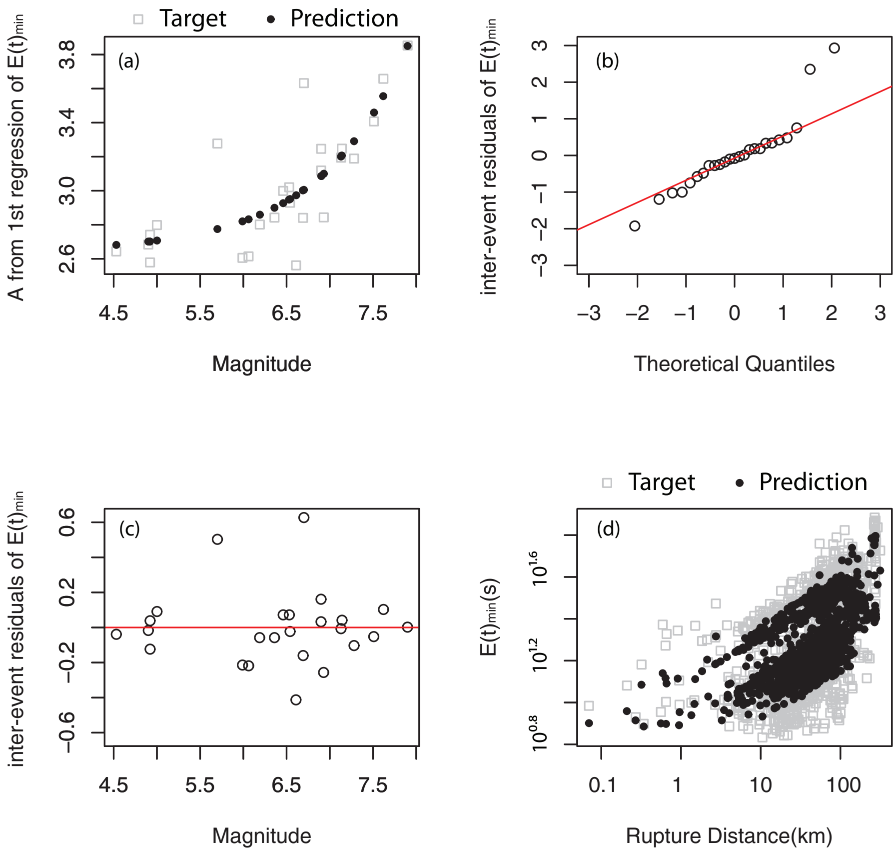

Figure 3.5: Second regression analysis of $E(t)$ in minor group (a) median prediction of A from the second regression, (b) quantile-quantile plot for intra event residuals, (c) inter event residuals versus moment magnitude, and and (d) median prediction from total regression.

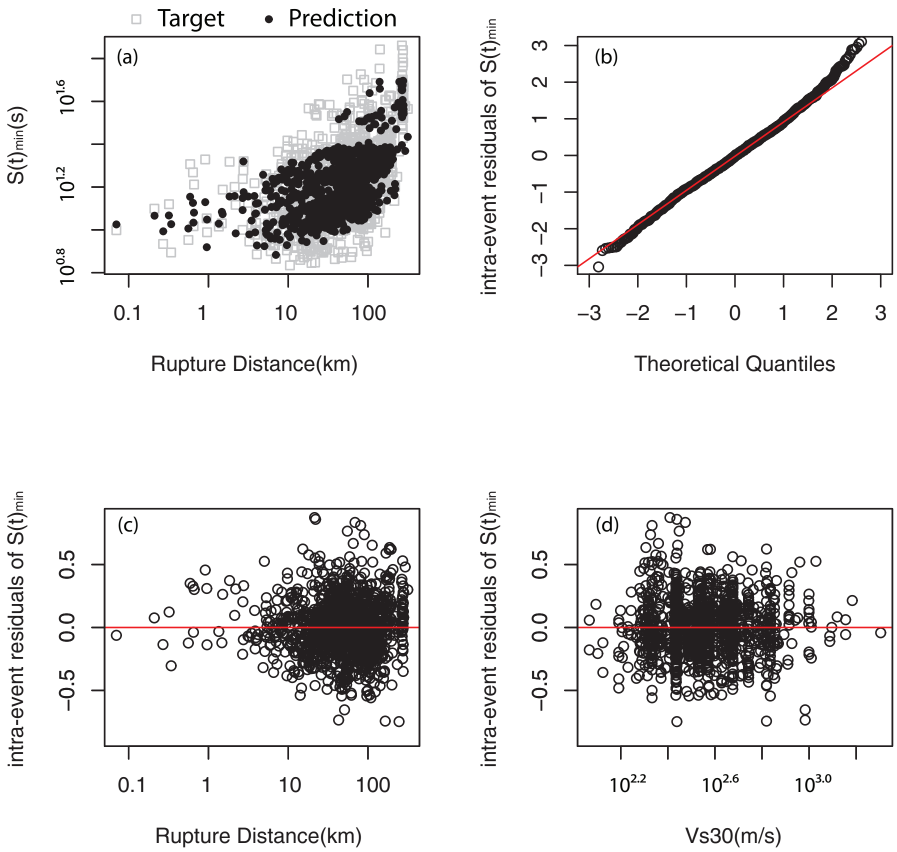

Figure 3.6: First regression analysis of $S(t)$ in minor group (a) median prediction from the first regression, (b) quantile-quantile plot for intra event residuals, (c) intra event residuals versus rupture distance, and (d) intra event residuals versus V_{S30}.

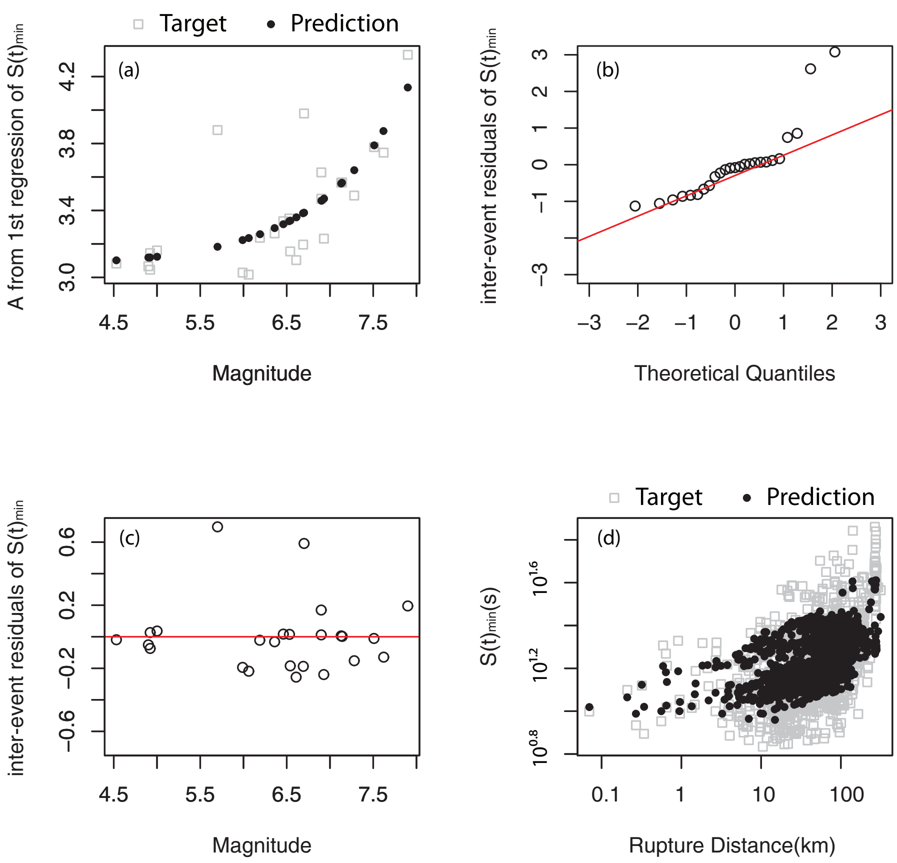

Figure 3.7: Second regression analysis of $S(t)$ in minor group (a) median prediction of A from the second regression, (b) quantile-quantile plot for intra event residuals, (c) inter event residuals versus moment magnitude, and and (d) median prediction from total regression.

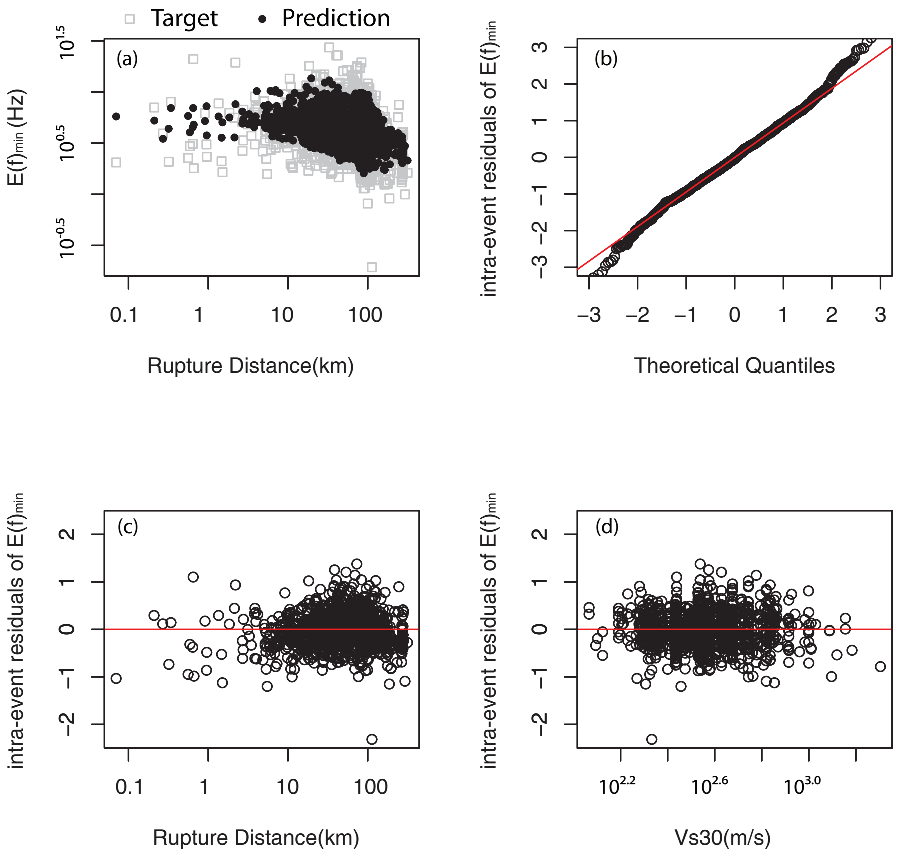

Figure 3.8: First regression analysis of $E(f)$ in minor group (a) median prediction from the first regression, (b) quantile-quantile plot for intra event residuals, (c) intra event residuals versus rupture distance, and (d) intra event residuals versus V_{S30}.

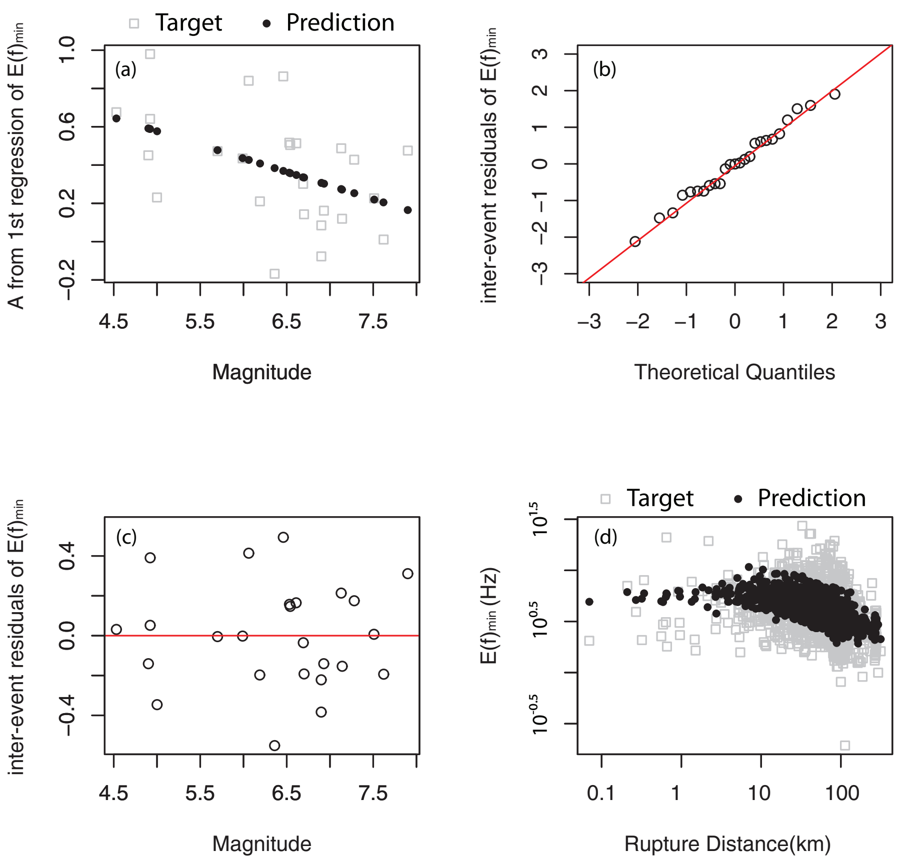

Figure 3.9: Second regression analysis of $E(f)$ in minor group (a) median prediction of A from the second regression, (b) quantile-quantile plot for intra event residuals, (c) inter event residuals versus moment magnitude, and and (d) median prediction from total regression.

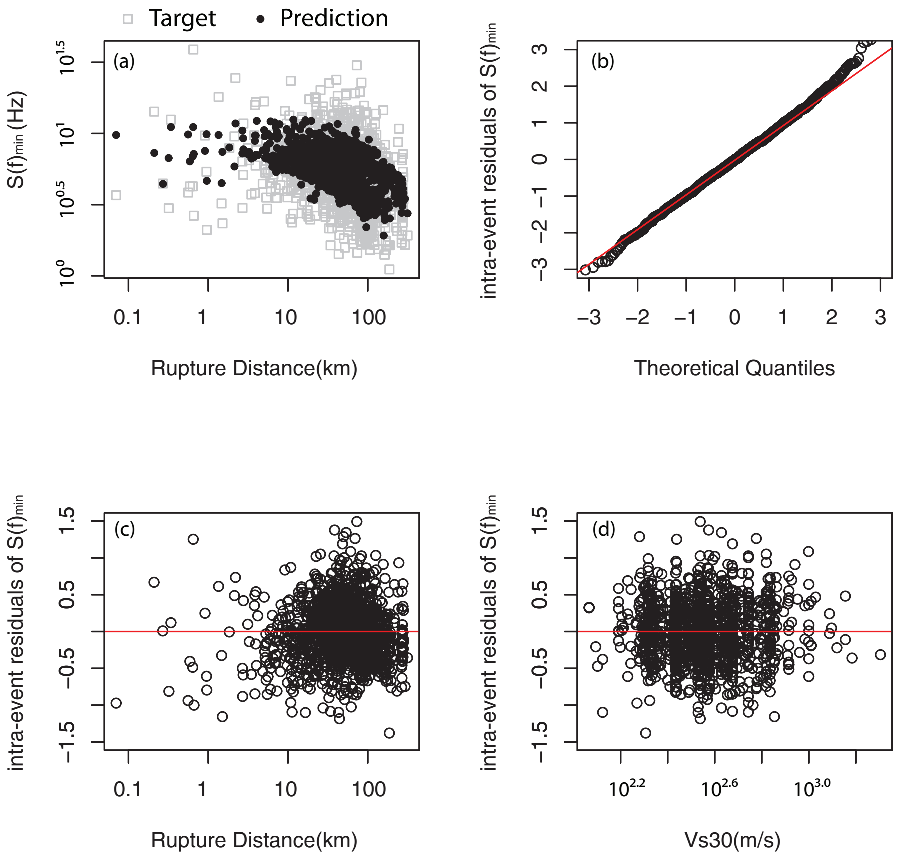

Figure 3.10: First regression analysis of $S(f)$ in minor group (a) median prediction from the first regression, (b) quantile-quantile plot for intra event residuals, (c) intra event residuals versus rupture distance, and (d) intra event residuals versus V_{S30}.

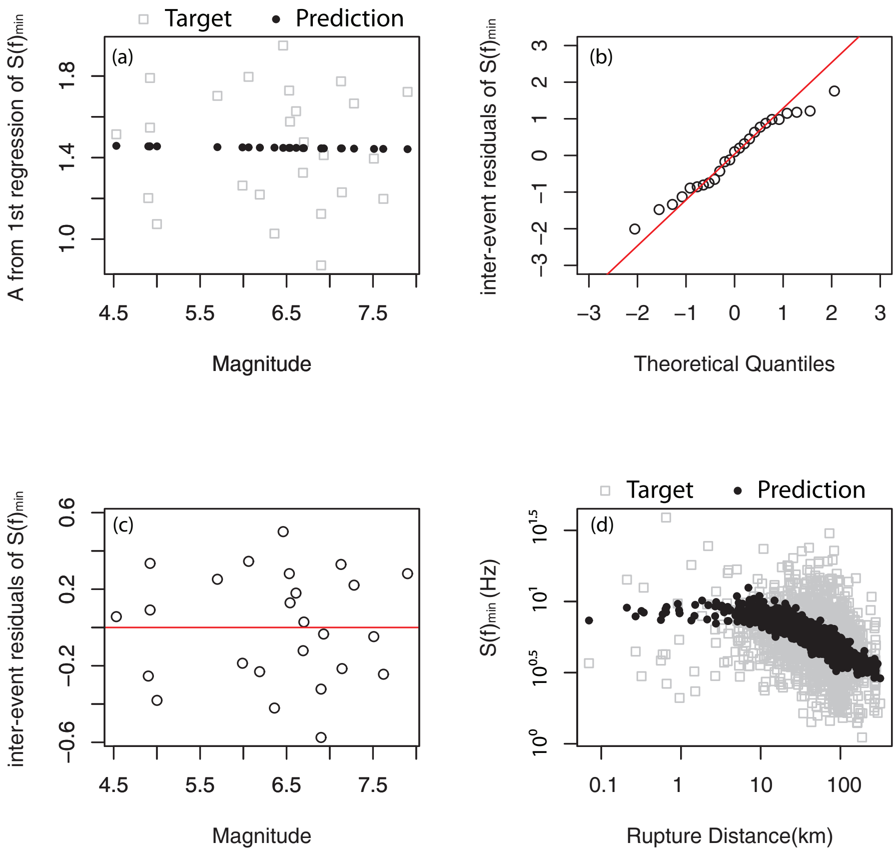

Figure 3.11: Second regression analysis of $S(f)$ in minor group (a) median prediction of A from the second regression, (b) quantile-quantile plot for intra event residuals, (c) inter event residuals versus moment magnitude, and and (d) median prediction from total regression.

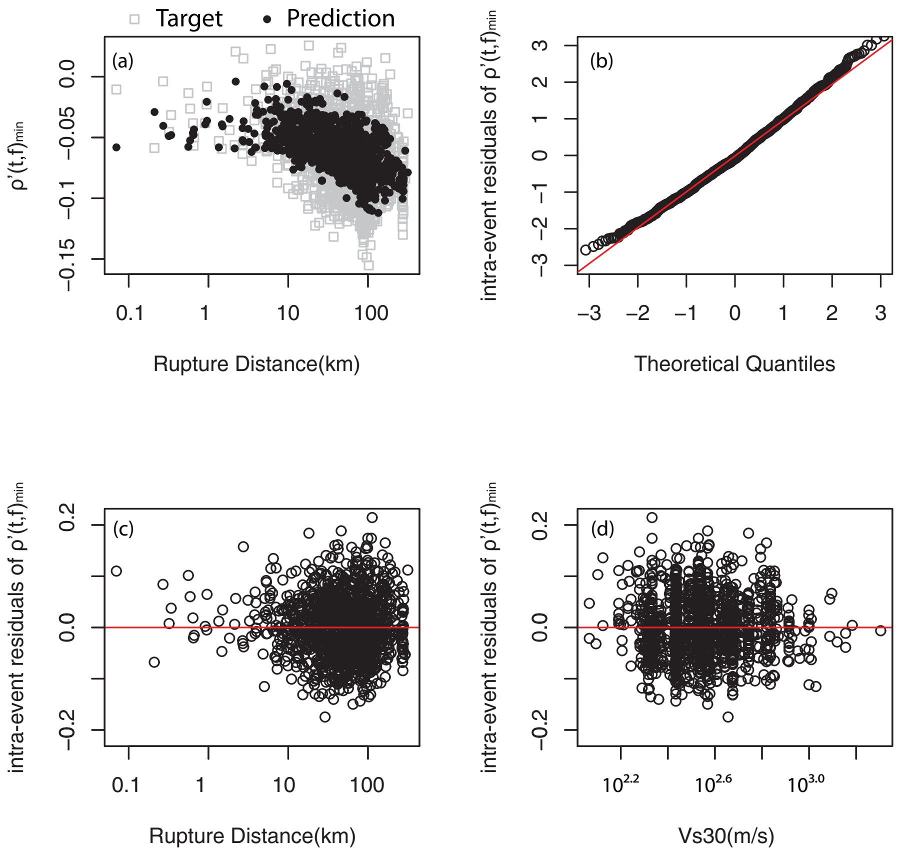

Figure 3.12: First regression analysis of $\rho'(t,f)$ in minor group (a) median prediction from the first regression, (b) quantile-quantile plot for intra event residuals, (c) intra event residuals versus rupture distance, and (d) intra event residuals versus V_{S30}.

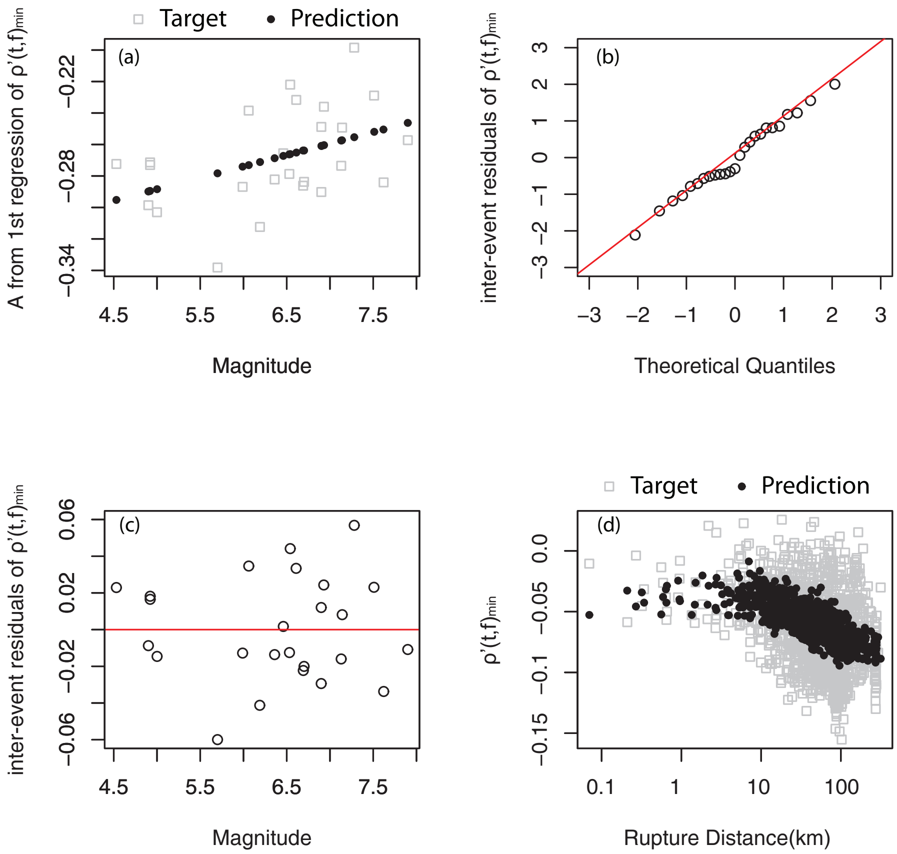

Figure 3.13: Second regression analysis of $\rho'(t, f)$ in minor group (a) median prediction of A from the second regression, (b) quantile-quantile plot for intra event residuals, (c) inter event residuals versus moment magnitude, and and (d) median prediction from total regression.

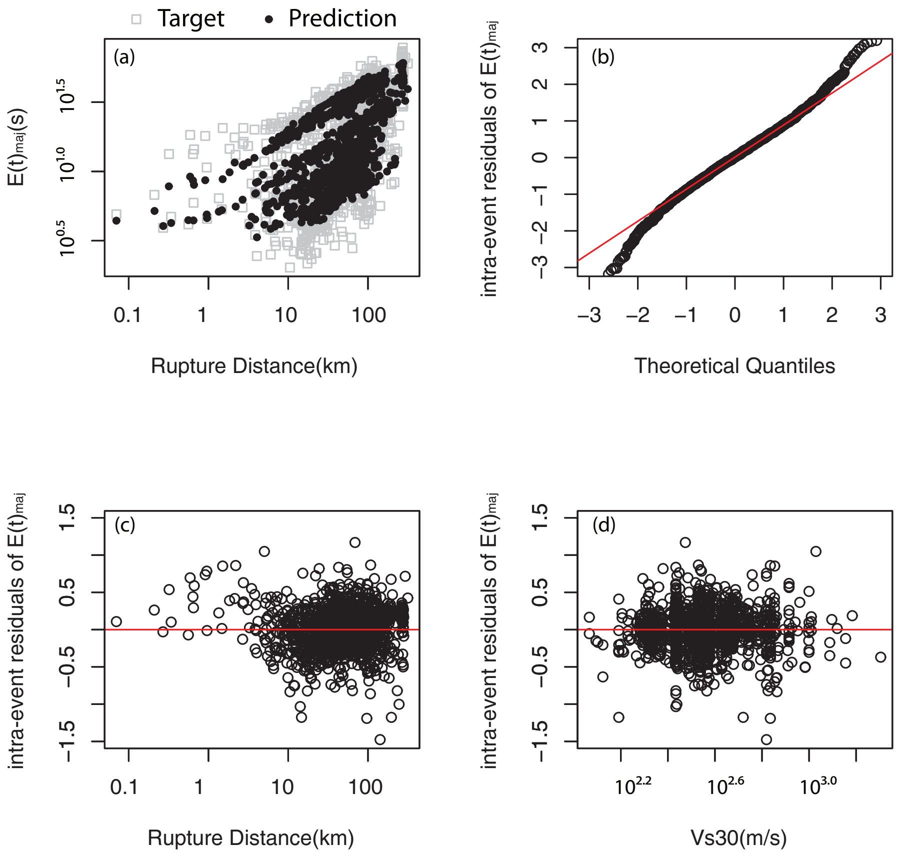

Figure 3.14: First regression analysis of $E(t)$ in major group (a) median prediction from the first regression, (b) quantile-quantile plot for intra event residuals, (c) intra event residuals versus rupture distance, and (d) intra event residuals versus V_{S30}.

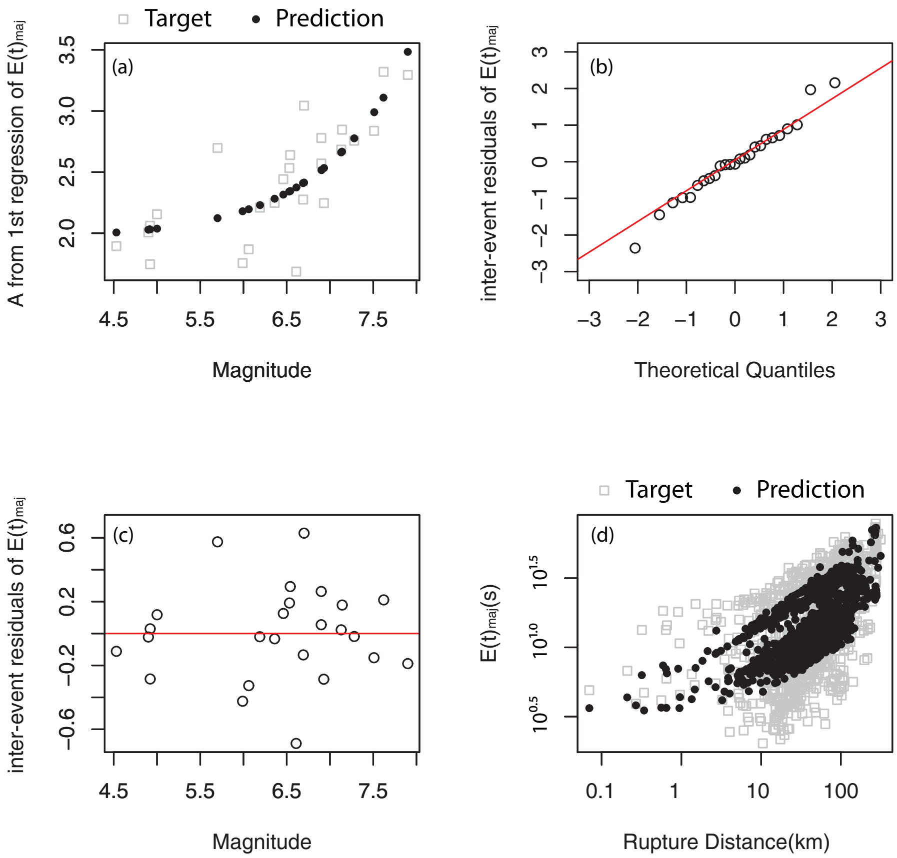

Figure 3.15: Second regression analysis of $E(t)$ in major group (a) median prediction of A from the second regression, (b) quantile-quantile plot for intra event residuals, (c) inter event residuals versus moment magnitude, and and (d) median prediction from total regression.

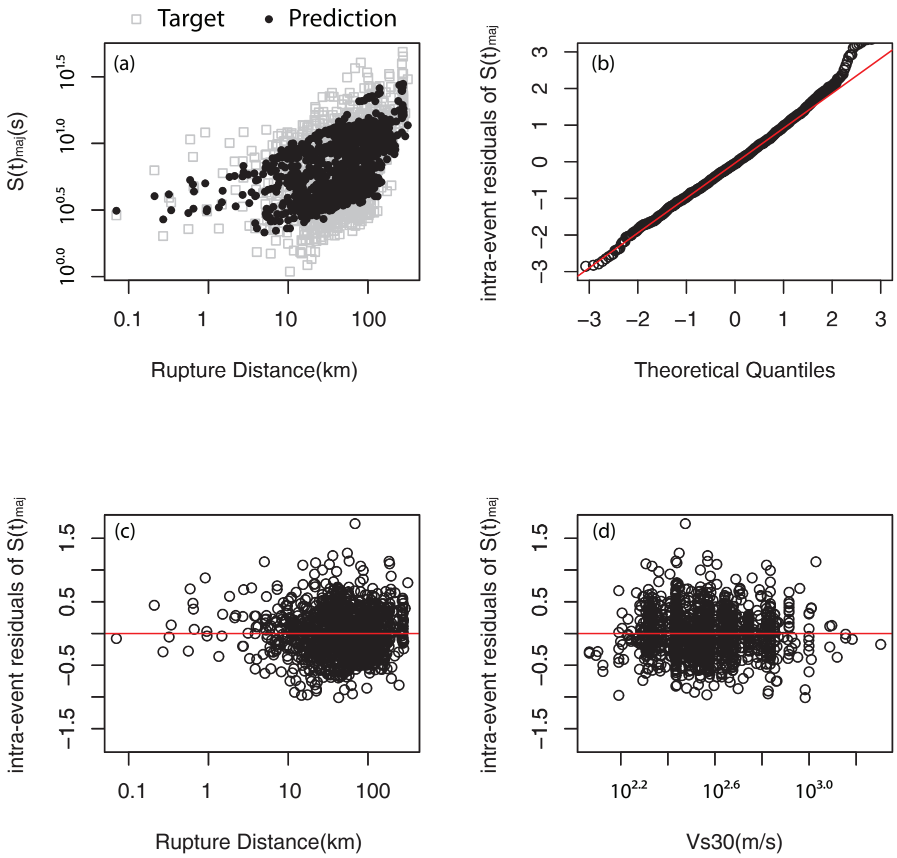

Figure 3.16: First regression analysis of $S(t)$ in major group (a) median prediction from the first regression, (b) quantile-quantile plot for intra event residuals, (c) intra event residuals versus rupture distance, and (d) intra event residuals versus V_{S30}.

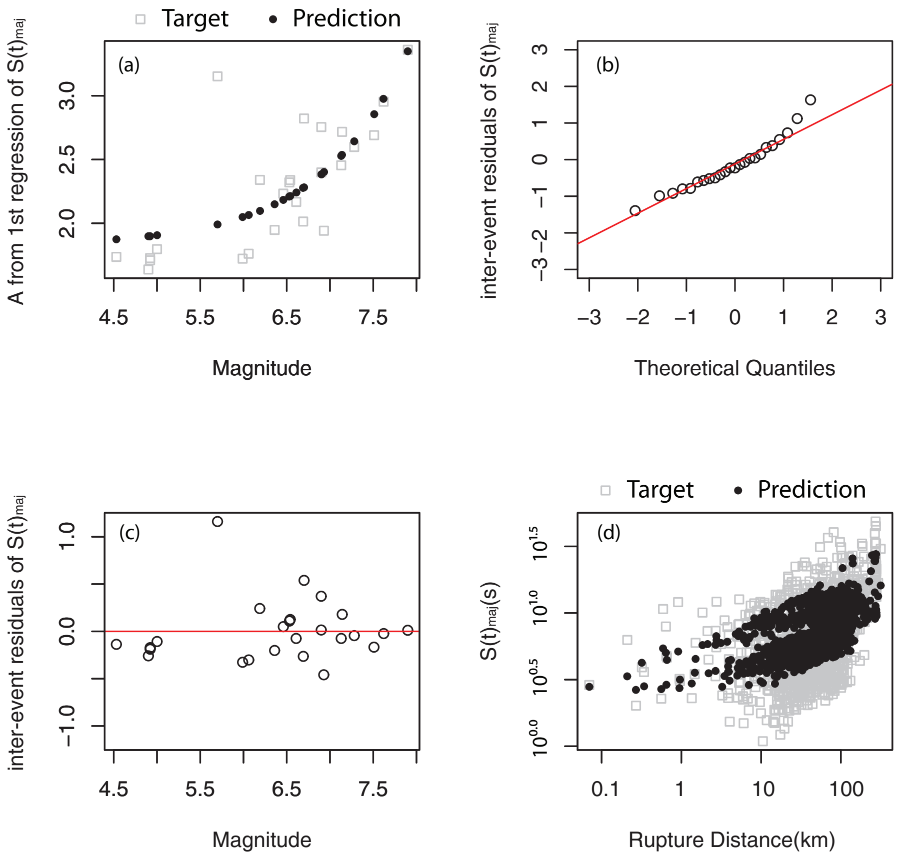

Figure 3.17: Second regression analysis of $S(t)$ in major group (a) median prediction of A from the second regression, (b) quantile-quantile plot for intra event residuals, (c) inter event residuals versus moment magnitude, and and (d) median prediction from total regression.

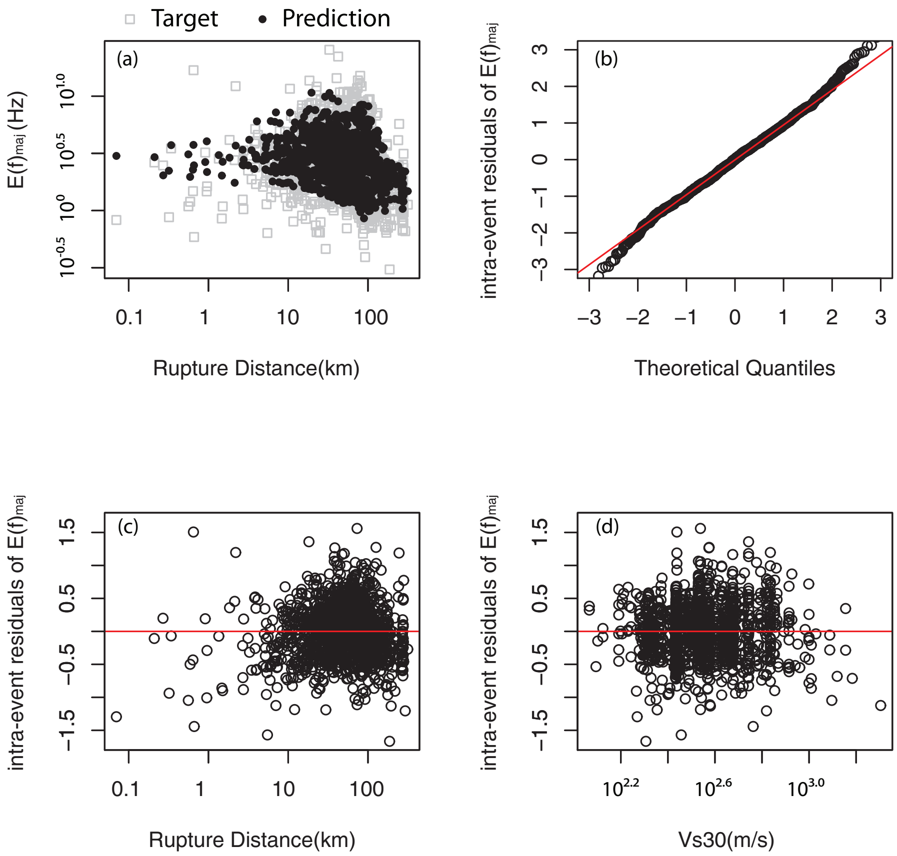

Figure 3.18: First regression analysis of $E(f)$ in major group (a) median prediction from the first regression, (b) quantile-quantile plot for intra event residuals, (c) intra event residuals versus rupture distance, and (d) intra event residuals versus V_{S30}.

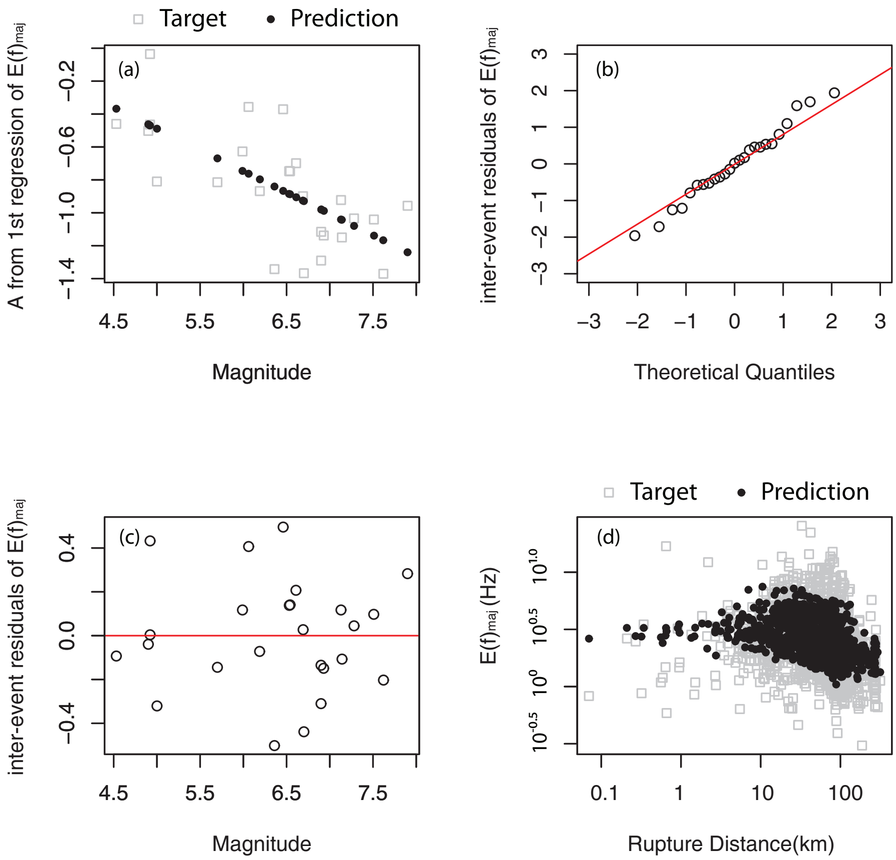

Figure 3.19: Second regression analysis of $E(f)$ in major group (a) median prediction of A from the second regression, (b) quantile-quantile plot for intra event residuals, (c) inter event residuals versus moment magnitude, and and (d) median prediction from total regression.

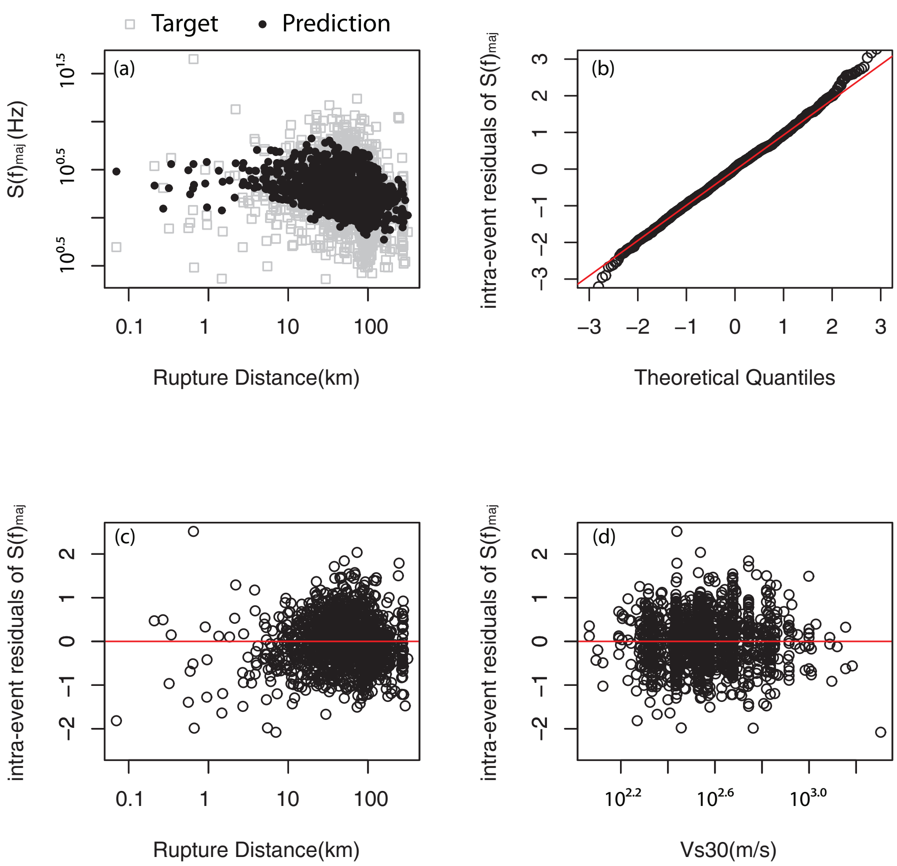

Figure 3.20: First regression analysis of $S(f)$ in major group (a) median prediction from the first regression, (b) quantile-quantile plot for intra event residuals, (c) intra event residuals versus rupture distance, and (d) intra event residuals versus V_{S30}.

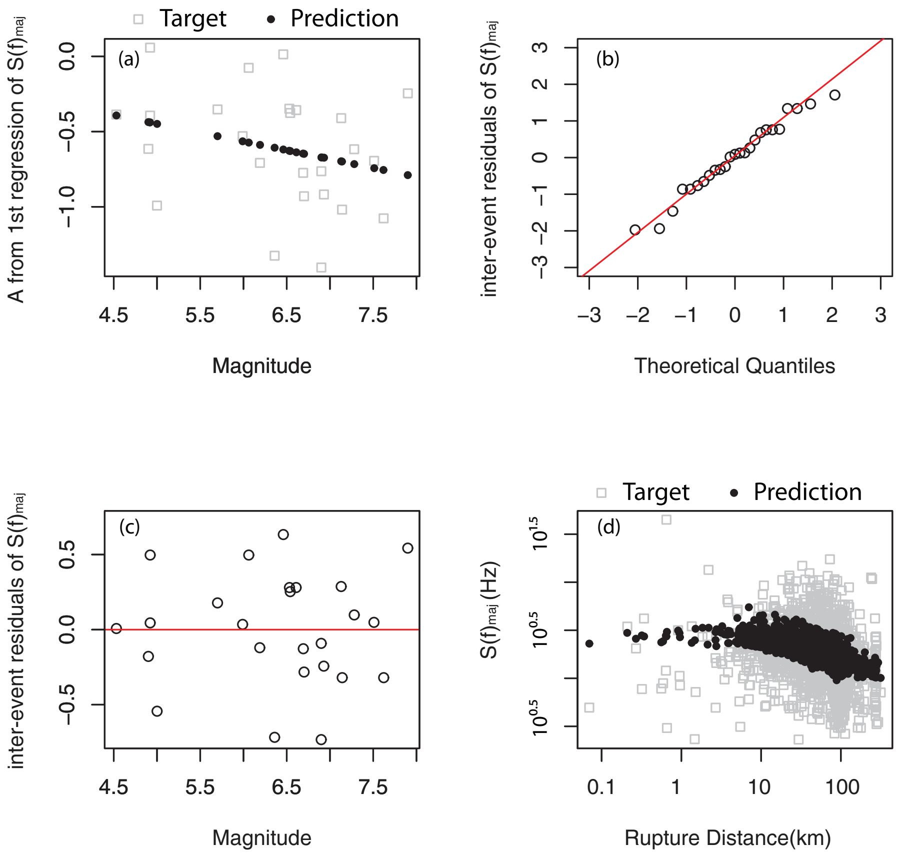

Figure 3.21: Second regression analysis of $S(f)$ in major group (a) median prediction of A from the second regression, (b) quantile-quantile plot for intra event residuals, (c) inter event residuals versus moment magnitude, and and (d) median prediction from total regression.

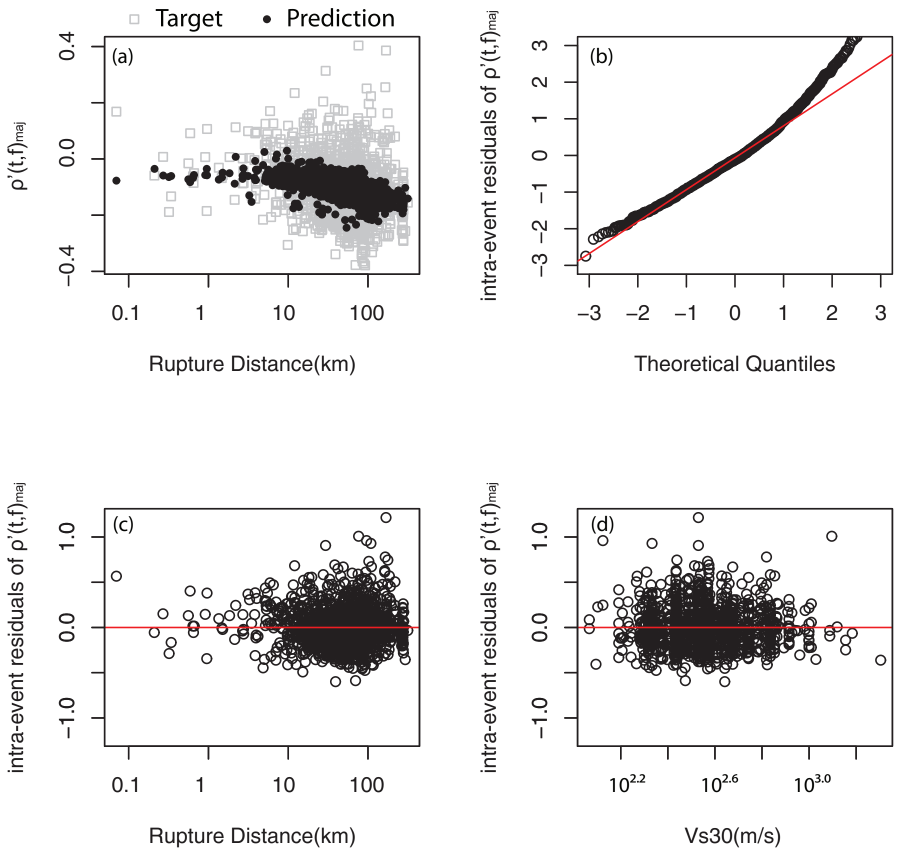

Figure 3.22: First regression analysis of $\rho'(t,f)$ in major group (a) median prediction from the first regression, (b) quantile-quantile plot for intra event residuals, (c) intra event residuals versus rupture distance, and (d) intra event residuals versus V_{S30}.

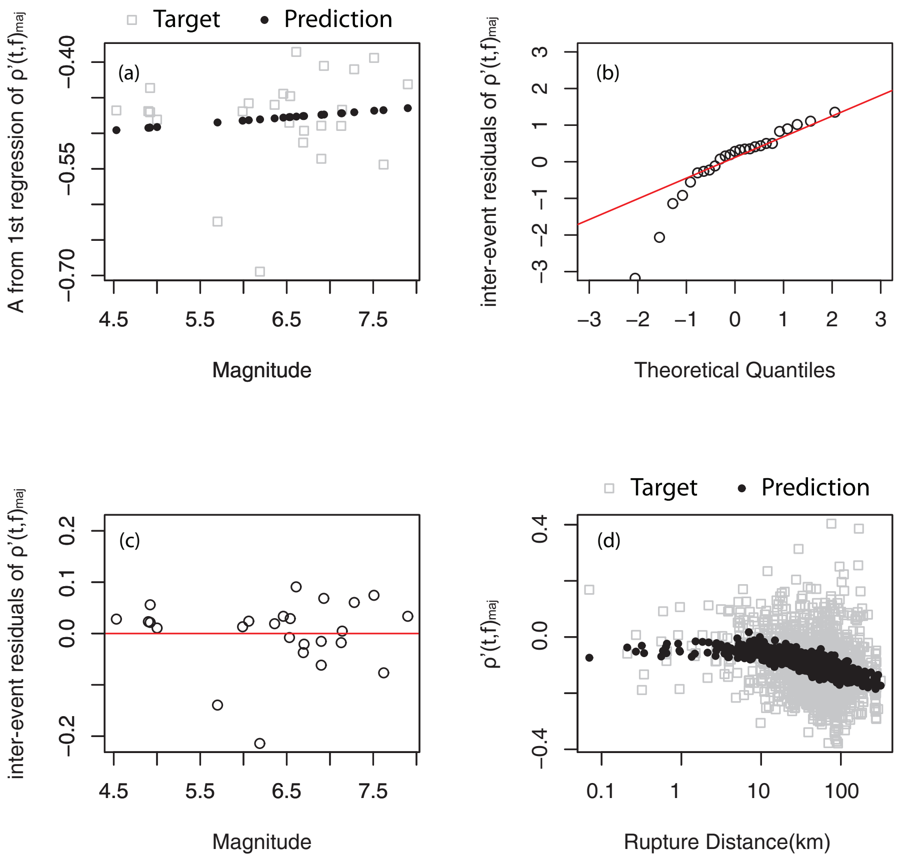

Figure 3.23: Second regression analysis of $\rho'(t, f)$ in major group (a) median prediction of A from the second regression, (b) quantile-quantile plot for intra event residuals, (c) inter event residuals versus moment magnitude, and and (d) median prediction from total regression.

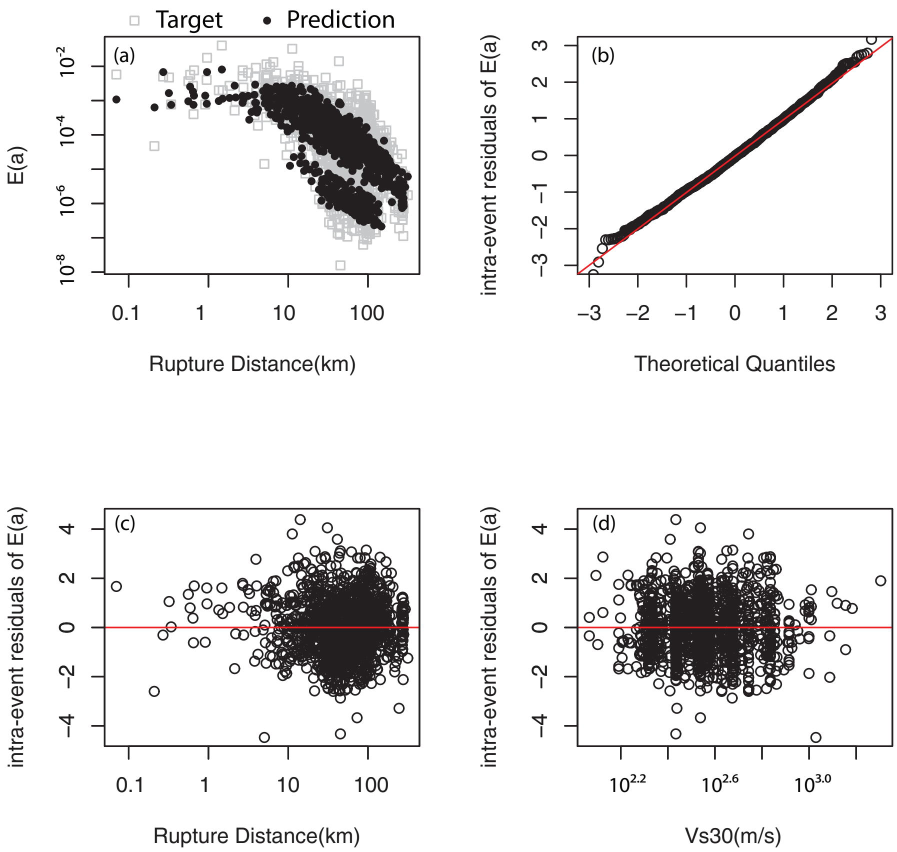

Figure 3.24: First regression analysis of $E(a)$ in major group (a) median prediction from the first regression, (b) quantile-quantile plot for intra event residuals, (c) intra event residuals versus rupture distance, and (d) intra event residuals versus V_{S30}.

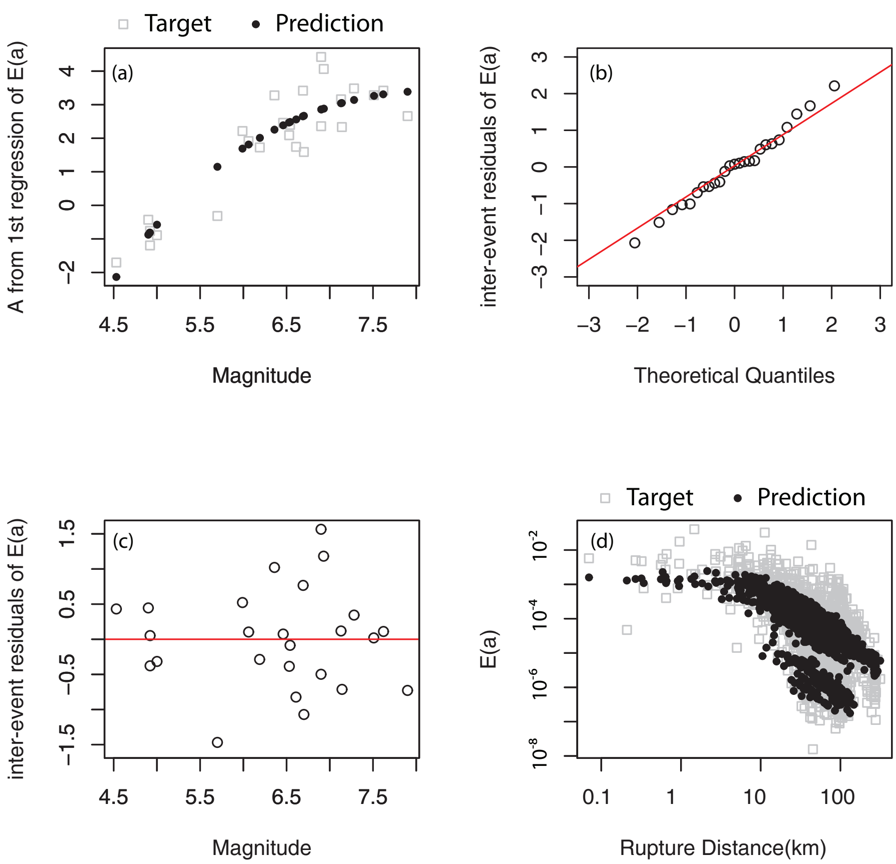

Figure 3.25: Second regression analysis of $E(a)$ in major group (a) median prediction of A from the second regression, (b) quantile-quantile plot for intra event residuals, (c) inter event residuals versus moment magnitude, and and (d) median prediction from total regression.

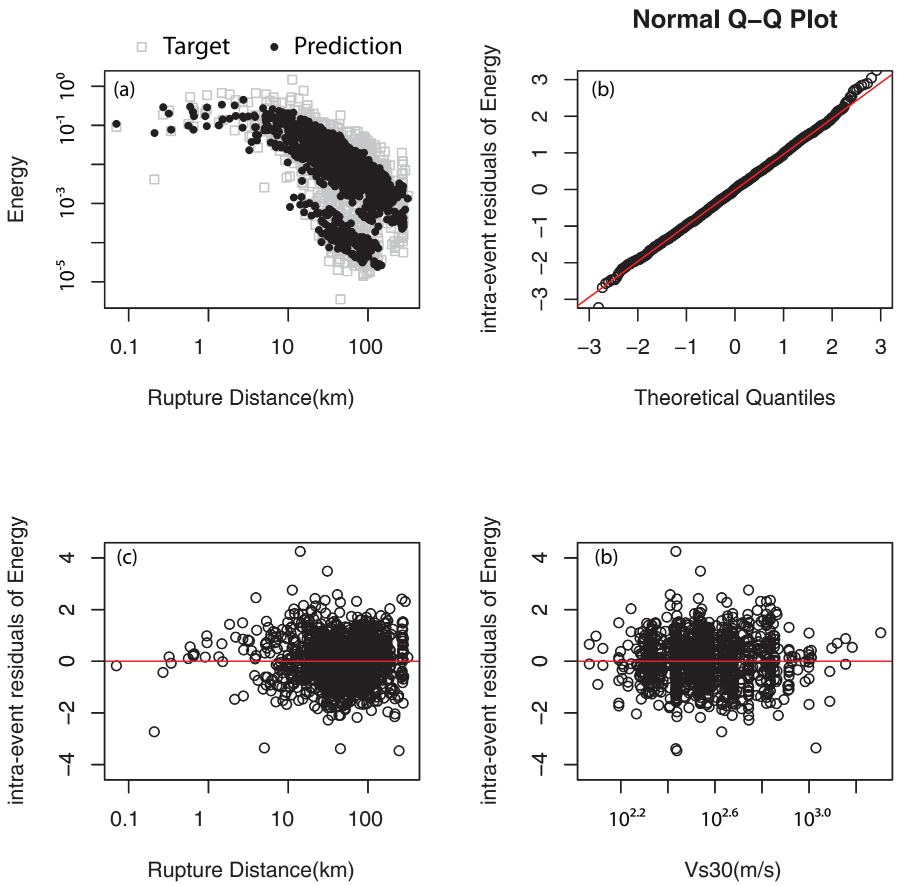

Figure 3.26: First regression analysis of Energy (a) median prediction from the first regression, (b) quantile-quantile plot for intra event residuals, (c) intra event residuals versus rupture distance, and (d) intra event residuals versus V_{S30}.

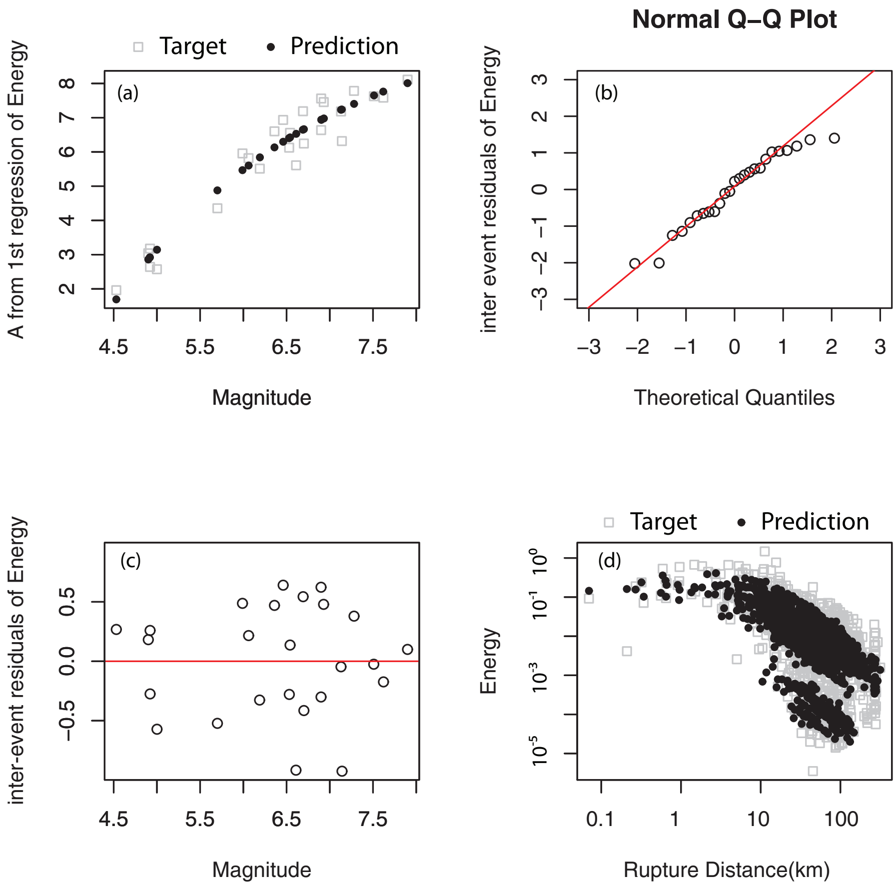

Figure 3.27: Second regression analysis of Energy (a) median prediction of A from the second regression, (b) quantile-quantile plot for intra event residuals, (c) inter event residuals versus moment magnitude, and and (d) median prediction from total regression.

3.5 Effect of model parameters on logarithmic standard deviation of spectral acceleration

Spectral acceleration is an important property of the simulated ground motions because it indicates the "intensity" of the ground motions with respect to their effect on structures. We can also compare spectral accelerations from simulations to observed ground motions to evaluate the realism of the simulations. Here the relative importance of the model parameters are examined by evaluating impact their on logarithmic standard deviations of S_a.

Table 3.5: Simulation cases for relative importance of model parameters

name	the parameter with uncertainty of regression
Case 0	None
Case 1	$E(t)_{min}$
Case 2	$S(t)_{min}$
Case 3	$E(f)_{min}$
Case 4	$S(f)_{min}$
Case 5	$\rho(t,f)_{min}$
Case 6	$E(t)_{maj}$
Case 7	$S(t)_{maj}$
Case 8	$E(f)_{maj}$
Case 9	$S(f)_{maj}$
Case 10	$\rho(t,f)_{maj}$
Case 11	$E(a)_{maj}$
Case 12	E_{acc}

Figures 3.28 and 3.29 show 300 spectral responses of the simulated ground motions with uncertainty in one of the model parameters considered at a time as listed in Table 3.5. The median spectral amplitudes are almost the same for all cases.

According to the figures, the uncertainty in E_{acc}, $E(f)$, and $S(f)$ are important for the logarithmic standard deviation of S_a. The mean energy (E_{acc}) scales $\sigma_{\ln S_a}$ up at all periods because E_{acc} is independent of frequency. The uncertainty in $E(f)$ and $S(f)$ makes $\sigma_{\ln S_a}$ larger at long periods because $E(f)$ changes the peak period of S_a and it changes the period of the large $\ln S_a$. The uncertainties in the other parameters have lower influence on the logarithmic standard deviation of S_a than these three parameters.

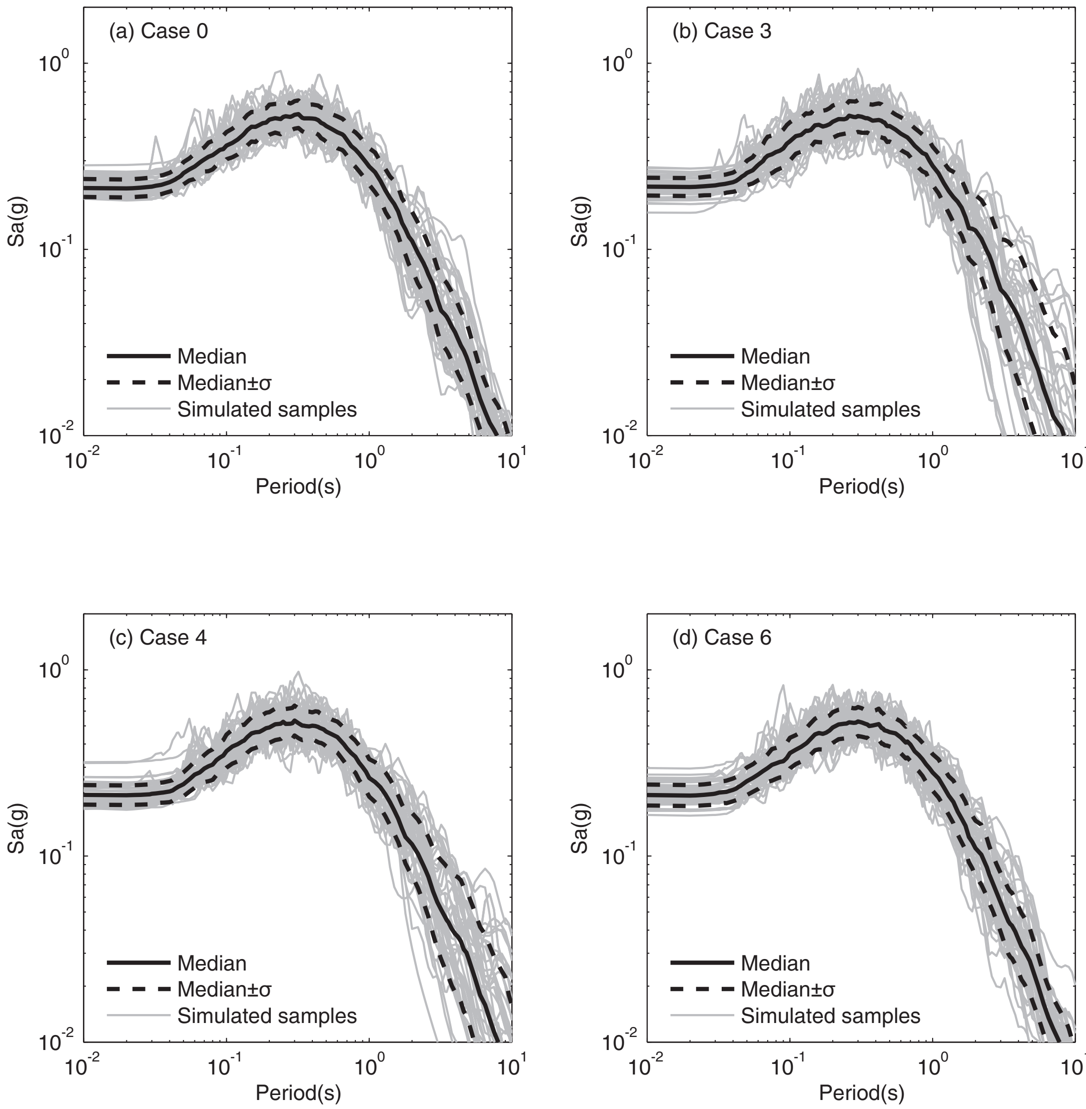

Figure 3.28: Comparison of median spectral accelerations of simulated ground motion based on predicted parameter (a) Case 0: without residuals, (b) Case 3: with residuals of Energy, (c) Case 4: with residuals of $E(f)$ in minor, and (d) Case 6: with residuals of $S(f)$ in minor.

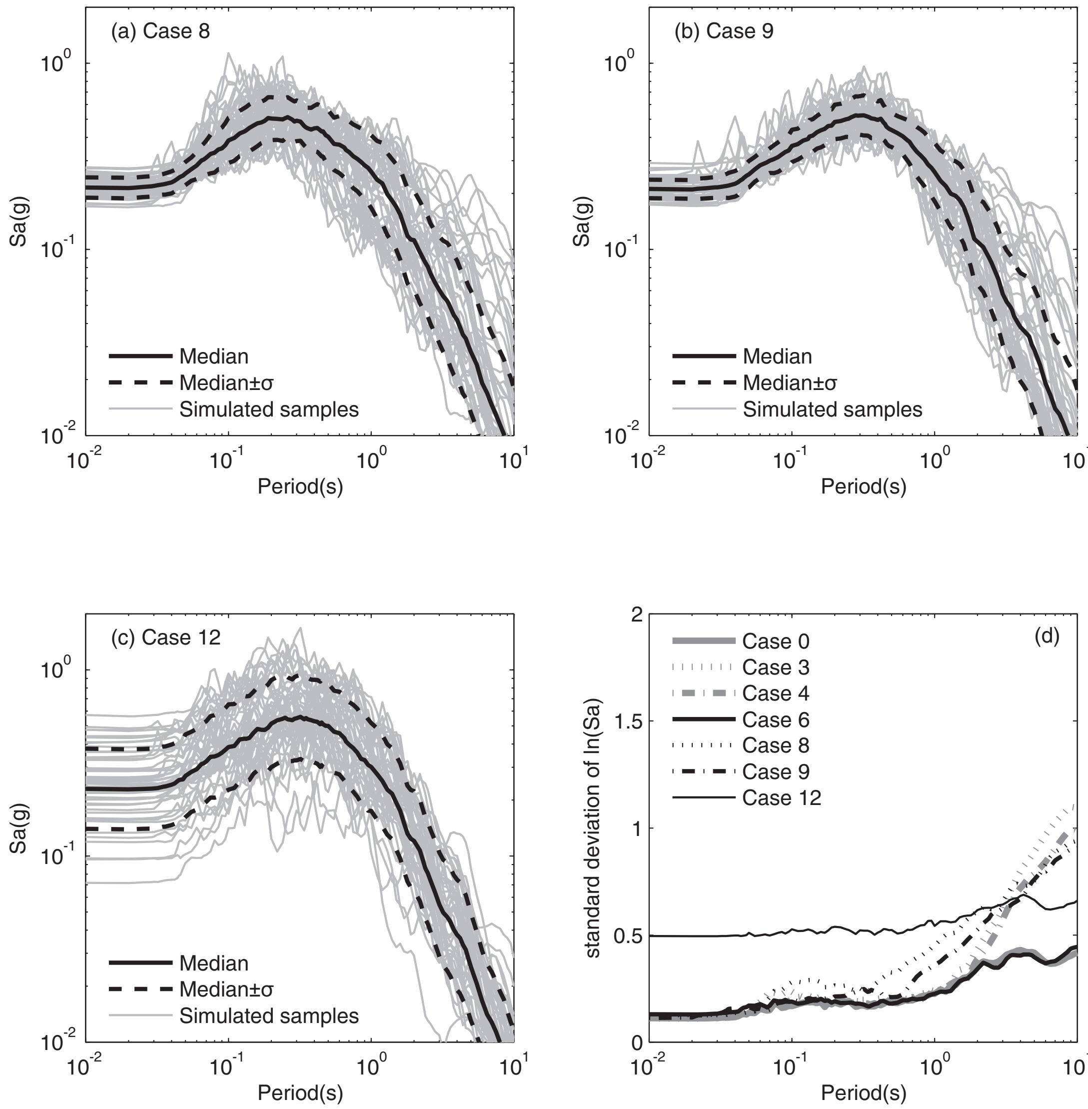

Figure 3.29: Comparison of median spectral accelerations of simulated ground motion based on predicted parameter (a) Case 8: with residuals of $E(t)$ in major, (b) Case 9: with residuals of $E(f)$ in major, (c) Case 12: with residuals of $S(f)$ in major, and (d) comparison of logarithmic standard deviation of S_a; each case represent the simulated ground motions with uncertainty in one of the model parameters considered at a time, Case 0: no uncertainty in model parameters, Case 3: $E(f)_{min}$, Case 4: $S(f)_{min}$, Case 6: $E(t)_{maj}$, Case 8: $E(f)_{maj}$, Case 9: $S(f)_{maj}$, Case 12: E_{acc}.

3.5.1 Magnitude scaling

The simulated ground motions are generated with $R_{rup} = 10km$, $R_{hyp} = 10km$, $V_{S30} = 400m/s$, and $M = 5, 6, 7$ and 8. Figure 3.30 shows the median and logarithmic standard deviation of the simulated ground motions for each case. The logarithmic standard deviations of S_a increases with period, and the periods where the logarithmic standard deviations start increasing are associated with the peak periods of S_a, which are associated with the spectral centroid of the wavelet packets in both the major and minor groups. From the regression analysis for the model parameters, the spectral centroids have negative trends with M. Therefore the peak periods of S_a increase with M, consistent with trends in recorded ground motions.

As seen in Figure 3.30, the logarithmic standard deviations start increasing at periods where S_as decline. S_a at short periods has smaller logarithmic standard deviation than at long periods because S_a is controlled by peak amplitude based on the shape of the transfer function that is described in Section 2.7.1. Also, we have uncertainty in the spectral centroid, so the fluctuation of the peak period affects the logarithmic standard deviation of S_a around the peak of S_a. Hence, at periods greater than the peak S_a, the logarithmic standard deviations significantly increase with period.

A second explanation for this increase in standard deviation is that the wavelet transform has limited period resolution at these long periods, due to its finite time-domain resolution. These large standard deviations of $\ln S_a$ at long periods are a weakness of the proposed stochastic model, as these standard deviations are larger than those seen in recorded ground motions. Although the problem arises at long periods and for small-magnitude earthquakes, the standard deviations of $\ln S_a$ for large-magnitude earthquake are still large. Fortunately, however, the standard deviations $\ln S_a$ for spectral acceleration conditioned by a particular period of engineering interest are observed to be small enough in comparison with recorded ground motions. This is discussed further in Chapter 6.

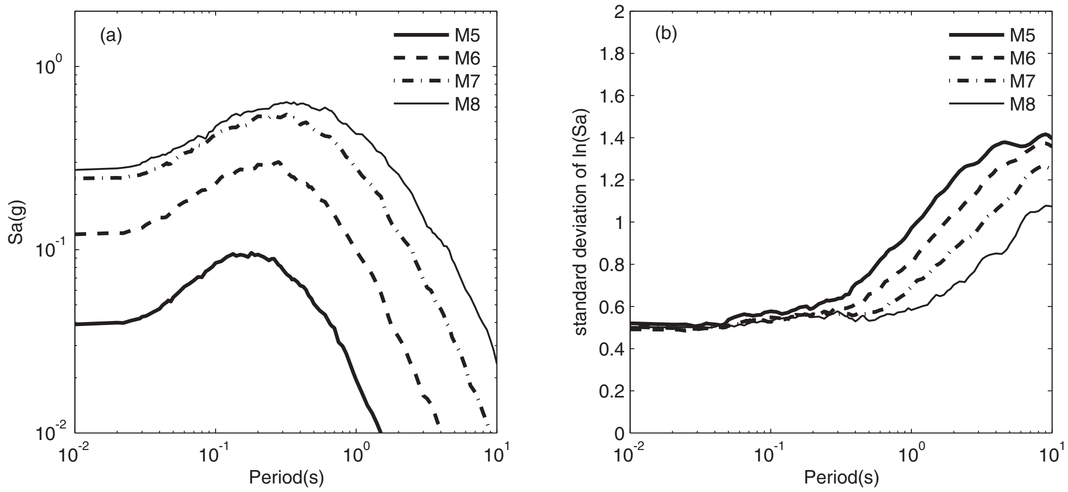

Figure 3.30: Spectral accelerations of simulated ground motions with a distance of 10km and various magnitudes (a) median of S_a, (b) logarithmic standard deviation of S_a.

3.5.2 Variation in simulated ground motions as a function of source-to-site geometry

To illustrate the effect of source-to-site geometry, simulated ground motions for nine different locations surrounding on earthquake rupture. The model parameters are predicted based on a surface-rupturing vertical strike-slip fault with $M = 7$, and $V_{S30} = 400m/s$ for all sites. Since the regression model uses two types of distance, R_{hyp} and R_{rup}, the proposed stochastic model can generate ground motions considering fault size and site locations.

The locations of the simulated ground motions are given in Figure 3.31 and Table 3.6. Based on the geometric relationship between the fault and the location of the simulated ground motions, the simulated ground motions at location F are expected to have a forward directivity effect, which causes a shorter duration and larger amplitude than those of ground motions recorded at the other locations.

In the proposed regression model, the duration decreases as $R_{hyp} - R_{rup}$ gets bigger, but the amount of energy in the ground motion does not change. Therefore, resulting simulated ground motions with large $R_{hyp} - R_{rup}$ have short durations and large amplitudes, which are consistent with the directivity effect. Cases D, E, F, G, H, and I have $R_{hyp} - R_{rup}$

Table 3.6: Distance values for simulated ground motions at the nine sites considered

Case	$R_{rup}(km)$	$R_{hyp}(km)$	$R_{hyp} - R_{rup}$
A	100	100	0
B	60	60	0
C	10	10	0
D	10	27	13
E	10	51	41
F	10	60	50
G	50	100	50
H	42	60	18
I	71	100	29

greater than zero, so they have some level of forward directivity. Cases A, B, and C have hypocentral distances R_{hyp} same as the rupture distances R_{rup}, therefore they don't have the forward directivity effect.

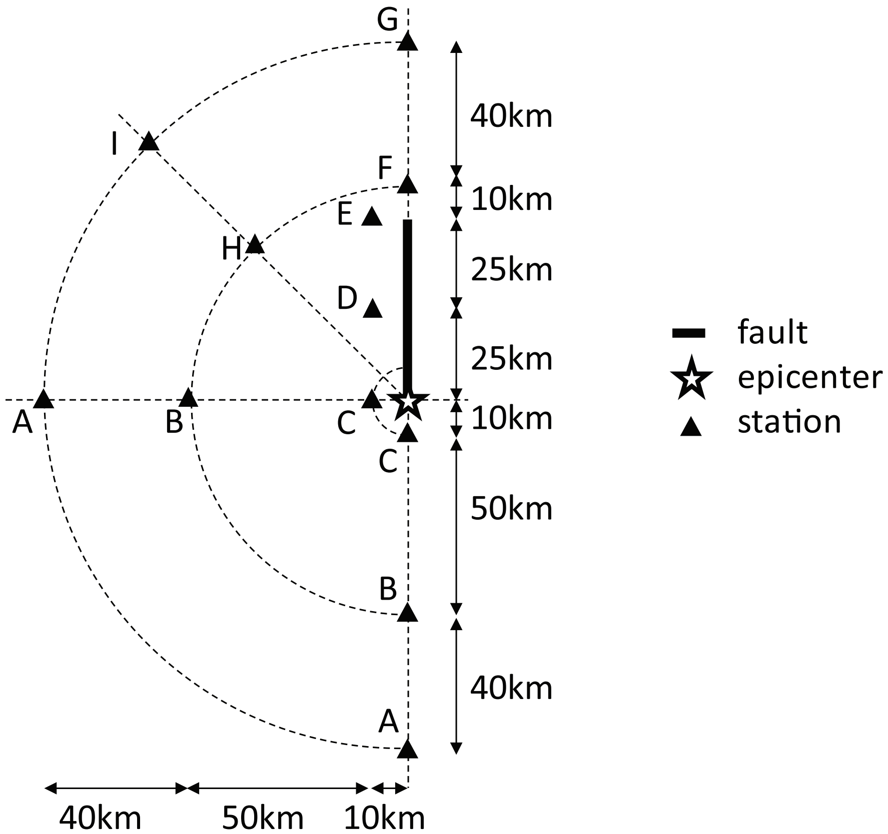

Figure 3.31: Map of fault, epicenter, and the nine locations of the simulated ground motions.

Three hundred simulated ground motions are generated for each location and one sample is selected based on the similarity of its spectral acceleration to the median of spectral accelerations from all 300. Figure 3.32 shows the median and logarithmic standard deviation of the spectra of the simulated ground motions for Cases A and C. The median S_a in Case C is larger than that in Case A, and the peak period in Case C is slightly longer than that in Case A because short period components attenuate relatively faster with distance. The logarithmic standard deviations of S_a of both cases are almost the same.

Figure 3.33 shows median and logarithmic standard deviations of S_a for Cases A, B, C, D, E, F, and G. The location of the simulated ground motions in these cases are on approximately a straight line along with the fault. Cases ordered according to median S_a (largest to smallest) are F, E, D, C, G, B, and A. The order of median S_a in Cases C, D, E, F, and G is reasonable since the forward directivity effect in Case F is the strongest, and the effect decreases in the order of F, E, D. The order of median S_a in Cases C, B, A is also reasonable as their distance from fault increases in that order. The logarithmic standard deviations of S_a of these cases are almost the same.

Figure 3.34 shows the median and logarithmic standard deviation of S_a for Cases F, G, H, and I. Cases H and I are located on a straight line angled 45 degrees from the strike of the fault. The median S_a in Case H is larger than that in Case I because of attenuation with distance. The median S_as in Cases F and G are larger than those in Cases H and I, respectively, since the directivity effect in Cases F and G are stronger than that in Cases H and I. The logarithmic standard deviations of S_a are nearly identical in call cases.

Figures 3.35, 3.36, and 3.37 show example acceleration, velocity, and displacement time series of the simulated ground motions, respectively, in Cases A, B, C, D, E, F, and G. The all time series in Cases D, E, and F have shorter duration than those in other cases since $E(t)$ and $S(t)$ of simulated ground motions decrease with increasing the difference between hypocentral distance and rupture distance (Table 3.2). Also, the all time series in Cases D, E, and F have larger amplitude than those in other cases since E_{acc} is independent of the difference of those distances. Therefore, the velocity time series in Case F looks more visually pulse-like than those in other cases.

Figures 3.38, 3.39, and 3.40 show example acceleration, velocity, and displacement time series of the simulated ground motions, respectively, for Cases F, G, H, and I. The time series in Cases F and H have shorter duration and larger amplitude than those in Cases G and I respectively, as would be expected based on attenuation and wave scattering effects.

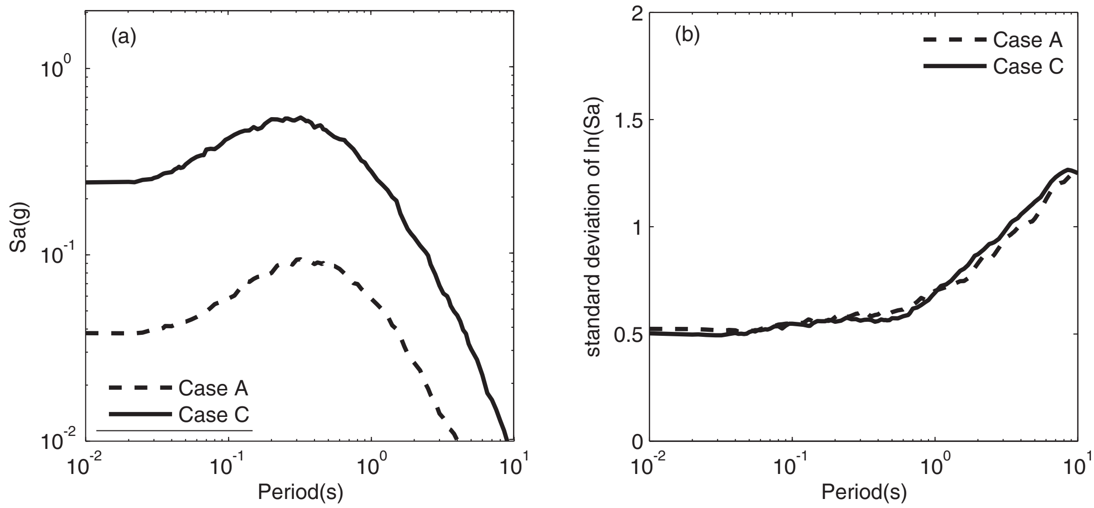

Figure 3.32: Spectral accelerations of simulated ground motion without forward and backward directivity (a) median S_a, (b) logarithmic standard deviation of S_a.

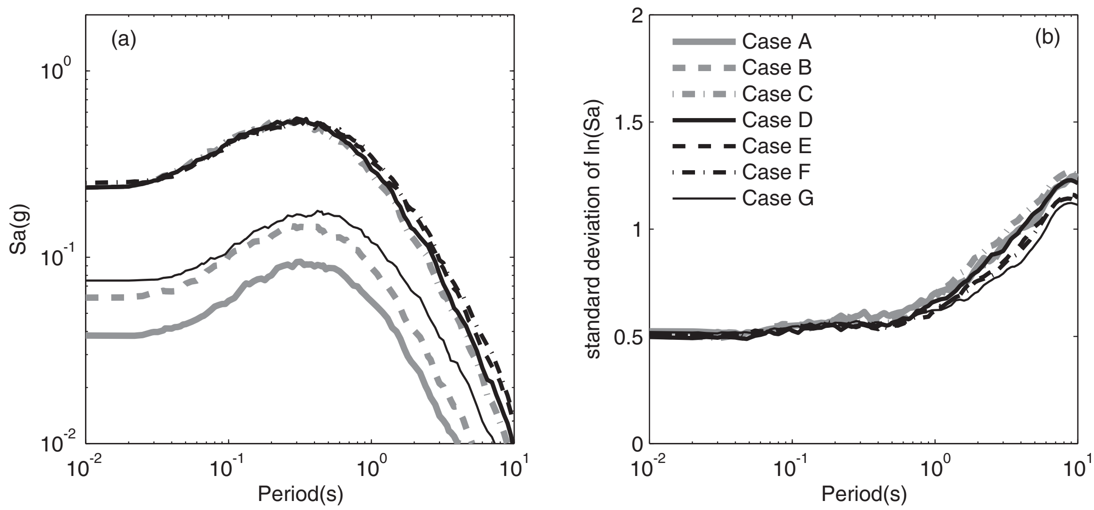

Figure 3.33: Spectral accelerations of simulated ground motion with forward and backward directivity (a) median S_a, (b) logarithmic standard deviation of S_a.

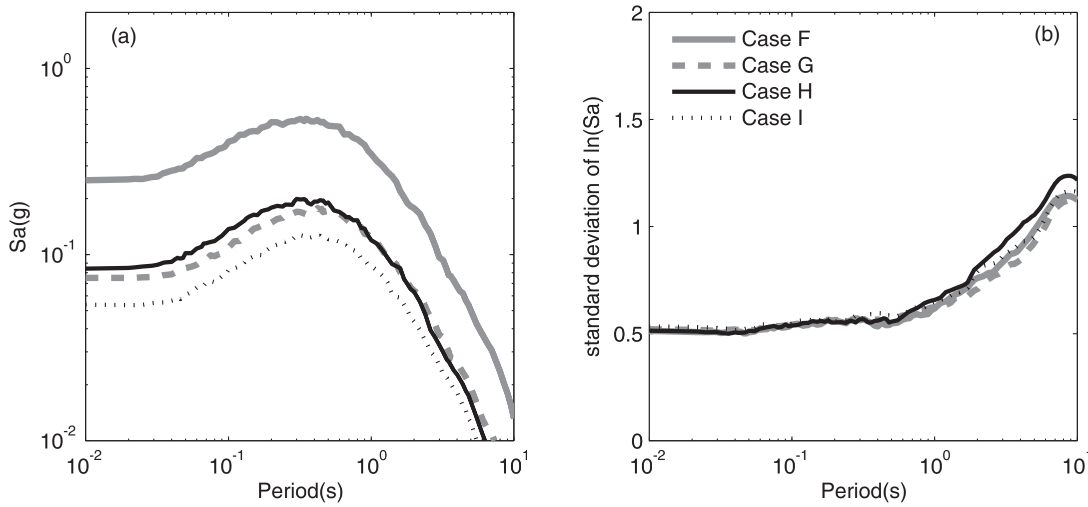

Figure 3.34: Spectral accelerations of simulated ground motion with strong and weak forward directivity (a) median S_a, (b) logarithmic standard deviation of S_a.

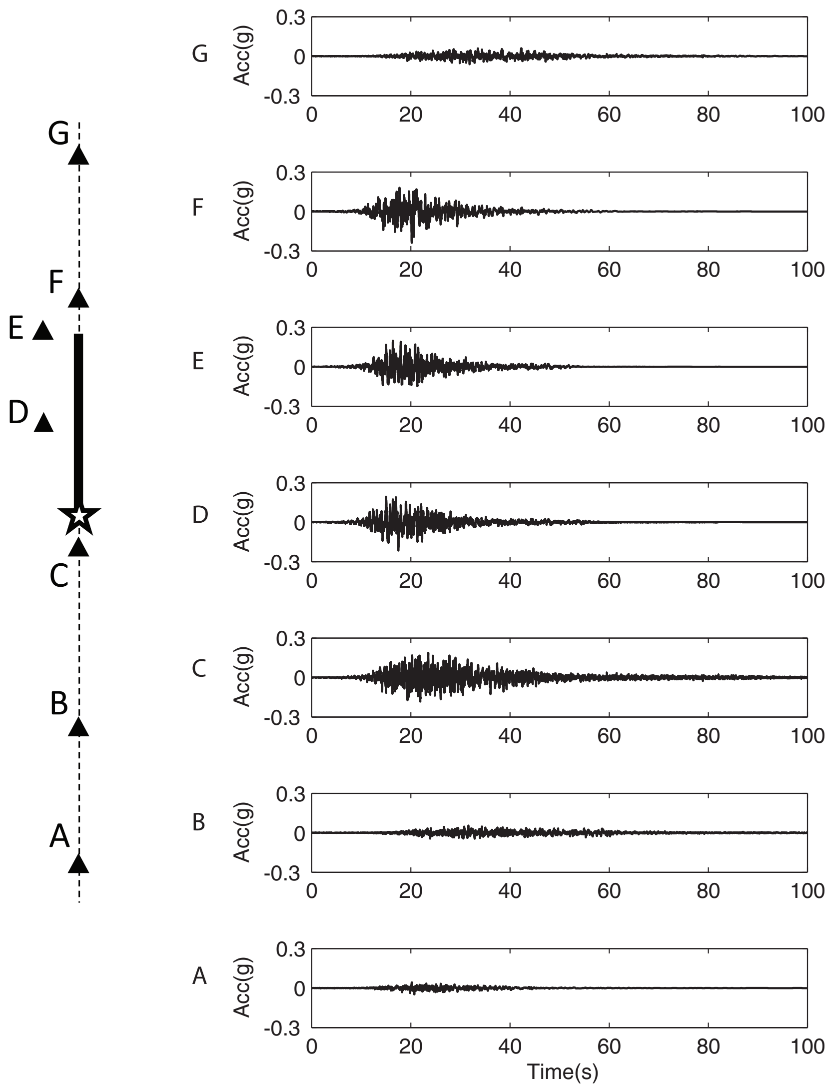

Figure 3.35: Acceleration time histories of simulated ground motions at various locations relative to the fault.

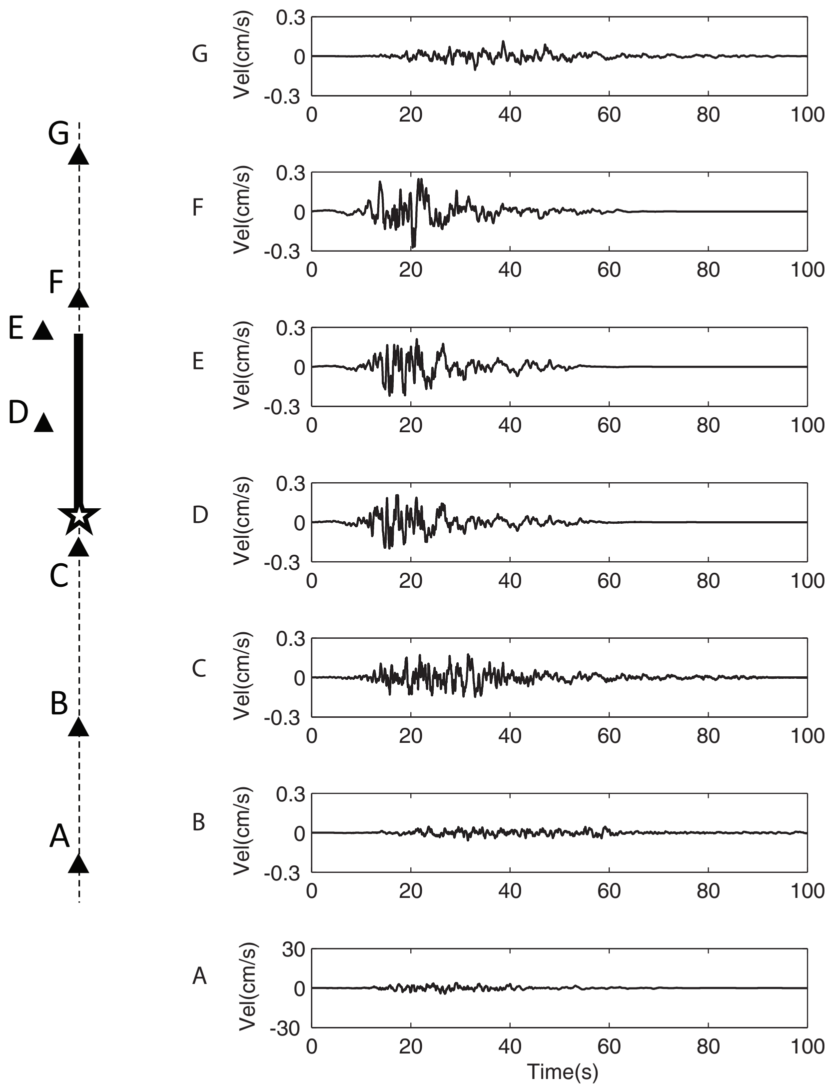

Figure 3.36: Velocity time histories of simulated ground motions at various locations relative to the fault.

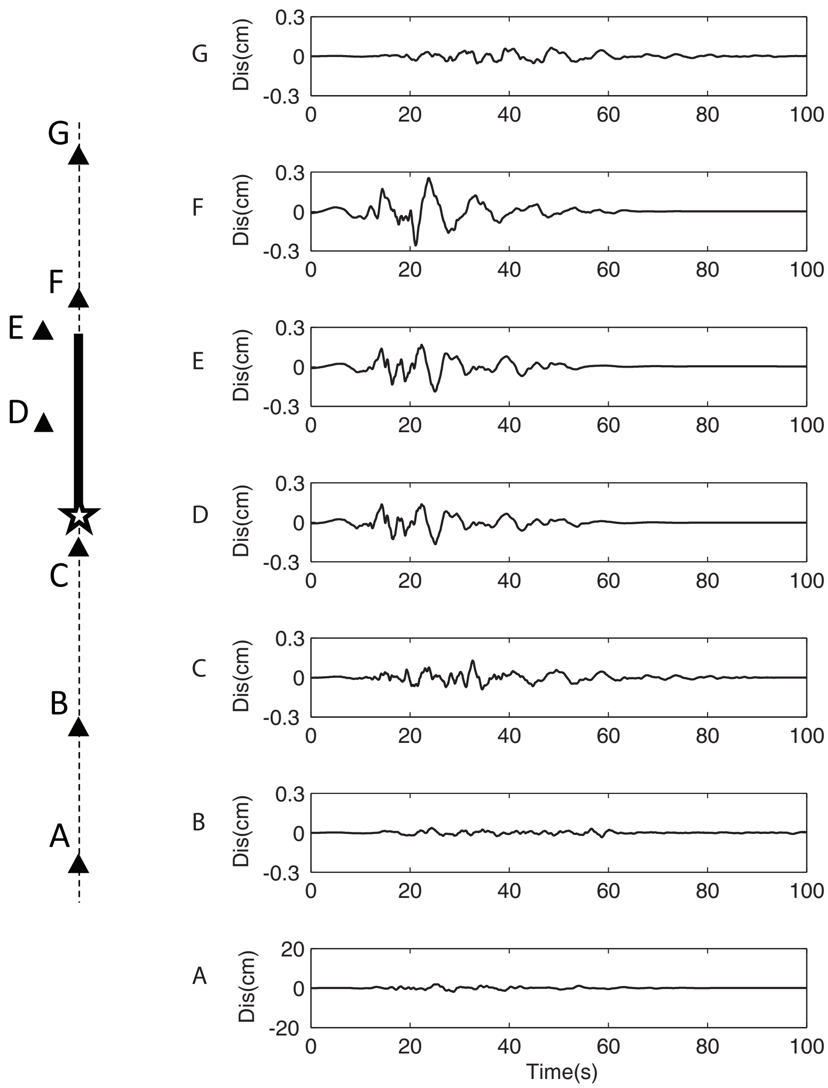

Figure 3.37: Displacement time histories of simulated ground motions at various locations relative to the fault.

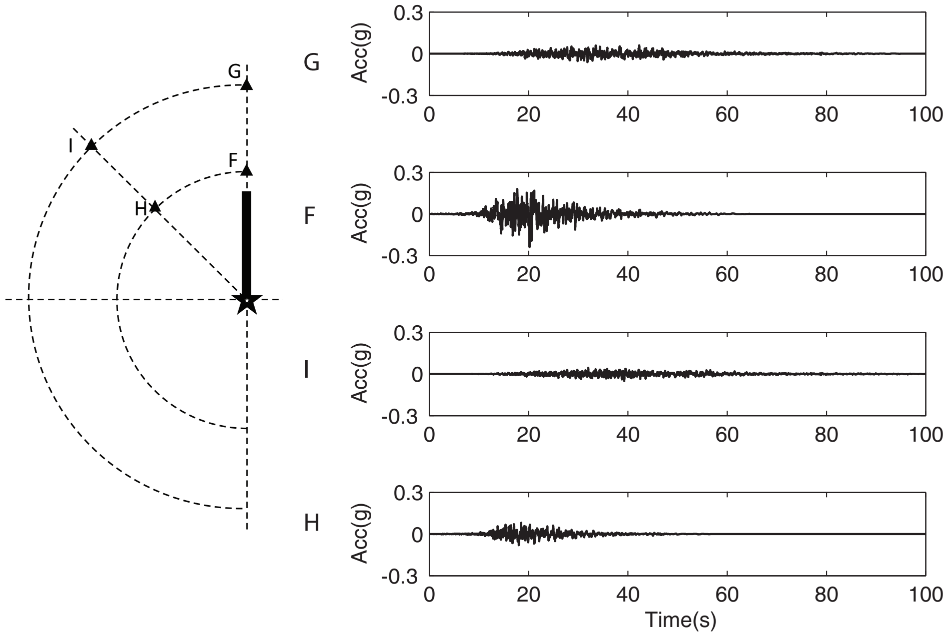

Figure 3.38: Acceleration time histories of simulated ground motions with weak directivity.

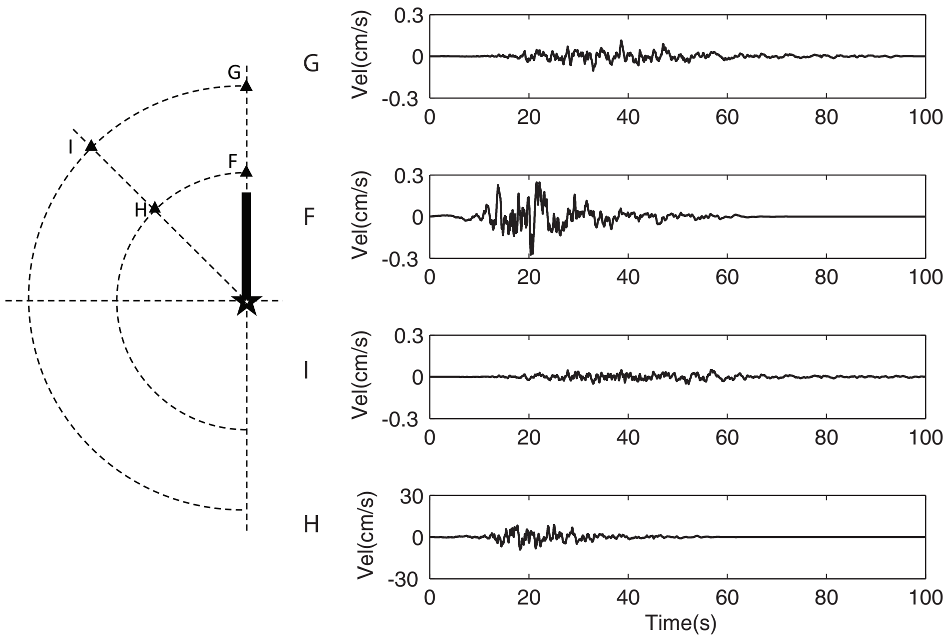

Figure 3.39: Velocity simulated time histories of ground motions with weak directivity.

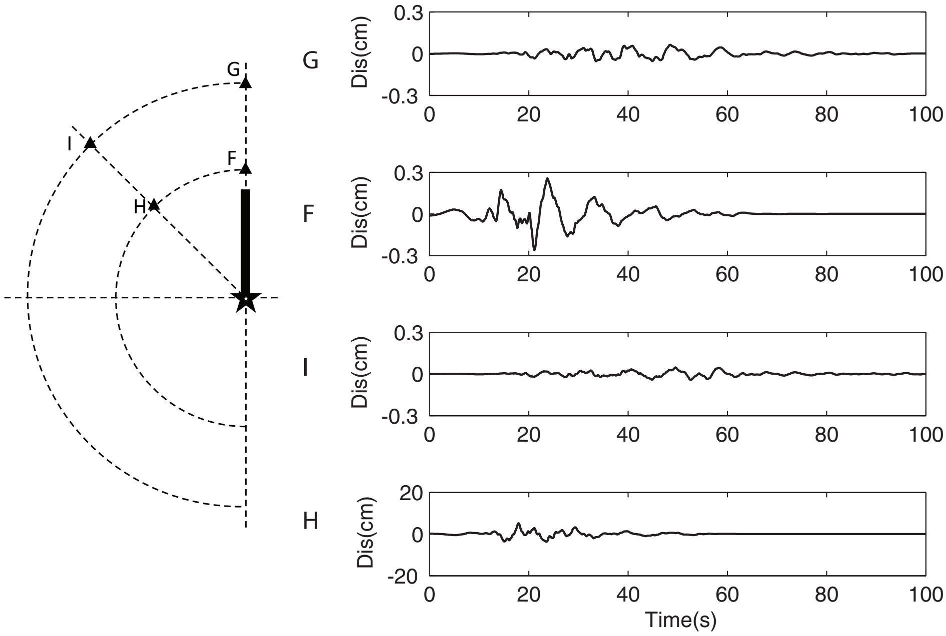

Figure 3.40: Displacement simulated time histories of ground motions with weak directivity.

3.6 Conclusions

A regression analysis of the 13 model parameters of the proposed stochastic model for simulating earthquake ground motions has been conducted. Earthquake magnitude, hypocentral distance, rupture distance, and V_{S30} were used as predictor variables to calibrate a regression model based on data from 1408 recorded fault normal ground motions from the NGA database. A two-stage regression analysis was employed, consistent with modern ground motion prediction model development (a model was also developed using Mixed Effects regression, and the results were nearly identical). Functional forms and predictor parameters were determined using standard regression model building techniques, including hypothesis testing to determine the statistical significance of each potential predictor variable. Normality of the model residuals were evaluated using quantile-quantile plots. The resulting regression coefficients were then inspected and all were found to be consistent with seismological concepts.

The resulting regression model provides mean values of the model parameters, standard deviations of variations around those means, and correlation coefficients between parameters (to capture the joint behavior of model errors for each pair of parameters). With this regression model calibrated, it is possible to simulate realizations of the 13 model parameters and generate corresponding ground motion time histories for any magnitude, distance, and site condition within the range of calibration. Time histories were simulated using this model, and characteristics of the resulting motions were studied. The simulated motions show effects of magnitude scaling, distance scaling, and directivity (in the time histories and response spectra) that are consistent with seismological expectations.

It is a straightforward to modify the predicted parameters, and the uncertainty in each predicted parameter, in order to study the impact on resulting ground motion time histories and response spectra. By varying these parameters, it was observed that uncertainty in the energy parameter and the frequency-related parameters have the greatest impact on the logarithmic standard deviation of S_a.

The results in this chapter suggest that the proposed regression model is appropriate to connect the wavelet-based model parameters with seismological variables, so that one can generate appropriate model parameters for any seismological condition of interest, even if one does not have a "seed ground motion" for the condition of interest. This approach is limited by the range of seismological conditions present in the data set used to calibrate the model (approximately $6 \leq M \leq 8$, $220 \leq V_{S30} \leq 760 m/s$, and $1 \leq R_{rup} \leq 100 km$), but nonetheless provides a valuable tool over a broad range of conditions.

Chapter 4

Comparison of simulation results with ground motion prediction models

4.1 Abstract

The proposed simulation approach can now be used to produce suites of ground motions for a given magnitude, distance, and site condition. The distributions of response spectra (and other Intensity Measures) resulting from suites of simulations for a given magnitude, distance, and site condition can be directly compared to results from empirical ground motion prediction models that produce predictions of those same distributions. The ground motions produced using this predictive model are studied extensively, and seen to have elastic and inelastic response spectra, durations, Arias intensity, mean periods, significant duration, and the characteristics of ε, that are consistent in both mean and variability to existing published predictive models for those properties. These results demonstrate the reasonableness of the simulation procedure, and its consistency with the ground motion database used for calibration. In this context, the simulation procedure can be viewed as comparable to those empirical predictive models, except that it produces entire ground motion time histories rather than just numerical values for individual Intensity Measures of interest.

4.2 Introduction

The stochastic ground motion model using wavelet packets has been developed for simulating ground motions with time and frequency nonstationarity. The 13 parameters required for the proposed stochastic ground motion model can be computed from regression equations given a target earthquake magnitude, hypocentral distance, rupture distance, and site condition. To use these simulated ground motions for probabilistic seismic hazard analysis and nonlinear structural analysis, the simulated ground motions computed from the predicted parameters need to be validated. Here the simulated ground motions generated by the proposed stochastic ground motion model are compared to the properties of recorded ground motions as predicted by existing ground motion prediction models (GMPM).

The following properties are selected to examine the properties of the simulated ground motions. Spectral acceleration (S_a) is one of the most important properties of strong ground motions for structures. It is the maximum absolute amplitude of response of a single-degree-of-freedom (SDOF) system with a given natural period and damping, and is computed as the maximum displacement multiplied by squared circular frequency ω^2. Results here will be for 5%-damped spectra. The spectral accelerations (S_a) of the simulated ground motions are compared here with those from Next Generation of Attenuation (NGA) GMPM. The NGA Relations Project developed ground motion prediction models for shallow crustal earthquakes in the western United States and similar active tectonic regions (Abrahamson and Silva 2008 (AS08), Boore and Atkinson 2008 (BA08), Campbell and Bozorgnia 2008 (CB08), Chiou and Youngs 2008 (CY08) and Idriss 2008 (I08)) and these models provide means and standard deviations of $\ln S_a$ with 5% damping ratio. Also, inelastic spectra is compared with predictions from the model of Bozorgnia et al. 2010 (CB10) that provides inelastic spectra with a specified ductility.

The residuals (ε) of recorded ground motions are studied to determine whether they are normally distributed and the inter-period correlations of the ε's are compared to predictions by Baker and Jayaram (2008). The parameter ε and its correlation between periods are related to the response of nonlinear multi-degree-of-freedom structures.

Arias intensity (I_a, Arias 1970) is a representative of the total energy of the ground motions, the significant duration (t_{95-5}, Trifunac and Brady 1975) is connected to the amount of input energy per time, and the mean period (T_m, Rathje et al. 2004) can affect the structural response of the structure with the same natural period Kumar et al. (2011). Arias intensity I_a is predicted by Travasarou et al. (2003), t_{95-5} is predicted by Abrahamson and Silva (1996), and T_m is predicted by Rathje et al. (2004).

The properties described above are all predicted directly by regression models with GMPMs. However, these properties from the simulated ground motions are not directly connected to our regression models because these parameters are computed by resulting time series data that is generated by our stochastic ground motion model with predicted parameters from our regression model. For example, regression models of NGA GMPM for S_a are constructed separately for each period using slightly different recorded ground motion databases; however, S_a from the simulated ground motions are computed from the time series with predicted parameters from the regression model. Therefore the comparisons of these properties from simulated ground motions with those from specifically estimated GMPMs is ambitious. This comparison is necessary, however, for comprehensive validation of our stochastic model and regression analysis.

To evaluate the regression equations and resulting simulations, 300 simulated ground motions are computed for each magnitude/distance/site condition of interest, and their ground motion properties are compared to those properties predicted by GMPM. The examined properties are reasonably observed to match those from GMPM for $6 \leq M \leq 8$, $220 \leq V_{S30} \leq 760 m/s$, $1 \leq R_{rup} \leq 100 km$, $0.01 \leq T \leq 3s$, and vertical strike-slip fault. The results suggest that the simulations produced by the proposed stochastic model and the regression analysis are reasonable under these conditions. This suggests that we can use the simulated ground motions for the probabilistic seismic hazard analysis and perhaps nonlinear dynamic structural analysis.

4.3 Comparison with NGA GMPM for spectral acceleration

4.3.1 Median and logarithmic standard deviation of response spectra

In this section, response spectra comparisons are performed, for vertical strike slip faults under a variety of earthquake magnitudes, distances and site conditions. The NGA models include additional predictor variables other than those used by the model proposed here, so appropriate values of those additional predictor variables are computed as follows, and used for the later comparisons of predictions.

In order to compare with the NGA GMPM, the median value of depth-to-top-of-rupture (Z_{tor}) is computed as: $6km$ for $M = 5$, $3km$ for $M = 6$, $1km$ for $M = 7$, and $0km$ for $M = 8$ based on the recommendation of Abrahamson et al. (2008), and R_{rup} is defined by the depth-to-top-of-rupture and R_{jb} as follows:

$$R_{rup} = \sqrt{R_{jb}^2 + Z_{tor}^2} \tag{4.1}$$

$Z_{1.0}$ values are inferred from V_{S30} using the suggested approaches by individual models. $Z_{1.0}$ for AS08 are from Abrahamson and Silva (2008), and $Z_{1.0}$ for CY08 is defined using the following equation from Chiou and Youngs (2008):

$$\ln(Z_{1.0}) = 28.5 - \frac{3.82}{8}\ln(V_{S30}^8 + 378.7^8) \tag{4.2}$$

Distance scaling

Predictions of PGA and S_a at three periods for varying distances, and for a soil site condition ($V_{S30} = 270m/s, Z_{1.0} = 492m$ for AS08, $Z_{1.0} = 327m$ for CY08, $Z_{2.5} = 0.64km$) are shown in Figures 4.1, 4.2, 4.3, and 4.4. We see that the medians of PGA and S_a observed in the simulations are smaller than those of the GMPMs for $R_{jb} < 10km$ and $M < 5$. This is in part because there are few events with small magnitude and close distance in the calibration dataset, so the regression model is less reliable in those cases. At larger magnitudes or distances, the agreement between the simulations and GMPMs is relatively good.

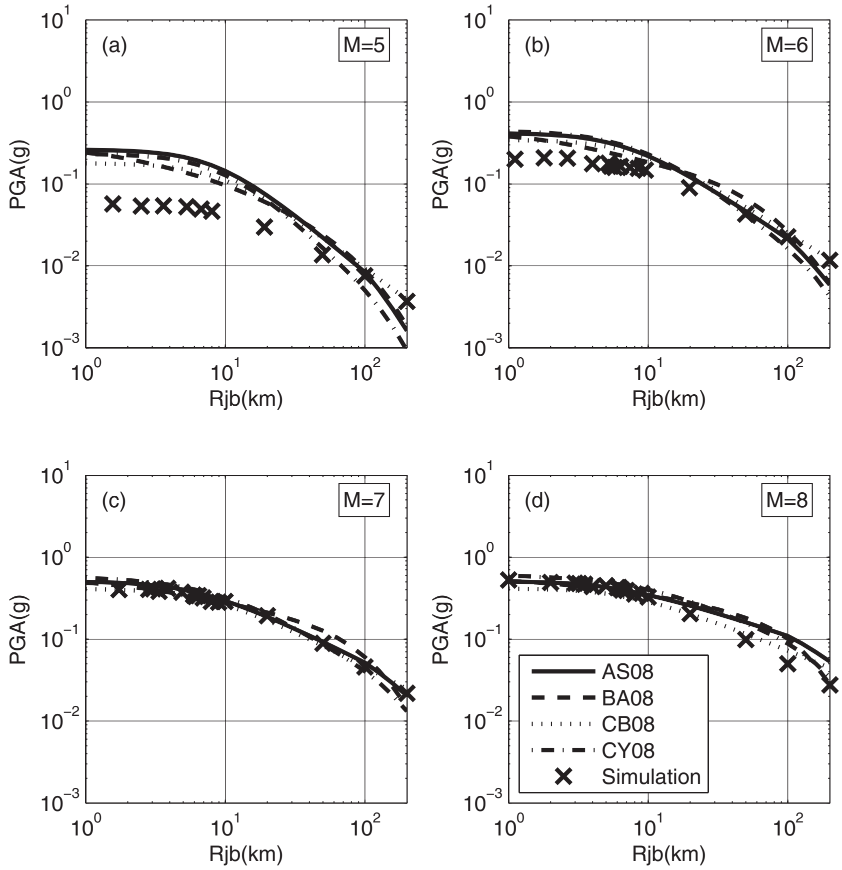

Figure 4.1: Median of PGA computed from the NGA GMPMs and simulations ($1 \leq R_{jb} \leq 200km, V_{S30} = 270m/s$). (a) $M = 5$, (b) $M = 6$, (c) $M = 7$, and (d) $M = 8$.

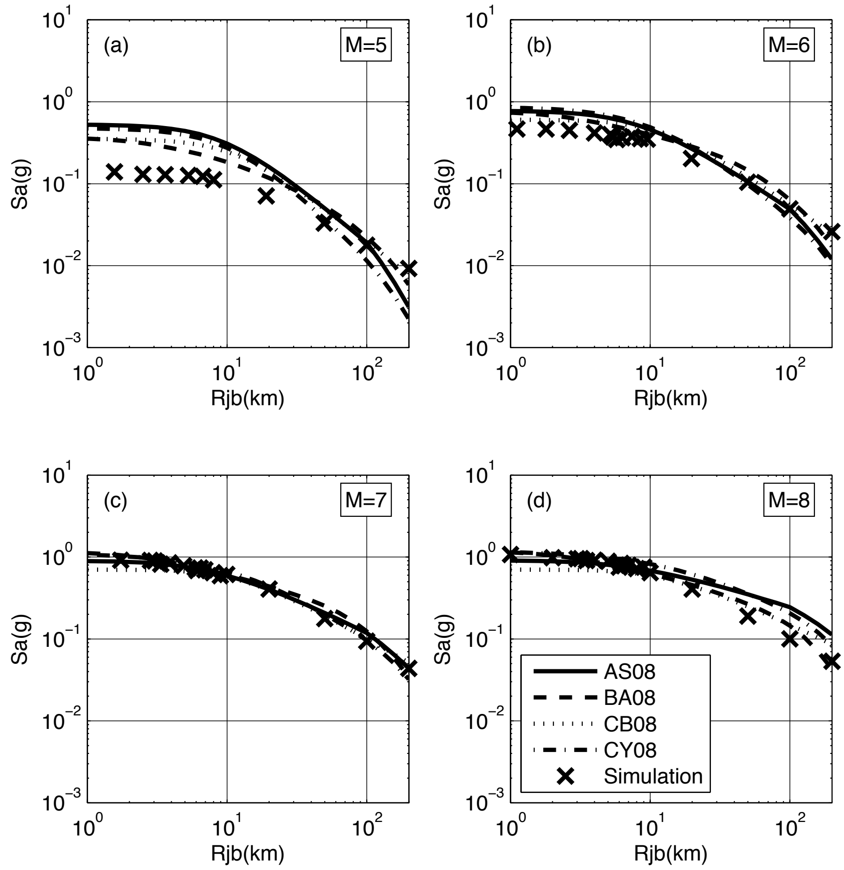

Figure 4.2: Median of elastic S_a at $T = 0.2s$ computed from the NGA GMPMs and simulations ($1 \leq R_{jb} \leq 200km$, $V_{S30} = 270m/s$). (a) $M = 5$, (b) $M = 6$, (c) $M = 7$, and (d) $M = 8$.

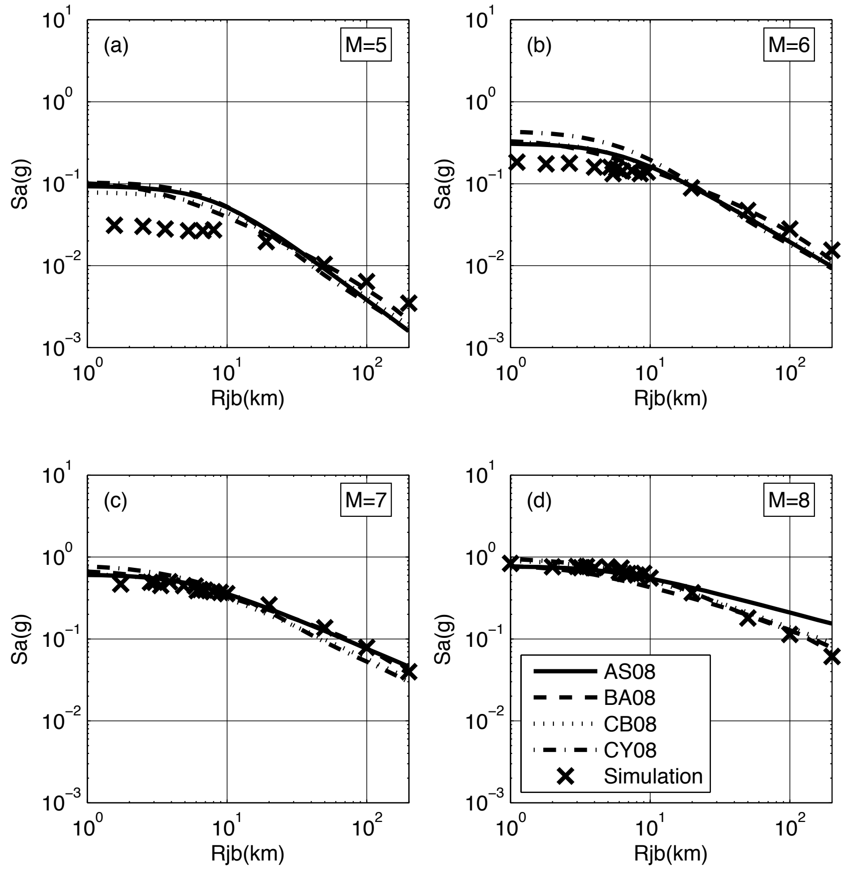

Figure 4.3: Median of elastic S_a at $T = 1s$ computed from the NGA GMPMs and simulations ($1 \leq R_{jb} \leq 200km$, $V_{S30} = 270m/s$). (a) $M = 5$, (b) $M = 6$, (c) $M = 7$, and (d) $M = 8$.

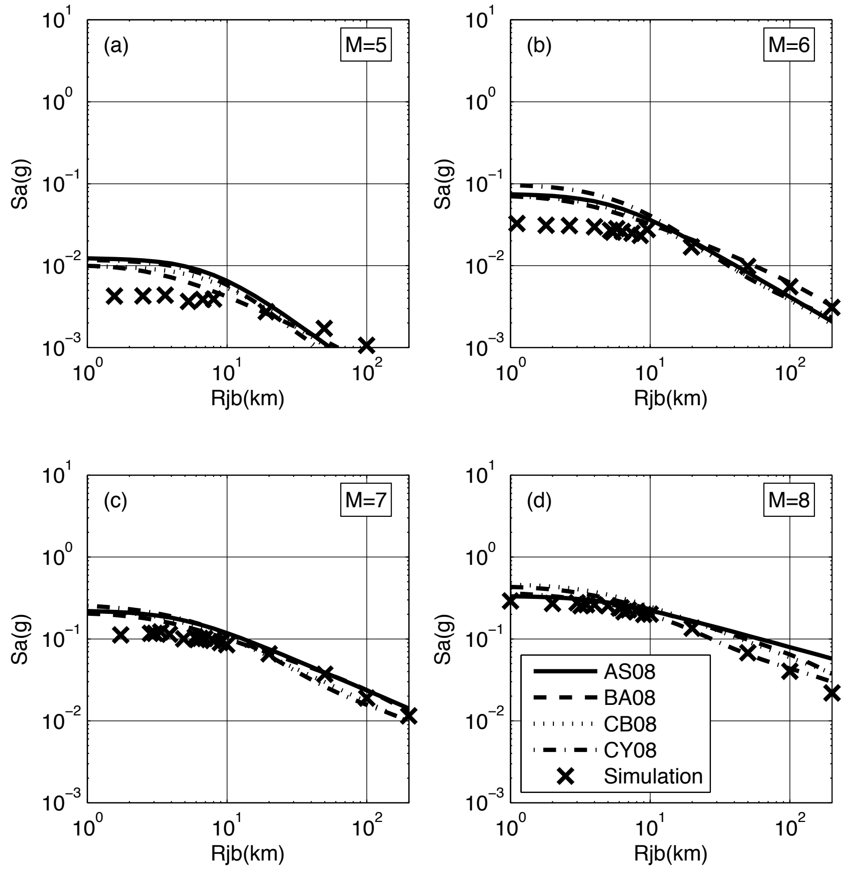

Figure 4.4: Median of elastic S_a at $T = 3s$ computed from the NGA GMPMs and simulations ($1 \leq R_{jb} \leq 200km$, $V_{S30} = 270m/s$). (a) $M = 5$, (b) $M = 6$, (c) $M = 7$, and (d) $M = 8$.

Magnitude scaling

The magnitude scaling of the median PGA and S_a at three periods for $R_{jb} = 10km$ and $30km$ are shown in Figures 4.5 and 4.6, respectively. For $M \geq 6$, the median S_as from the simulations again match reasonably those from GMPMs.

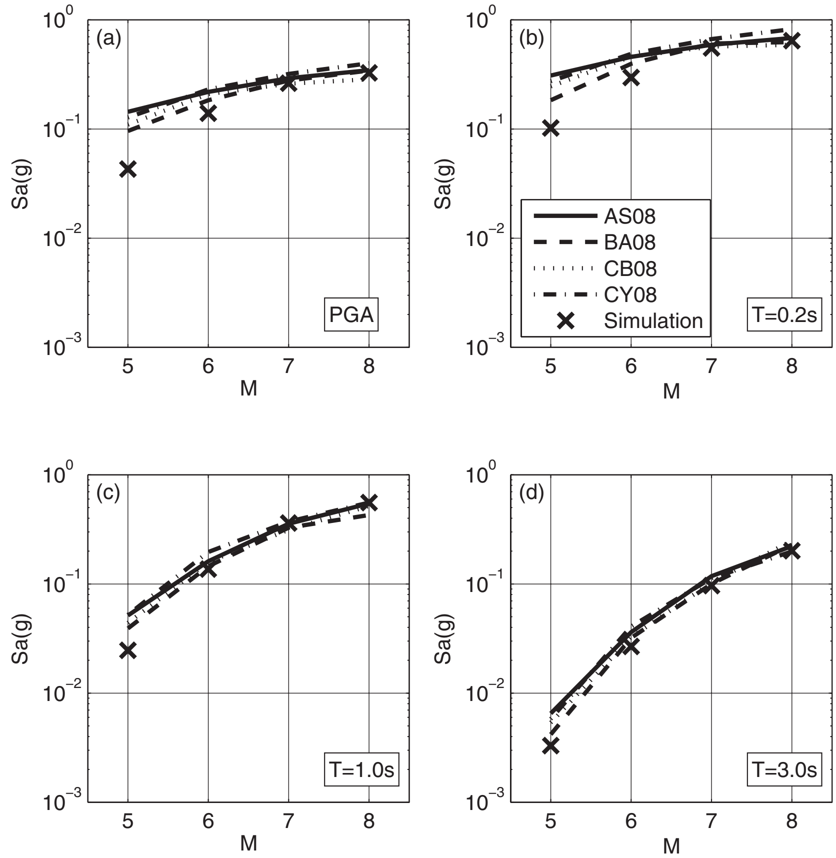

Figure 4.5: Median of PGA and elastic S_a computed from the NGA GMPMs and simulations ($5 \leq M \leq 8$, $R_{jb} = 10km$ $V_{S30} = 270m/s$). (a) PGA, (b) S_a at $T = 0.2s$, (c) S_a at $T = 1s$, and (d) S_a at $T = 3s$.

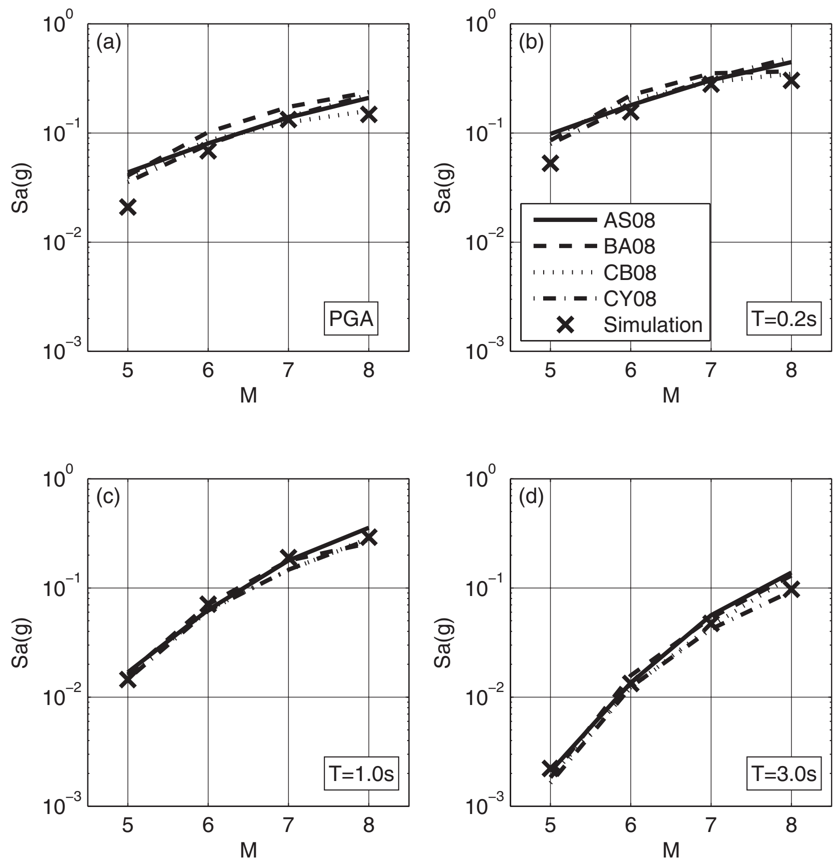

Figure 4.6: Median of PGA and elastic S_a computed from the NGA GMPMs and simulations ($5 \leq M \leq 8$, $R_{jb} = 30km$ $V_{S30} = 270m/s$). (a) PGA, (b) S_a at $T = 0.2s$, (c) S_a at $T = 1s$, and (d) S_a at $T = 3s$.

V_{S30} scaling

The V_{S30} scaling of the median PGA and spectral acceleration for $R_{jb} = 10, 30$, and $100km$ are shown in Figures 4.7, 4.8, and 4.9 for $M = 6$, Figures 4.10, 4.11, and 4.12 for $M = 7$, and Figures 4.13, 4.14, and 4.15 for $M = 8$. For $M = 6$ and $R_{jb} = 10km$, S_a of $V_{30} > 300m/s$ from the simulated ground motions are smaller than those from GMPMs since S_a with $R_{jb} < 10km$ is less reliable. For the other cases with $M = 6$, S_a from the simulated ground motions reasonably match those from GMPMs. Also, For $M = 7$, S_a from the simulated ground motions reasonably match those from GMPMs.

For $M = 8$ and $R_{jb} = 100km$, the spectra from the simulated ground motions are slightly smaller than those from GMPMs. For other cases with $M = 8$, the spectra from the simulated ground motions reasonably match those from GMPMs.

The discrepancies of S_a between the simulated ground motions and the GMPMs are caused by the difference of functional forms in the models. The regression functions of the GMPMs have a nonlinear term for V_{S30}; however, our model employs a linear term for V_{S30}.

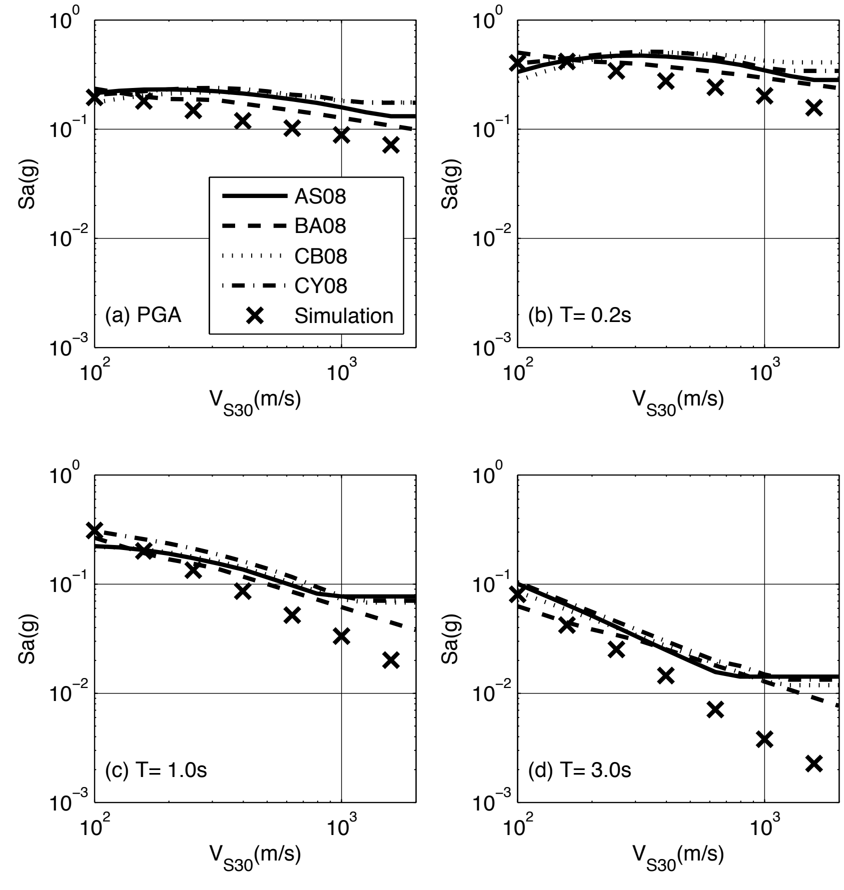

Figure 4.7: Median of PGA and elastic S_a computed from the NGA GMPMs and simulations ($M = 6, R_{jb} = 10km$, $100 \leq V_{S30} \leq 2000m/s$). (a) PGA, (b) S_a at $T = 0.2s$, (c) S_a at $T = 1s$, and (d) S_a at $T = 3s$.

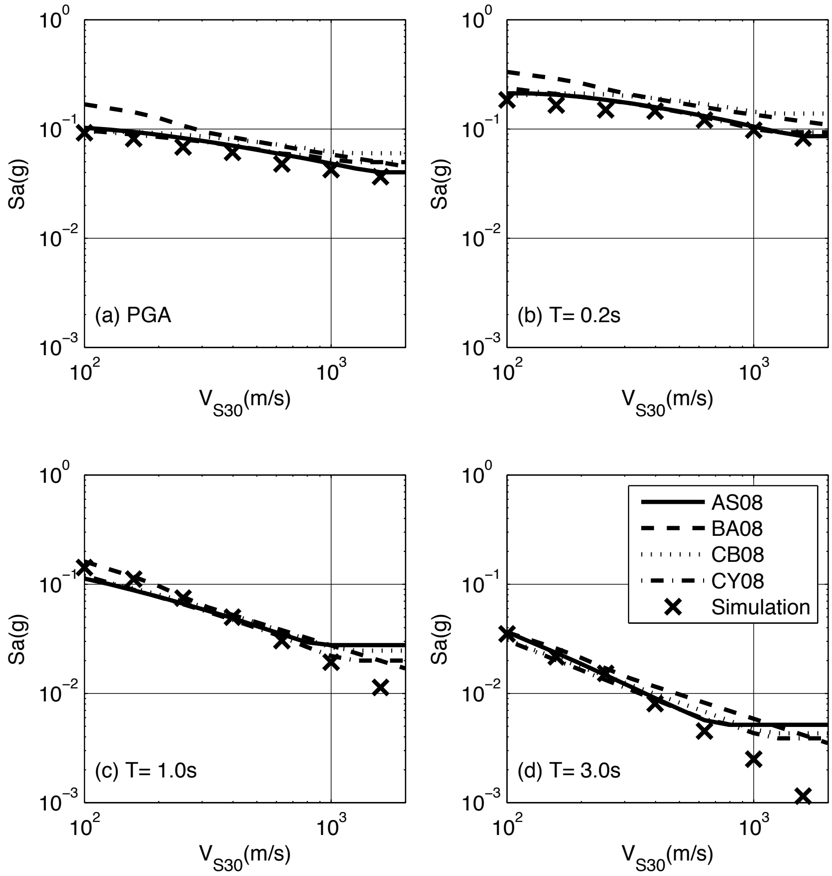

Figure 4.8: Median of PGA and elastic S_a computed from the NGA GMPMs and simulations ($M = 6$, $R_{jb} = 30km$, $100 \leq V_{S30} \leq 2000m/s$). (a) PGA, (b) S_a at $T = 0.2s$, (c) S_a at $T = 1s$, and (d) S_a at $T = 3s$.

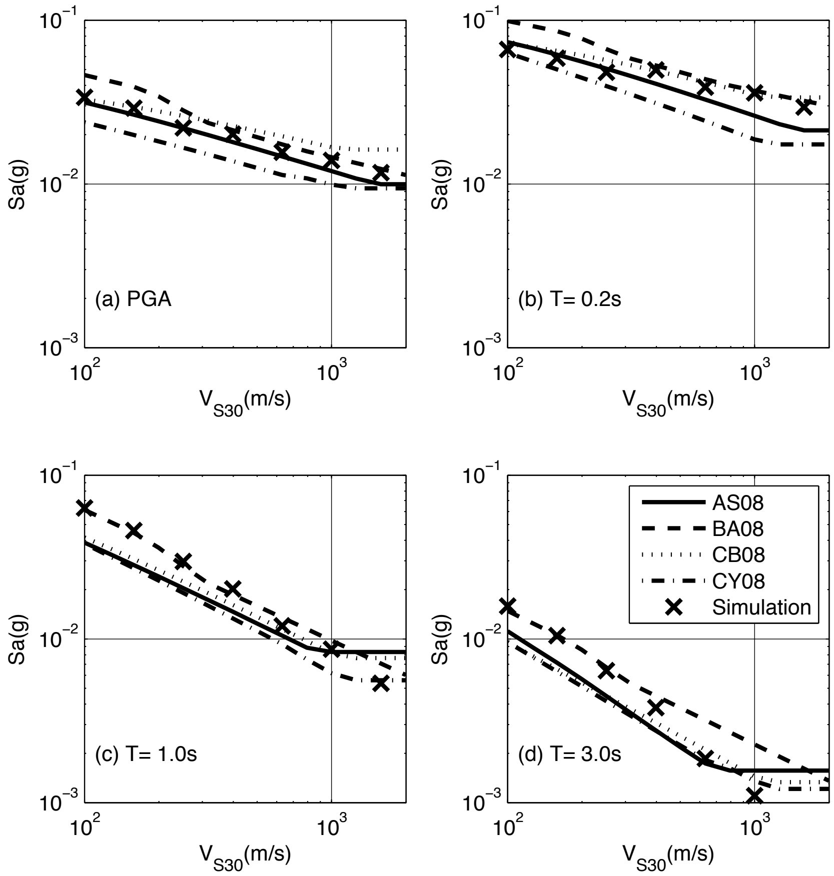

Figure 4.9: Median of PGA and elastic S_a computed from the NGA GMPMs and simulations ($M = 6, R_{jb} = 100km$, $100 \leq V_{S30} \leq 2000m/s$). (a) PGA, (b) S_a at $T = 0.2s$, (c) S_a at $T = 1s$, and (d) S_a at $T = 3s$.

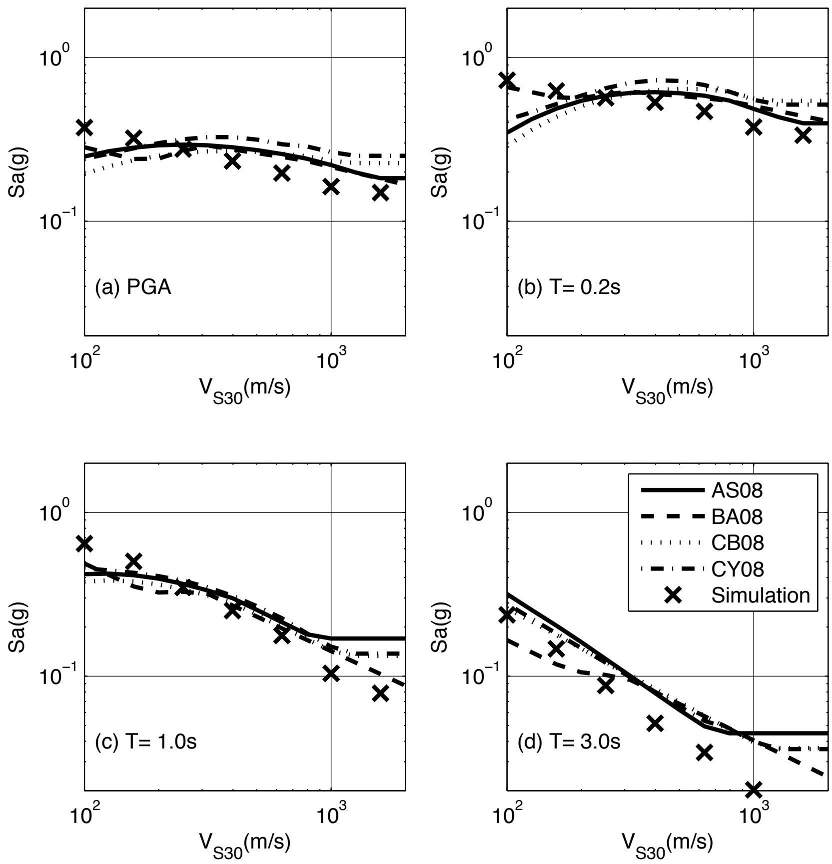

Figure 4.10: Median of PGA and elastic S_a computed from the NGA GMPMs and simulations ($M = 7, R_{jb} = 10km$, $100 \leq V_{S30} \leq 2000m/s$). (a) PGA, (b) S_a at $T = 0.2s$, (c) S_a at $T = 1s$, and (d) S_a at $T = 3s$.

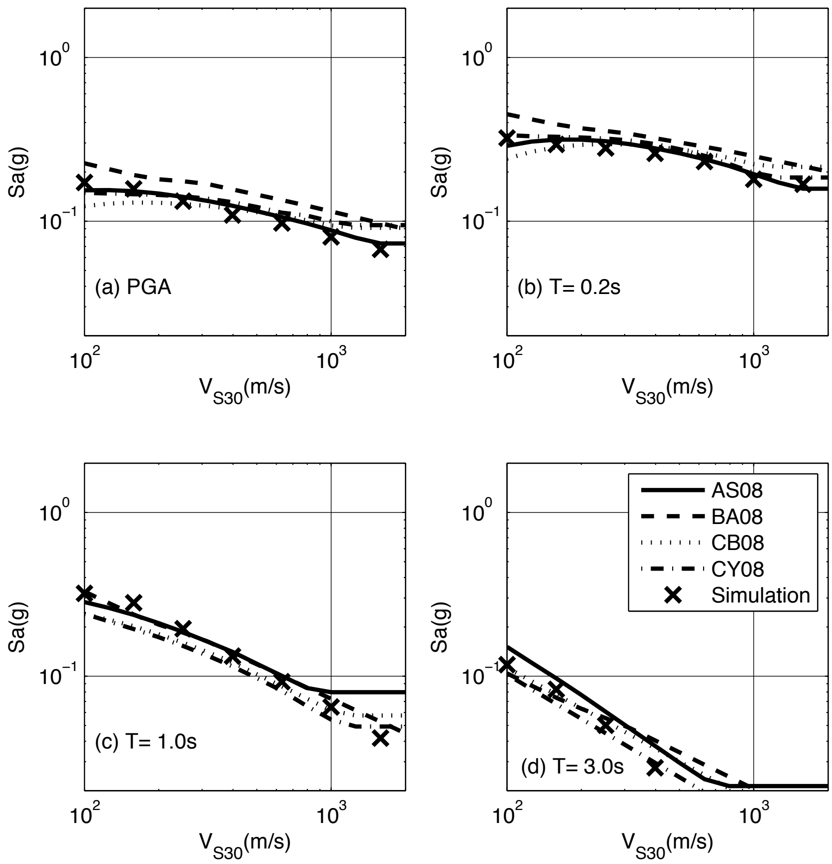

Figure 4.11: Median of PGA and elastic S_a computed from the NGA GMPMs and simulations ($M = 7, R_{jb} = 30km$, $100 \leq V_{S30} \leq 2000m/s$). (a) PGA, (b) S_a at $T = 0.2s$, (c) S_a at $T = 1s$, and (d) S_a at $T = 3s$.

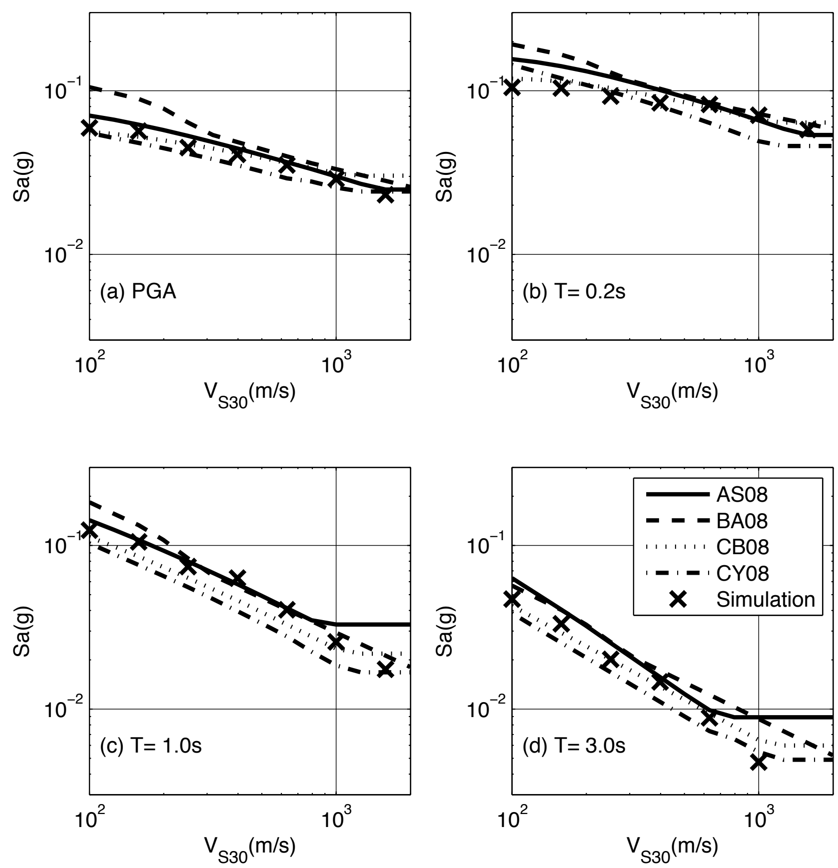

Figure 4.12: Median of PGA and elastic S_a computed from the NGA GMPMs and simulations ($M = 7, R_{jb} = 100km, 100 \leq V_{S30} \leq 2000m/s$). (a) PGA, (b) S_a at $T = 0.2s$, (c) S_a at $T = 1s$, and (d) S_a at $T = 3s$.

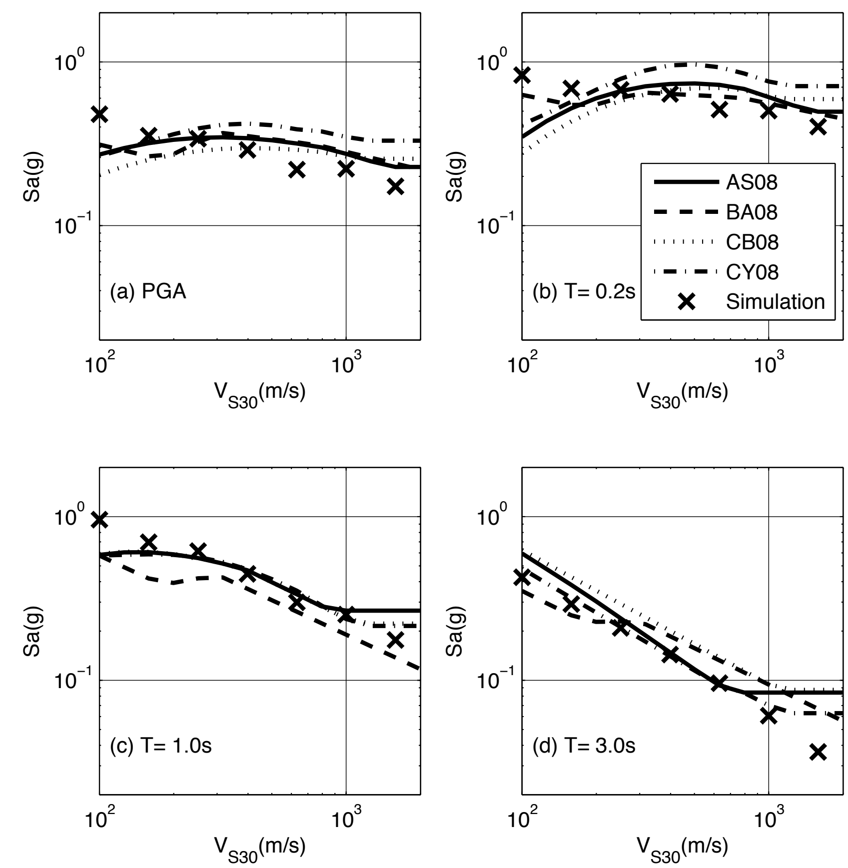

Figure 4.13: Median of PGA and elastic S_a computed from the NGA GMPMs and simulations ($M = 8, R_{jb} = 10km$, $100 \leq V_{S30} \leq 2000m/s$). (a) PGA, (b) S_a at $T = 0.2s$, (c) S_a at $T = 1s$, and (d) S_a at $T = 3s$.

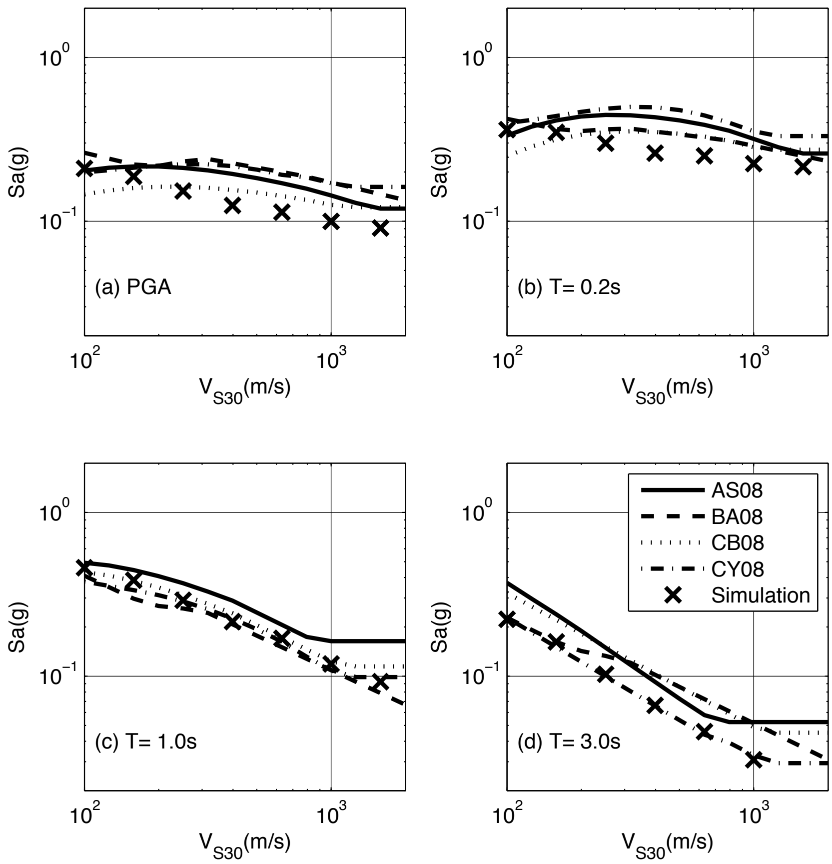

Figure 4.14: Median of PGA and elastic S_a computed from the NGA GMPMs and simulations ($M = 8, R_{jb} = 30km$, $100 \leq V_{S30} \leq 2000m/s$). (a) PGA, (b) S_a at $T = 0.2s$, (c) S_a at $T = 1s$, and (d) S_a at $T = 3s$.

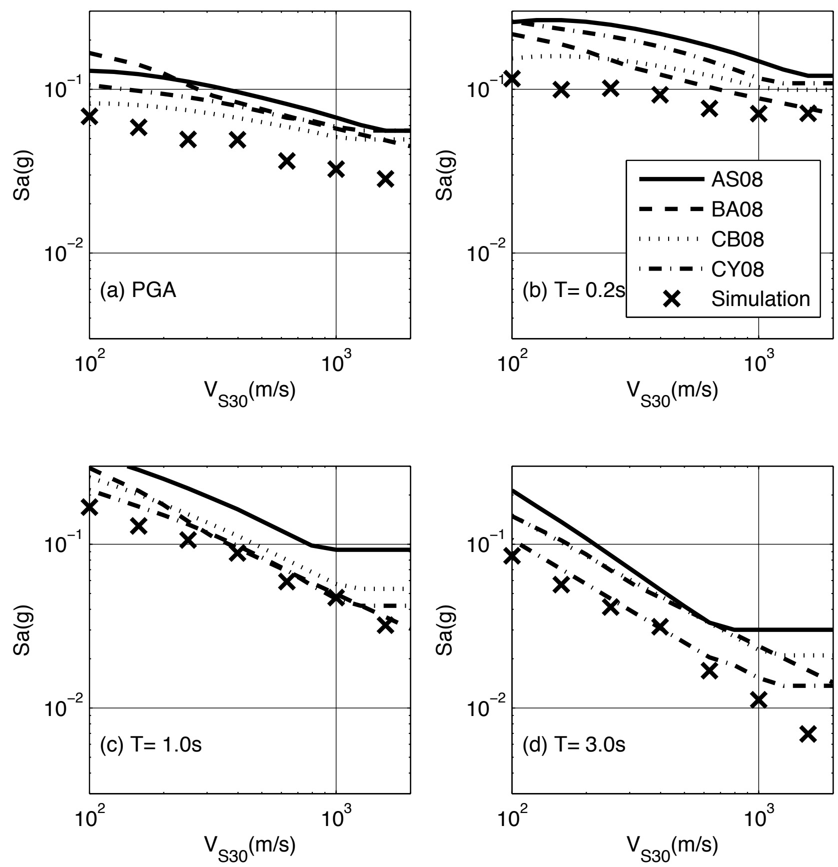

Figure 4.15: Median of PGA and elastic S_a computed from the NGA GMPMs and simulations ($M = 8, R_{jb} = 100km, 100 \leq V_{S30} \leq 2000m/s$). (a) PGA, (b) S_a at $T = 0.2s$, (c) S_a at $T = 1s$, and (d) S_a at $T = 3s$.

Variation of response spectra with period

The median response spectra for $M = 5$, 6, 7, and 8 for vertical strike-slip earthquakes with site $V_{S30} = 270m/s$ are shown in Figure 4.16 for $R_{jb} = 10km$ and Figure 4.17 for $R_{jb} = 30km$. For both cases, S_a from the simulated ground motions reasonably match those from GMPMs except the case of $M = 5$.

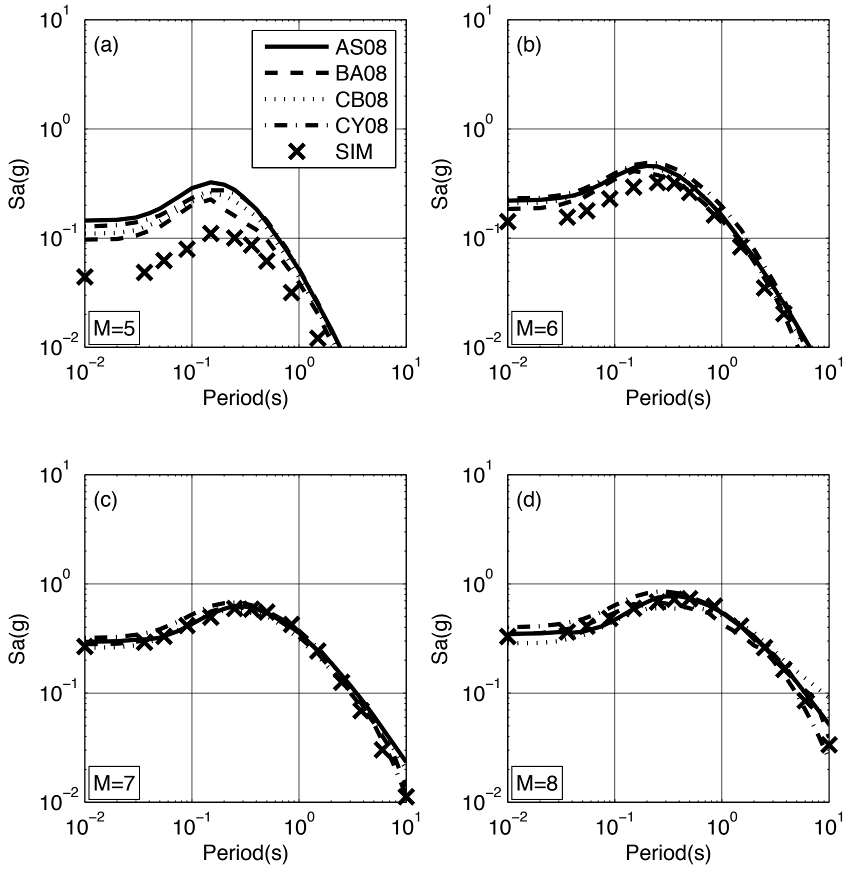

Figure 4.16: Median of elastic S_a computed from the NGA GMPMs and simulations ($R_{jb} = 10km, V_{S30} = 270m/s$) for (a) $M = 5$, (b) $M = 6$, (c) $M = 7$, and (d) $M = 8$.

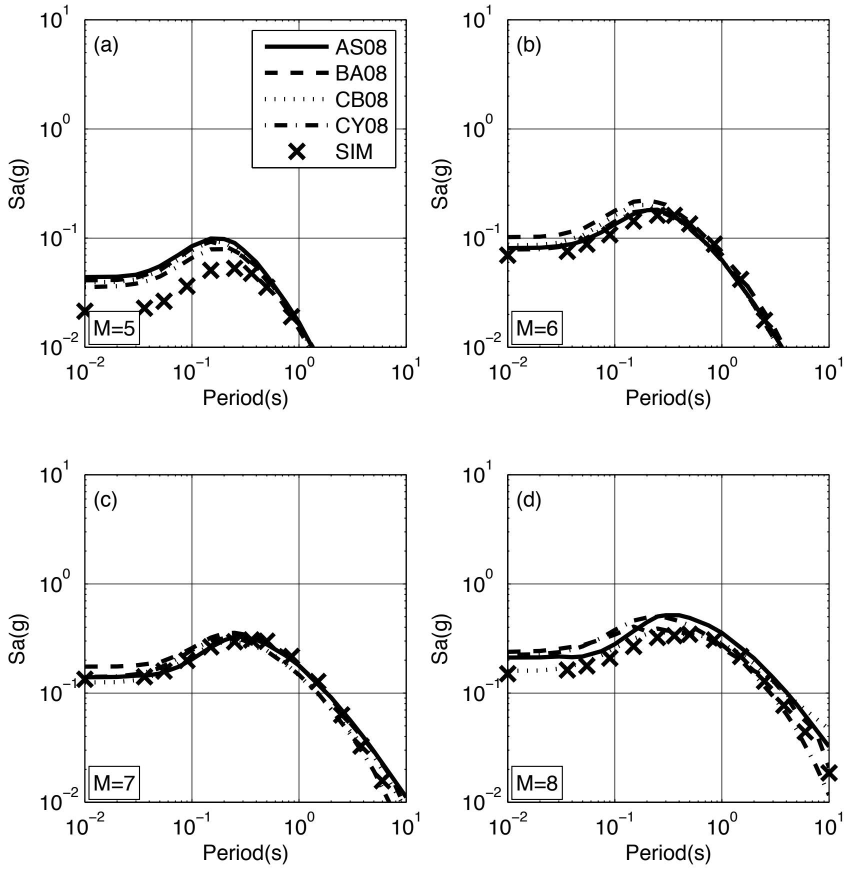

Figure 4.17: Median of elastic S_a computed from the NGA GMPMs and simulations ($R_{jb} = 30km, V_{S30} = 270m/s$) for (a) $M = 5$, (b) $M = 6$, (c) $M = 7$, and (d) $M = 8$.

Logarithmic standard deviation of spectral acceleration

The logarithmic standard deviations of response spectra for $M = 5, 6, 7$, and 8 for vertical strike-slip faults with site $V_{S30} = 270m/s$ are shown in Figures 4.18 for $R_{jb} = 10km$ and 4.19 for $R_{jb} = 30km$. For all cases, standard deviations from simulations are larger than those from GMPMs at long periods. This result from the relationship between wavelet packets and response spectra was discussed in Section 3.5.1.

The magnitude dependence of the standard deviation for $M = 5, 6, 7$, and 8 earthquakes is shown in Figure 4.20 for $R_{jb} = 10km$, and Figure 4.21 for $R_{jb} = 30km$. For all cases, the trend of the logarithmic standard deviation of S_a is the same as the previous cases.

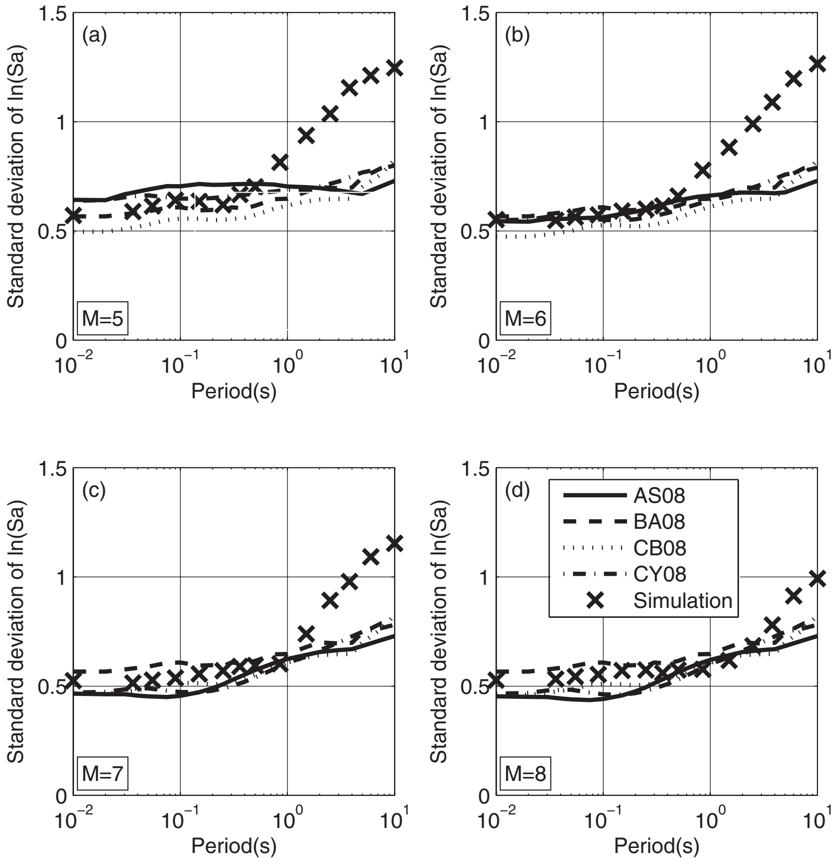

Figure 4.18: Logarithmic standard deviation of elastic S_a computed from the NGA GMPMs and simulations ($R_{jb} = 10km$, $V_{S30} = 270m/s$). (a) $M = 5$, (b) $M = 6$, (c) $M = 7$, and (d) $M = 8$.

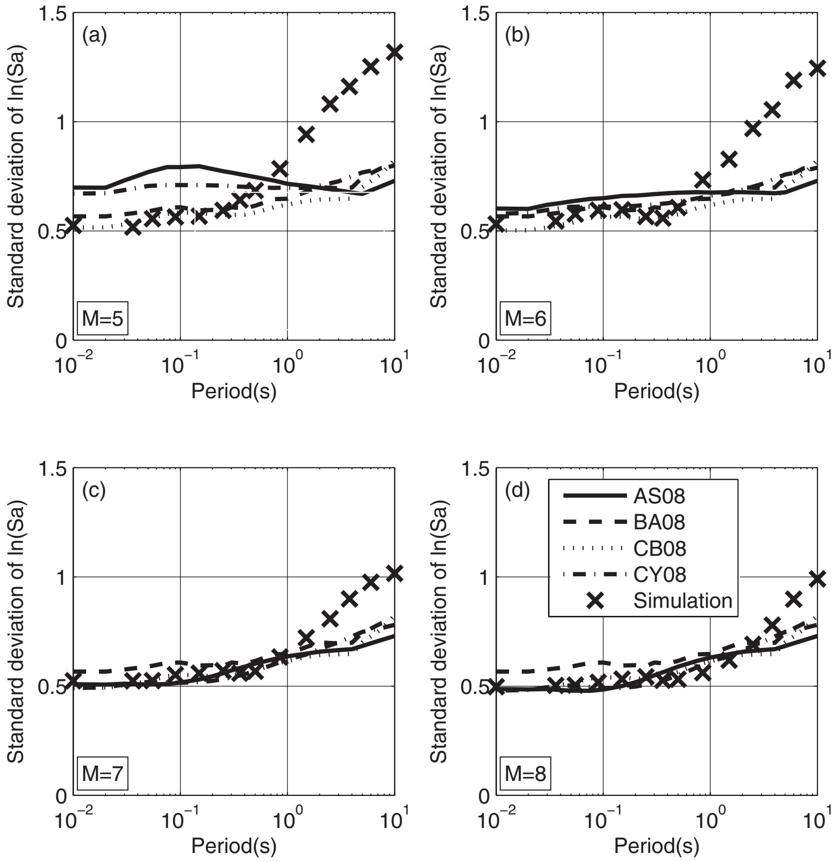

Figure 4.19: Logarithmic standard deviation of elastic S_a computed from the NGA GMPMs and simulations ($R_{jb} = 30km$, $V_{S30} = 270m/s$). (a) $M = 5$, (b) $M = 6$, (c) $M = 7$, and (d) $M = 8$.

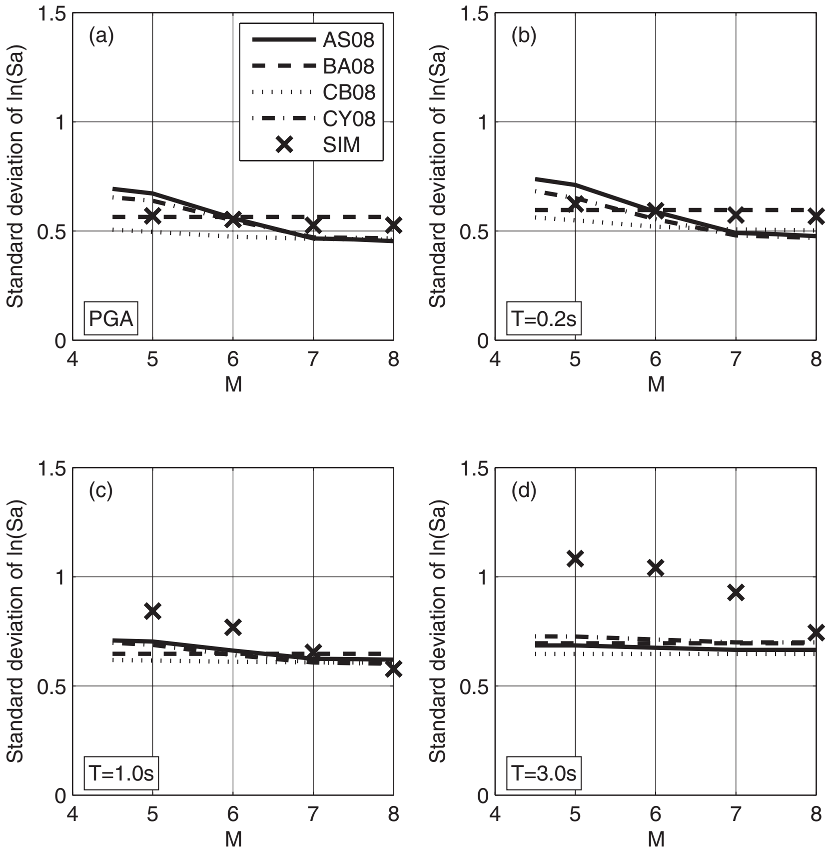

Figure 4.20: Logarithmic standard deviation of elastic S_a computed from the NGA GMPMs and simulations ($R_{jb} = 10km$, $V_{S30} = 270m/s$). (a) PGA, (b) $T = 0.2s$, (c) $T = 1.0s$, and (d) $T = 3.0s$.

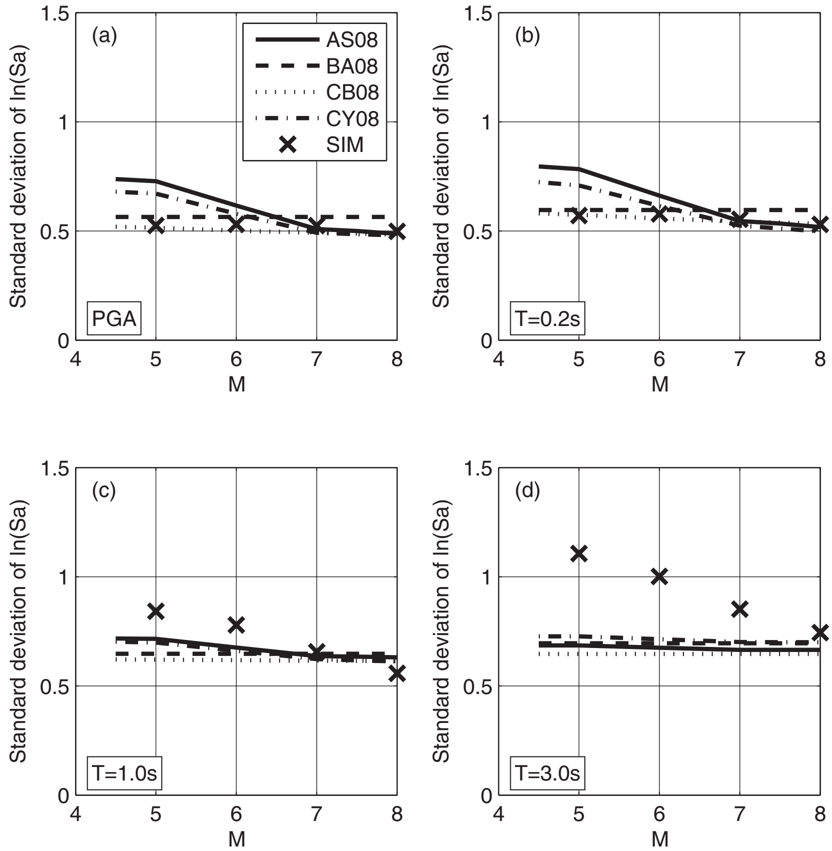

Figure 4.21: Logarithmic standard deviation of elastic S_a computed from the NGA GMPMs and simulations ($R_{jb} = 30km$, $V_{S30} = 270m/s$). (a) PGA, (b) $T = 0.2s$, (c) $T = 1.0s$, and (d) $T = 3.0s$.

4.3.2 Correlation of Epsilon

The residual of $\ln S_a$ from the mean prediction (ε) is defined by the following equation:

$$\varepsilon(T) = \frac{\ln Sa(T) - \mu_{\ln Sa(T)}(M,R,T)}{\sigma_{\ln Sa(T)}} \tag{4.3}$$

where S_a is spectral acceleration, $\mu_{\ln Sa}$ is the mean of logarithmic spectral acceleration from a ground motion prediction model, and $\sigma_{\ln Sa}$ is the logarithmic standard deviation of spectral acceleration from the ground motion prediction model. This ε is an implicit indicator of the "shape" of the response spectrum (Baker and Cornell 2005).

Values of ε at multiple periods can be considered as having multivariate normal distribution (from Jayaram and Baker 2008) and correlation of εs at different periods are modeled by Baker and Jayaram (2008). In general the correlation between εs at two periods decreases if the difference of periods increases. However, for short period components ($T < 0.1s$), the correlation of εs increases as the difference of periods increases. This increasing correlation is caused by the balance of short period components and long period components for impulse response function and Fourier amplitude (Okano et al. 2010). Based on the shape of the impulse response function of an SDOF system at period T_1, the response of an SDOF system can be affected by long period (greater than T_1) components more than short period (smaller than T_1) components of input. Also, Fourier amplitudes of most ground motion recordings decrease as the period gets shorter for short period components (less than 0.1s). Therefore, response of an SDOF system in shorter periods than a particular periods dominated by long period components and the resulting correlations of εs with short period increase even though the difference of periods increases. Figure 4.22 shows correlations of ε from our simulations and those from Baker and Jayaram (2008). Also the contours of the ε correlations computed by the simulated ground motions are shown in Figure 4.23. Our correlation results match those from Baker and Jayaram (2008) in short periods as well as in long periods.

One of the reasons for this good agreement is the wavelet packet transform approach that we are using for our model. The kernel function of the wavelet packet is localized in a range of time and frequency, and therefore, the response spectrum of the kernel function is also localized in a narrow range of periods. Hence, correlations of εs in different periods with small period differences are high and they decrease as the period difference increases.

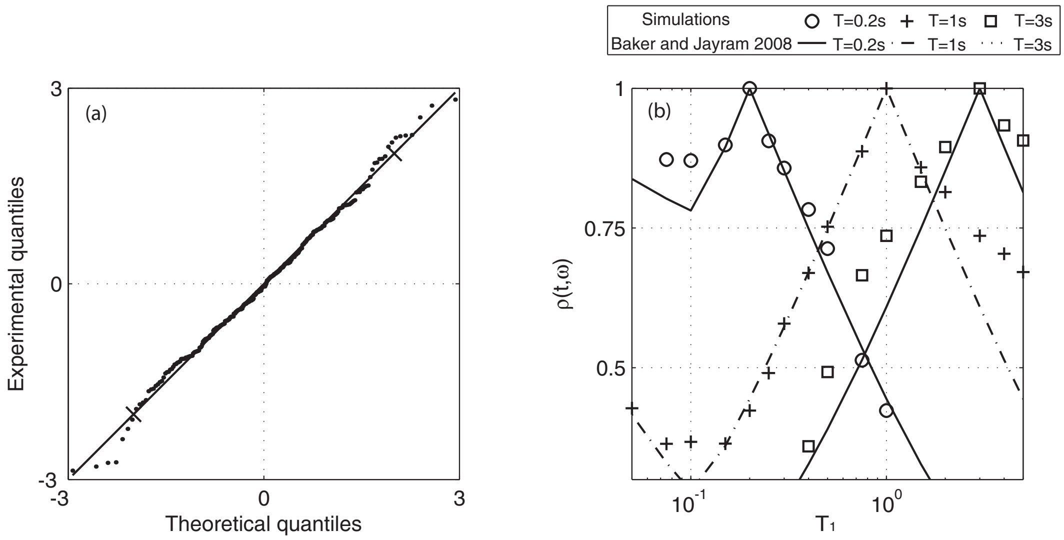

Figure 4.22: The characteristics of ε. (a) normal quantile-quantile plots of the ε and (b) the correlation of the ε in different periods.

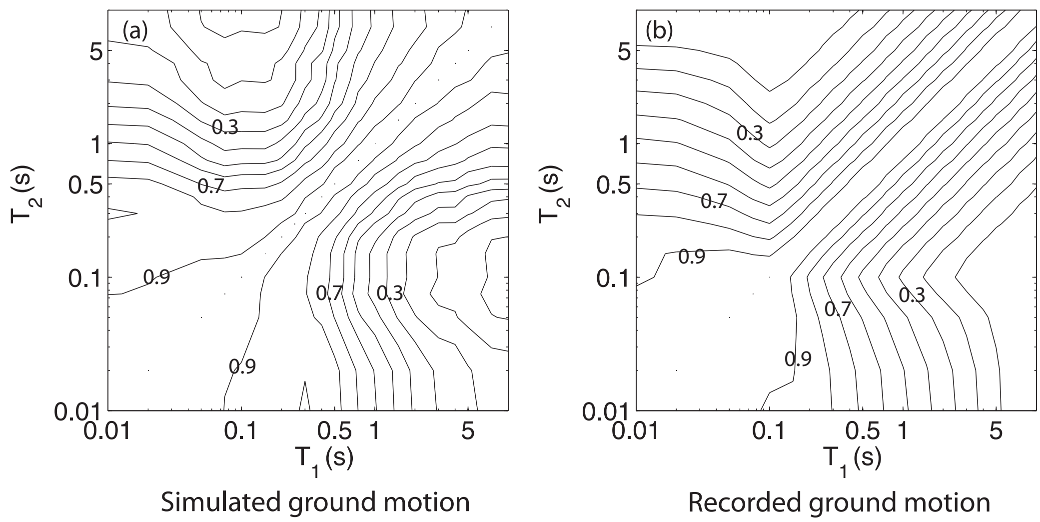

Figure 4.23: Contour of correlation coefficients versus ε for T_1 and T_2. (a) empirical correlation coefficients computed by the simulated ground motions, (b) correlation coefficients computed by Baker and Jayaram (2008).

4.4 Inelastic response spectra

We can also evaluate the inelastic response spectra from the simulated time series data. The Inelastic response spectra here is defined as F_y/W (where F_y is the yield strength and W is the weight of the SDOF), and are computed for elastic-perfectly-plastic (EPP) systems with 5% viscous damping ratio and ductility ratio $\mu = 8$ for inelastic behavior of force and displacement (Chopra 2007). We compared inelastic response spectra observed from the simulations with predictions from Bozorgnia et al. (2010) (CB10) with constant ductility.

The medians and logarithmic standard deviations of F_y/W for $M = 6, 7,$ and 8 and soil site conditions ($V_{S30} = 270m/s$) are shown in Figures 4.24, 4.25, and 4.26. These figures show the same trends as were observed from elastic response spectra. In the long period cases, logarithmic standard deviations from simulations are again larger than those from GMPMs.

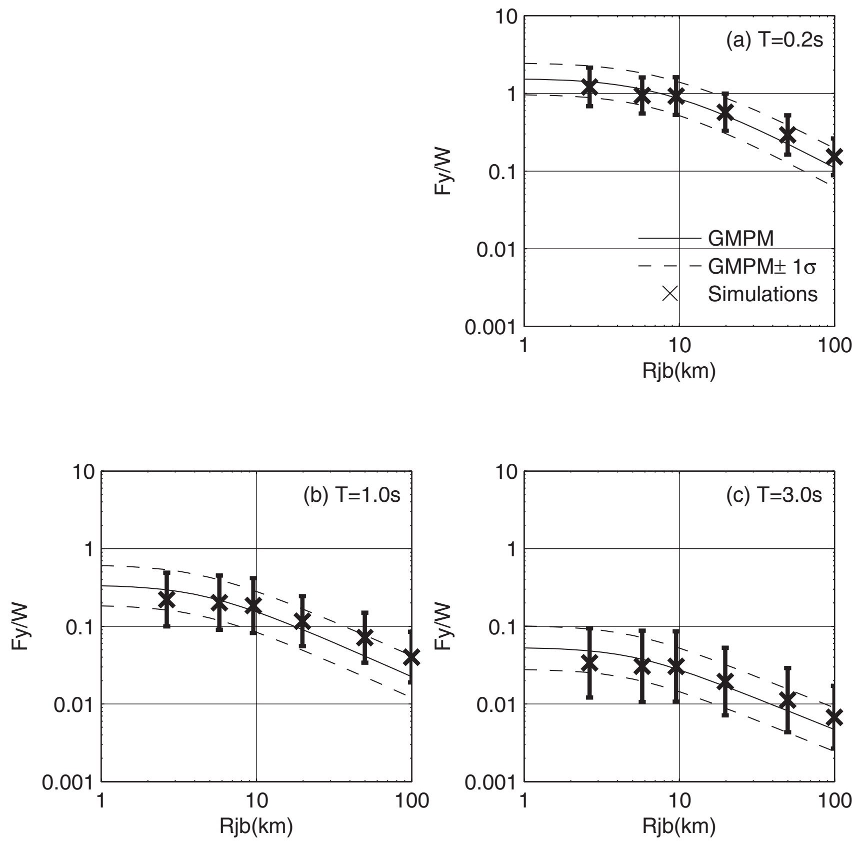

Figure 4.24: Median and logarithmic standard deviation of inelastic response spectra F_y/W computed from the GMPM and simulations ($M = 6, V_{S30} = 270m/s$, $\mu = 8$). (a) $T = 0.2s$, (b) $T = 1s$, and (c) $T = 3s$.

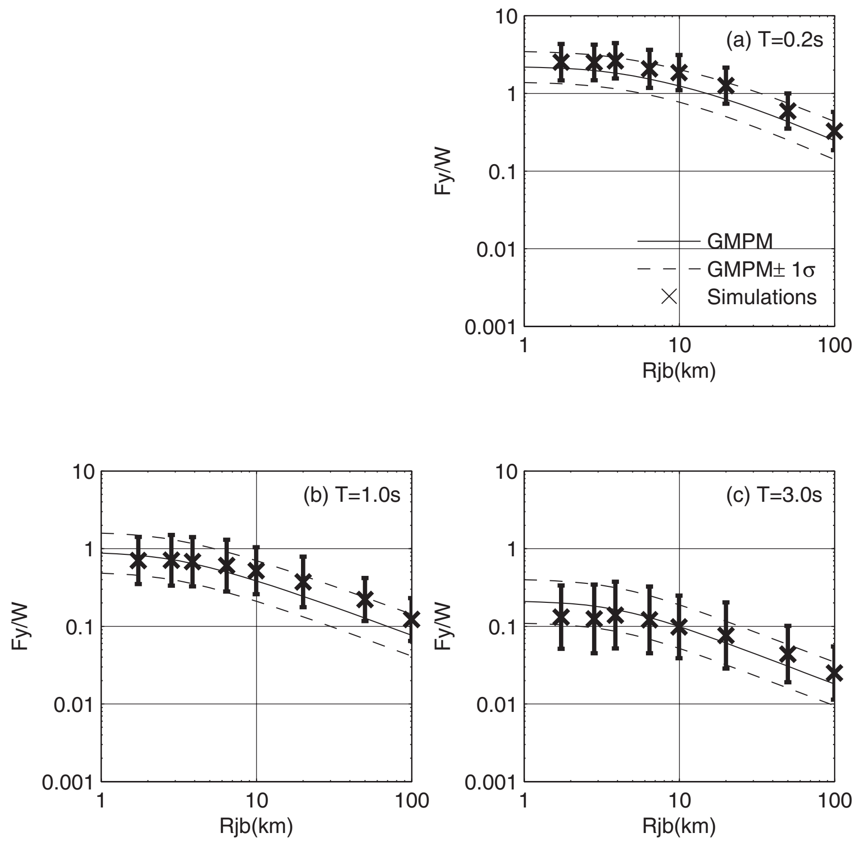

Figure 4.25: Median and logarithmic standard deviation of inelastic response spectra F_y/W computed from the GMPM and simulations ($M = 7, V_{S30} = 270m/s$, $\mu = 8$). (a) $T = 0.2s$, (b) $T = 1s$, and (c) $T = 3s$.

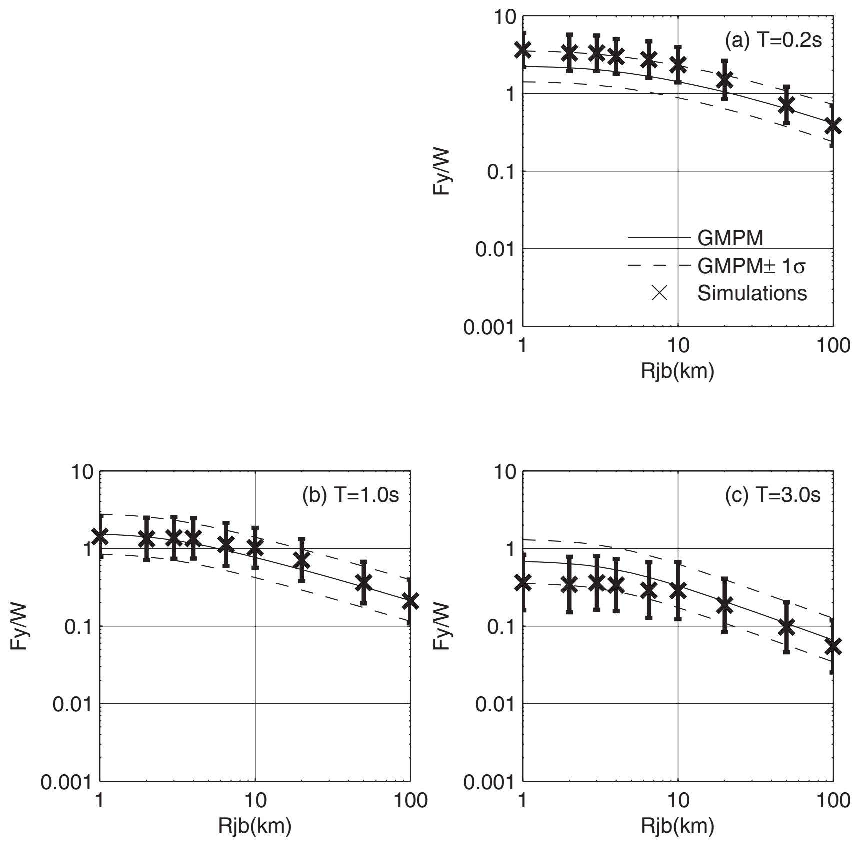

Figure 4.26: Median and logarithmic standard deviation of inelastic response spectra F_y/W computed from the GMPM and simulations ($M = 8, V_{S30} = 270m/s$, $\mu = 8$). (a) $T = 0.2s$, (b) $T = 1s$, and (c) $T = 3s$.

4.5 Arias intensity

Arias intensity (I_a, Arias 1970) is defined as follows:

$$I_a = \frac{\pi}{2g} \int_0^\infty \{x(t)\}^2 \tag{4.4}$$

where $x(t)$ is acceleration time series in units of g and g is acceleration of gravity $981cm/s^2$.

Arias intensity I_a from the simulated ground motions and those from GMPM (Travasarou et al. 2003) are shown in Figure 4.27, and they reasonably match each other.

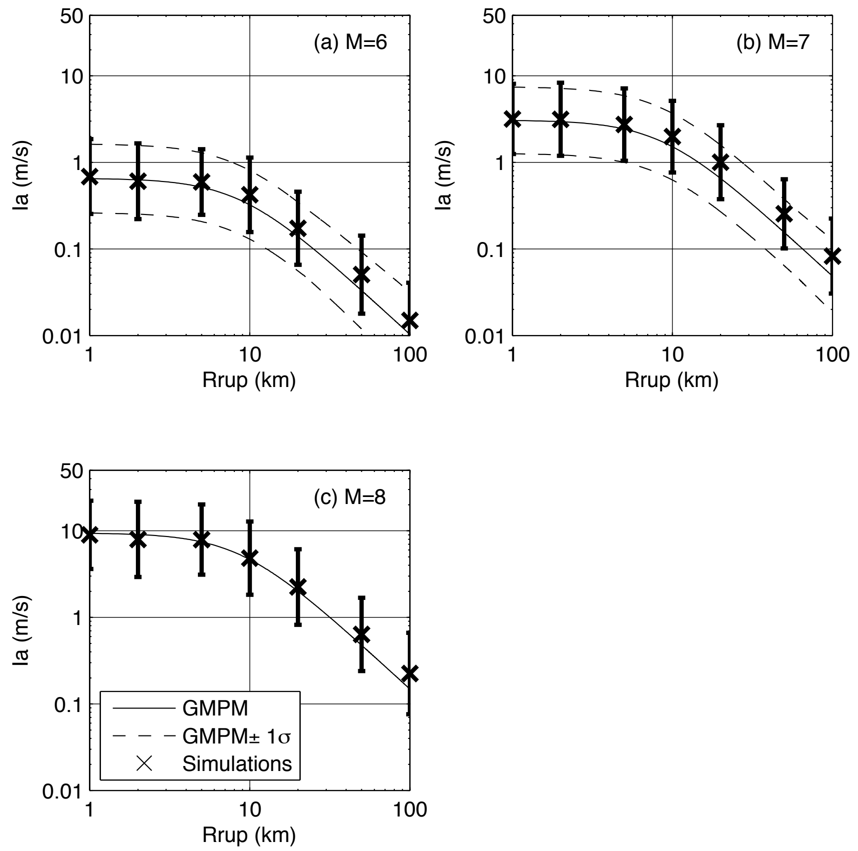

Figure 4.27: Median and logarithmic standard deviation of I_A computed from the GMPM and simulations ($V_{S30} = 270m/s$). (a) $M = 6$, (b) $M = 7$, and (c) $M = 8$.

4.6 Significant duration

Significant duration (Trifunac and Brady 1975) was defined earlier in Equation 2.29. The significant duration (t_{95-5}) from the simulated ground motions and those from GMPMs (Trifunac and Brady 1975 (TB1975) and Abrahamson and Silva 1996 (AS1996)) are shown in Figure 4.28. The AS1996 model is not widely published, but is documented by Stewart et al. (2001). The median of t_{95-5} from the simulated ground motions is close to those from TB1975 when $M = 6$ and to those from both GMPMs when $M = 7$. When $M = 8$, the median of t_{95-5} is larger than those from both GMPMs. This is caused by differences in the model functional forms. From the regression analysis for $S(t)$, the significant duration has approximately linear relationship with logarithmic distance; however, AS1996 employed separate functional forms for $R_{rup} < 10km$ and $R_{rup} > 10km$, and the significant duration from TB1975 has a linear relationship with distance. These differences cause the discrepancy of t_{95-5} between simulations and the GMPMs.

Also, t_{95-5} here is computed by the simulated ground motions with $R_{hyp} = R_{rup}$, which is for a point-source or backward directivity effect. Therefore the median of t_{95-5} is slightly larger than other models for large magnitudes.

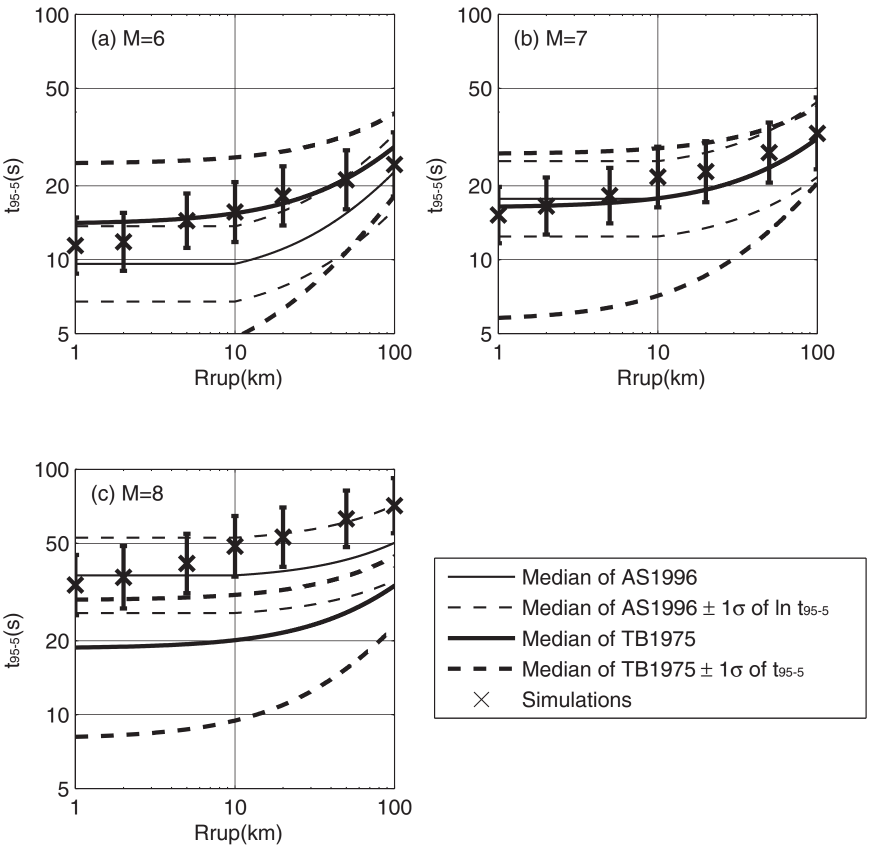

Figure 4.28: Median and logarithmic standard deviation of significant duration computed from the GMPM and simulations ($V_{S30} = 270m/s$). (a) $M = 6$, (b) $M = 7$, and (c) $M = 8$. AS1996 is the prediction from Abrahamson and Silva (1996), as reproduced in Stewart et al. (2001), and TB1975 is the prediction from Trifunac and Brady (1975).

4.7 Mean period

Mean period is defined by Rathje et al. (2004) as follows:

$$T_m = \frac{\sum_i \frac{C_i^2}{f_i}}{\sum_i C_i^2} \tag{4.5}$$

where f_i is frequency i and C_i is the Fourier amplitude of the ground motion at that frequency and $0.25 \leq f_i \leq 20Hz$ with $\Delta f \leq 0.05Hz$.

The mean period (T_m) from the simulated ground motions and those from GMPM are shown in Figure 4.29. Since the reliable magnitude range of the regression model for T_m is from 5.5 to 7.6 in Rathje et al. (2004), the figure shows T_m only for $M = 6$ and 7. The GMPM predictions and simulations reasonably match each other, indicating another form of agreement between the frequency content of the simulated ground motions and observed ground motions.

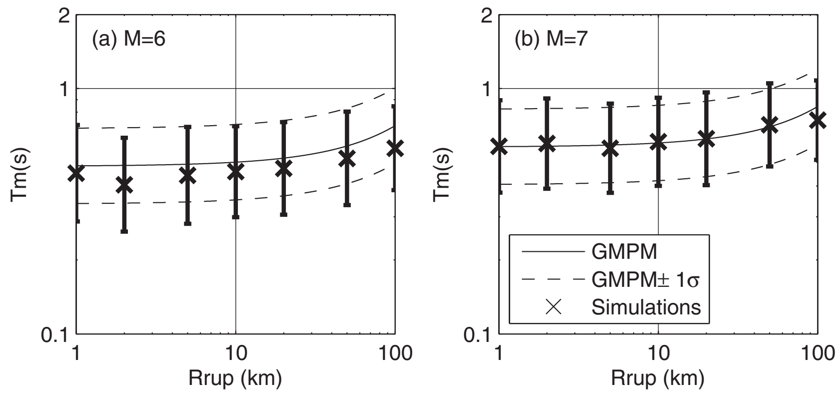

Figure 4.29: Median and logarithmic standard deviation of mean period computed from the Rathje et al. (2004) GMPM and simulations ($V_{S30} = 270m/s$). (a) $M = 6$ and (b) $M = 7$.

4.8 Conclusions

Properties of ground motions simulated using the proposed stochastic model have been compared to empirical models that predict various properties of ground motions. Properties considered include elastic and inelastic response spectra, significant duration, mean period and Arias intensity. Simulations were produced and evaluated for vertical strike-slip faults with $5 \leq M \leq 8$, $200 \leq V_{S30} \leq 2000m/s$, $1 \leq R_{rup} \leq 100km$, and $0.01 \leq T \leq 10s$.

For large ranges of those considered conditions, the properties of the simulated motions were seen to be consistent with the properties in recorded ground motions. Conditions under which the matches were good were $6 \leq M \leq 8$, $220 \leq V_{S30} \leq 760m/s$, $1 \leq R_{rup} \leq 100km$, and $0.01 \leq T \leq 3s$. Over that range, elastic and inelastic response spectra were similar to predictions from empirical GMPMs, in terms of both median values and standard deviations of log spectra. The residuals between spectra of the simulations and corresponding median predictions were also studied. These residuals ("εs") were seen to be normally distributed. Correlations between values at pairs of periods were studied for all period pairs in the period range of interest, and seen to be consistent with observed correlations in recorded motions. Arias intensity and mean period were seen to be generally consistent, in both median and log standard deviation, with recent empirical models. The significant duration here is computed by the simulated ground motions with $R_{hyp} = R_{rup}$, which is for a point-source or backward directivity effect. Therefore the median of t_{95-5} is slightly larger than other models in large magnitudes because the earthquake with large magnitudes have large fault and R_{hyp} and R_{rup} are different in most sites.

Given the comparison of these various ground motion properties with empirical predictive models, the simulated ground motions are suitable for use in a simulation-based probabilistic seismic hazard analysis procedure that will be described next. The reasonable match also suggests that the simulations may be appropriate for use in nonlinear dynamic structural analyses as input ground motions, although that topic will be studied in more detail later before a firm conclusion is drawn.

Chapter 5

Simulation-based probabilistic seismic hazard analysis

5.1 Abstract

Given the comparison of the simulated ground motions with empirical ground motion prediction models (GMPMs) for elastic spectral acceleration and other parameters, the proposed simulation model can be used in place of those GMPMs in probabilistic seismic hazard analysis (PSHA) calculations. The proposed procedure utilizes Monte Carlo Simulation to produce a large suite of ground motions representing potential future ground motions at the site of interest. This suite of ground motions can be directly compared to traditional seismic hazard curves, and the availability of corresponding time histories facilitates a variety of calculations relating to deaggregation and vector-valued PSHA that are not as easily achievable using more traditional approaches. This simulation-based procedure works as follows: first we simulate an earthquake scenario (magnitude/distance/etc.) using the same seismic source model used in traditional PSHA; then we simulate a corresponding ground motion using the model proposed earlier. We repeat this simulation procedure many times to obtain a suite of potential ground motions. A traditional seismic hazard curve provides the rate (or annual probability) of exceeding a given level of spectral displacement at a specified period and a specified damping ratio; with this method the same result can

be obtained by finding the fraction of the simulated ground motions having a spectral displacement larger than the level of interest at that period. But in addition to computing the parameters for which GMPMs are available, the proposed simulation-based PSHA can provide other parameters (e.g. spectral ordinates at other values of damping, hysteretic energy demands, etc). This chapter will describe the simulation procedure, demonstrate its equivalence to traditional PSHA, and then illustrate some of the additional hazard calculations that are feasible here but not possible using the traditional approach.

5.2 Introduction

The proposed stochastic ground motion model can simulate ground motions corresponding to a given magnitude, distance and site condition, and their characteristics are generally consistent with S_d, I_a, t_{95-5}, T_m and inelastic response spectra values predicted by existing ground motion prediction models (GMPMs). In this chapter, those properties are used to compute seismic hazard curves using simulated ground motions. In traditional probabilistic seismic hazard analysis (PSHA, Kramer 1996, McGuire 2004), we compute the annual exceedance of $S_d(T)$ at a target site combining the probability distribution of earthquake magnitudes and distances (the "source model") with the predicted probability that $S_d(T)$ exceeds x given each magnitude and distance (the GMPMs). Here we use the same PSHA source model to generate Monte Carlo Simulations of magnitudes and distances of potential earthquakes, and then use the proposed stochastic model to simulate a ground motion corresponding to each magnitude and distance. This procedure produces a synthetic catalog of potential earthquake ground motions at the site, and we can compute a seismic hazard curve by simply counting how often the simulated ground motions in this catalog cause exceedance of the ground motion intensity level of interest.

In the simulation-based PSHA in this dissertation, 10,000 simulated ground motions are generated using the proposed stochastic ground motion model, and used to compute seismic hazard curves. A physics-based seismic hazard project named CyberShake (Graves et al. 2010) aims to produce the same output; that project computes the annual exceedance rates of S_d using ground motions generated by physics-based simulation. Their physics-based simulations are desirable, as discussed in Chapter 1, because they can consider path effects and rupture characteristics in their simulations. That approach also has limitations, however, as it cannot currently simulate periods lower than $0.5s$, and as computation of their results requires a petascale supercomputer (Cui et al. 2010). In contrast, our model can compute the required time series quickly (1,000 simulations per hour) with high frequency components, which is beneficial for performing fast analyses on standard computer hardware.

One advantage of the simulation-based PSHA is that we just need to count the number of the simulated ground motions whose intensity exceeds the specified threshold and we can efficiently compute hazard curves in this way for any ground motion intensity measure (such as inelastic response spectra) using the same procedure. Another advantage of the simulation-based PSHA is its ability to perform deaggregation in a very flexible manner. Deaggregation of probabilistic seismic hazard analysis results (McGuire 1995, Bazzurro and Cornell 1999) is a procedure to compute the contribution of each potential earthquake magnitude and distance to occurrence of a given S_d level. In traditional PSHA, we can only deaggregate the model parameters required by GMPM (e.g. magnitude and distance). However, in simulation-based PSHA, we can perform a deaggregation-like calculation to determine the distribution of any parameter that can be computed from time series (e.g. duration, Arias intensity, and dominant frequency).

In this chapter, the simulation-based PSHA procedure is described and used to produce example seismic hazard curves. Simulation-based hazard curves for spectral displacement are compared to results from traditional PSHA, and seen to be comparable. Magnitude deaggregation results are also produced and seen to be equivalent to magnitude deaggregation in terms of its probability distributions given S_d levels for the example site obtained using traditional procedures. Additionally, the ground motion parameters, I_a, t_{95-5} and T_m are deaggregated for the hazard curve of $S_d(T)$ and inelastic $S_d(T)$. These results are novel, and can be used to understand what properties of ground motions impact hazard curves for ground motion parameters such as $S_d(T)$ and inelastic $S_d(T)$.

5.3 Simulation-based PSHA and deaggregation

The traditional PSHA calculation is defined as follows:

$$\nu_{S_d(T)}(x) = \sum_i \nu_i \int\int P(S_d(T) > x|r,m) f_i(m,r) dmdr, \tag{5.1}$$

where ν_{S_d} is the mean annual rate of ground motions with S_d greater than x, and ν_i is the mean annual rate of earthquakes on seismic source i above a minimum magnitude. The conditional probability $P(S_d > x|r,m)$ is computed using a GMPM and $f_i(m,r)$ is the joint probabilistic density function of earthquake magnitudes and distances on seismic source i as specified by an earthquake recurrence model and geometric information.

In the following example, we will consider an example site with unknown magnitudes but a fixed distance and V_{S30}. In such a case, Equation 5.1 can be simplified to

$$\nu_{S_d(T)}(x) = \sum_i \nu_i \int P(S_d(T) > x|m) f_i(m) dm. \tag{5.2}$$

The deaggregation for moment magnitude $M = m$ given $S_d(T) > x$ is computed as follows

$$P(M = m|S_d(T) > x) = \frac{\nu_{S_d(T)>x,M=m}}{\nu_{S_d(T)>x}} \tag{5.3}$$

$$= \frac{\nu_{S_d(T)>x|M=m} f_i(m)}{\nu_{S_d(T)>x}} \tag{5.4}$$

Alternatively we can define the deaggregation for $S_d = x$ using following equation (Bazzurro 1998):

$$\begin{aligned} &P(M = m|S_d(T) = x_k) \\ &\quad = \frac{P(M = m, S_d(T) = x_k)}{P(S_d(T) = x_k)} \\ &\quad = \frac{P(M = m, S_d(T) > x_{k+1}) - P(M = m, S_d(T) > x_{k-1})}{P(S_d(T) > x_{k+1}) - P(S_d(T) > x_{k-1})}. \end{aligned} \tag{5.5}$$

If we use simulated ground motions instead of traditional PSHA, we can compute

$\nu_{S_d(T)}(x)$ as follows:

$$\nu_{S_d(T)}(x) = \sum_i \nu_i \sum_{j=1}^{n} \frac{1}{n} I(S_{d,j}(T) > x) \tag{5.6}$$

$$I(S_{d,j} > x) = \begin{cases} 1 & S_{d,j}(T) > x \\ 0 & \text{otherwise} \end{cases} \tag{5.7}$$

where I is indicator function, n is the number of simulations and $S_{d,j}(T)$ is the $S_d(T)$ value of the jth simulated ground motion. The magnitudes of the simulated ground motions are generated from $f_i(m)$. With this approach we are computing the hazard curve for $S_d(T)$ by counting number of the ground motions whose S_d is greater than x instead of computing $P(S_d(T) > x|m)$ from a GMPM.

Simulation-based PHSA also can be used for deaggregation. We can compute the deaggregation distribution by counting the fraction of simulated ground motions with a particular S_d level that also have the specified magnitude value of interest:

$$P(M = m|S_d(T) = x) = \frac{\sum_{j=1}^{n} I(S_{d,j}(T) = x, M_j = m)}{\sum_{j=1}^{n} I(S_{d,j}(T) = x)} \tag{5.8}$$

where

$$I(S_{d,j}(T) = x) = \begin{cases} 1 & S_{d,j}(T) = x \\ 0 & \text{otherwise} \end{cases} \tag{5.9}$$

$$I(S_{d,j} = x, M_j = m) = \begin{cases} 1 & S_{d,j}(T) = x \text{ and } M_j = m \\ 0 & \text{otherwise} \end{cases} \tag{5.10}$$

The magnitudes of the simulated ground motions are generated from $f_i(m)$, the distribution of magnitudes from earthquake source i. Large magnitude earthquakes are generally rare relative to smaller magnitude earthquakes on a given source. This causes some numerical challenges, because even a large set of simulated ground motions may not have many ground motions from extremely large magnitude events, and thus the contributions of those events to large-amplitude S_d values (which are generally of most engineering interest may not be known with great confidence). To overcome this shortage of the simulated ground motions with large magnitudes, we can use an alternate form of Monte Carlo Simulation known as Importance Sampling.

With Importance Sampling, we generate samples (of earthquake magnitudes, in this particular application) from a sampling distribution, denoted $k_i(m)$, rather than from the real distribution of that variable. The differences between the sampling distribution and the real target distribution are then reconciled by weighting each sample in proportion to the differences between the two distributions' probability density functions, and evaluated at the value of that particular sample. Here we will use a uniform distribution for magnitudes as a sampling distribution $k_i(m)$, which will produce many more large magnitude simulations than the real distribution $f_i(m)$.

The simulation-based PSHA calculation using these importance-sampled simulations is then computed as follows:

$$\nu_{S_d(T)}(x) = \sum_i \nu_i \frac{1}{n} \sum_{j=1}^{n} I(S_{d,j}(T) > x) \frac{f_i(m_j)}{k_i(m_j)} \tag{5.11}$$

$$I(S_{d,j}(T) > x) = \begin{cases} 1 & S_{d,j}(T) > x \\ 0 & \text{otherwise} \end{cases} \tag{5.12}$$

We can also compute deaggregation results by counting the number of simulated ground motions multiplied by their importance sampling weights

$$P(M = m | S_d(T) = x) = \frac{\sum_{j=1}^{n} I(S_{d,j}(T) = x, M_j = m) \frac{f_i(m)}{k_i(m)}}{\sum_{j=1}^{n} I(S_{d,j}(T) = x) \frac{f_i(m_j)}{k_i(m_j)}} \tag{5.13}$$

With this simulation-based PSHA approach, the S_d values counted above are associated with full simulated ground motion time histories, and so these S_d values are naturally connected to other ground motion intensity measures. Below, we will compute deaggregation results that provide the distributions of Arias intensity, significant duration, and mean period associated with ground motions having a specified spectral displacement, by substituting any of these parameters for magnitude in Equation 5.13.

5.4 Example site description

Next we will perform a series of calculations to demonstrate the above equations, so we must first define an example site to perform hazard calculations at. The example site has a single vertical strike-slip fault at a distance of 10 kilometers (i.e., $R_{hyp} = R_{rup} = 10km$ for all earthquakes), and the site V_{S30} value is $400m/s$. Earthquakes on this source have magnitudes with a characteristic earthquake recurrence law described in more detail below (Youngs and Coppersmith 1985), and there are 0.2 earthquakes per year with a minimum magnitude (i.e. $\nu_i = 0.2$). This simple site description was chosen because it can demonstrate the hazard calculation procedure, including deaggregation to find the contributions of the various magnitudes to each S_d amplitude, but it is simple enough that the results will be transparent. These conditions approximate those for a site located near a single active fault such as is the case at many sites in the Bay Area of northern California.

The characteristic earthquake recurrence law is based on the assumption that a fault tends to have relatively frequent earthquakes with a characteristic magnitude, and that occurrence of earthquakes at lower magnitudes is well described by a model called the Gutenberg-Richter recurrence law. The standard Gutenberg-Richter recurrence law is defined as follows:

$$\log(\nu_m) = a - bm \tag{5.14}$$

where ν_m is the mean annual rate of earthquakes with magnitude greater than m, and a and b are constants.

The characteristic earthquake recurrence law is defined by the following probability density function (PDF).

$$f_M(m) = \begin{cases} 0 & m < m_0 \\ c10^{a-bm} & m_0 < m < m' \\ f_M(m^c) & m' < m < m^u \\ 0 & m > m^u \end{cases} \tag{5.15}$$

where m_0 is the minimum magnitude, m^u is the upper bound magnitude, m' is lower bound magnitude of characteristic earthquakes, m^c is the earthquake magnitude with a probability of occurrence equal to the probability of occurrence of an magnitude in the characteristic range, and c is a constant determined by the need to have the area under this probability density function equal one. For the example site considered here, we use $b = 1$, $m_0 = 5$, $m^u = 7.9$, $m' = 7.4$, $m^c = 6.4$. Figure 5.1 shows a plot of this density function.

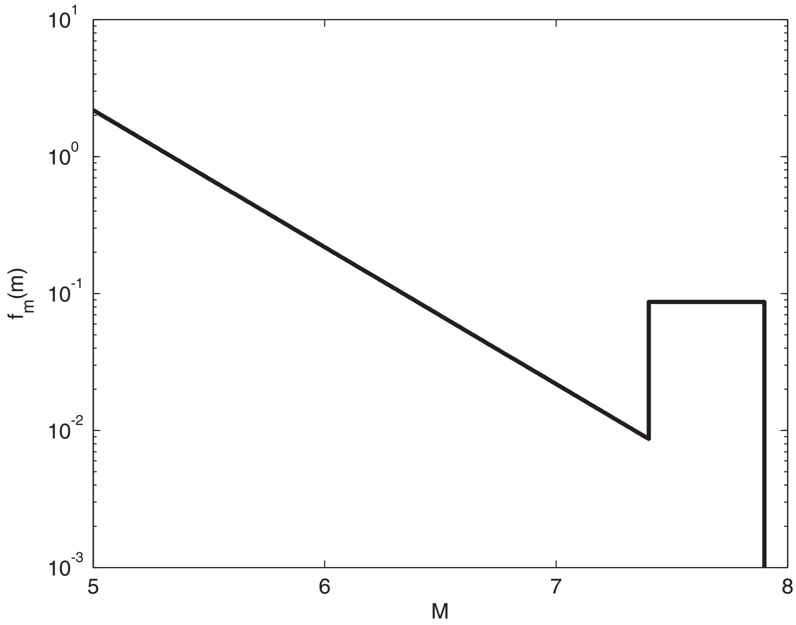

Figure 5.1: Probability density function for earthquake magnitudes for the example site, using the Gutenberg-Richter recurrence law with the characteristic earthquake model (y axis in logarithmic scale).

Figure 5.2 shows the histogram of the 10,000 earthquake magnitudes generated using this characteristic earthquake recurrence law. Note that the shape of the histogram in Figure 5.1 appears to differ from the shape of the PDF in Figure 5.2, but that is because the y axis of the former is plotted with a logarithmic scale (to highlight the log-linearity of the probabilities), while the latter is plotted in linear scale to emphasize true proportions of simulations with a given range of magnitudes. Note that in Figure 5.2 there are relatively few simulations with large magnitudes, so as an alternative we also simulate 10,000 uniformly distributed magnitudes generated to use with importance sampling, as shown in the histogram of Figure 5.3.

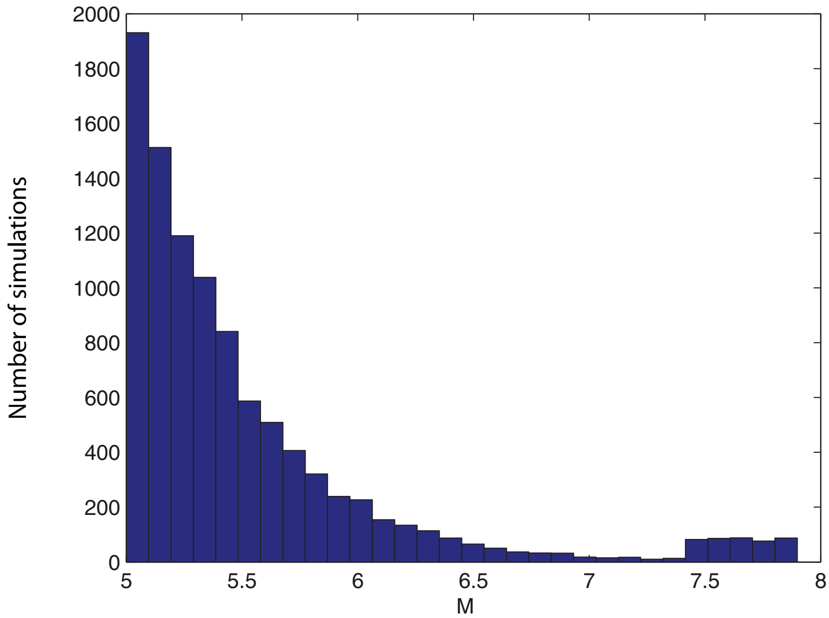

Figure 5.2: Histogram of moment magnitude of simulated ground motion based on characteristic recurrence model.

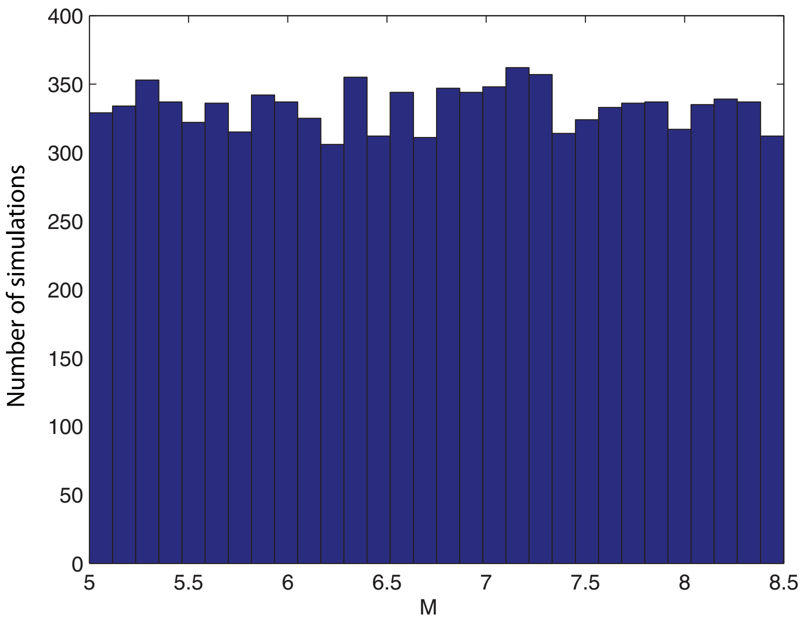

Figure 5.3: Histogram of moment magnitude of simulated ground motion for importance sampling.

5.5 Hazard curves for elastic and inelastic spectral displacement

The hazard curves for the example site described in the previous section are computed using both the traditional PSHA approach and the proposed simulation-based PSHA approach. The Boore and Atkinson (2008) GMPM is used for the traditional PSHA calculation. For the simulation-based calculations, both the direct Monte Carlo simulations and the Importance Sampling simulations are used, and the two sets of results are reported separately. Hazard curves are computed for periods of $T = 0.5s$, $0.95s$, and $2.6s$ for each case ($0.95s$ and $2.6s$ are associated with the fundamental periods of 4- and 20-story buildings, respectively, used in the next chapter, and 0.5s was added so that a shorter period could also be considered). The hazard curves are plotted in Figure 5.4.

A few observations can be made from these results. First, the hazard curves from all three calculation approaches are in very good agreement, especially for annual rates of exceedance greater than 10^{-3}. At lower rates of exceedance, the simulation-based results are less stable–particularly the direct Monte Carlo results. At rates down near 10^{-5}, the corresponding S_d values from the Monte Carlo approach are based on observations of only a few ground motions (since these rates are by definition rare). The importance sampled results are more stable, since strong ground motions have been preferentially sampled in that case; this is the reason why computing the hazard curve using importance sampling is a desirable approach.

The match between the simulation-based and traditional hazard curves depends on the simulated ground motions having response spectra comparable to the spectra predicted by the GMPM used in PSHA. The simulated ground motions used here are comparable, but there were discrepancies in some cases that did not influence these hazard curves to the extent that one might expect. In Chapters 3 and 4, the standard deviation of $\ln S_d$ ($\sigma_{\ln S_d}$) values at long periods from the simulations was observed to be larger than predicted by GMPMs, which might have been expected to produce larger hazard at small rates of exceedance (i.e., in the "tail of the hazard curve"). However, as observed in Section 3.5.1, $\sigma_{\ln S_d}$, this problem was less significant for large-magnitude ground motions, and the tail of the hazard curve is primarily controlled by ground motions from large magnitudes, so this problem did not manifest itself here.

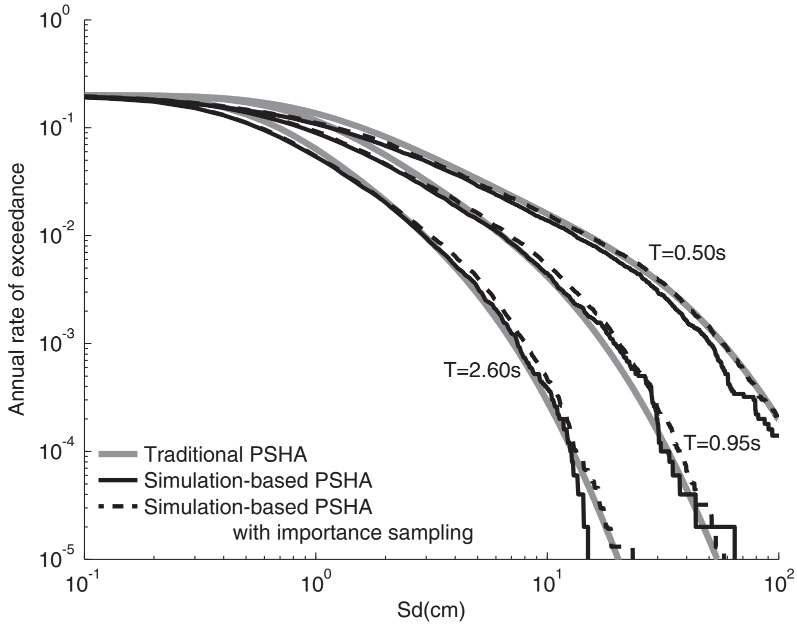

Figure 5.4: Hazard curves for S_d based on the characteristic recurrence model.

Hazard curves for inelastic S_d are plotted in Figure 5.5, using both traditional and simulation-based PSHA. The traditional PSHA results were computed using the model of Boore and Atkinson (2008) for elastic S_d and the model of Tothong and Cornell (2006) for the ratio of inelastic to elastic spectral displacement; together these two models form the required GMPM. The inelastic S_d were computed using a non-deteriorating bilinear oscillator with a positive hardening stiffness ratio $\alpha = 0.05$ (Chopra 2007). Yield displacement d_y is computed using a constant yield acceleration of $0.2g$, with the corresponding yield displacement for each period T then defined as follows:

$$d_y = 0.2g\left\{\frac{T}{2\pi}\right\}^2, \tag{5.16}$$

where g is acceleration of gravity ($981cm/s^2$). This is an assumption for the performance of the simulation-based hazard analysis and deaggregation although it is not a realistic assumption to design buildings. Again the simulation-based hazard curves obtained using

Importance Sampling are seen to be more stable than those from basic Monte Carlo simulation at S_d levels with low exceedance rates. The hazard curves from the simulation-based PSHA and the traditional PSHA reasonably match for rates greater than $5*10^{-3}$. At lower rates, the two do not agree as closely, but it is not clear whether one approach is systematically biased high or low with respect to the other.

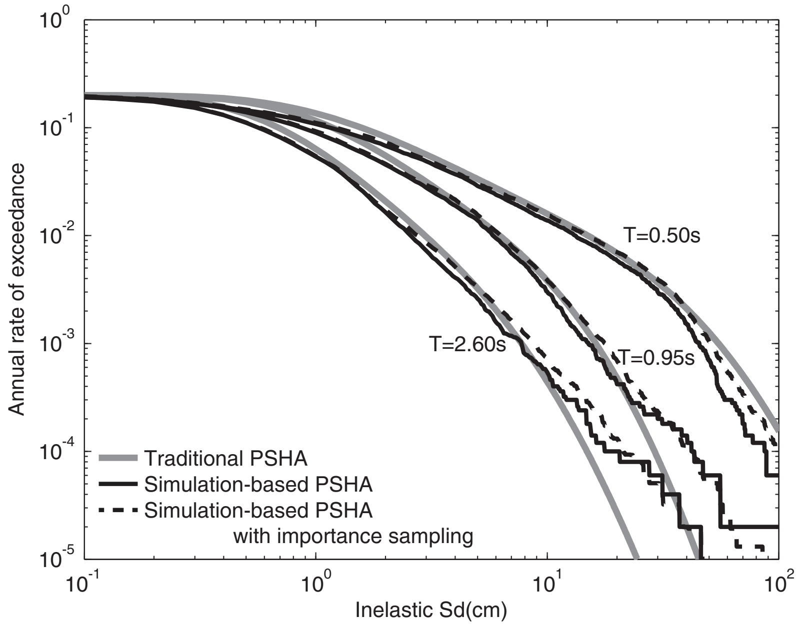

Figure 5.5: Hazard curve of inelastic S_d based on characteristic recurrence model.

5.6 Deaggregation of hazard curve

5.6.1 Deaggregation of moment magnitude

Figures 5.6, 5.7, and 5.8 show the deaggregation of magnitude given elastic $S_d(T)$ for $T = 0.5, 0.95$, and $2.6s$, respectively. The deaggregations are computed for S_d levels having two exceedance probabilities: 10% probability of exceedance in 50 years, and 2% probability of exceedance in 50 years. Results are shown for both the simulation-based procedure and the traditional procedure, and the two show good agreement. The lower tail of the probability of the deaggregated magnitude has low-resolution predictions from the simulation-based procedure. This is caused by the deaggregation using importance sampling (Equation 5.13). In the deaggregation using importance sampling, the weight $f_i(m)$ is applied to the number of simulated ground motions with a particular S_d level. Therefore, even though the number is small, the large probability appears in the small magnitude

The deaggregation distributions clearly vary as the S_d level (and associated exceedance probability) varies. The S_d at high exceedance probabilities are likely to be caused by ground motions with small magnitudes, and the S_d with low exceedance probabilities are more likely to be caused by ground motions with large magnitudes.

Figure 5.9 shows the mean M given an elastic or inelastic S_d level. In both cases, M increases with increasing elastic and inelastic S_d. Since the maximum M of the characteristic recurrence law that we used is 7.9, the maximum mean M of deaggregation is less than 7.9. The mean magnitudes for in both cases decrease with increasing T. Also, the mean magnitude for a given inelastic S_d is slightly larger than that for the corresponding elastic S_d since the ground motions with large magnitude are likely to have longer period components than those with small magnitude.

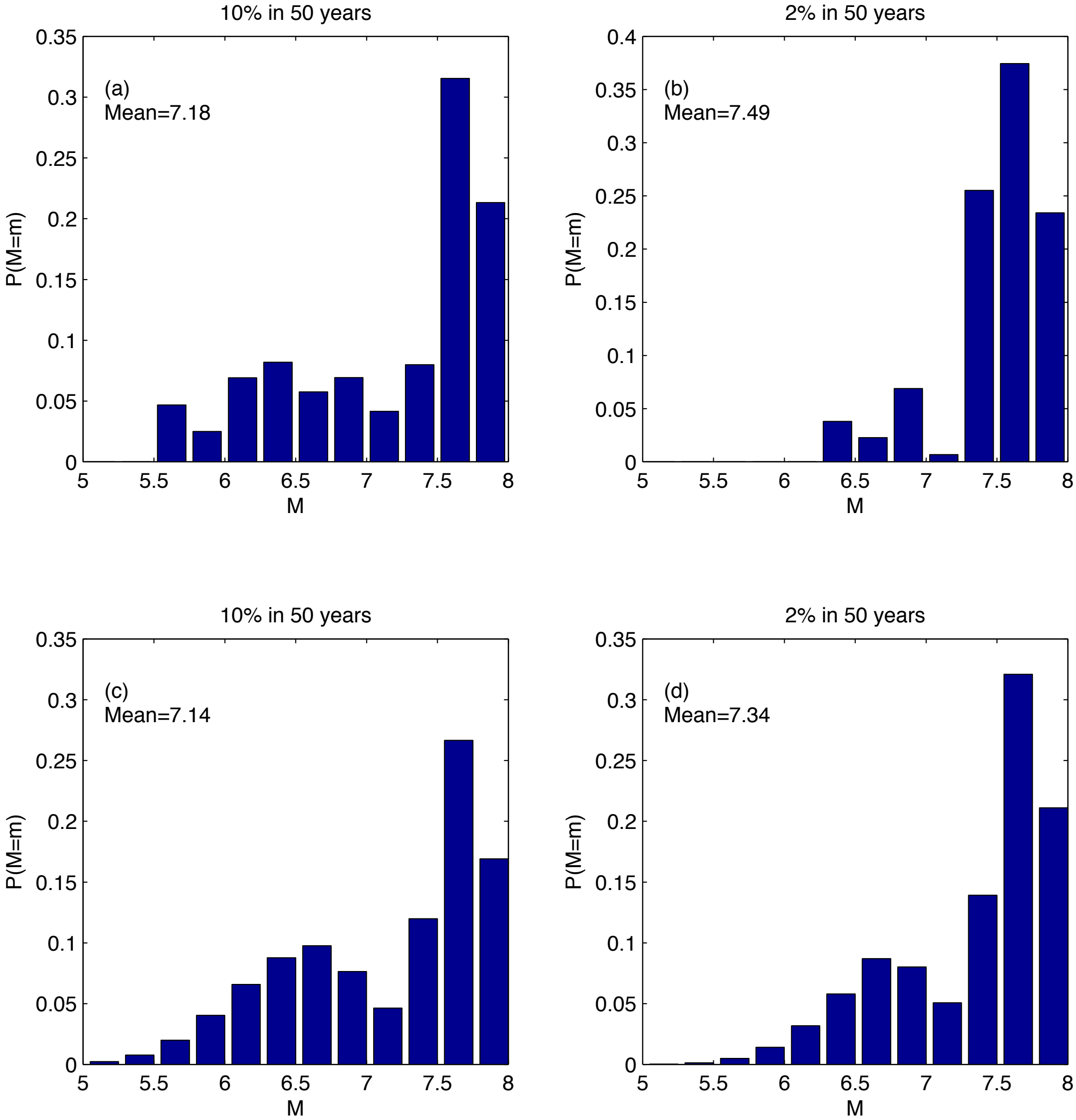

Figure 5.6: Probability of M given $S_d(0.5s)$ (a) $S_d(0.5s)$ with 10% probability of exceedance in 50 years, (b) $S_d(0.5s)$ with 2% in probability of exceedance 50 years from simulation-based PSHA, (c) $S_d(0.5s)$ with 10% probability of exceedance in 50 years, (d) $S_d(0.5s)$ with 2% probability of exceedance in 50 years from traditional PSHA. Mean values of deaggregated magnitudes are noted in each sub-figure.

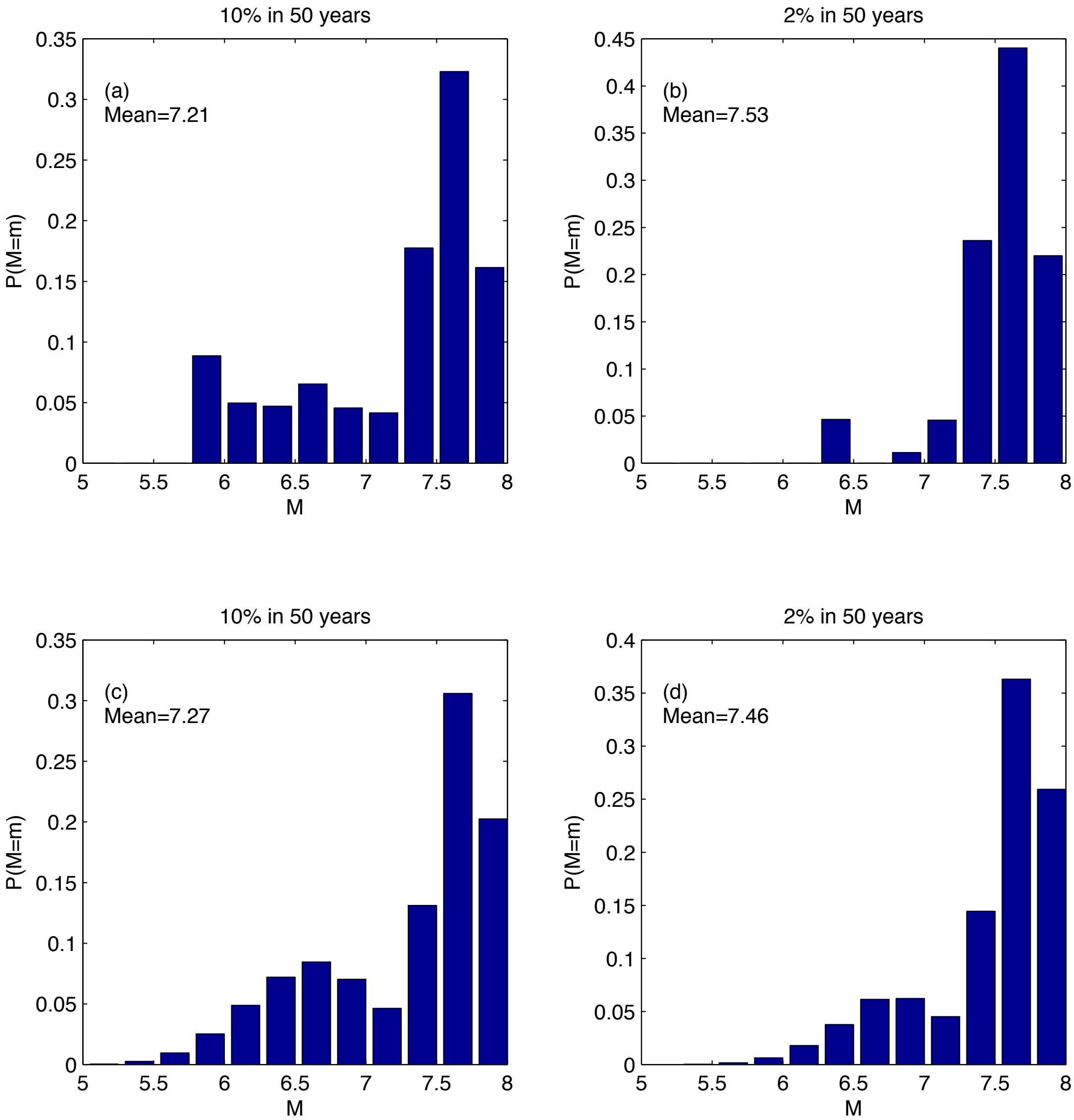

Figure 5.7: Probability of M given $S_d(0.95s)$ (a) $S_d(0.95s)$ with 10% probability of exceedance in 50 years, (b) $S_d(0.95s)$ with 2% probability of exceedance in 50 years from simulation-based PSHA, (c) $S_d(0.95s)$ with 10% probability of exceedance in 50 years, (d) $S_d(0.95s)$ with 2% probability of exceedance in 50 years from traditional PSHA. Mean values of deaggregated magnitudes are noted in each sub-figure.

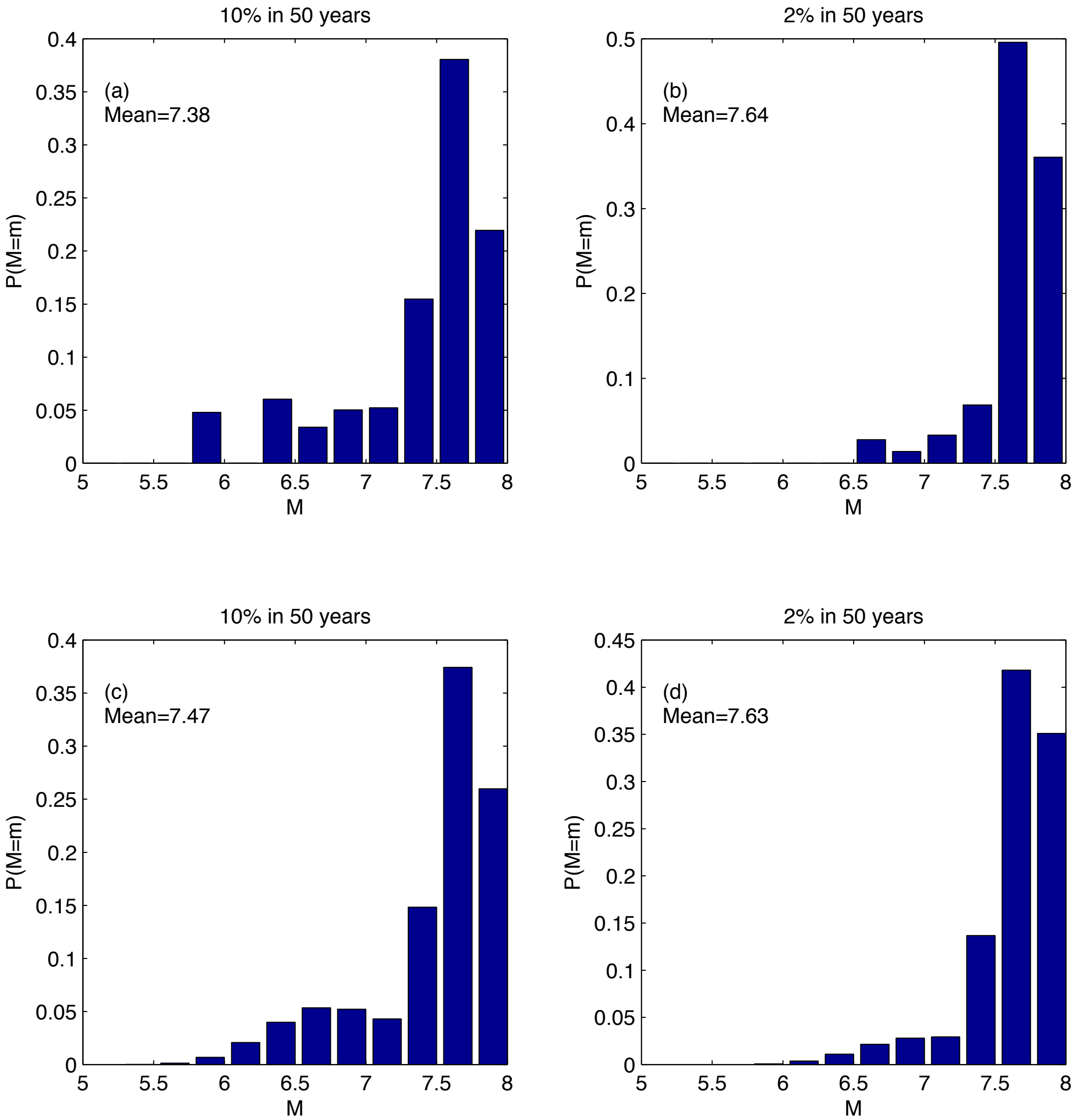

Figure 5.8: Probability of M given $S_d(2.6s)$ (a) $S_d(2.6s)$ with 10% probability of exceedance in 50 years, (b) $S_d(2.6s)$ with 2% probability of exceedance in 50 years from simulation-based PSHA, (c) $S_d(2.6s)$ with 10% probability of exceedance in 50 years, (d) $S_d(2.6s)$ with 2% probability of exceedance in 50 years from traditional PSHA. Mean values of deaggregated magnitudes are noted in each sub-figure.

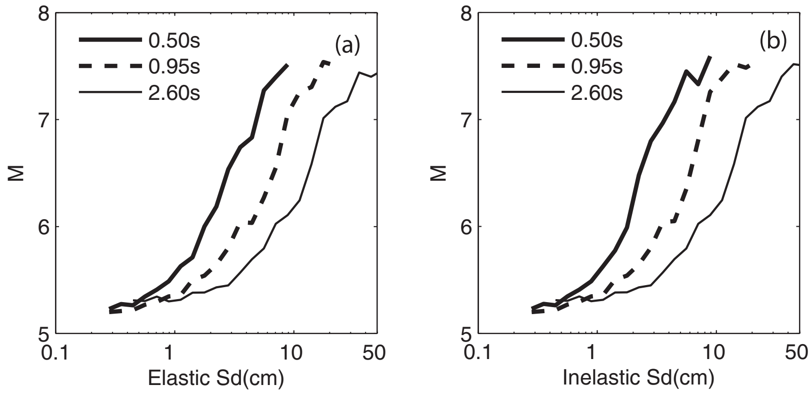

Figure 5.9: Mean M given S_d for the example site (a) for elastic S_d (b) for inelastic S_d.

5.6.2 Deaggregation of Arias intensity

Deaggregation results for Arias intensity given elastic and inelastic $S_d(T)$ for $T = 0.5, 0.95$, and 2.6s are computed. The Arias intensity for a given ground motion (I_a, Arias 1970) is defined as follows:

$$I_a = \frac{\pi}{2g} \int_0^\infty \{x(t)\}^2 \tag{5.17}$$

where $x(t)$ is the ground motion's acceleration time series and g is acceleration of gravity 981cm/s^2. This is one potential measure of total input energy in a ground motion.

Deaggregation of the Arias intensity given elastic and inelastic $S_d(T)$ for $T = 0.5, 0.95$, and 2.6s are computed. The deaggregation of the Arias intensity is only available from simulation-based PSHA for the reasons discussed earlier. Figure 5.10 shows the mean of I_a given a target elastic or inelastic S_d level. In both cases, I_a linearly increases with increasing elastic and inelastic S_d in logarithmic axes. This suggests that large elastic or inelastic S_d are likely to be caused by ground motions with large I_a. Also, the correlations of mean I_a and elastic or inelastic S_d decrease with increasing T. The maximum deaggregation I_a for all periods are almost identical since the maximum I_a depends on the maximum observed valued in the simulated ground motions. The difference between the elastic and inelastic

S_d cases is very small. These trends are similar to those of the deaggregation of magnitude and they are consistent with the regression analysis since E_{acc} is positively correlated with magnitude in Figure 3.27 and E_{acc} and I_a have strong correlation by definition, as indicated in equations 2.27 and 5.17.

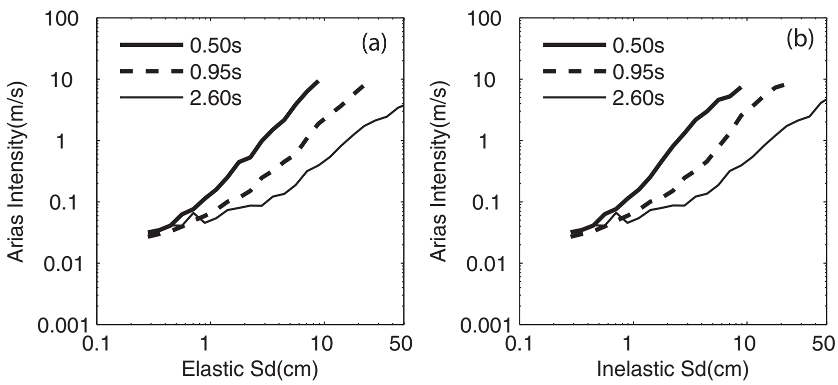

Figure 5.10: Mean I_a given S_d for the example site (a) for elastic S_d (b) for inelastic S_d at $T = 0.5, 0.95$, and $2.6s$.

5.6.3 Deaggregation of significant duration

The $5-95\%$ significant duration, denoted t_{95-5}, is the duration of the ground motion that contains 90% of its total energy. It is defined by the upper limit of the first integral in the following equations:

$$\frac{\int_{t_5}^{t_5+t_{95-5}} |x(t)|^2 \, dt}{E_{acc}} = 0.9, \ \frac{\int_0^{t_5} |x(t)|^2 \, dt}{E_{acc}} = 0.05 \tag{5.18}$$

where E_{acc} is the total energy of the time series and $x(t)$ is the ground motion's acceleration time series.

Deaggregation of the significant duration given elastic and inelastic $S_d(T)$ for $T = 0.5$, 0.95, and $2.6s$ are computed. The deaggregation of this parameter is also only available from simulation-based PSHA for the reasons discussed earlier. Figure 5.11 shows the mean of significant duration given a target elastic or inelastic S_d level. In both cases, the mean of the significant duration increases as the target level increases. This suggests that large elastic and inelastic S_d are likely to be caused by ground motions with long significant duration. In addition, the mean t_{95-5} in both cases decrease with increasing T when elastic or inelastic $S_d > 2cm$. Since the maximum t_{95-5} deaggregation value is limited by the maximum observed value in any of the simulated ground motions, the maximum t_{95-5} of deaggregation is almost identical in all cases. The difference between the elastic and inelastic cases is very small.

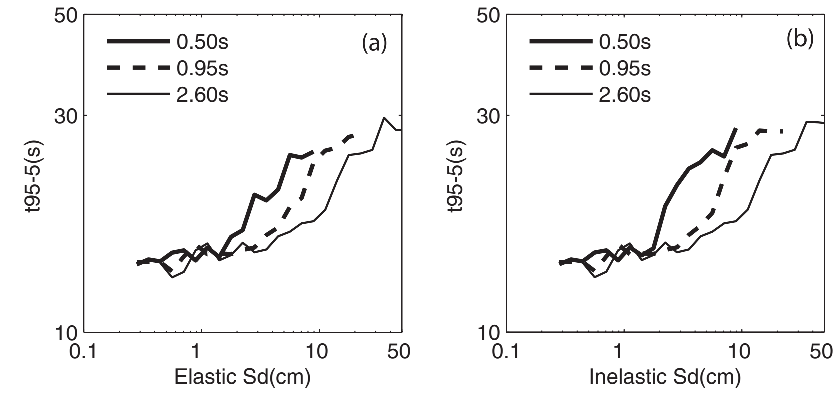

Figure 5.11: Mean t_{95-5} given S_d for the example site (a) for elastic S_d (b) for inelastic S_d at $T = 0.5, 0.95$, and $2.6s$.

5.6.4 Deaggregation of mean period

Mean period (T_m) is defined by Rathje et al. (2004) as follows:

$$T_m = \frac{\sum_i \frac{C_i^2}{f_i}}{\sum_i C_i^2} \tag{5.19}$$

where f_i is frequency i and C_i is the Fourier amplitude of the ground motion at that frequency and $0.25 \leq f_i \leq 20Hz$ with $\Delta f \leq 0.05Hz$. This parameter is of potential interest here because Rathje et al. (2004) found it to influence site response and Kumar et al. (2011)

found that it influences MIDR in structural analysis.

Deaggregation of the mean period given elastic and inelastic $S_d(T)$ for $T = 0.5, 0.95$, and $2.6s$ are computed. Figure 5.12 shows the mean of the significant duration given a target elastic or inelastic S_d level. The mean period T_m is clearly related to the elastic and inelastic S_d level, indicating that large elastic and inelastic S_d are likely to be caused by ground motions with long mean period. The relationship between mean T_m and elastic or inelastic S_d are approximately identical for all periods, but slightly decrease with increasing T. The difference between the elastic and inelastic cases is very small.

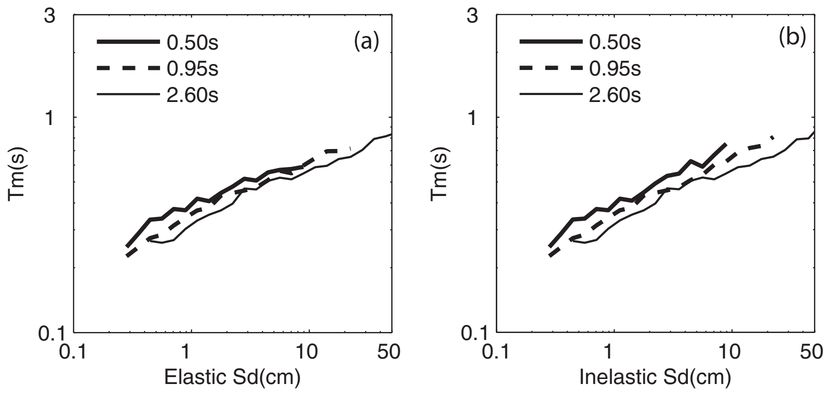

Figure 5.12: Mean T_m given S_d for the example site (a) for elastic S_d (b) for inelastic S_d at $T = 0.5, 0.95$, and $2.6s$.

5.6.5 Deaggregation of response spectra

Rather than look at a single ground motion parameter, we can also study entire response spectra from ground motions having a certain level of S_d at a specified period. Using the traditional approach, the conditional mean spectrum (CMS) (Baker 2011) provides an analogous prediction of the response spectra having a given S_d at a conditioning period, and corresponding magnitude and distance from deaggregation. The CMS is defined as follows:

$$\mu_{\ln S_d(T_i)|\ln S_d(T_1)} = \mu_{\ln S_d}(M, R_{rup}, T_i) + \rho(T_i, T_1)\varepsilon(T_1)\sigma_{\ln S_d}(T_i) \tag{5.20}$$

$$\sigma_{\ln S_d(T_i)|\ln S_d(T_1)} = \sigma_{\ln S_d(T_1)}\sqrt{1-\rho(T_i, T_1)^2} \tag{5.21}$$

$$\varepsilon(T) = \frac{\ln S_d(T) - \mu_{\ln S_d}(M, R_{rup}, T)}{\sigma_{\ln S_d}(T)}, \tag{5.22}$$

where $\mu_{\ln S_d(T_i)|\ln S_d(T_1)}$ and $\sigma_{\ln S_d(T_i)|\ln S_d(T_1)}$ are the predicted mean and standard deviations of $\ln S_d$ (i.e., median prediction and logarithmic standard deviation of the response spectra) predicted by the CMS, $\mu_{\ln S_d}(M,R,T)$ and $\sigma_{\ln S_d}(T)$ are the predicted median and logarithmic standard deviation of S_d provided by a GMPM, M and R_{rup} are the magnitude and rupture distance for which the GMPM is evaluated, and $\rho(T_i, T_1)$ is correlation between $\varepsilon(T_i)$ and $\varepsilon(T_1)$. In the equations above, T_1 denotes the period at which the hazard analysis is being performed, and T_i denotes the other periods of interest.

Figures 5.13 and 5.14 show the response spectra of the simulated ground motions with $S_d(0.5s)$ amplitudes exceeded with target probabilities: 10% and 2% in 50 years. Also shown on that plot are the median and two percentiles of the response spectra, and corresponding predictions from the CMS calculations above. Figures 5.15 through 5.18 show the same results for $S_d(0.95s)$ and $S_d(2.6s)$. Several observations can be made from these figures.

The response spectra are pinched at 0.5s because the motions are selected based on their amplitude at that period. The median percentiles of the record spectra reasonably match the corresponding CMS values superimposed on these figures. This is the result of the means, standard deviations and correlations of $\ln S_d$ values from the simulations being comparable to the values predicted by the models used to compute the CMS. This is also a useful independent validation of CMS concepts, as the CMS calculations are intended to predict the spectra of ground motions, conditional on their spectral value at a single period; we see here from simulated ground motions satisfying that condition that the CMS makes relatively accurate predictions.

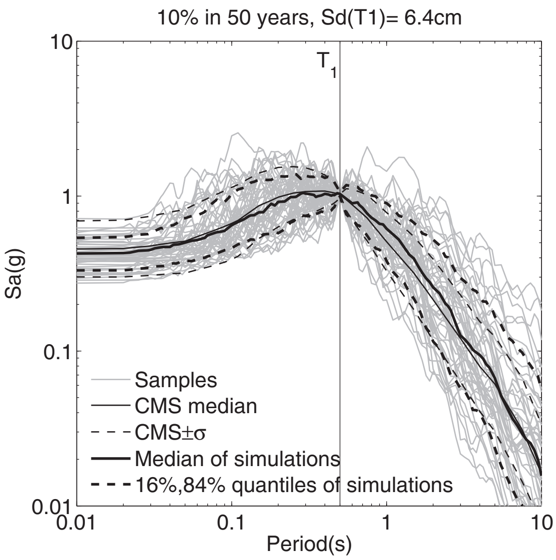

Figure 5.13: Response spectra of ground motions selected based on their match with the $S_d(0.5s)$ amplitude exceeded with in 10% probability in 50 years.

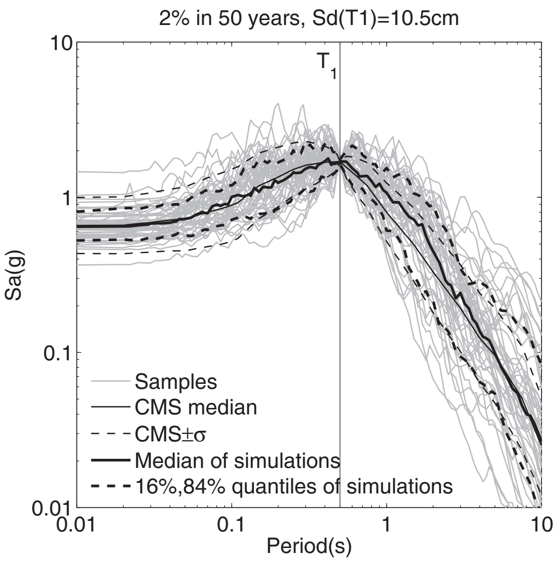

Figure 5.14: Response spectra of ground motions selected based on their match with the $S_d(0.5s)$ amplitude exceeded with in 2% probability in 50 years.

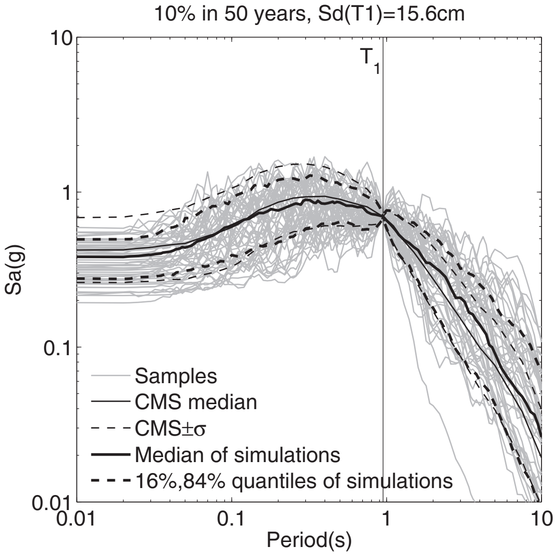

Figure 5.15: Response spectra of ground motions selected based on their match with the $S_d(0.95s)$ amplitude exceeded with in 10% probability in 50 years.

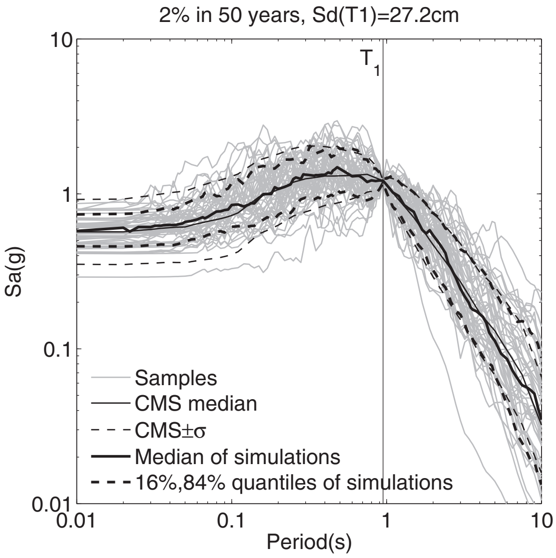

Figure 5.16: Response spectra of ground motions selected based on their match with the $S_d(0.95s)$ amplitude exceeded with in 2% probability in 50 years.

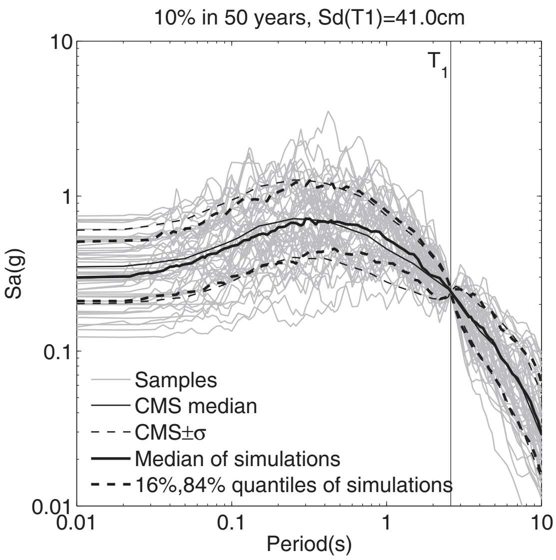

Figure 5.17: Response spectra of ground motions selected based on their match with the $S_d(2.6s)$ amplitude exceeded with in 10% probability in 50 years.

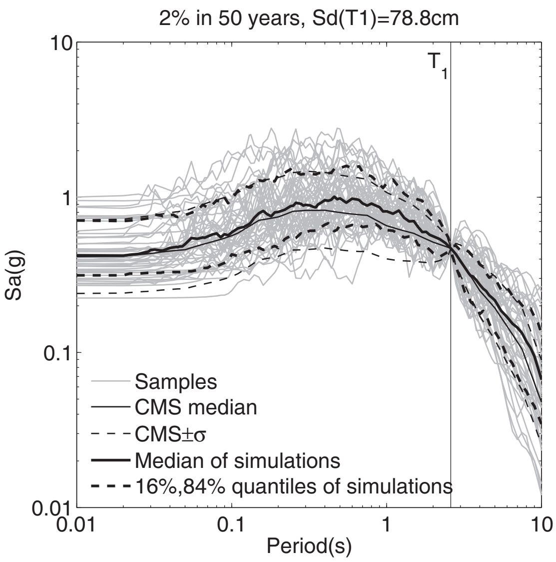

Figure 5.18: Response spectra of ground motions selected based on their match with the $S_d(2.6s)$ amplitude exceeded with in 2% probability in 50 years.

5.6.6 Deaggregation of response spectra, conditioned on an inelastic spectral value at a single period

In this section we repeat the calculations of the previous section, but here the simulated ground motions are selected to match a certain level of inelastic S_d at the conditioning period. Figures 5.19 and 5.20 show (elastic) response spectra of those simulated ground motions with inelastic $S_d(0.5s)$ equal to the amplitudes with exceedance probabilities of 10% and 2% in 50 years, respectively. Also shown for reference are the median and two percentiles of those spectra, and comparable elastic CMS predictions. The CMS predictions are not expected to be precise representations of the observed spectra, because the CMS is computed conditional on an elastic spectral value rather than an inelastic spectral value. They are nonetheless included to aid in highlighting the effect of switching to an inelastic spectral value for conditioning.

The spectra shown in Figure 5.19 and are not pinched at the conditioning period, because these simulated ground motions are selected based on the inelastic S_d and so there is no expectation that their elastic spectra at that same period would be identical for each ground motion. The 16% and 84% percentiles of the spectra are relatively narrow over a range of periods from the conditioning period to some longer period. These are the range of periods for which the elastic spectra are correlated with the inelastic spectra amplitude used for conditioning; this is intuitive based on the concept that the inelastic oscillator's period effectively "lengthens" when its stiffness reduces due to nonlinearity, and thus the elastic spectra at these lengthened periods are similar for ground motions with a given inelastic spectral value. There is no narrowing of the percentiles of the spectra at periods shorter than the conditioning period, as there are no higher modes that contribute to response of this single-degree-of-freedom oscillator. The same effect is observed in Figure 5.20, but the range of periods with similar spectra is broader due to the greater nonlinearity of the oscillator in that case.

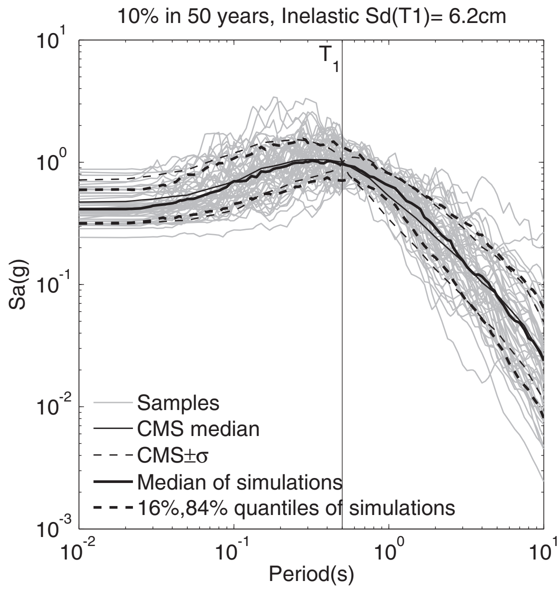

Figure 5.19: Response spectra of ground motions selected based on their match with the inelstic $S_d(0.5s)$ amplitude exceeded with in 10% probability in 50 years.

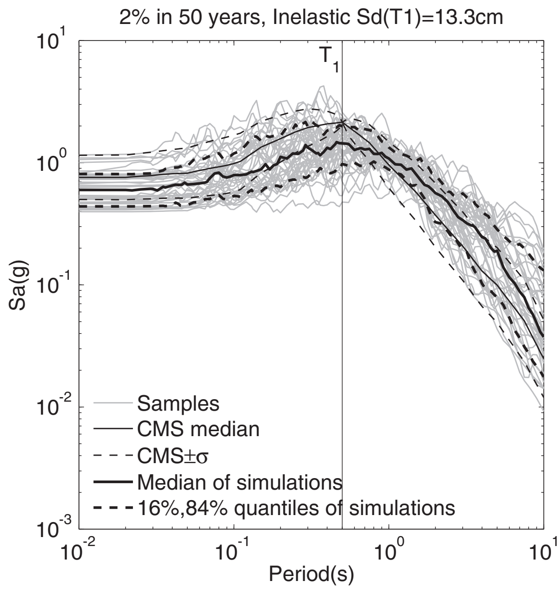

Figure 5.20: Response spectra of ground motions selected based on their match with the inelstic $S_d(0.5s)$ amplitude exceeded with in 2% probability in 50 years.

Figures 5.21 and 5.22 show response spectra of simulated ground motions with inelastic $S_d(0.95s)$ equal to the amplitudes with exceedance probabilities of 10% and 2% in 50 years, respectively. Figures 5.23 and 5.24 show response spectra of simulated ground motions with inelastic $S_d(2.6s)$ equal to the amplitudes with exceedance probabilities of 10% and 2% in 50 years, respectively. These figures all have the same trends as were observed in Figures 5.19 and 5.20 .

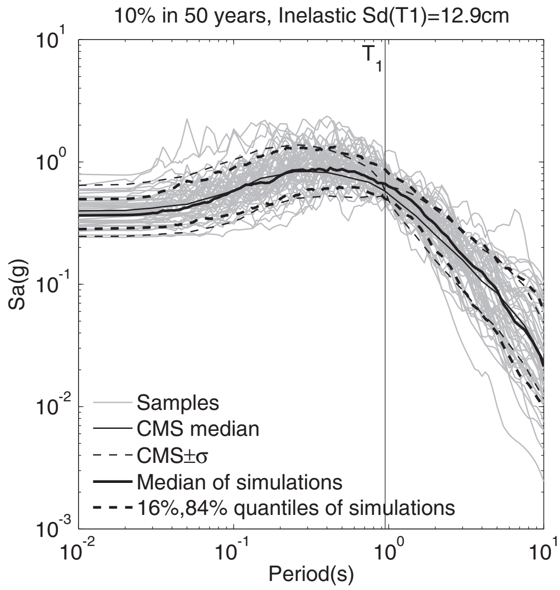

Figure 5.21: Response spectra of ground motions selected based on their match with the inelstic $S_d(0.95s)$ amplitude exceeded with in 10% probability in 50 years.

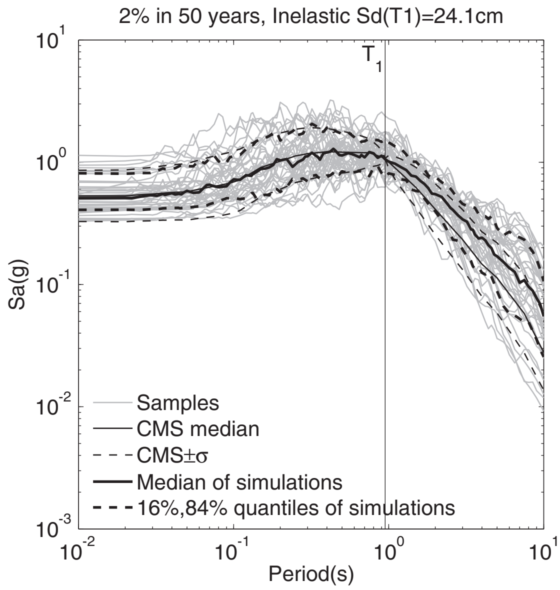

Figure 5.22: Response spectra of ground motions selected based on their match with the inelstic $S_d(0.95s)$ amplitude exceeded with in 2% probability in 50 years.

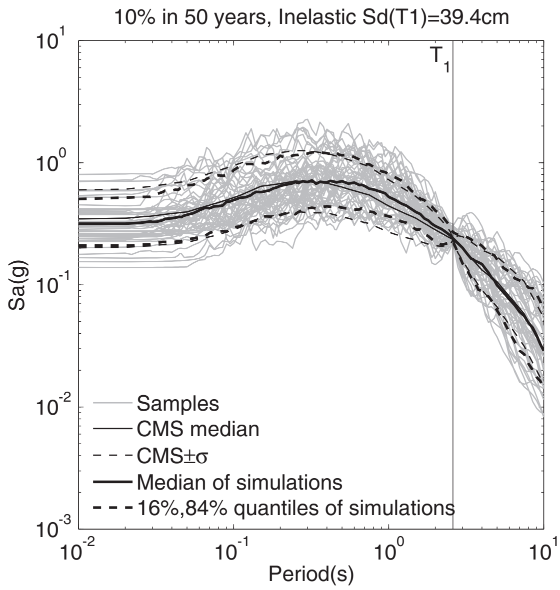

Figure 5.23: Response spectra of ground motions selected based on their match with the inelstic $S_d(2.6s)$ amplitude exceeded with in 10% probability in 50 years.

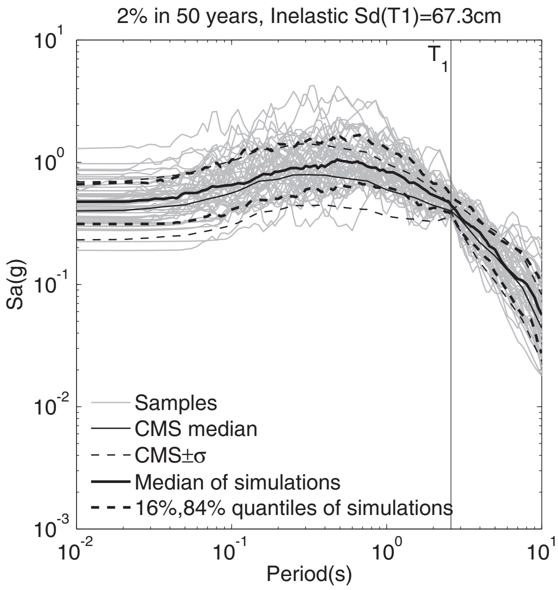

Figure 5.24: Response spectra of ground motions selected based on their match with the inelstic $S_d(2.6s)$ amplitude exceeded with in 2% probability in 50 years.

5.7 Conclusions

Seismic hazard analysis using simulated ground motions has been proposed and compared with traditional PSHA (which uses ground motion prediction models in place of simulations). The simulated ground motions were generated by the proposed stochastic model for distributions of earthquake magnitudes and distances that may occur at the site of interest. Hazard curves from the simulation-based PSHA are efficient to compute, as they only require counting the number of simulated ground motions whose IM of interest exceeds the specified threshold instead of calculating integration of probabilistic density function of IM. Deaggregation of magnitude was also computed. Example results demonstrated that the hazard curves and deaggregated magnitudes from simulation-based PSHA match those from traditional PSHA.

Additionally deaggregations of other characteristics of the time series were computed. We examined the deaggregation of Arias intensity, significant duration, and mean period. These parameters were observed to have relationships with the amplitude of S_d, and the relationships and deaggregation results were physically reasonable. Finally we examined the spectral shape of ground motions having a certain S_d or inelastic S_d at a given period. The response spectra of ground motions having a given $S_d(T)$ were by definition "pinched" to a single value at the conditioning period T_1. At other periods, the spectra were consistent with empirical equations for the Conditional Mean Spectrum. The elastic response spectra of ground motions having a specified inelastic S_d are not pinched at any single period. These spectra did have a narrow distribution at periods from T_1 (the conditioning period) to approximately $2T_1$. This is consistent with concepts that the "equivalent period" of a nonlinear oscillator lengthens, and thus elastic response spectra at lengthened periods are indicators of inelastic oscillator response.

Using simulation-based PSHA, we can compute hazard curves for a wide variety of ground motion properties, and also compute deaggregation results for a variety of characteristics of time series with a given intensity level. The method used here for simulation-based PSHA will later be extended to compute hazard curves for structural response levels rather than ground motion hazard, by inputting all of the simulated ground motions into a structural model and computing the fraction of ground motions causing exceedance of some level of structural response. We will compute this response hazard in Chapter 7, but first we study structural responses from simulated ground motions and recorded ground motions in the following chapter.

Chapter 6

Structural analysis using simulated ground motions

6.1 Abstract

The previous chapters of this dissertation have indicated that ground motions simulated using the proposed approach are in general statistically consistent with recorded ground motions in terms of their elastic and inelastic response spectra, durations, Arias intensities, mean periods, and characteristics of ε. But these are only useful proxies for the most important parameter, which is the response of a nonlinear multi-degree-of-freedom (MDOF) model. This chapter will study the statistical distributions of displacements and accelerations observed in two nonlinear MDOF models subjected to the simulations developed here, and compare them to those obtained using recorded ground motions. The procedure used to identify appropriate simulated and recorded ground motions is described, and the structural models and response metrics are introduced. A variety of comparisons indicate that, to the extent that there exist comparable sets of observed and simulated ground motions, the distributions of structural responses resulting from the two sets are comparable with respect to the parameters described above. Notably, the complete distribution of structural responses are comparable–not only the mean or median response. These results suggest that the proposed simulated ground motions are suitable for use in "performance-based" engineering assessments that require the estimation of probability distributions for structural responses

under earthquake shaking.

6.2 Introduction

Performance based engineering requires a large number of input ground motions in order to evaluate the structural behavior in earthquakes in terms of probabilistic characterization of engineering demand parameters. However, the number of recorded ground motions is often not sufficient for a given analysis situation, so ground motion scaling and spectrum matching are used to overcome the shortage of recorded ground motions. Simulated ground motions can be used instead if their properties are comparable with those of recorded ground motions. Many characteristics of the simulated ground motions generated by the proposed stochastic model were evaluated in Chapter 4 and found to be consistent with corresponding GMPMs. In this chapter, the characteristics of the simulated ground motions are examined in terms of the following Engineering Demand Parameters (EDPs): ductility, maximum inter-story drift ratio (MIDR), and peak floor acceleration (PFA). The EDPs are computed for 4- and 20-story RC moment frame buildings, which were developed by Haselton et al. (2009). Forty recorded ground motions are selected and scaled to match either a fixed target spectrum or to match a distribution of spectra (i.e., a mean and standard deviation of $\ln S_a$) using the approach of Jayaram et al. (2011). The target spectra is computed by Campbell and Bozorgnia (2008) for a scenario with $M = 7$, $R_{rup} = 10km$, $V_{S30} = 400m/s$, and vertical strike-slip fault. A third set of the input ground motions are selected from the simulated ground motions to match the target spectra at a fundamental period of each building.

The probabilistic characteristics of the EDPs computed using the simulated ground motions reasonably match those using the recorded ground motions selected to match the mean and standard deviation of the target spectra in terms of empirical cumulative distribution functions. These results suggest that the simulated ground motions can be used for nonlinear structural dynamic analysis and response hazard analysis.

6.3 Structural model

A series of inelastic single-degree-of-freedom (SDOF) systems and two multiple-degree-of-freedom structures (MDOFs) are considered in this chapter to compare the structural response to simulated ground motions generated with the proposed procedure and compare it to the structural response of the same structures but to recorded ground motions. For inelastic SDOF systems we employ six non-deteriorating bilinear oscillators characterized by a postelastic stiffness ratio of $\alpha = 0.10$ and a period of vibration of $T = 0.5s$. The yield displacement, and hence lateral strength since the period of vibration is the same for all six systems, of each non-deteriorating oscillator is related to the spectral ordinates as follows

$$d_y = \frac{S_a(T)}{R} \left\{ \frac{T}{2\pi} \right\}^2 \tag{6.1}$$

We consider three levels of ground motion intensity, characterized by ε values of 0, 1 and 2 and two strength ratios $R = 4$ and 8 for a total of six different SDOF oscillators, all with the same period of vibration but the six have different yield displacements and different lateral strengths.

For MDOF models we used two buildings models that have been used in the past by other investigators (Haselton and Deierlein 2008) and are well documented in the literature (Haselton et al. 2009) and each of these two models is subjected to simulated and recorded ground motions with three levels of intensity. The first, second, and third mode periods (T_1, T_2, and T_3) for 4-story building are $0.94s$, $0.3s$, and $0.17s$, and for 20-story building are $2.63s$, $0.85s$, and $0.46s$, respectively.

6.4 Input ground motions

Ten thousand simulated ground motions are generated for a scenario with $M = 7$, $V_{S30} = 400m/s$, $R_{hyp} = 10km$, $R_{rup} = 10km$, $Z_{VS} = 2km$, $Z_{TOR} = 0$, vertical strike-slip fault, and arbitrary component. The input ground motions are selected that match target $\ln S_a(T_1)$ values equal to the mean prediction, mean$+1\sigma$, and mean$+2\sigma$ from Campbell and Bozorgnia

2008 (denoted here asCB08) ground motion prediction model. Note that spectral accelerations for a given earthquake scenario are lognormally distributed, so their distributions are often described in terms of the mean and standard deviation of logarithmic S_a values; the exponential of the mean $\ln S_a$ value is the median of the non-logarithmic S_a, so the terms mean and median are both used to describe these target S_a values.

The number of selected ground motions are shown in Table 6.1. The number of available appropriate ground motions decreases with increasing ε since spectral accelerations with large ε are by definition rare. Figures 6.1, 6.2, and 6.3 show the means and standard deviations of logarithmic spectral accelerations with 5% damping computed from the simulated ground motions, the conditional mean spectrum (CMS, Baker 2011), and the uniform hazard spectrum (UHS). The CMS is computed by the following equations:

$$\mu_{\ln S_a(T_i)|\ln S_a(T_1)} = \mu_{\ln S_a}(M,R,T_i) + \rho(T_i,T_1)\varepsilon(T_1)\sigma_{\ln S_a}(T_i) \tag{6.2}$$

$$\sigma_{\ln S_a(T_i)|\ln S_a(T_1)} = \sigma_{\ln S_a(T_1)}\sqrt{1-\rho(T_i,T_1)^2} \tag{6.3}$$

$$\varepsilon(T) = \frac{\ln S_a(T) - \mu_{\ln S_a}(M,R,T)}{\sigma_{\ln S_a}(T)} \tag{6.4}$$

where $\mu_{\ln S_a(T_i)|\ln S_a(T_1)}$ and $\sigma_{\ln S_a(T_i)|\ln S_a(T_1)}$ are the mean and standard deviation of log spectral accelerations, conditioned on a known value of $S_a(T_1)$, and $\mu_{\ln S_a}(M,R,T)$ and $\sigma_{\ln S_a}(T)$ are the predicted mean and standard deviation of $\ln S_a$ at all periods, and we always condition on the 1st mode period T_1. The UHS is computed by the mean $\ln S_a$ prediction of CB08 plus $\varepsilon \times \sigma$ (i.e., a fixed number of standard deviations larger than the mean prediction). The above calculations imply that the CMS equals to the UHS when $\varepsilon = 0$, because both are equal to the mean $\ln S_a$ prediction in that case.

The $\mu_{\ln S_a(T_i)|\ln S_a(T_1)}$ of the selected ground motions with $\varepsilon = 0$ are slightly smaller than the CMS at long periods, consistent with Figure 4.4 earlier. Also, $\sigma_{\ln S_a(T_i)|\ln S_a(T_1)}$ of the selected ground motions with $\varepsilon = 0$ are slightly larger than the CMS at long periods (maximum factor is 1.4 for $T_1 = 0.5s$), consistent with Figure 4.18 earlier. These are cause by

Table 6.1: Number of selected ground motions

	$\varepsilon = 0$	$\varepsilon = 1$	$\varepsilon = 2$
$T_1 = 0.5s$ for SDOF	1552	812	126
$T_1 = 0.94s$ for 4-story	1394	764	147
$T_1 = 2.63s$ for 20-story	1040	601	133

the limited period resolution at these long periods, due to the finite time-domain resolution of the wavelet packet transform. However, $\mu_{\ln S_a(T_i)|\ln S_a(T_1)}$ and $\sigma_{\ln S_a(T_i)|\ln S_a(T_1)}$ of the selected ground motions reasonably match those of the CMS in the case of $\varepsilon = 1$ and $\varepsilon = 2$ in Figures 6.1, 6.2, and 6.3. Since the logarithmic standard deviation of S_a of simulated ground motions are larger than those of GMPM and the inter-period correlations of ε in long periods are also larger than those of Baker and Jayaram (2008), the logarithmic standard deviation of S_a conditioned by $S_a(T_1)$ is comparable to that of the CMS (Figure 6.4). In Equation 6.3, we can see the trade-off between $\sigma_{\ln S_a(T_1)}$ and $\rho(T_i, T_1)$. Similarly the mean of S_a conditioned by $S_a(T_1)$ is comparable to that of the CMS.

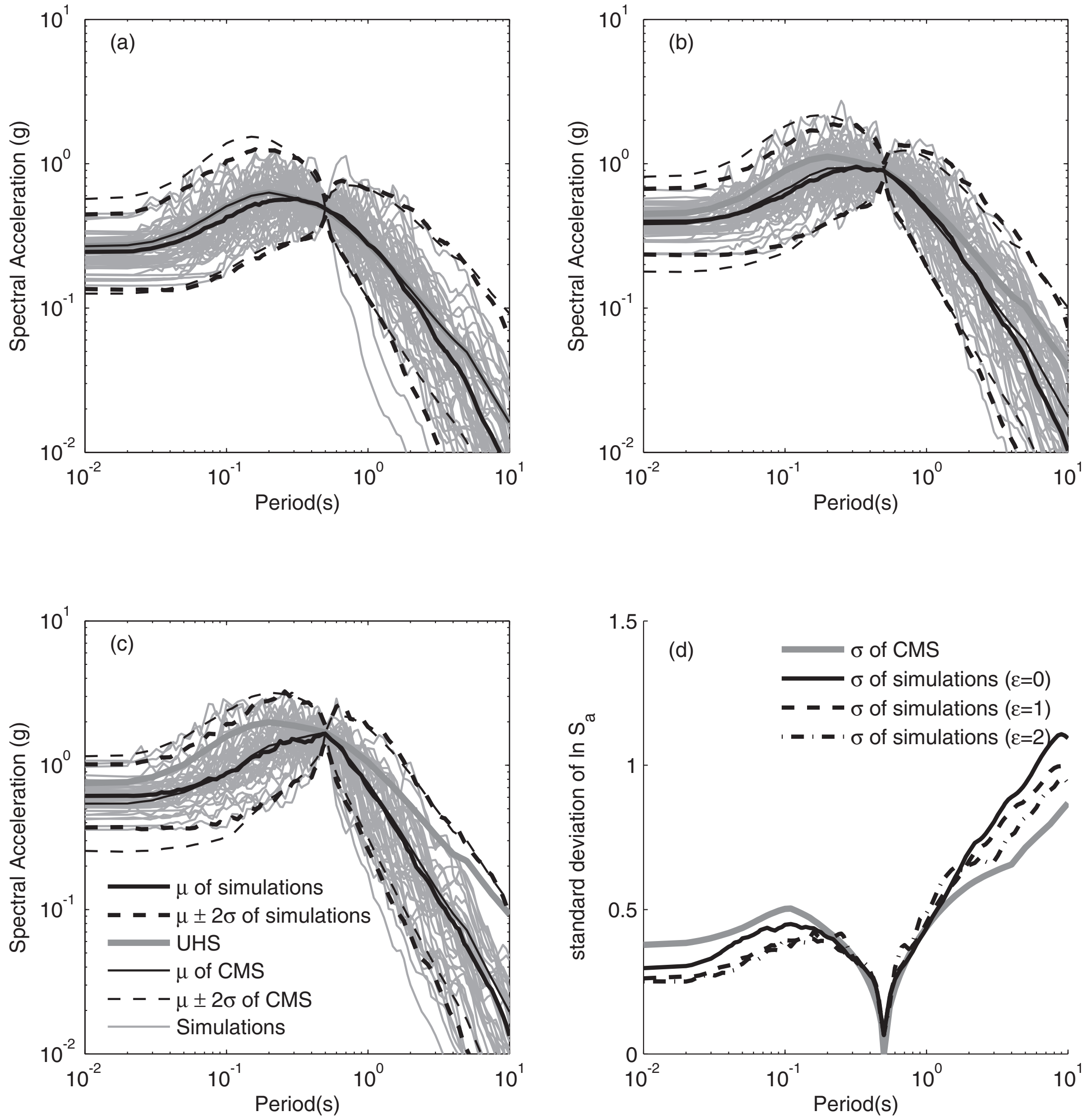

Figure 6.1: Spectral accelerations of selected ground motions for $T_1 = 0.5s$ (a) $\varepsilon = 0$, (b) $\varepsilon = 1$, (c) $\varepsilon = 2$, (d) logarithmic standard deviation for all ε.

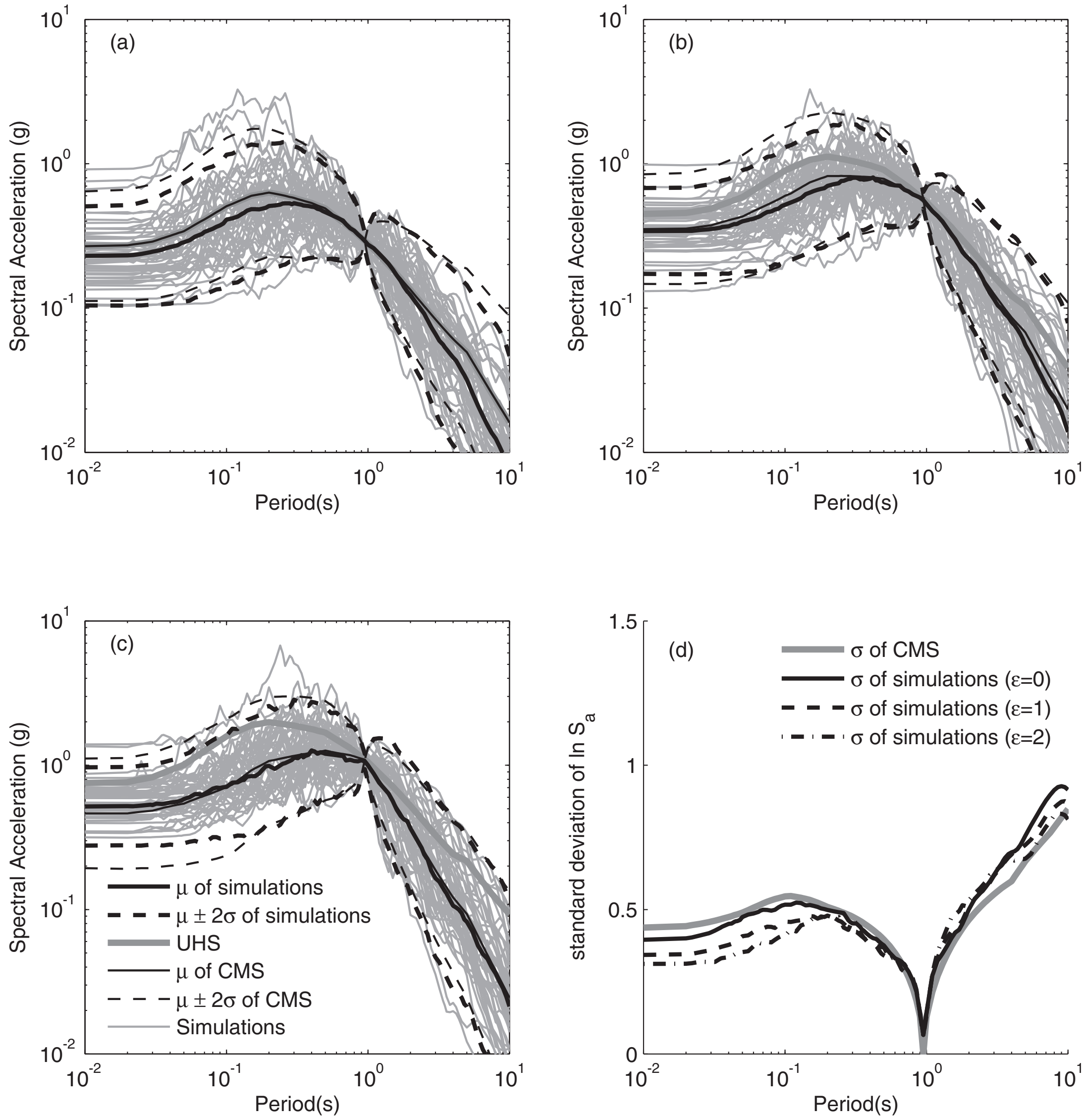

Figure 6.2: Spectral accelerations of selected ground motions for $T_1 = 0.94s$ (a) $\varepsilon = 0$, (b) $\varepsilon = 1$, (c) $\varepsilon = 2$, (d) logarithmic standard deviation for all ε.

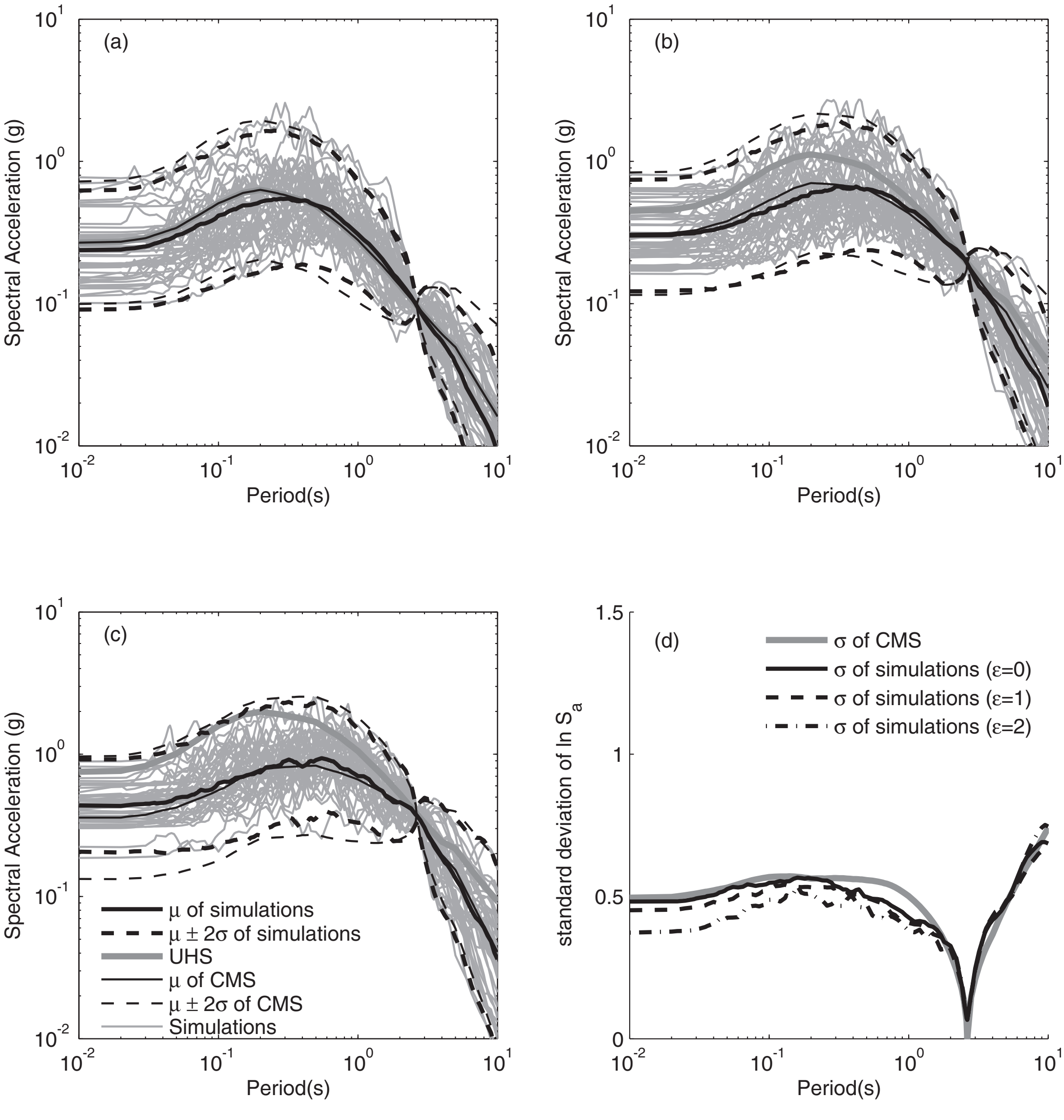

Figure 6.3: Spectral accelerations of selected ground motions for $T_1 = 2.63s$ (a) $\varepsilon = 0$, (b) $\varepsilon = 1$, (c) $\varepsilon = 2$, (d) logarithmic standard deviation for all ε.

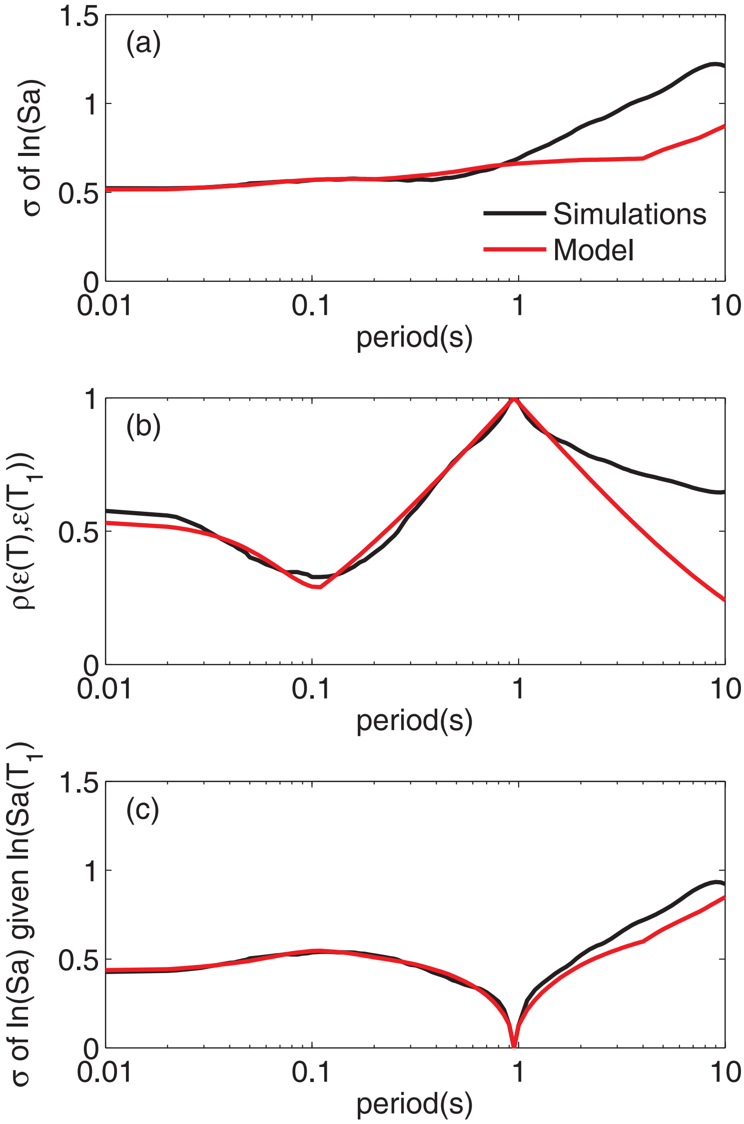

Figure 6.4: Relationship between (a) logarithmic standard deviation of spectral acceleration, (b) inter-period correlation of ε, and (c) logarithmic standard deviation of spectral acceleration conditioned by spectral acceleration at $T_1 = 0.94s$.

6.5 Structural analysis for SDOF system

Dynamic nonlinear structural analysis of the SDOF system for the three types of input ground motions are computed: 1) Recorded 1: recorded ground motions are selected and scaled based on their match to the target mean CMS, 2) Recorded 2: recorded ground motions are selected and scaled based on their match to the mean and standard deviation of the target CMS using the approach of Jayaram et al. (2011), 3) Simulated: simulated ground motions are selected to match $S_a(T_1)$ associated with the target ε. No further effort was made to select simulated motions where spectra matched some specific target. The statistical characteristics of the ductility demands of the six SDOF non-degrading oscillators are shown in Table 6.2, and the cumulative probabilities of ductility demands are shown in Figures 6.5, 6.6, and 6.7 for $\varepsilon = 0, 1$, and 2, respectively. As shown in Table 6.2, for a given level of ε, median ductility demands are much larger for the systems with $R = 8$ than for the systems with $R = 4$ because the former systems have half the lateral strength than the latter systems. Since these as short period systems, as expected, the median ductility demands of the weaker systems ($R = 8$) are more than twice the median ductility demand of the stronger systems ($R = 4$). For a given strength ratio, the median ductility demands exhibit are similar with small reductions in median ductility demand because systems subjected to $\varepsilon = 1$ records are stronger than SDOF systems subjected to $\varepsilon = 0$ records and, similarly, SDOF systems subjected to $\varepsilon = 2$ records are stronger than SDOF systems subjected to $\varepsilon = 1$ records. The small reduction in ε is due to the relationship between the effective periods in nonlinear structural behavior and the spectral shape of the input ground motions: the S_a's of the input ground motions with large ε decrease more quickly for $T > T_1$ than those with small ε. In all ε cases, the probability distributions of the Recorded 2 set have heavier tails than those of the Recorded 1 set because the input ground motions of the Recorded 2 set consider not only mean but also standard deviations of $\ln S_a$. The probability distributions of the Simulated set are closer to those from the Recorded 2 set than those from the Recorded 1 set, especially for the upper tail, because the input ground motions from the simulated ground motions have natural dispersion comparable to that in the Recorded 2 set and this dispersion in $\ln S_a$ produces large variation structural responses.

Table 6.2: Statistics of ductility from SDOF system analyses, as a function of ground motion set, ductility, and target ε

ε	R	Median Ductility			Dispersion of Ductility		
		Recorded 1	Recorded 2	Simulated	Recorded 1	Recorded 2	Simulated
0	4	3.93	3.76	3.61	0.24	0.31	0.32
	8	10.76	9.97	8.48	0.28	0.42	0.47
1	4	3.55	3.35	3.38	0.22	0.33	0.32
	8	8.04	8.16	7.58	0.28	0.44	0.45
2	4	3.27	3.04	2.91	0.19	0.28	0.26
	8	6.90	7.44	6.12	0.24	0.41	0.38

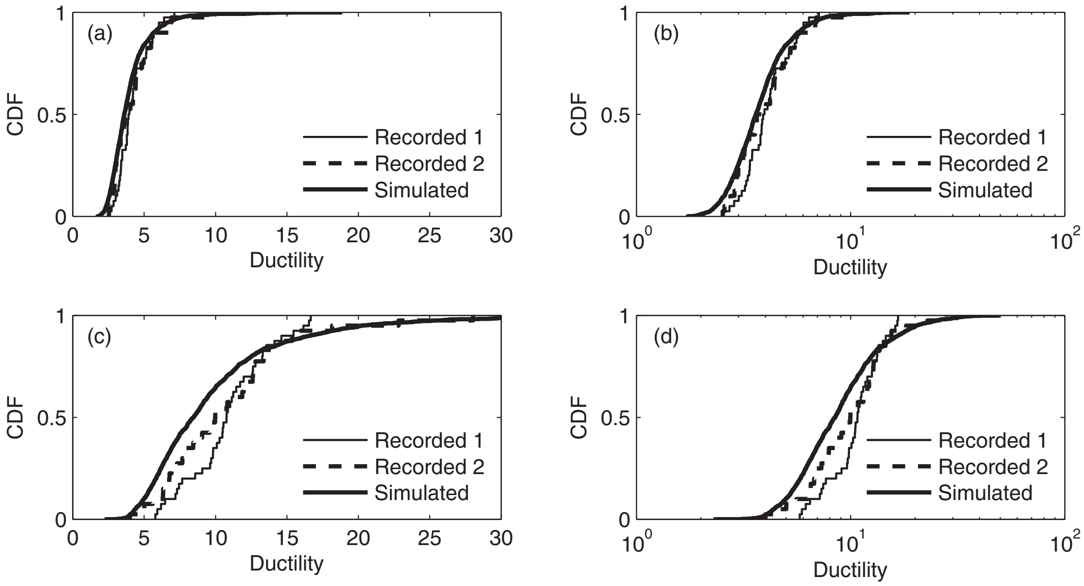

Figure 6.5: CDF of ductility of the SDOF system, $\varepsilon = 0$, (a) R=4 on linear axis, (b) R=4 on logarithmic axis, (c) R=8 on linear axis, (d) R=8 on logarithmic axis.

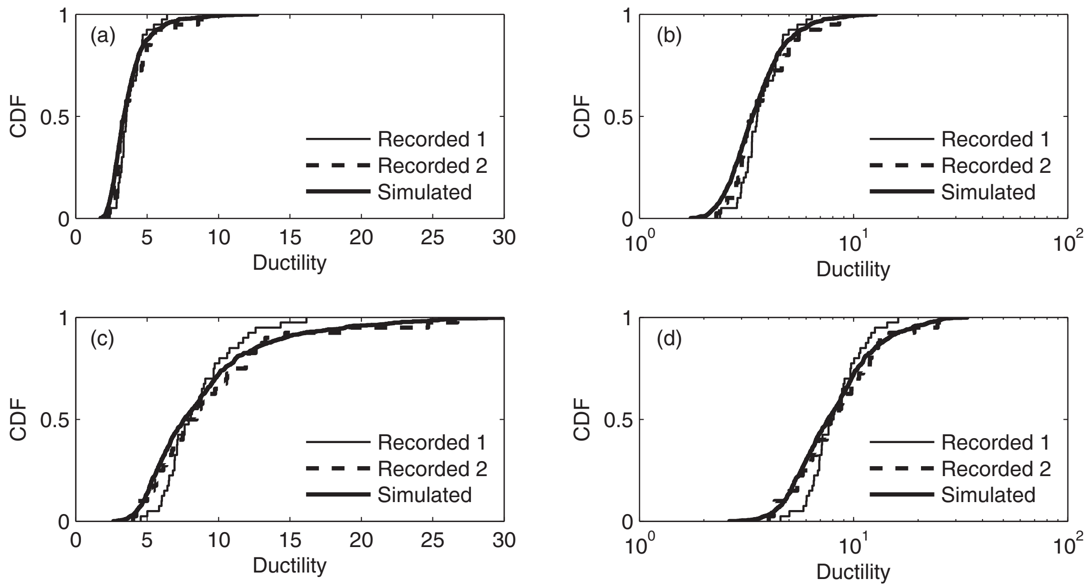

Figure 6.6: CDF of ductility of the SDOF system, $\varepsilon = 1$, (a) R=4 on linear axis, (b) R=4 on logarithmic axis, (c) R=8 on linear axis, (d) R=8 on logarithmic axis.

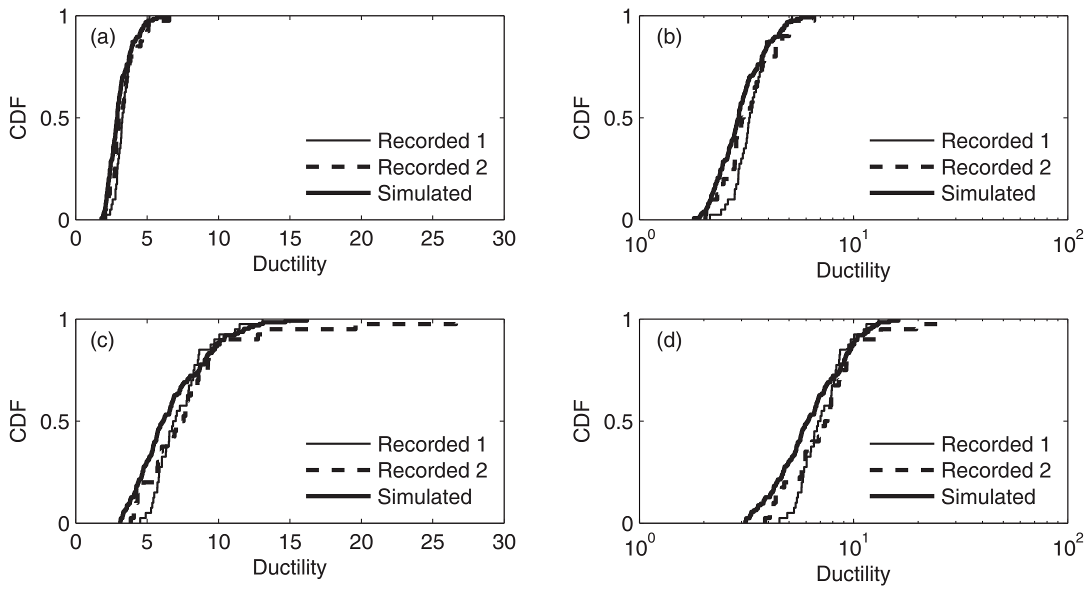

Figure 6.7: CDF of ductility of the SDOF system, $\varepsilon = 2$, (a) R=4 on linear axis, (b) R=4 on logarithmic axis, (c) R=8 on linear axis, (d) R=8 on logarithmic axis.

6.6 Structural analysis for MDOF system

Here dynamic nonlinear structural analysis for three types of input ground motions are performed: 1) Recorded 1: recorded ground motions are selected and scaled to match the mean of the target CMS, 2) Recorded 2: recorded ground motions are selected and scaled to match the mean and standard deviation of the target CMS, 3) Simulated: simulated ground motions are selected to match the target $S_a(T_1)$. Maximum inter-story drift ratios (MIDR) and peak floor accelerations (PFA) are computed in each case since they are useful indicators of structural and non-structural damage, respectively.

6.6.1 MIDR results

The statistical characteristics of MIDR are reported in Table 6.3. In examining these results, the reader should keep in mind that contrary to SDOF results previously discussed in which the non-degrading oscillators had lateral strengths proportional to the spectral ordinates (related to ε), for the MDOF structures a given structure (with a fixed strength and stiffness) was subjected to ground motions with three increasing levels of ground motion intensity. Therefore, for the MDOF structures, and as expected, median MIDR increases as ε increases as expected because the input ground motions with large ε have large S_a (see Figures 6.1, 6.2 and 6.3). In the Recorded 1 and 2 sets, and the Simulated set, the medians of MIDR are all within a factor of 1.3. The logarithmic standard deviations of MIDR of the Recorded 2 set are larger than those of the Recorded 1 set because the input ground motions of the Recorded 2 set are selected considering the mean and logarithmic standard deviation in their response spectra. The logarithmic standard deviations of MIDR of the Simulated set are closer to those of the Recorded 2 set than those of the Recorded 1 set because the input ground motions of the Simulated set naturally satisfy the target dispersion of response spectra.

Figure 6.8 shows the relationship between $S_a(T_1)$ and MIDR of the simulated ground motions for each ε. The median MIDR is linearly related to $S_a(T_1)$. It suggests in many cases the structures are still in linear status or weakly nonlinear status. However, MIDR has heavier upper tail on $S_a(T_1)$ since some cases appear to be in strong nonlinear status.

The cumulative probabilities of MIDR are shown in Figure 6.9 and 6.10 for the 4-

and 20-story buildings, respectively. The differences between the results of the Recorded 1 and 2 sets are the largest for $\varepsilon = 2$ because the difference of the input ground motions' spectra for those cases are the largest. The probability distributions of the Simulated set are closer to those of the Recorded 2 set than those of the Recorded 1 set because the simulated ground motions naturally satisfy the dispersion of the target response spectra.

Table 6.3: MIDR from MDOF system

Building	ε	Median MIDR			Dispersion of MIDR		
		Recorded 1	Recorded 2	Simulated	Recorded 1	Recorded 2	Simulated
20-story	0	0.0044	0.0043	0.0045	0.18	0.32	0.27
moment	1	0.0096	0.0086	0.0086	0.24	0.29	0.30
frame	2	0.0186	0.0196	0.0164	0.25	0.43	0.39
4-story	0	0.0072	0.0072	0.0070	0.09	0.09	0.11
moment	1	0.0137	0.0139	0.0125	0.26	0.29	0.29
frame	2	0.0279	0.0237	0.0232	0.28	0.46	0.44

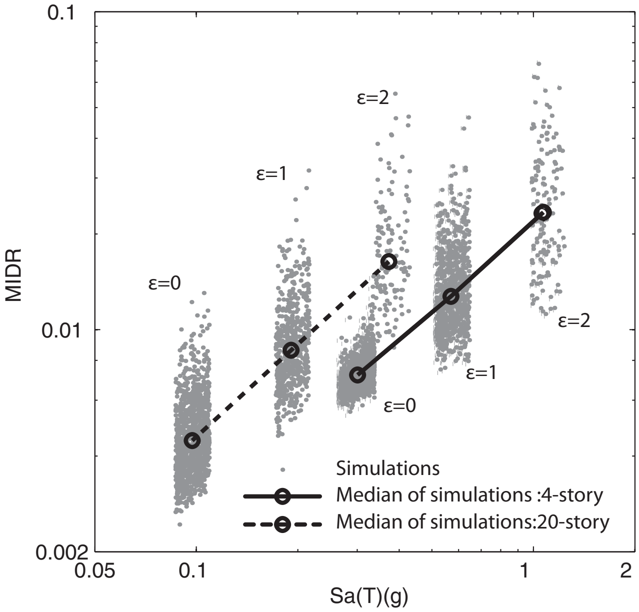

Figure 6.8: Relationship between $S_a(T_1)$ and median MIDR.

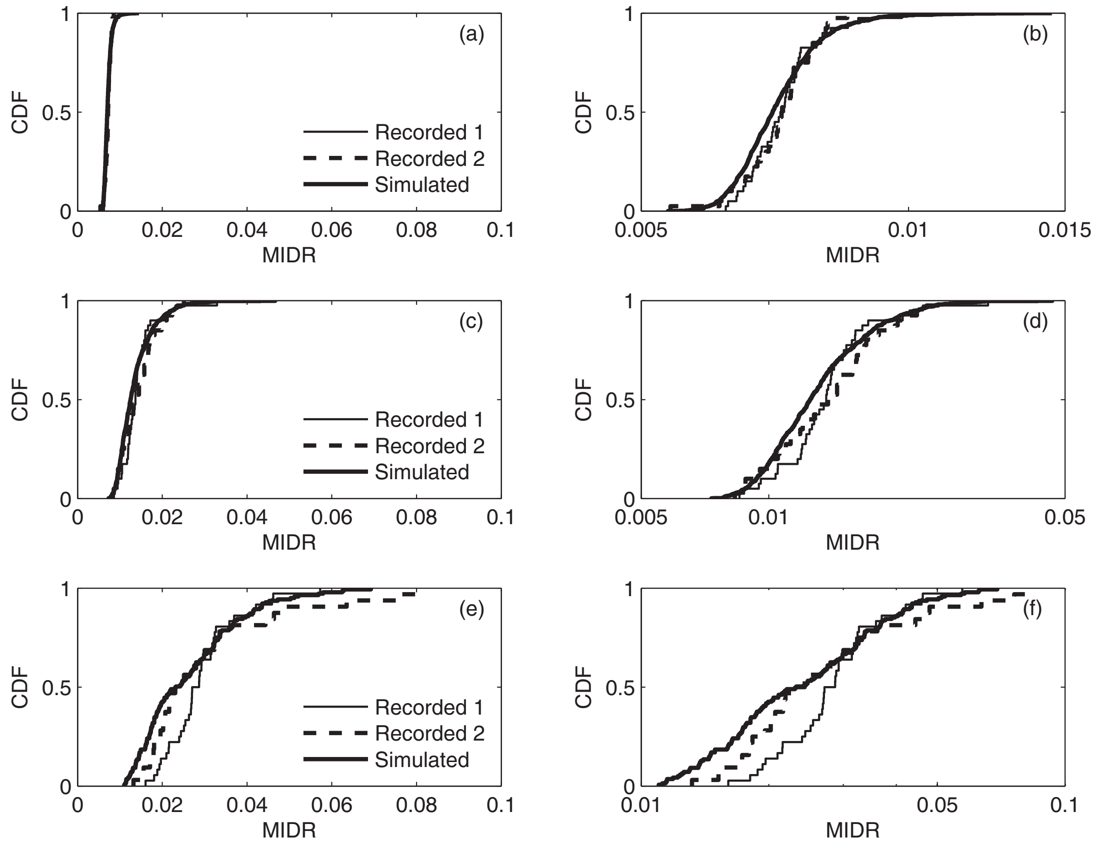

Figure 6.9: CDF of maximum inter-story drift ratio for 4-story building (a) $\varepsilon = 0$ on linear axis, (b) $\varepsilon = 0$ on logarithmic axis, (c) $\varepsilon = 1$ on linear axis, (d) $\varepsilon = 1$ on logarithmic axis, (e) $\varepsilon = 2$ on linear axis, (f) $\varepsilon = 2$ on logarithmic axis.

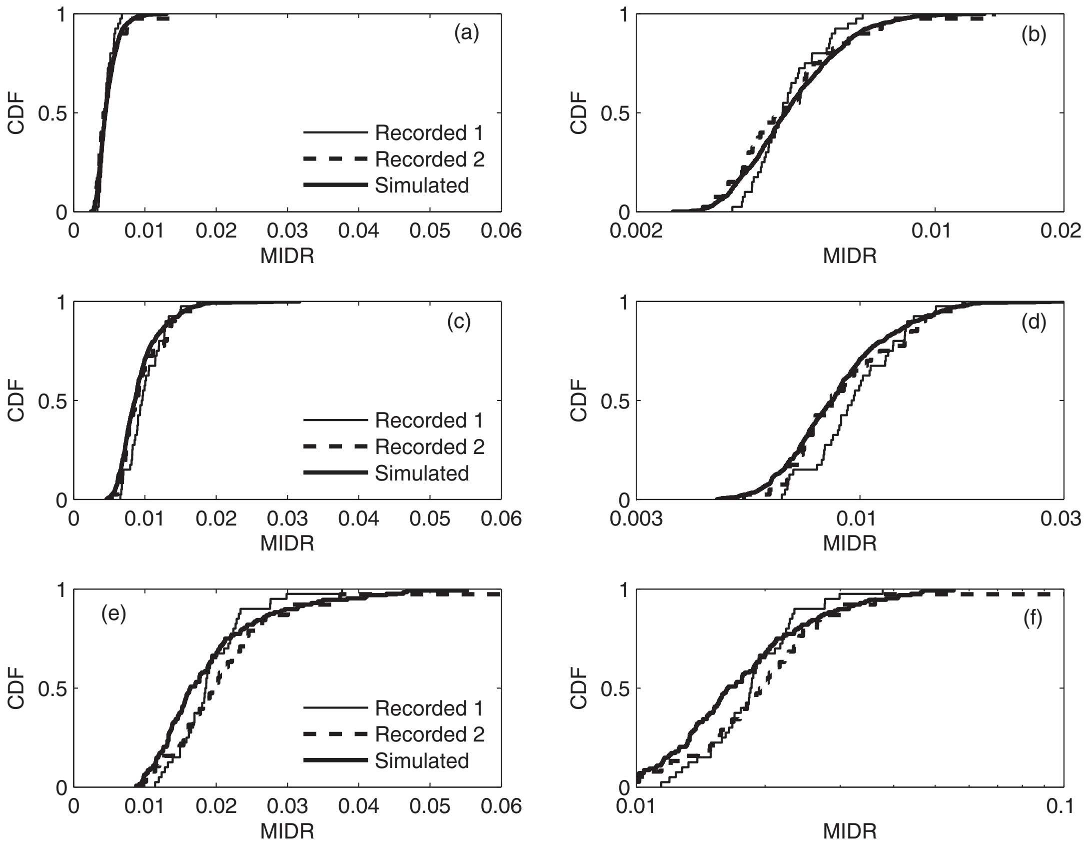

Figure 6.10: CDF of maximum inter-story drift ratio for 20-story building (a) $\varepsilon = 0$ on linear axis, (b) $\varepsilon = 0$ on logarithmic axis, (c) $\varepsilon = 1$ on linear axis, (d) $\varepsilon = 1$ on logarithmic axis, (e) $\varepsilon = 2$ on linear axis, (f) $\varepsilon = 2$ on logarithmic axis.

6.6.2 PFA results

The statistical characteristics of PFA are reported in Table 6.4 and the cumulative probabilities of PFA are shown in Figures 6.11 and 6.12 for the 4- and 20-story buildings, respectively. They indicate the same trend as the MIDR results in the previous section. The results from the Simulated set are close to those from the Recorded 2 set since the input ground motions of the Simulated set naturally satisfy the target dispersion of response spectra.

The difference of the probability distribution of Simulated and the Recorded 2 set in PFA are smaller than those of MIDR. PFA is controlled primarily by the short period components of the ground motions. This suggests that the short period components of the simulated ground motions are more similar to the recorded ground motions than their long period components.

Table 6.4: PFA from MDOF system

Building	ε	Median PFA			Dispersion of PFA		
		Recorded 1	Recorded 2	Simulated	Recorded 1	Recorded 2	Simulated
20-story	0	0.36	0.33	0.33	0.16	0.39	0.32
moment	1	0.39	0.38	0.37	0.14	0.37	0.32
frame	2	0.46	0.45	0.47	0.14	0.37	0.34
4-story	0	0.40	0.41	0.39	0.13	0.23	0.21
moment	1	0.45	0.50	0.46	0.15	0.25	0.21
frame	2	0.57	0.55	0.53	0.17	0.34	0.26

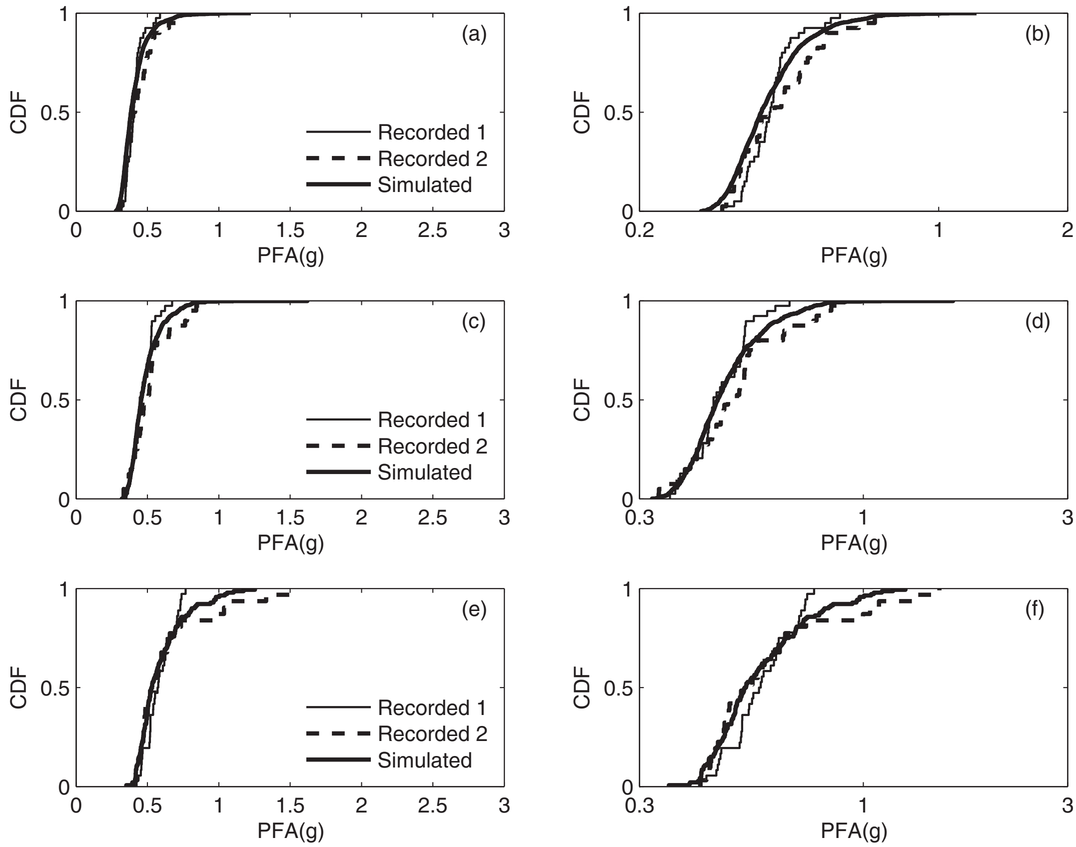

Figure 6.11: CDF of peak floor acceleration for 4-story building (a) $\varepsilon = 0$ on linear axis, (b) $\varepsilon = 0$ on logarithmic axis, (c) $\varepsilon = 1$ on linear axis, (d) $\varepsilon = 1$ on logarithmic axis, (e) $\varepsilon = 2$ on linear axis, (f) $\varepsilon = 2$ on logarithmic axis.

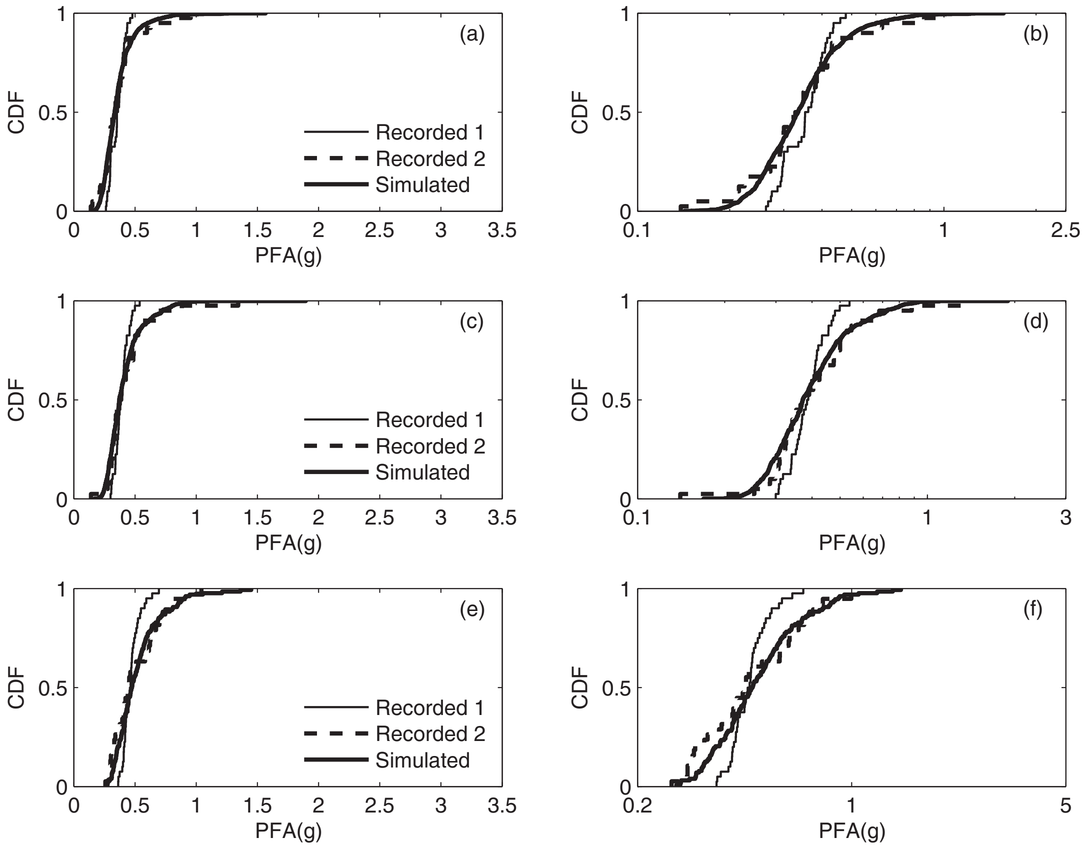

Figure 6.12: CDF of peak floor acceleration for 20-story building (a) $\varepsilon = 0$ on linear axis, (b) $\varepsilon = 0$ on logarithmic axis, (c) $\varepsilon = 1$ on linear axis, (d) $\varepsilon = 1$ on logarithmic axis, (e) $\varepsilon = 2$ on linear axis, (f) $\varepsilon = 2$ on logarithmic axis.

6.7 Conclusion

Nonlinear dynamic structural analysis was conducted for a single-degree-of-freedom oscillator, and for 4- and 20-story reinforced concrete moment frame buildings. These analyses were used to evaluate the effect of variations in input ground motions on resulting structural response metrics. Structural responses were quantified using ductility for the SDOF system, and maximum inter-story drift ratio (MIDR) and peak floor acceleration (PFA) for the multistory buildings.

Three types of input ground motions were used for the analysis: 1) recorded ground motions that were selected and scaled to match the conditional mean spectrum (CMS), 2) recorded ground motions that were selected and scaled to match the conditional spectrum (CS) which includes a mean and standard deviation of logarithmic spectral accelerations, 3) simulated ground motions that were selected to match the target $S_a(T_1)$. No criteria were used for selecting the simulated ground motions other than their match to the target $S_a(T_1)$. The recorded ground motions were selected to try to match appropriate ground motion properties for high amplitude $S_a(T_1)$, using conditional mean concepts; this was needed because the recorded motions were being scaled and their scaled properties would not necessarily be appropriate. The conditional mean spectrum concepts are believed to represent the best prediction of the spectra associated with ground motions having a given $S_a(T_1)$, so those ground motions (in particular, set #2) are used as a benchmark for evaluating the simulated motions.

The results presented in this chapter suggest that the probabilistic characteristics of ductility, MIDR, and PFA produced by the simulated ground motions reasonably match those of the selected and scaled recorded ground motions if the ground motions are selected and scaled to match the target mean and standard deviation of $\ln S_a$ as computed using Conditional Spectrum equations. Additionally, the spectral shapes of the simulated ground motions selected based on $S_a(T_1)$ are in very close agreement with predictions from CMS equations. This very close agreement arose in spite of some shortcomings in properties of the simulations at long periods, as was discussed in chapter 4, because discrepancies in variability and correlations of spectra from the simulations have offsetting effects in terms of the spectra associated with a a given $S_a(T_1)$ value. These analysis results suggest that the structural responses of the simulated ground motions generated by the proposed method produce structural responses that are comparable to responses from recorded ground motions having a given $S_a(T_1)$ value.

It should be noted that observations and conclusions are limited to results from only two multi-degree-of-freedom structures and some analysis of SDOF oscillators, and to only a limited set of ground motion scenarios. Full validation of these conclusions would require further testing, but this chapter has nonetheless described a procedure for doing such validations, and shown that the simulated ground motion results are reasonable in the limited cases considered.

Chapter 7

Simulation-based probabilistic seismic demand analysis

7.1 Abstract

The proposed stochastic ground motion model has been shown to produce ground motions with intensities similar to the ground motion prediction models (as measured using spectral accelerations, inelastic response spectra, durations, Arias intensities, and mean periods), and have also been shown to produce the similar probabilistic distributions of structural response in nonlinear multi-degree-of-freedom (MDOF) structural models to those produced by recorded ground motions. These features allow the simulation procedure to be used to evaluate the reliability of structures under uncertain earthquake shaking in a more direct manner than has previously been possible using only recorded ground motions. In this chapter, this direct reliability assessment is explored by simulating a large suite of potential ground motions as discussed in Chapter 5, and then using these simulations as inputs for nonlinear dynamic analysis a structure. The probability of the structure experiencing a drift or acceleration greater than some threshold can then be directly computed as the fraction of simulated ground motions that cause exceedance of this threshold.

Current approaches to estimate this structural reliability metric rely on more indirect methods, because fast and realistic simulation methods are not widely available, and because there aren't a sufficient number of recorded ground motions to enable construction

of large suites of all potential ground motions. Instead, the current methods generally use small sets of scaled recorded ground motions, with the response results weighted by a hazard curve for the site, but that approach requires a variety of assumptions regarding important properties of ground motions and the impacts of ground motion scaling. The approach proposed here facilitates examination of those assumptions and provides a variety of other relevant information not available from that traditional approach. In this chapter the proposed direct analysis approach will be described, utilized for a variety of example assessments, and the examples used to demonstrate the additional insights available from this approach. While the direct estimation approach may not be suitable for implementation in design practice due to the large number of required structural analyses, the insights it provides are valuable for understanding whether current procedures using recorded ground motions are appropriate (for example, questions as to whether the Conditional Mean Spectrum is an appropriate target for ground motion selection can be addressed more directly here than has previously been possible). This approach also provides a benchmark reliability result that can be used to evaluate whether current practices using much smaller numbers of ground motions are effective in accurately assessing the reliability of structures subject to earthquake shaking.

7.2 Introduction

Performance based earthquake engineering assessments potentially require a large number of input ground motions to evaluate the probability distributions of structural response engineering demand parameters (EDP). The number of recorded ground motions may not be sufficient to compute these probability distributions directly, so ground motion scaling and spectrum matching are widely used recently to overcome the shortage of the number of ground motion recordings. Simulated ground motions generated by the proposed stochastic model can be used for this problem since the characteristics of the simulated ground motions are consistent with those predicted by various types of GMPM (Chapter 4) and the structural responses produced by the simulated ground motions are consistent with those from the recorded ground motions in terms of ductility, maximum inter-story drift ratio (MIDR), and peak floor acceleration (PFA) (Chapter 6).

In this chapter, the probabilistic seismic demand analysis using the simulated ground motions (termed “simulation-based PSDA”) is proposed to directly compute the hazard curves of EDP. In the simulation-based PSDA, the hazard curve of any EDP can be computed by nonlinear dynamic structural response analysis using the simulated ground motions produced using Monte Carlo simulation (a procedure described in Chapter 5). Since only a few ground motions produce the large EDP values observed with the low exceedance rate, crude Monte Carlo simulation can be inefficient and so importance sampling is also employed to produce the simulated ground motions.

Simulation-based PSDA in general requires more structural response analyses than current procedures to compute the hazard curves for EDP (Bazzurro 1998, Shome et al. 1998). However, the simulation-based PSDA does not require the use of a ground motion intensity measure, scaling of ground motions, or assumptions regarding functional forms and probability distributions of EDP values. Also we can perform a deaggregation-like computation to determine the characteristics of the simulated ground motions that produce a given level of EDP, giving insights into ground motion properties that influence structural behavior and thus potentially informing procedures for selecting and scaling recorded ground motions. Thus, despite the procedure’s computational expense, it serves as a potentially useful alternate method of evaluating structural reliability.

Further, simulation-based PSDA can be extended to compute the rate of jointly exceeding specified thresholds for two or more EDP parameters–a calculation which is difficult to perform using recorded ground motions. To demonstrate, joint hazard contours (as opposed to hazard curves for a single parameter) of maximum inter-story drift ratio (MIDR) and peak floor acceleration (PFA) are produced. Various points on these contours are deaggregated to identify response spectra associated with each, and the relationship between spectral shape, MIDR and PFA are discussed.

7.3 Simulation-based probabilistic seismic demand analysis

In the simulation-based PSDA, the mean annual rate of some EDP exceeding z, denoted $\nu_{EDP}(z)$ is computed using Monte Carlo simulation and Importance Sampling as follows:

$$\nu_{EDP}(z) = \sum_i \nu_i \frac{1}{n} \sum_{j=1}^{n} I(EDP_j > z) \frac{f_i(m_j)}{k_i(m_j)} \tag{7.1}$$

$$I(EDP_j > z) = \begin{cases} 1 & EDP_j > z \\ 0 & \text{otherwise} \end{cases} \tag{7.2}$$

where n is a number of simulated ground motions, EDP_j is the jth realization of the engineering demand parameter value, I is as indicator function, $f_i(m_j)$ is a probability density function of magnitudes for source i evaluated at magnitude m_j, and the subscript j is the index indicating the simulated ground motion. The function $k_i(m_j)$ is a sampling distribution and $f_i(m_j)$ is a target distribution for importance sampling. This equation is the same as equation 5.11 except using EDP instead of S_d.

Here we employ maximum inter-story drift ratio (MIDR) and peak floor acceleration (PFA) as EDP, and compute ν_{EDP} for the example site described in Chapter 5. This site has a single nearby vertical strike-slip fault, with a characteristic distribution of magnitudes, hypocentral distance and rupture distance of $10km$, and $V_{S30} = 400m/s$. Ten thousand simulated ground motions are sampled with uniformly distributed magnitude (i.e., using importance sampling) and Equation 7.1 is applied to correct for this importance sampling using the characteristic distribution as the target distribution $f_i(m_j)$.

The above equations produce EDP hazard curves, and those curves can also be deaggregated to identify the distribution of ground motion parameters that produce a given EDP value. For example, we can compute a distribution of earthquake magnitudes associated with occurrence of a given EDP level as follows:

$$P(M=m|EDP=z) = \frac{\sum_{j=1}^{n} I(EDP_j=z, M_j=m)\frac{f_i(m)}{k_i(m)}}{\sum_{j=1}^{n} I(EDP_j=z)\frac{f_i(m_j)}{k_i(m_j)}} \tag{7.3}$$

$$I(EDP_j=z) = \begin{cases} 1 & EDP_j=z \\ 0 & \text{otherwise} \end{cases} \tag{7.4}$$

$$I(EDP_j=z, M_j=m) = \begin{cases} 1 & EDP_j=z, M_j=m \\ 0 & \text{otherwise} \end{cases} \tag{7.5}$$

Below we will also compute deaggregation results for Arias intensity, significant duration, and mean period by substituting any of these parameters for magnitude in the above equation.

7.4 Probabilistic seismic demand analysis

The EDP hazard curves for the 4- and 20-story buildings described in Section 6.3 are computed using equation 7.1 for the example site described above. The hazard curves for MIDR and PFA are shown in Figures 7.1 and 7.2, respectively. The hazard curve for PGA is also shown in Figure 7.2. The annual exceedance rates for a given MIDR are higher for the 4-story building than for the 20-story building, and the horizontal tails are associated with the probabilities of collapse. The rates of exceedance of a given PFA are also higher for the 4-story building than for the 20-story building. The hazard curves for PFA of both buildings are higher than that for PGA of high annual rates of exceedance ($>$ 10% in 50 years). As low annual rates of exceedance ($\leq$ 10% in 50 years), the hazard curves of both buildings are close to that of PGA, since PFAs occur on the first floor and are close to PGA when the building experiences strong nonlinear behavior Aslani and Miranda (2005).

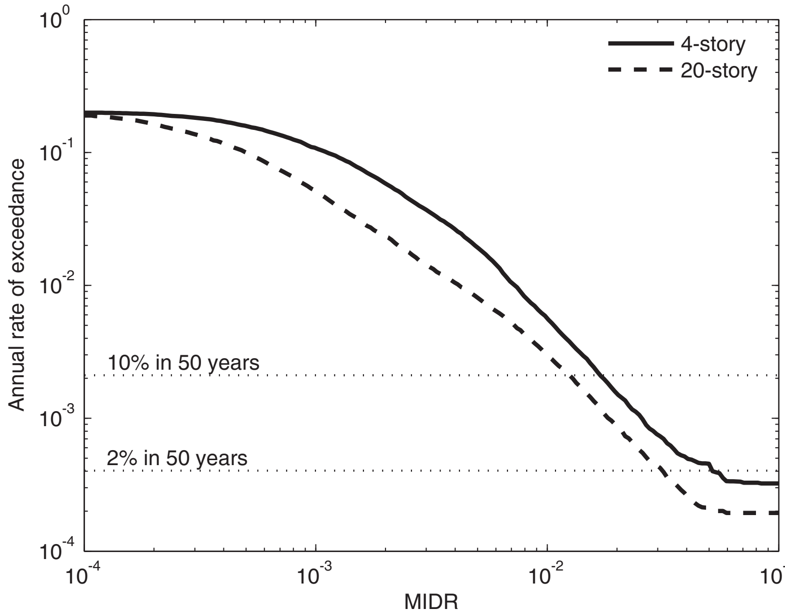

Figure 7.1: Hazard curves for MIDR using simulated ground motions, for the example site and the two example buildings.

7.4.1 Hazard curve of PFA

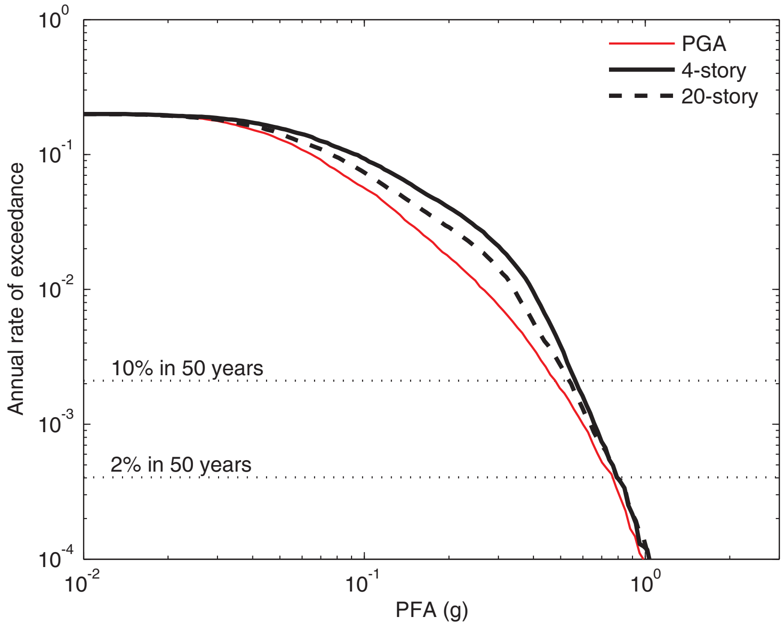

Figure 7.2: Hazard curves for PFA using simulated ground motions, for the example site and the two example buildings.

7.5 Drift hazard deaggregation results

7.5.1 Moment magnitude given MIDR or PFA

Figures 7.3 and 7.4 show the deaggregation of mganitude given MIDR for the 4- and 20-story buildings, respectively, and Figures 7.5 and 7.6 show the deaggregation of M given PFA for the 4- and 20-story buildings respectively. The deaggregations are computed for two exceedance probabilities: 10% in 50 years, and 2% in 50 years.

The magnitudes clearly vary somewhat depending upon the EDP parameter of interest and the response level associated with the target probability of exceedance. The MIDRs and PFAs with lower exceedance probabilities tend to be caused by ground motions with larger magnitudes.

In all of these figures, the histograms indicate low-resolution predictions at low magnitudes. This is most evident in Figures 7.4(b) and 7.5(b) where there are large spikes in probability at some low magnitudes. It is also apparent to a lesser degree in Figure 7.3(a). This low resolution is an artifact of the Importance Sampling approach used here. Rather than use a crude Monte Carlo simulation of the ground motions (which would have produced many small-magnitude motions), a uniform Importance Sampling distribution was used (which produced relatively more large-magnitude motions) and the simulations were then weighted to readjust for this sampling distribution, as discussed earlier. This approach produces much better resolution in predictions of the rate of exceeding large EDP values (since the suite of simulated motions contains more large-magnitude motions), but at the expense of having few small-magnitude motions. Further, the few small-magnitude motions receive large weights in equations 7.1 and 7.3, so in the few cases that a small-magnitude motion produces a large MIDR or PFA, it shows up as a large probability spike in the figures below. These spikes would be smoothed out if a larger set of simulated motions was used, or if the importance sampling distribution was adjusted. This low resolution result suggests that further work could be done to refine the simulation procedure (using either more simulations or a different sampling distribution) if deaggregation results are of interest.

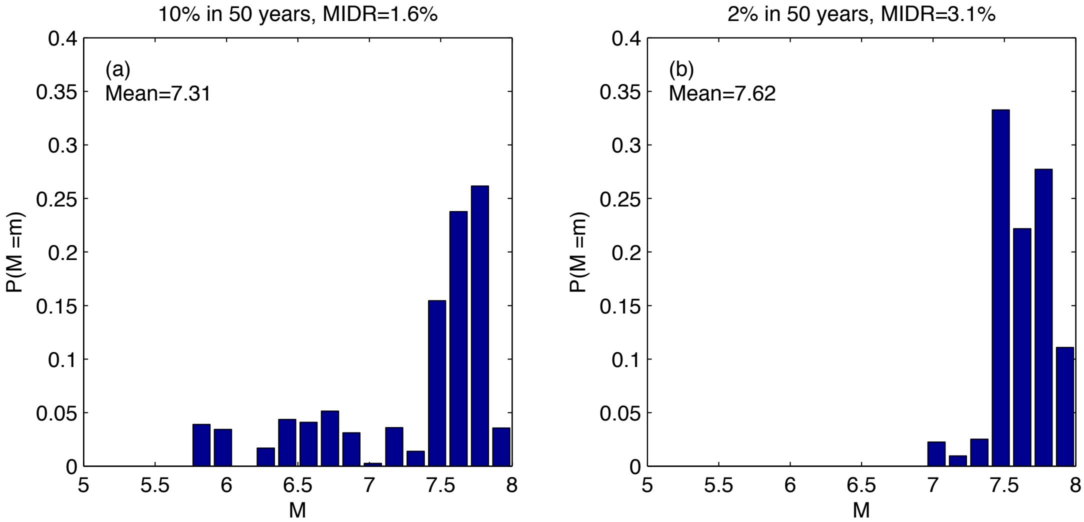

Figure 7.3: Probability distribution of M given MIDR with a specified probability of exceedance for the 4-story building at the example site (a) MIDR with 10% probability of exceedance in 50 years, (b) MIDR with 2% probability of exceedance in 50 years. Mean values of the magnitude distributions are noted in text in each subfigure.

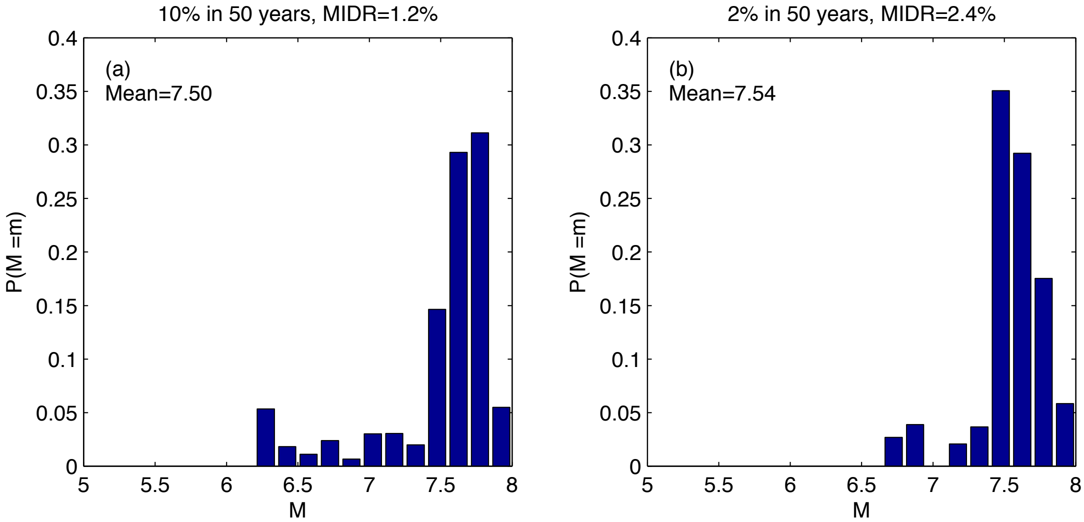

Figure 7.4: Probability distribution of M given MIDR with a specified probability of exceedance for the 20-story building at the example site (a) MIDR with 10% probability of exceedance in 50 years, (b) MIDR with 2% probability of exceedance in 50 years. Mean values of the magnitude distributions are noted in text in each subfigure.

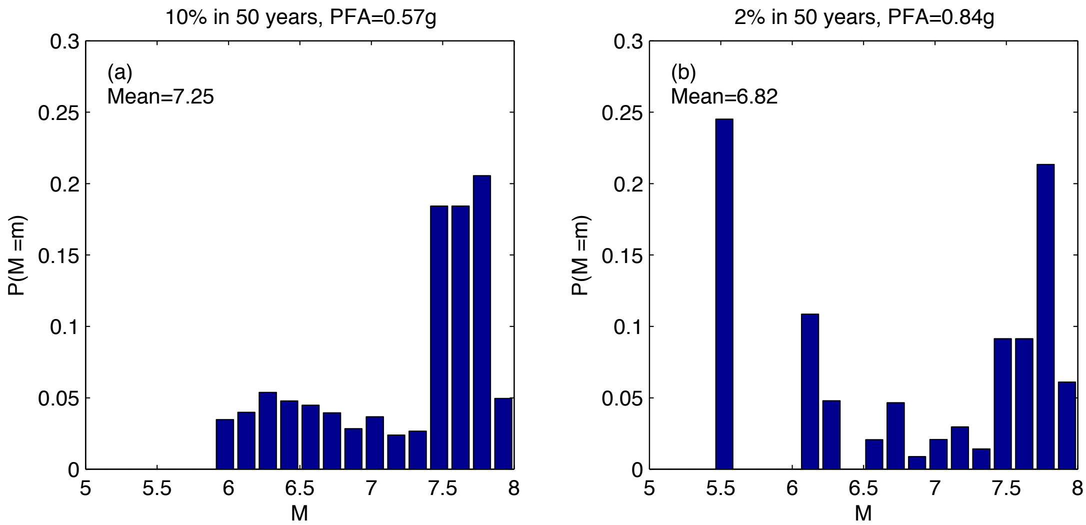

Figure 7.5: Probability distribution of M given PFA with a specified probability of exceedance for the 4-story building at the example site (a) PFA with 10% probability of exceedance in 50 years, (b) PFA with 2% probability of exceedance in 50 years. Mean values of the magnitude distributions are noted in text in each subfigure.

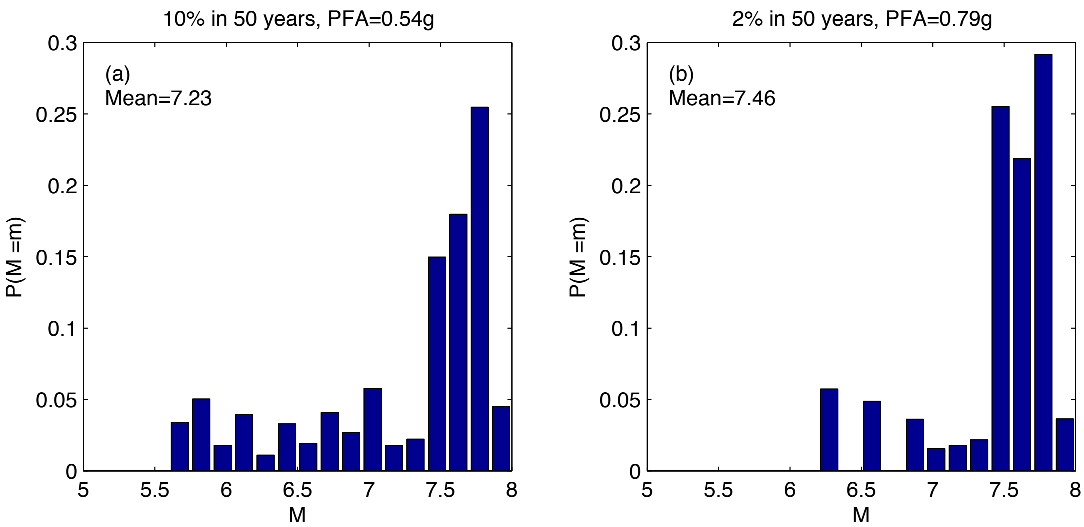

Figure 7.6: Probability distribution of M given PFA with a specified probability of exceedance for the 20-story building at the example site (a) PFA with 10% probability of exceedance in 50 years, (b) PFA with 2% probability of exceedance in 50 years. Mean values of the magnitude distributions are noted in text in each subfigure.

Figures 7.7 and 7.8 show the mean values of the conditional M distributions as a function of MIDR or PFA level. In both cases the conditional mean magnitudes is strongly dependent on the response level of interest, with the small frequent EDP occurrences being caused primarily by the frequent small-magnitude earthquakes, and occurrences of large EDP values being caused only by the large-magnitude earthquake ground motions. The maximum magnitudes for both buildings saturate at the maximum possible magnitude of earthquakes possible at the site (7.9 in this example). The trends for both buildings are similar, and this trend is consistent with widely observed general trends in magnitude deaggregation from ground motion hazard analysis (comparable results for drift hazard analysis are not widely reported since this is a difficult result to obtain when using recorded ground motions, but the observed trend is not surprising).

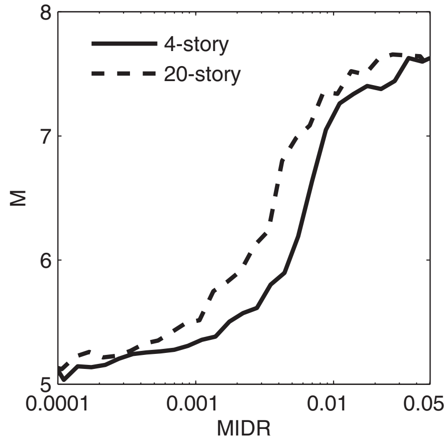

Figure 7.7: Mean *M* from deaggregations on MIDR for the two buildings at the example site.

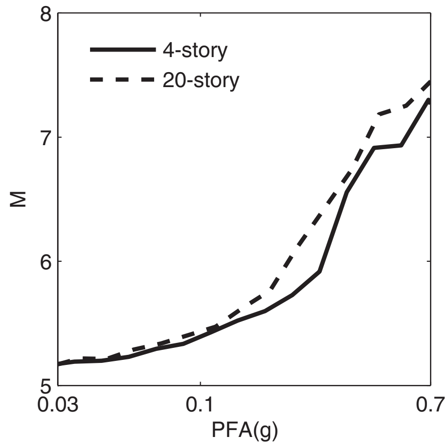

Figure 7.8: Mean *M* from deaggregations on PFA for the two buildings at the example site.

7.5.2 Arias intensity

Next deaggregation results for Arias intensity are computed. The Arias intensity for a given ground motion (I_a, Arias 1970) is defined as follows:

$$I_a = \frac{\pi}{2g} \int_0^\infty \{x(t)\}^2 \tag{7.6}$$

where $x(t)$ is the ground motion's acceleration time series and g is acceleration of gravity $981 cm/s^2$. This is one potential measure of total input energy in a ground motion. The deaggregation result is computed using Equation 7.3, but substituting I_a for M in those equations. Figures 7.9 and 7.10 show the mean values of the conditional I_a distributions as a function of MIDR or PFA level. The I_a saturates for both buildings at the maximum I_a observed in any of the input ground motions.

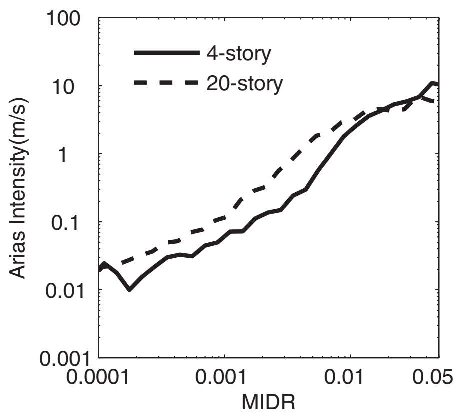

Figure 7.9: Mean Arias intensity from deaggregations on MIDR for the two buildings at the example site.

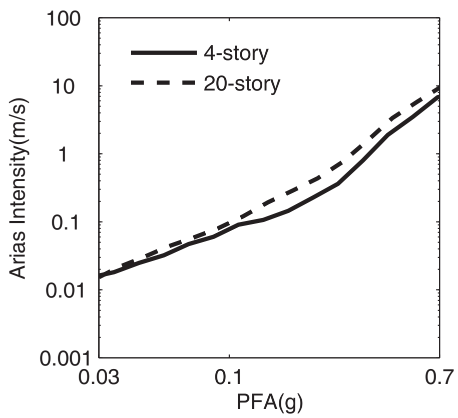

Figure 7.10: Mean Arias intensity from deaggregations on MIDR for the two buildings at the example site.

7.5.3 Significant duration

The $5-95\%$ significant duration (Trifunac and Brady 1975), denoted t_{95-5}, is the duration of the ground motion that contains 90% of its total energy. It is defined by the upper limit of the first integral in the following equations:

$$\frac{\int_{t_5}^{t_5+t_{95-5}} |x(t)|^2 \, dt}{E_{acc}} = 0.9, \; \frac{\int_0^{t_5} |x(t)|^2 \, dt}{E_{acc}} = 0.05 \tag{7.7}$$

where E_{acc} is the total energy of the time series and $x(t)$ is the ground motion's acceleration time series.

Figures 7.11 and 7.12 show mean values of t_{95-5} from deaggregations given a specified MIDR or PFA. The mean values of t_{95-5} given MIDR are increasing with increasing MIDR, suggesting that there is a duration dependence of the structural responses (i.e., large MIDR is more likely to be caused by input ground motions with long duration). PFA shows no dependence on t_{95-5} in small PFA; however, it shows a litlle dependence in large PFA.

Ground motion duration is correlated with the causal earthquake magnitude, however, so another potential explanation is that the trend in duration given MIDR is reflecting the trend in magnitude deaggregation given MIDR, and the magnitude dependence indicates either a relationship with overall ground motion intensity, or a relationship with response spectral shape.

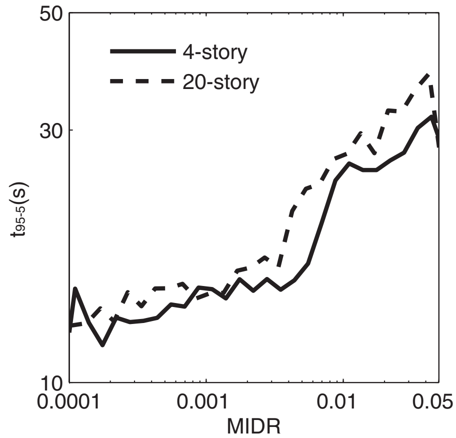

Figure 7.11: Mean significant duration intensity given MIDR for an example site.

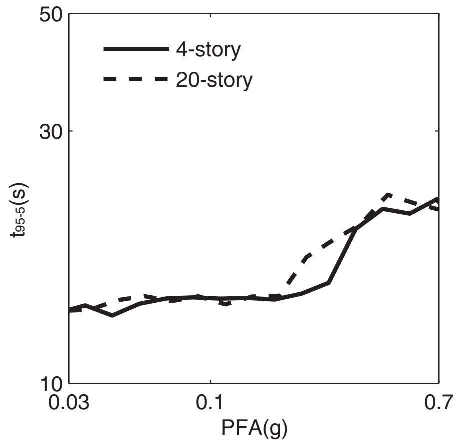

Figure 7.12: Mean significant duration intensity given PFA for an example site.

7.5.4 Mean period

Mean period (T_m) is defined by Rathje et al. (2004) as follows:

$$T_m = \frac{\sum_i \frac{C_i^2}{f_i}}{\sum_i C_i^2} \tag{7.8}$$

where f_i is frequency i, C_i is the Fourier amplitude of the ground motion at that frequency and $0.25 \leq f_i \leq 20Hz$ with $\Delta f \leq 0.05Hz$. This parameter is of potential interest here because Rathje et al. (2004) found it to influence site response and Kumar et al. (2011) found that it influences MIDR in structural analysis.

Figures 7.13 and 7.14 show mean values of the deaggregation distributions of T_m for a given MIDR or PFA level and for a given structure. The mean values of T_m given MIDR monotonically increase with MIDR for both structures. This is because for both structures typical T_m values are shorter than the first mode periods (T_1) of the structures, so as T_m gets larger the energy in the ground motion is more centered near T_1 and larger MIDR values tend to result. The mean value of T_m given PFA varies with PFA because of the same reason as T_m given MIDR. This trend stops when PFA is greater than 0.3g, however, because PFAs of buildings with strong nonlinear behavior are close to PGA regardless of the value of T_m.

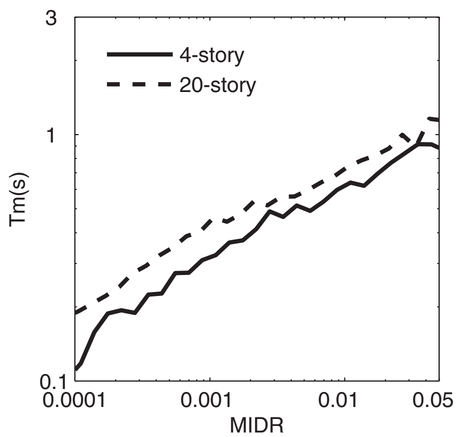

Figure 7.13: Mean period intensity given MIDR for an example site.

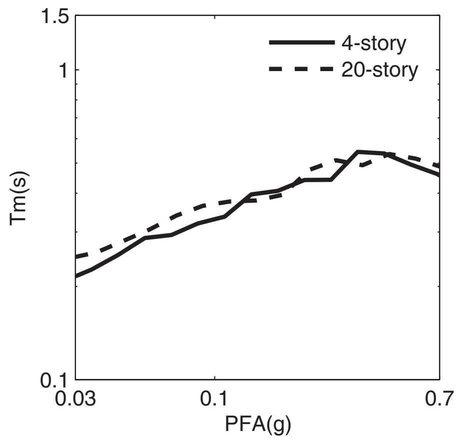

Figure 7.14: Mean period intensity given PFA for an example site.

7.5.5 Response spectra for a given MIDR

In addition to measuring the properties of a single ground motion parameter conditioned on a given EDP level, it is possible to study patterns in overall response spectra from the ground motions that produce a given EDP level. Response spectra conditioned on a given MIDR are shown in Figures 7.15, 7.16, 7.17, and 7.18, for exceedance probabilities of 10% and 2% in 50 years, and for the 4- and 20-story buildings, respectively. The spectra of all ground motions producing the target MIDR are plotted, along with the median and median +/- one standard deviation of the spectra. The modal periods of the buildings are also noted on each figure, along with two periods longer than the first model period that will serve as useful references.

We can study these figures to identify the properties of these response spectra that seem to be predictive of the resulting MIDR. For the 4-story building with 10% in 50 years MIDR (Figure 7.15), the variation in response spectra is lowest for periods between T_1 to $2T_1$. Response spectra at T_1 are known to be good predictors of resulting MIDR in first-mode dominated structures such as this four-story structure. The spectra at longer periods show small variability also, presumably because the structure is responding nonlinearly and its "effective period" has lengthened somewhat, making spectra at these longer periods also useful predictors of structural response. The spectra conditioned on MIDR with 2%

probability of exceedance in 50 years (Figure 7.16) show similar patterns, although the pinched spectra now extend from T_1 out to $3T_1$, likely due to additional period lengthening at this higher response level. In both of these figures the response spectra are widely varying at the 2nd and 3rd model periods (denoted T_2 and T_3 in the figures), even though the MIDR level is nearly identical in each case. This suggests that higher mode excitations are not significantly influencing MIDR values, consistent with our expectation that MIDR values in this structure are first-mode dominated.

As we make these observations, and other similar observations below, it is worth recalling that no assumptions were made a priori regarding the properties of ground motions influencing structural response, because no ground motions were pre-selected or scaled to match target intensity measure values. We simply analyze the large suite of simulated ground motions and study the properties of whatever simulated motions happened to produce large EDP values. The lack of required prior assumptions makes these results unique and interesting.

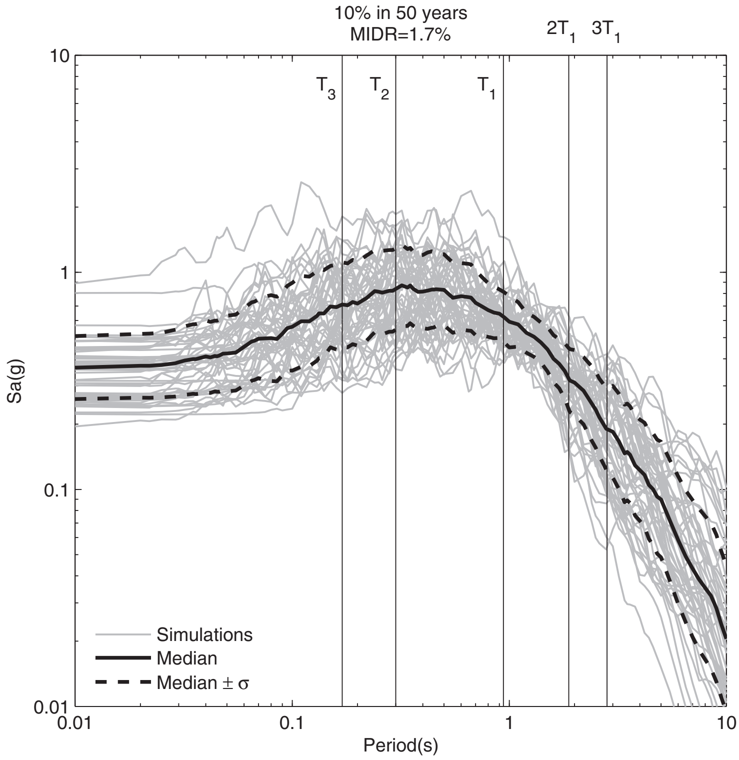

Figure 7.15: Response spectra of ground motions causing an MIDR in the 4-story building that has a 10% probability of exceedance in 50 years. Vertical lines on the plot indicate several periods of interest, denoted as follows: T1 = first mode period 0.94s, T2 = second mode period 0.3s, T3 = third mode period 0.17s.

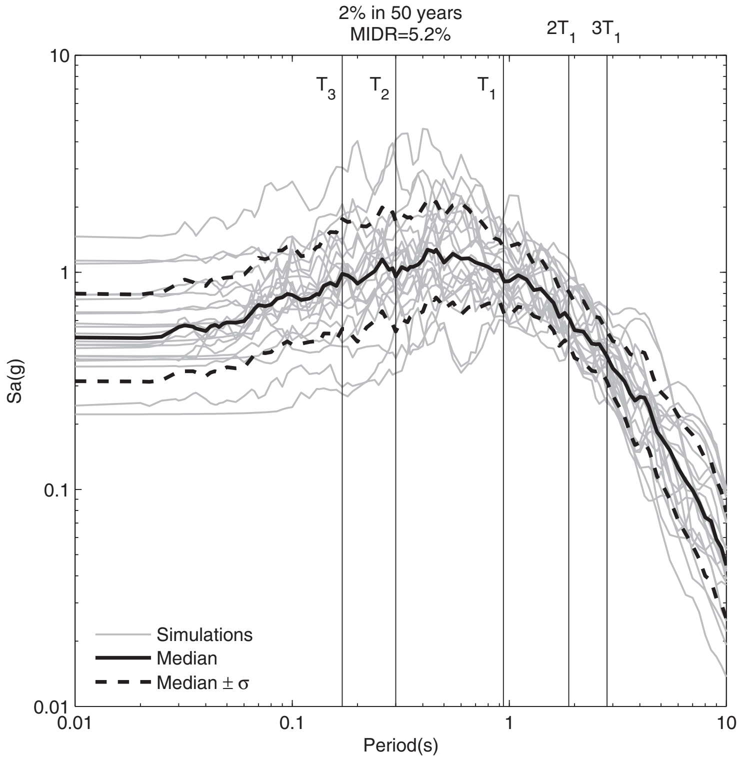

Figure 7.16: Response spectra of ground motions causing an MIDR in the 4-story building that has a 2% probability of exceedance in 50 years. Vertical lines on the plot indicate several periods of interest, denoted as follows: T1 = first mode period 0.94s, T2 = second mode period 0.3s, T3 = third mode period 0.17s.

Looking at similar results for the 20-story building in Figures 7.17 and 7.18, in the case of the lower MIDR (that associated with 10% in 50 years exceedance probability), the associated response spectra are narrowest around T_1. But both longer and shorter periods are also slightly pinched, indicating some effect of both nonlinear period lengthening and the contribution of the higher modes. For the MIDR associated with 2% probability of exceedance in 50 years, the response spectra are relatively narrower between T_1 and $3T_1$ because of increased nonlinearity in these responses.

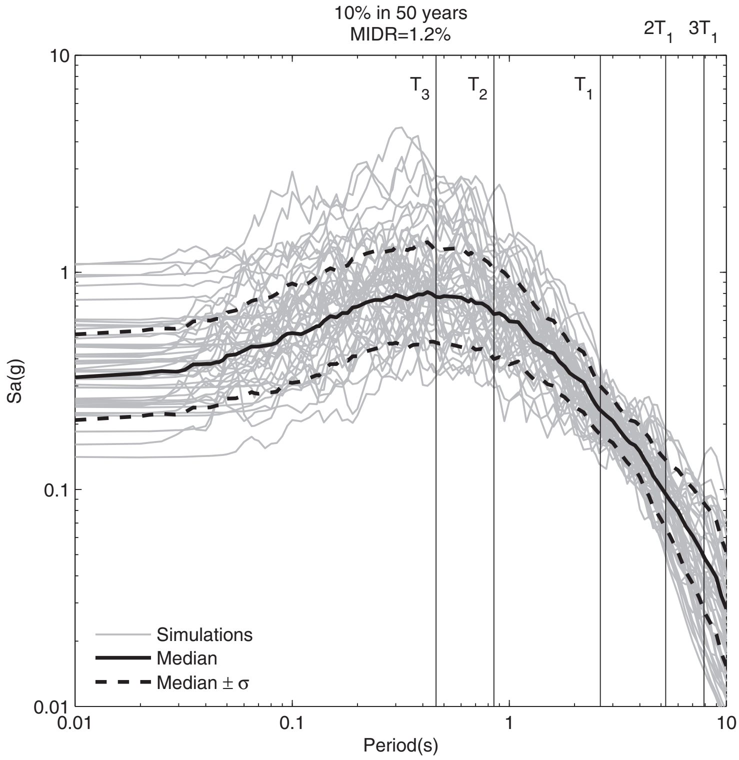

Figure 7.17: Response spectra of ground motions causing an MIDR in the 20-story building that has a 10% probability of exceedance in 50 years. Vertical lines on the plot indicate several periods of interest, denoted as follows: T1 = first mode period 2.63s, T2 = second mode period 0.85s, T3 = third mode period 0.46s.

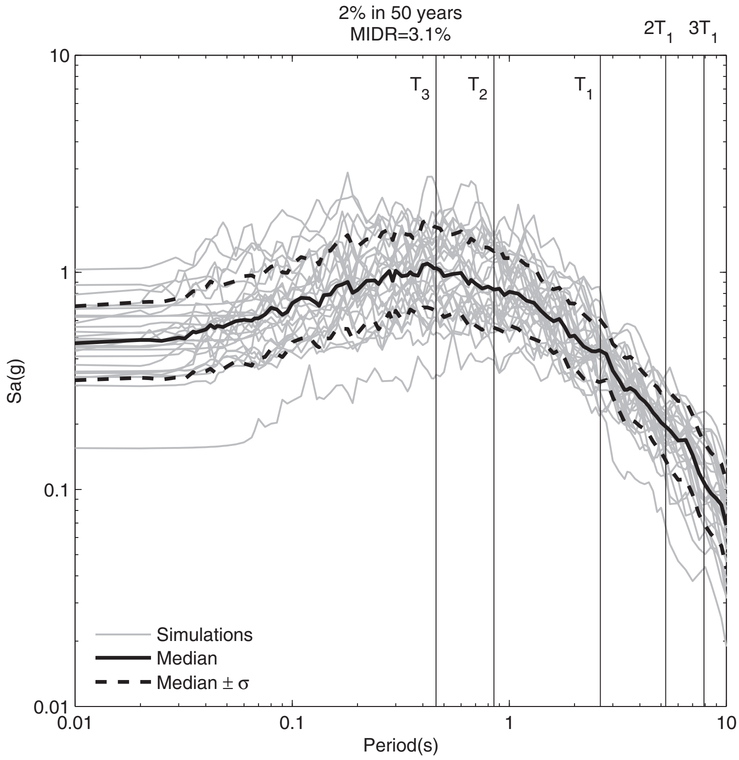

Figure 7.18: Response spectra of ground motions causing an MIDR in the 20-story building that has a 5% probability of exceedance in 50 years. Vertical lines on the plot indicate several periods of interest, denoted as follows: T1 = first mode period 2.63s, T2 = second mode period 0.85s, T3 = third mode period 0.46s.

7.5.6 Response spectra for a given PFA

Response spectra associated with a given PFA are shown in Figures 7.19, 7.20, 7.21, and 7.22, for 10% and 2% probabilities of exceedance in 50 years for the 4-story building and 10% and 2% probabilities of exceedance in 50 years for the 20-story building, respectively.

These figures look remarkably different from the figures in the prior section that were conditioned on MIDR. In every case, the variability in response spectra is very small at short periods, and quite large at longer periods. This suggests that S_a at short periods (or *PGA*) is the strongest predictor of PFA values (Taghavi and Miranda 2003) and the influence of higher mode is relatively larger than those in MIDR. This is expected from other studies of peak floor accelerations in buildings, but these results are a useful check of that intuition using the newly proposed approach.

Figure 7.22 shows a few simulated ground motions with small S_a at $T > T_3$; however, these ground motions have relatively larger S_a at $T < T_3$ where the relationship with PFA is strongest, and so the resulting PFA is the same as for the other simulated ground motions in this figure.

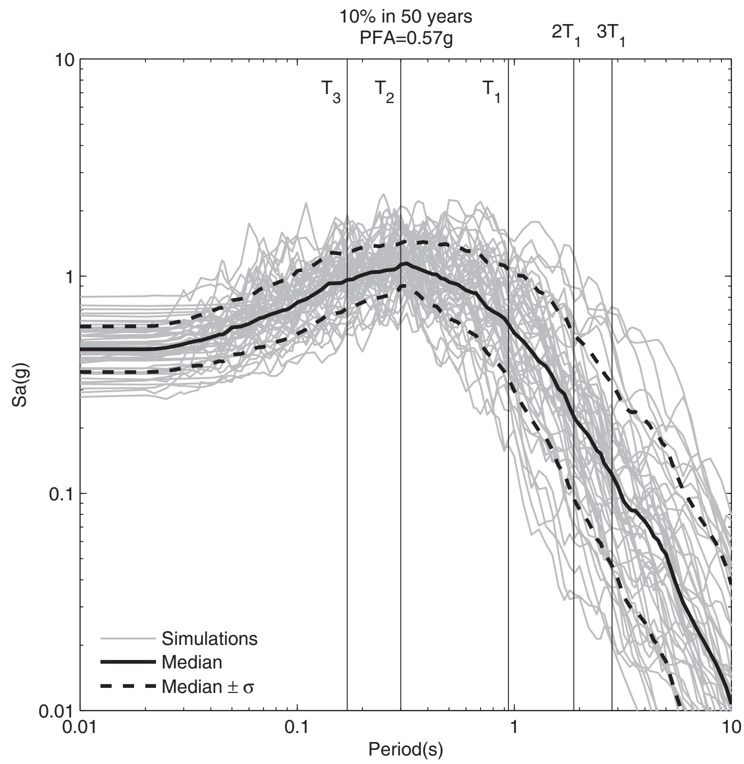

Figure 7.19: Response spectra of ground motions causing an PFA in the 4-story building that has a 10% probability of exceedance in 50 years. Vertical lines on the plot indicate several periods of interest, denoted as follows: T1 = first mode period 0.94s, T2 = second mode period 0.3s, T3 = third mode period 0.17s.

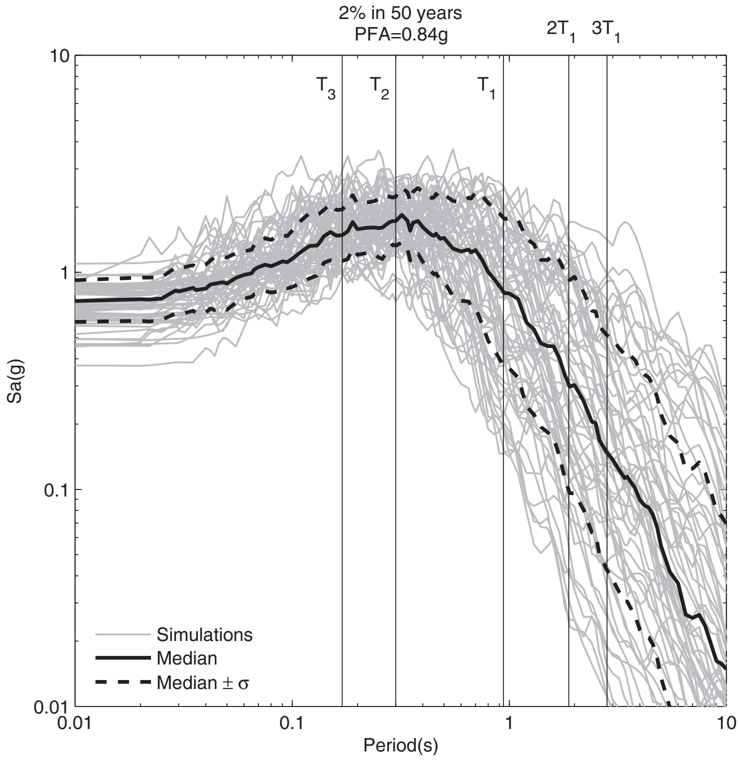

Figure 7.20: Response spectra of ground motions causing an PFA in the 4-story building that has a 2% probability of exceedance in 50 years. Vertical lines on the plot indicate several periods of interest, denoted as follows: T1 = first mode period 0.94s, T2 = second mode period 0.3s, T3 = third mode period 0.17s.

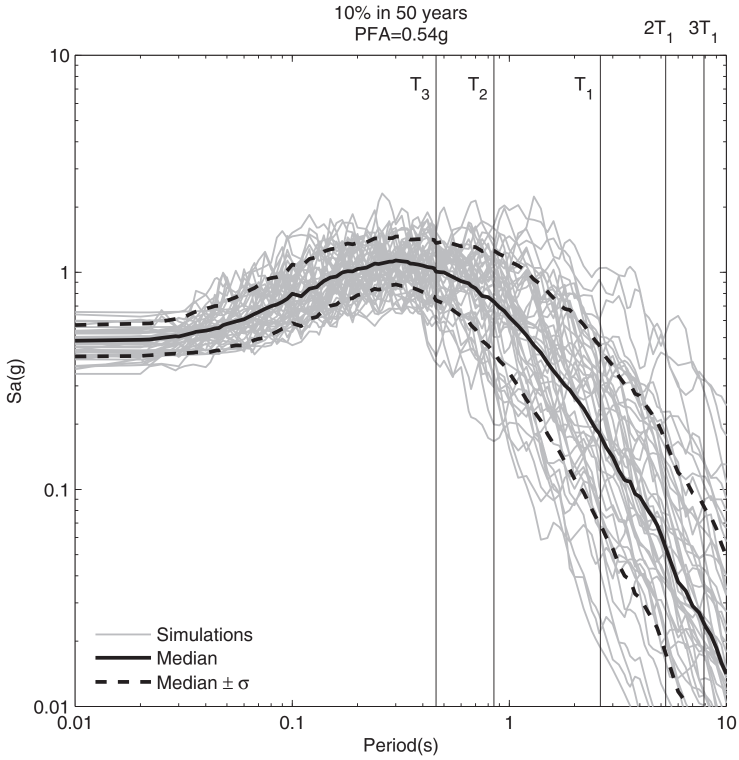

Figure 7.21: Response spectra of ground motions causing an PFA in the 20-story building that has a 10% probability of exceedance in 50 years. Vertical lines on the plot indicate several periods of interest, denoted as follows: T1 = first mode period 2.63s, T2 = second mode period 0.85s, T3 = third mode period 0.46s.

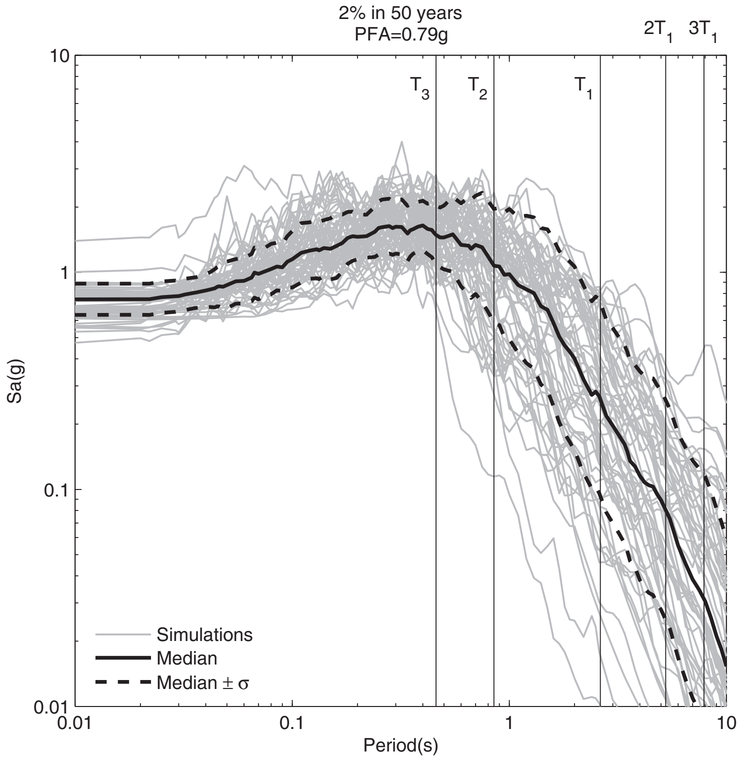

Figure 7.22: Response spectra of ground motions causing an PFA in the 20-story building that has a 2% probability of exceedance in 50 years. Vertical lines on the plot indicate several periods of interest, denoted as follows: T1 = first mode period 2.63s, T2 = second mode period 0.85s, T3 = third mode period 0.46s.

7.6 Hazard analysis for joint exceedances of multiple EDP parameters

To assess the performance of a structure while considering impacts of both MIDR and PFA (or any other vector of EDP parameters), it may be of interest to compute the joint behavior of these vectors of parameters, for instance by computing the rate of simultaneously exceeding both a given MIDR and a given PFA. Since simulation-based PSDA implicitly maintains the relationship between any EDPs of interest via the large set of simulated responses, joint hazard analysis for multiple EDPs can also be computed using this simulation-based method. This section will demonstrate these calculations for MIDR and PFA. Also, the properties of ground motions that produce large values of both EDP parameters will be studied. The joint hazard computation is performed as follows:

$$\nu_{EDP_1,EDP_2}(z_1,z_2) = \sum_i \nu_i \frac{1}{n} \sum_{j=1}^{n} I(EDP_{j,1} > z_1, EDP_{j,2} > z_2) \frac{f_i(m_j)}{k_i(m_j)} \quad (7.9)$$

$$I(EDP_{j,1} > z_1, EDP_{j,2} > z_2) = \begin{cases} 1 & EDP_{j,1} > z_1, EDP_{j,2} > z_2 \\ 0 & \text{otherwise} \end{cases} \quad (7.10)$$

And the deaggregation computation is performed as follows:

$$P(M = m \mid EDP_1 = z_1, EDP_2 = z_2) = \frac{\sum_{j=1}^{n} I(EDP_{j,1} = z_1, EDP_{j,2} = z_2, M_j = m) \frac{f_i(m)}{k_i(m)}}{\sum_{j=1}^{n} I(EDP_{j,1} = z_1, EDP_{j,2} = z_2) \frac{f_i(m_j)}{k_i(m_j)}} \quad (7.11)$$

$$I(EDP_{j,1} = z_1, EDP_{j,2} = z_2) = \begin{cases} 1 & EDP_{j,1} = z_1, EDP_{j,2} = z_2 \\ 0 & \text{otherwise} \end{cases} \quad (7.12)$$

$$I(EDP_{j,1} = z_1, EDP_{j,2} = z_2, M_j = m) = \begin{cases} 1 & EDP_{j,1} = z_1, EDP_{j,2} = z_2, M_j = m \\ 0 & \text{otherwise} \end{cases} \quad (7.13)$$

These are very similar to the equations introduced earlier in these chapters, but replace the previous indicator functions with indicator functions that check multiple EDP parameters. Using these equations, we will perform several example calculations in the following subsections.

Figures 7.23 and 7.24 show contours of rates of simultaneous exceedance of MIDR and PFA for the 4- and 20-story buildings, respectively. Points on the plot indicate results from individual ground motions, and the lines indicate contours of constant joint exceedance rate. Exceedance rates corresponding to 2% and 10% probabilities of exceedance in 50 years are highlighted. We see from the scatter plots of analysis results that the MIDR and PFA values from a given ground motion are correlated, but not perfectly correlated.

Figure 7.23 indicates the saturation of PFA in high MIDR since MIDR increases to infinity when the structure collapses (Figure 7.1), while PFA saturates to PGA (Figure 7.2) under strong nonlinear behavior. For the 4-story building, the PFA is observed to be truncated at some lower bound. This is caused by the 4-story building that have little higher mode contribution. For 20-story building, there is no sharp lower bound on the PFAs for a given MIDR. For both buildings, the correlation between PFA and MIDR is changed where MIDR is around 0.007 because these buildings yield at approximately this point.

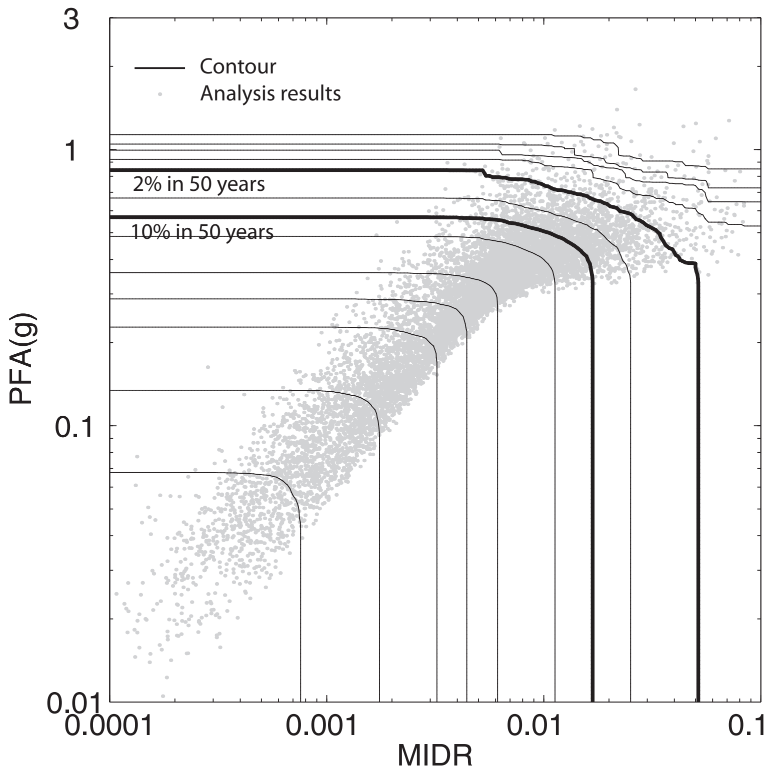

Figure 7.23: Hazard contours for joint EDP (MIDR and PFA) for 4-story building.

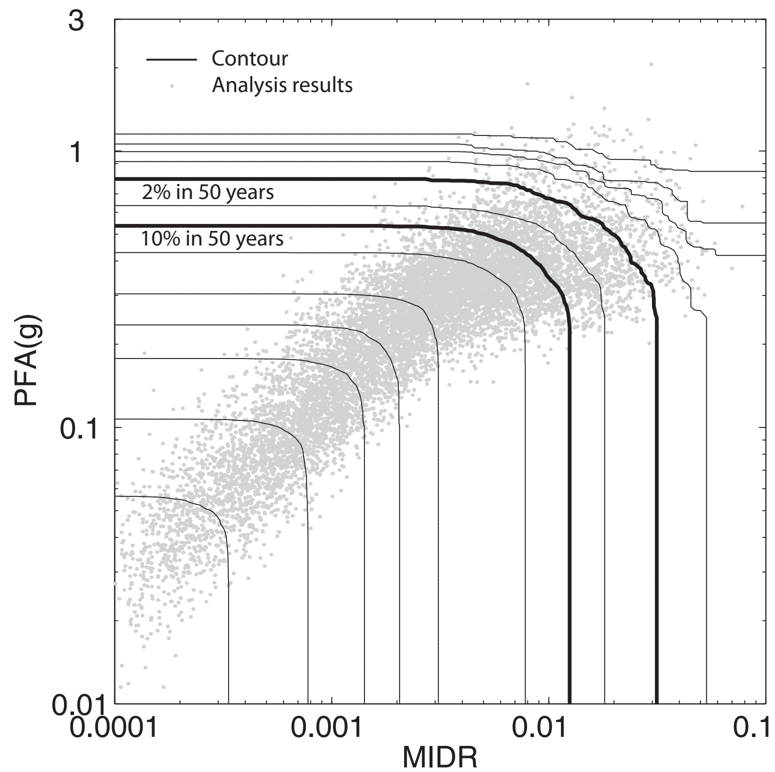

Figure 7.24: Hazard contour of joint EDP (MIDR and PFA) for 20-story building.

Figures 7.25, 7.26, 7.27, and 7.28 show probability distributions for the magnitudes, Arias intensities, significant durations, and mean periods that produce specific EDP values in the 20-story building. The EDP values of interest are combinations of MIDR and PFA that are jointly exceeded with 10% probability in 50 years. There are multiple combinations of MIDR and PFA that satisfy this criteria, so we examine three combinations (which are noted in the figures): the PFA that is exceeded with 10% probability in 50 years, plus whatever MIDR is associated with those large PFAs (box a in the figure), the MIDR exceeded with 10% probability in 50 years, plus whatever PFA is associated with those large MIDRs (box c in the figures), or combinations of MIDR and PFA that are both large, and are jointly exceeded with 10% probability in 50 years (box b in the figures).

Figure 7.25 shows the median magnitude associated with large PFA is similar to the results in Figure 7.8 and those of other cases are similar to the results in Figure 7.7. It suggest that magnitude cannot be determined by the only MIDR or PFA. The Arias intensities have the same trend as the magnitudes. However, the significant durations and the mean periods have the trends different from the magnitudes and Arias intensities. They vary only with MIDR, because MIDR has stronger correlation with the significant durations and the mean periods than PFA.

Looking at these four figures, we see two overall trends. First, the large MIDRs are caused by ground motions with large magnitude, long duration, and long mean period. Second, the large PFAs are caused by ground motions with relatively smaller magnitude, shorter duration, and smaller mean period. The Arias intensity distributions do not seem to vary significantly depending upon the EDP case. These variations in properties exist even though every case is conditioned on EDP values with 10% exceedance probability in 50 years. This suggests that there isn't a ground motion type that will universally produce all EDP values with a target exceedance probability, but rather that the important ground motion properties depend on the EDP parameters of interest (Taghavi and Miranda 2003). These types of comparisons are readily performed using this simulation-based PSDA approach, facilitating the study of questions such as this that are difficult to consider when using limited sets of recorded ground motions that require scaling.

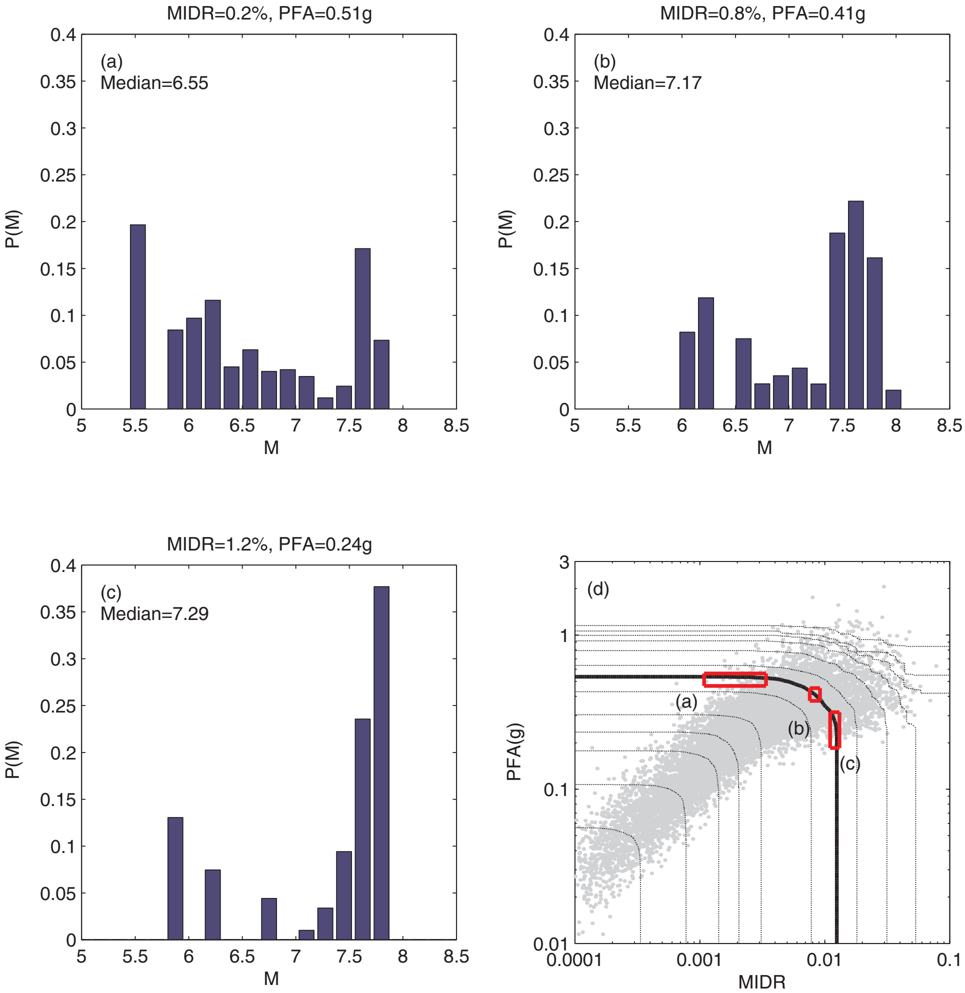

Figure 7.25: Probability distributions of magnitude given MIDR and PFA with 10% exceedance probability in 50 years for the 20-story building (a) MIDR=0.002 and PFA=0.51g, (b) MIDR=0.008 and PFA=0.41g, (c) MIDR=0.012 and PFA=0.24g, and (d) joint hazard contour of MIDR and PFA indicating the regions being studied.

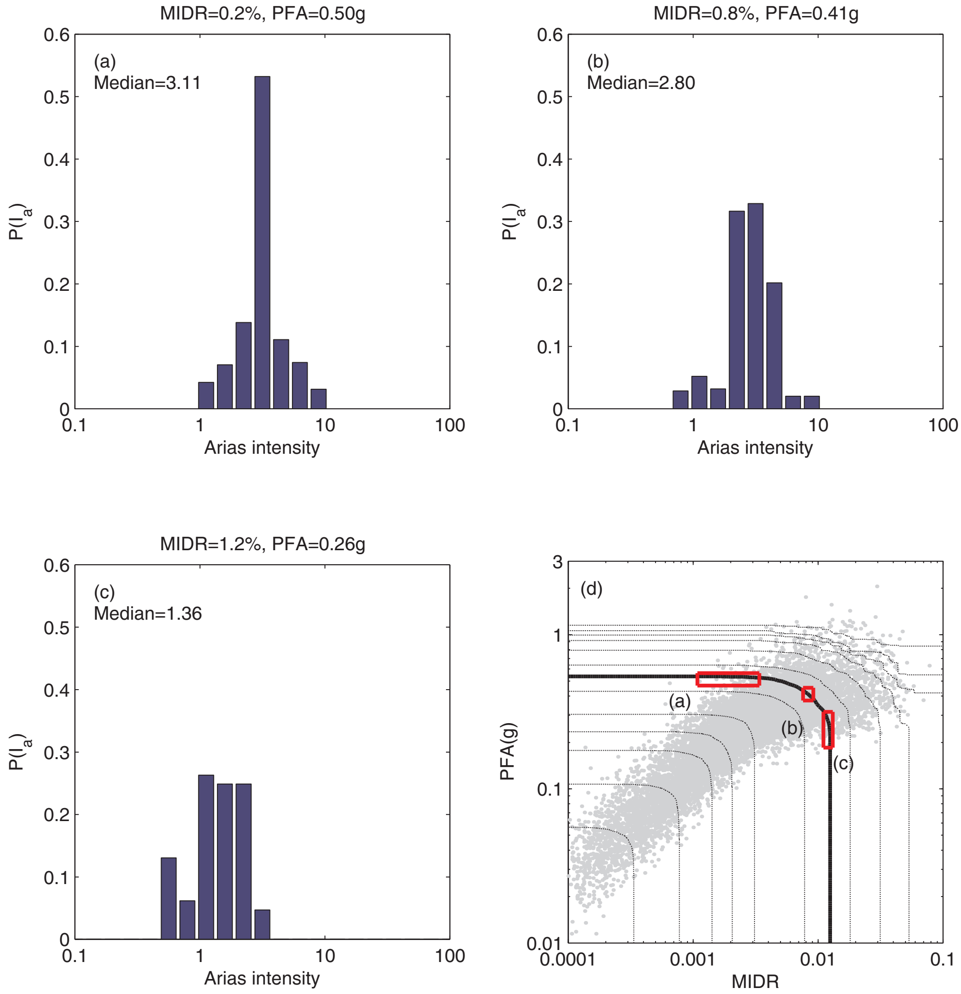

Figure 7.26: Probability distributions of Arias intensity given MIDR and PFA with 10% exceedance probability in 50 years for the 20-story building (a) MIDR=0.002 and PFA=0.51g, (b) MIDR=0.008 and PFA=0.41g, (c) MIDR=0.012 and PFA=0.24g, and (d) joint hazard contour of MIDR and PFA indicating the regions being studied.

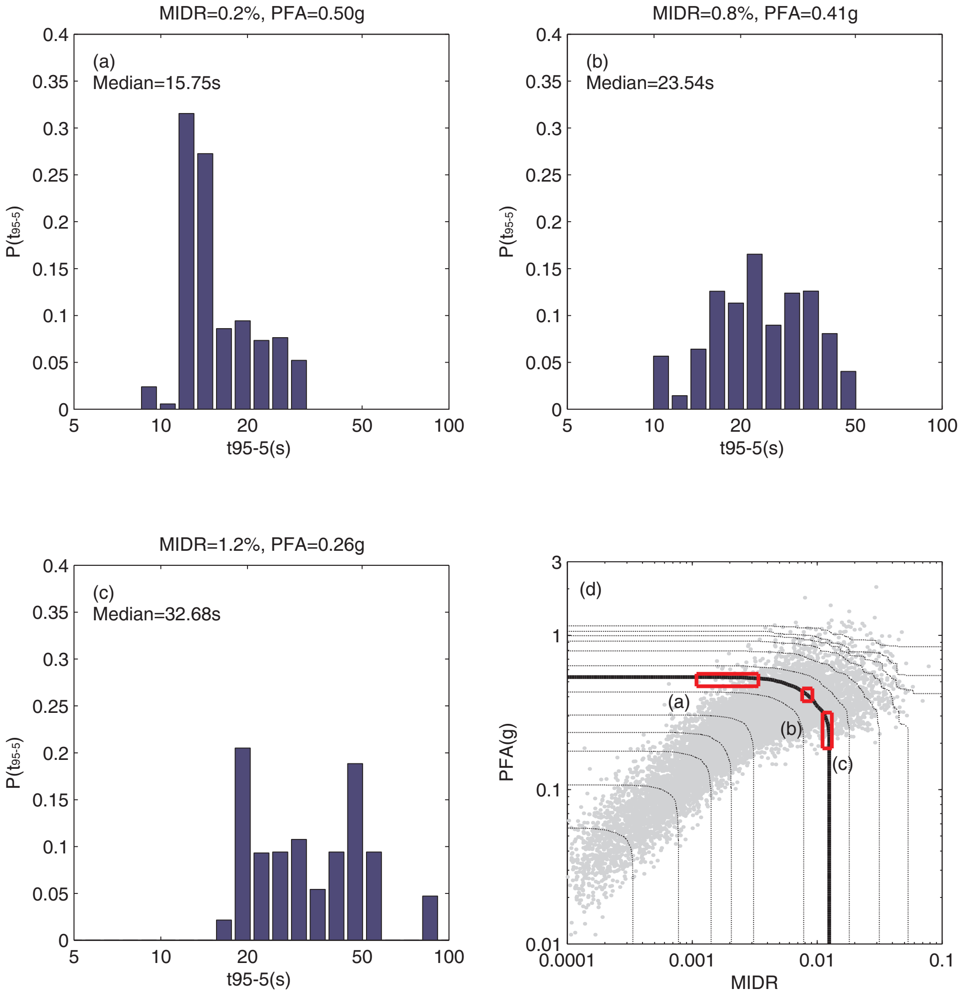

Figure 7.27: Probability distributions of significant duration given MIDR and PFA with 10% exceedance probability in 50 years for the 20-story building (a) MIDR=0.002 and PFA=0.51g, (b) MIDR=0.008 and PFA=0.41g, (c) MIDR=0.012 and PFA=0.24g, and (d) joint hazard contour of MIDR and PFA indicating the regions being studied.

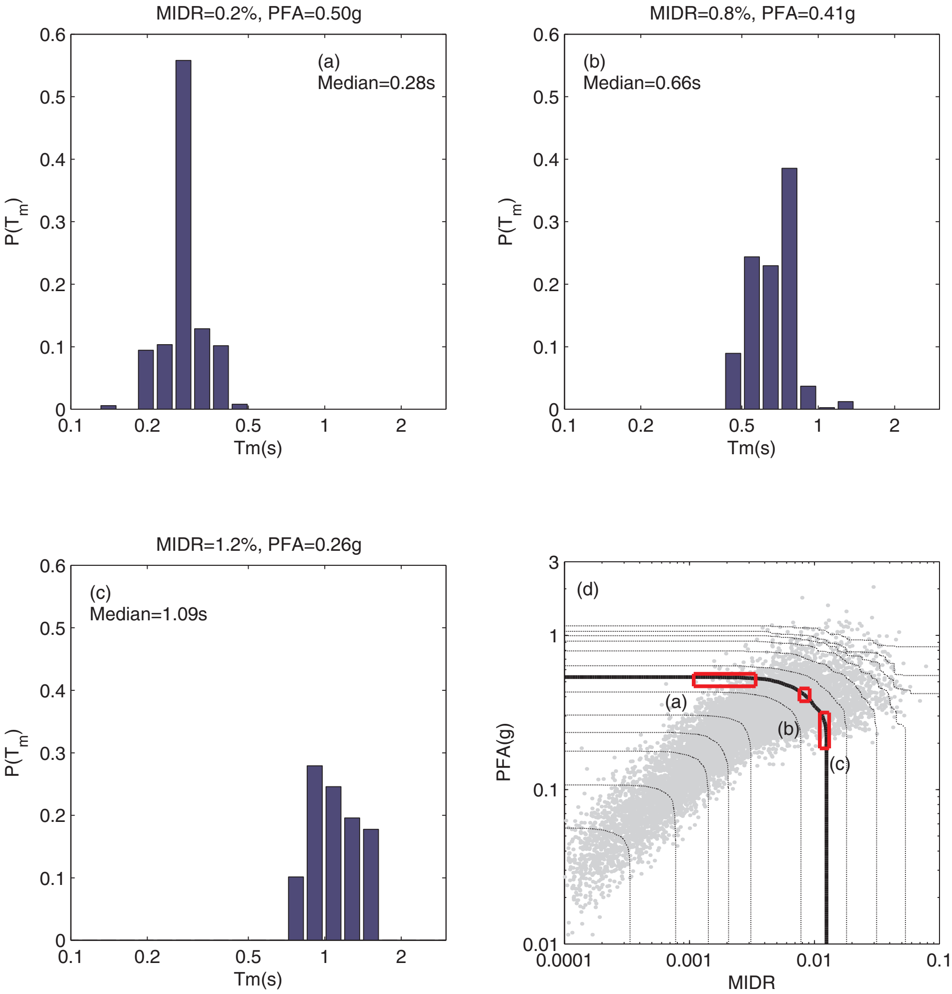

Figure 7.28: Probability distributions of mean period given MIDR and PFA with 10% exceedance probability in 50 years for the 20-story building (a) MIDR=0.002 and PFA=0.51g, (b) MIDR=0.008 and PFA=0.41g, (c) MIDR=0.012 and PFA=0.24g, and (d) joint hazard contour of MIDR and PFA indicating the regions being studied.

Figures 7.29 and 7.30 show the response spectra of ground motions producing target MIDR and PFA levels in the 20-story building. The same three MIDR and PFA values with 10% joint exceedance probability in 50 years are considered. Subfigures a, b and c show spectra for boxes a, b and c in the previous figures. Figures 7.29d shows the medians of the spectra in these three cases, along with the 10% in 50 years Uniform Hazard Spectrum for the example site, and Figure 7.30 shows the standard deviations of the logarithms of these three sets of spectra.

Several observations can be made from these figures. The dominant period of the spectra depends on whether the ground motions were selected because they produced a large PFA, produced a large MIDR or produced a combination of the two. The median S_a in Figures 7.29(a) has the shortest dominant period, Figures 7.29(c) has the longest dominant period, and Figures 7.29(b) is in between those two. This is consistent with the probability distributions of mean period in Figure 7.28. The 10% in 50 years uniform hazard spectrum (UHS), which is computed using the ground motions only and does not utilize information about the structural responses, envelopes all three median spectra, although the median spectra get very close to the UHS at some periods. It is notable that these median spectra are comparable in shape to Conditional Mean Spectra, even though no analysis related to Conditional Mean Spectra are used to produce any of the results in this chapter.

The logarithmic standard deviations of S_a ($\sigma_{\ln S_a}$) are relatively smaller at period ranges where the ground motions' spectra are good predictors of the EDP of interest. The spectra for cases a and b have small $\sigma_{\ln S_a}$ at short periods, because these short period spectra are correlated with the PFA value used for conditioning. In cases b and c, the spectra have the smallest $\sigma_{\ln S_a}$ at long periods, because spectra at those periods are highly correlated with the MIDR value used for conditioning. These results suggest the distribution of response spectra associated with ground motions producing an "X% probability of exceedance EDP" are not uniquely defined, but rather depend on the EDP parameter(s) of interest and what properties of ground motions they are most highly correlated with.

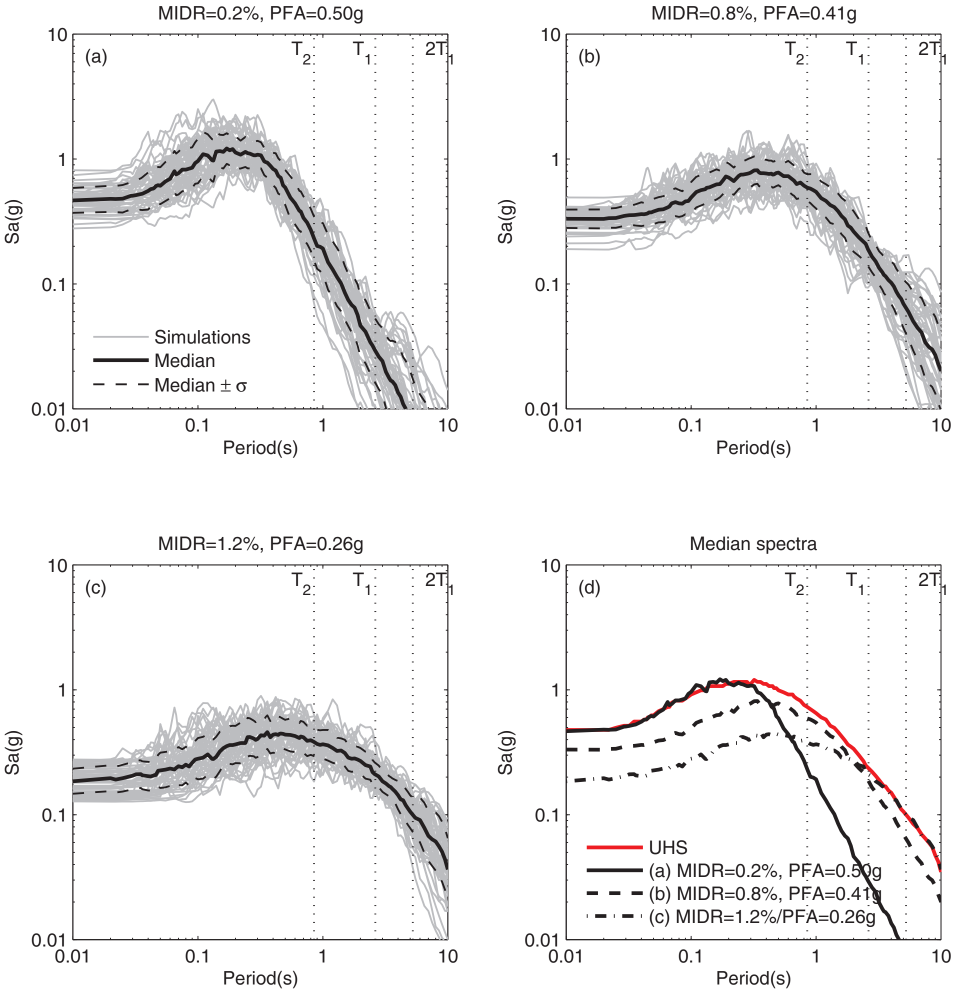

Figure 7.29: Response spectra of ground motions producing MIDR and PFA levels jointly exceeded with 10% probability in 50 years in the 20-story building (a) Spectra of ground motions producing MIDR=0.002 and PFA=0.51, (b) Spectra of ground motions producing MIDR=0.008 and PFA=0.41, (c) Spectra of ground motions producing MIDR=0.012 and PFA=0.24, and (d) median spectra of (a),(b), and (c).

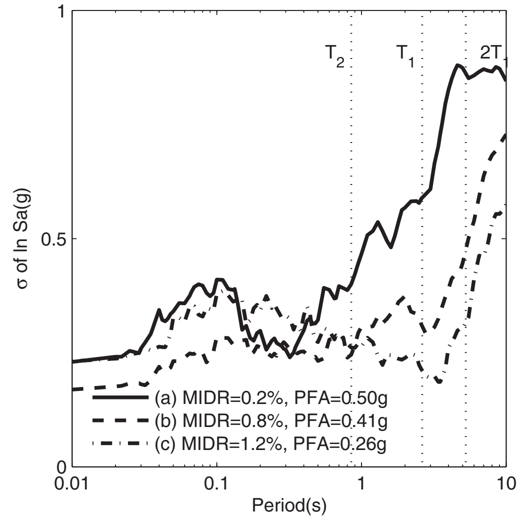

Figure 7.30: Logarithmic standard deviation of the response spectra shown in Figure 7.29a-c (a) Spectra of ground motions producing MIDR=0.002 and PFA=0.51, (b) Spectra of ground motions producing MIDR=0.008 and PFA=0.41, and (c) Spectra of ground motions producing MIDR=0.012 and PFA=0.24.

7.7 Conclusions

Simulation-based probabilistic seismic demand analysis has been introduced and computed using the simulated ground motions generated by the proposed stochastic ground motion model. Example PSDA hazard curves were produced for MIDR and PFA of 4- and 20-story buildings. The annual exceedance rates for a given MIDR are higher for the 4-story building than for the 20-story building, and the horizontal tails are associated with the probabilities of collapse. The rates of exceedance of a given PFA are also higher for the 4-story building than for the 20-story building. The hazard curves for PFA of both buildings are higher than that for PGA of high annual rates of exceedance ($>$ 10% in 50 years). As low annual rates of exceedance ($\leq$ 10% in 50 years), the hazard curves of both buildings are close to that of PGA, since PFAs occur on the first floor and are close to PGA when the building experiences strong nonlinear behavior Aslani and Miranda (2005). Deaggregation results for M, I_a, t_{95-5}, and T_m by MIDR and PFA are computed. These parameters are correlated to MIDR and PFA and their trends are similar except t_{95-5}. The significant duration t_{95-5} is strongly correlated to MIDR, however, it is less correlation with PFA. It suggests that ground motion with long t_{95-5} is likely to cause large MIDR but less likely to cause large PFA. Also, deaggregation results for S_a conditioned by MIDR and PFA are computed. The results showed that for the example cases considered, MIDR is correlated with S_a from T_1 and longer for the 4-story building and T_2 and longer for the 20-story building. Peak floor accelerations were seen to be correlated with S_a at short periods. These period ranges were explained intuitively based on the expected contributions of nonlinear responses and higher-mode contributions to the EDP parameters of interest at the varying amplitudes considered.

Further, joint hazard contours for MIDR and PFA were computed for the 4- and 20-story buildings. For both buildings, MIDR and PFA are strongly correlated, however, the correlation is changed where MIDR is around 0.007 because, in general, RC building will yield at approximately this point.

The response spectra associated with ground motions producing various combinations of MIDR and PFA were studied. The amplitudes and variability of the deaggregated spectra were again intuitively related to the effect of nonlinear responses and higher-mode contributions to the joint EDP parameters of interest. The results show that the distribution of response spectra associated with ground motions producing an “X% probability of exceedance EDP” are not uniquely defined, but rather depend on the EDP parameter(s) of interest and what properties of ground motions they are most highly correlated with.

These analyses are only example applications of simulation-based PSHA and PSDA. Further study of these ground motion properties producing a given target EDP (or vector or EDPs) will likely produce further insights of use when selecting and scaling recorded ground motions for structural analysis.

Chapter 8

Conclusions

This dissertation focuses on constructing a stochastic ground motion model with time-frequency nonstationarity and on applications for probabilistic assessment of seismic performance of structures using the resulting simulated ground motions. Simulation-based probabilistic assessments of seismic structural performance require simulated ground motions whose characteristics are consistent with those of real ground motions, as well as procedures to ground motion hazard and structural response hazard. Contributions have been made in both of these areas. The following subsections briefly summarize the important findings of this work, the limitations of this work, and suggested future work related to this dissertation.

8.1 Contributions and practical implications

8.1.1 Stochastic ground motion model with time-frequency nonstationarity

Several stochastic ground motion models with time-frequency nonstationarity have been proposed previously. In Chapter 2 of this dissertation, the difference between past models and the proposed model is discussed. The proposed model is based on Thráinsson and Kiremidjian (2002), which used Fourier amplitudes and phase differences to simulate ground motions and attenuation models to predict the model parameters. We extend their model using the wavelet packet transform since it can control the time and frequency characteristic of time series. This model employs wavelet packets as a tractable representation of evolutionary power spectral density (EPSD) in the time and frequency domain and uses regression analysis to predict the 13 required model parameters as a function of earthquake magnitude, distance and site condition. The model has the following advantages: a) the temporal and the spectral nonstationarity can be fully controlled by adjusting the model parameters, b) the model is empirically calibrated and produces motions that are consistent in their important characteristics with observed ground motion recordings, and c) the procedure is computationally inexpensive (1000 simulations per hour can be produced on a standard desktop PC), so obtaining large numbers of ground motions is relatively fast.

8.1.2 Consistency of characteristics of simulated ground motions with ground motion prediction models

The 13 model parameters are connected to magnitude, hypocentral distance, rupture distance, and site condition using two-stage regression analysis in Chapter 3. The characteristics of the resulting simulated ground motions were examined in Chapter 4 by comparing observed values of spectral acceleration, inelastic response spectra, Arias intensity, significant duration, and mean period with comparable predictions from ground motion prediction models (GMPMs) (Thráinsson and Kiremidjian 2002).

These properties are predicted directly by the GMPM regression models. However, these properties from the simulated ground motions are not directly connected to our regression models because these parameters are computed by evaluating time series data generated by the proposed stochastic ground motion model and regression model. For example, the GMPM predictions for spectral acceleration (S_a) are constructed independently for each period, with different subsets of the recorded ground motion database used at each period. S_a predictions from the simulated ground motions, however, are computed from the simulated time series with predicted parameters from regression model using one database. The comparisons of these properties from simulated ground motions with those from GMPM was thus ambitious, but was necessary for comprehensive validation of the proposed stochastic model and regression analysis.

The parameters computed from the simulated ground motions were observed to be generally consistent with those from the GMPMs under the following conditions: $6 \leq M \leq 8$, $220 \leq V_{S30} \leq 760(m/s)$, $1 \leq R_{rup} \leq 100(km)$, $0.01 \leq T \leq 3(s)$, and vertical strike-slip rupture mechanism.

Furthermore, the characteristics of the prediction errors of S_a (i.e., ε) were examined. The characteristics of ε are related to the probabilistic characteristics of the spectral shape of ground motions. The prediction errors ε were seen to be normally distributed (as is also the case with recorded ground motions) and have correlations that are consistent with an existing empirical model calibrated from recordings (Baker and Jayaram 2008).

Additionally the magnitude scaling, distance scaling, and duration scaling apparent in the acceleration, velocity, and displacement time series are consistent with expectations based on theory and observed trends in recorded motions.

8.1.3 Consistency of structural responses from simulated ground motions with those from recorded ground motions

In Chapter 6, the characteristics of the simulated ground motions were examined in terms of structural responses they produced. Nonlinear dynamic structural analyses were conducted for 4- and 20-story reinforced concrete moment frame buildings. Input ground motions were selected using the following three procedures: 1) recorded ground motions were selected and scaled to match the median of the target conditional mean spectrum (CMS), 2) recorded ground motions were selected and scaled to match the target conditional mean spectrum as well as its corresponding logarithmic standard deviation, 3) simulated ground motions were selected to match the target $S_a(T_1)$. The probabilistic characteristics of the structural responses obtained using the simulated ground motions were compared with those using recorded ground motions in terms of ductility, maximum inter-story drift ratio (MIDR), and peak floor acceleration (PFA). The probabilistic characteristics of the ductility, MIDR, and PFA using the simulated ground motions were observed to match those using the recorded ground motions selected and scaled to match the median and standard deviations of the target CMS.

8.1.4 Probabilistic assessment of the seismic performance of structures

In chapters 5 and 7, simulation-based probabilistic seismic hazard analysis (PSHA) and simulation-based probabilistic seismic demand analysis (PSDA) were proposed. These procedures compute the rates of exceeding a ground motion intensity measure or structural engineering demand parameter, respectively, using the simulated ground motions generated by the proposed stochastic ground motion model.

Spectral displacement ground motion hazard curves for an example site, for three periods, were studied and observed to be equivalent to those from traditional probabilistic seismic hazard analysis (PSHA). This was expected, since the characteristics of the simulated ground motions were consistent with those from the spectral acceleration ground motion prediction model (Chapter 4), and the same earthquake source model is used in both cases. Magnitude deaggregation results were also observed to be consistent in both cases.

The hazard curves of spectral displacement and their deaggregation for magnitude are consistent with those from GMPM. Additionally, the simulation-based hazard curves were deaggregated to identify the Arias intensity, significant duration, mean period, and spectral acceleration associated with occurrence of a given MIDR or PFA were. Studies of the response spectral properties associated with a given level of structural response are informative, as they indicate properties of ground motions critical to structural response (in a clearer manner than can be done with recorded ground motions whose properties cannot be controlled). MIDR was observed to be frequently controlled by spectral acceleration at periods from T_1 to $3T_1$ for the 4-story building and T_2 to $3T_1$ for 20-story building (because of nonlinear effects and higher mode responses), while PFA is more closely related to S_a at short periods.

Further, the joint hazard contours (indicating rates of simultaneously exceeding a given MIDR and PFA) were computed for the 4- and 20-story buildings. The response spectra associated with ground motions causing both a large MIDR and a large PFA were observed to have relatively smaller standard deviations from the periods T_2 to $2T_1$ than those given only one of those EDP (since PFA and MIDR are sensitive to different period ranges in the response spectra). Also the deaggregations for moment magnitude, Arias intensity, significant duration, mean period, and spectral acceleration were computed conditioned by both MIDR and PFA. These deaggregation analyses are currently only possible to perform by using simulation-based PSDA.

These assorted analyses demonstrate that using the proposed simulated ground motions allows one to explore and directly understand seismic hazard in unique ways, and also provides a great deal of flexibility in studying the probabilistic characteristics of structural responses and the deaggregation of any type of ground motion characteristics associated with those structural responses.

8.1.5 Validation of ground motion simulations for engineering use

This dissertation presented a variety of techniques for validating simulated ground motions, in terms of comparisons with ground motion prediction models, comparison of structural responses to comparable responses from recorded ground motions, and comparison of full drift hazard curves. This suite of tests used here is believed to be more comprehensive than has been performed for other ground motion simulation efforts, and was utilized specifically for evaluating whether a ground motion simulation procedure is appropriate for use in a performance based seismic reliability analysis. The proposed tests may thus be useful for evaluating other types of simulated ground motions, such as physics-based simulations. Validation of simulations in general is topic of active discussion among researchers at the seismology/engineering interface, and so the development and documentation of these procedures is a relevant contribution to that discussion. The philosophy used here is that the ground motion simulations are appropriate for engineering applications if the ground motion intensity measures and structural response properties are consistent with our best understanding of what those values should look like (as determined from comparable observations of real ground motions). This does not ensure that a simulation approach will produce good results in terms of waveform properties or inversion to source parameters, but focusing on properties most relevant to engineering calculations is important when considering engineering applications for use of simulations, and these tests are useful complements to other validation techniques in widespread use in the earth science community for validating waveform time histories and other properties.

Further, the calibrated wavelet packet model developed here is in itself a potentially useful tool for validating physics-based ground motion simulations. Those physics-based simulations could be analyzed using the wavelet-packet decomposition, and if the properties of the wavelet packet coefficients differed significantly from predictions of those properties provided by this model, then that might indicate some property of the simulations that was potentially inconsistent with recorded motions. This comparison need not be done on a record-by-record basis, given the regression model that was developed here. Instead, for example, simulations could be produced for a variety of earthquake magnitudes (even extending past the magnitude range considered here), and the scaling of the nonstationarity parameters or the duration parameters in the simulations could be studied to see if they scale with magnitude in a manner similar to that predicted by the model proposed here. This type of validation would provide different information from validation computations in use today, so it may prove to be a useful additional check.

8.1.6 Software

The stochastic model described in this dissertation has been implemented in the Matlab programming environment using the Matlab Wavelet Toolbox. To supplement the documentation provided by this dissertation, simulation source code is available at our website (`www.stanford.edu/~bakerjw/gm_simulation.html`). The web site also contains further detailed documentation such as regression coefficients, a table of earthquake ground motions used in regression analysis, and other relevant information for the validation of the model. The current software produces 1000 simulations per hour on a desktop computer (Dell Optiplex 740 with AMD Athlon 64 dual core and 2GB of RAM).

8.2 Limitations and future work

8.2.1 Range of seismological conditions for which simulations can be produced

The simulated ground motions were validated by comparison with ground motion prediction models in Chapter 4 and by comparing structural responses from recorded and simulated ground motions in Chapter 6. These results suggested that one can use the simulated ground motions as input ground motions of the performance based earthquake engineering, but there were limitations on the circumstances under which that observation is valid.

The proposed regression model and the proposed stochastic model were calibrated using recorded ground motions, and limitations on the ground motion library constrain the range of conditions over which the simulations are expected to be valid. The following ranges are proposed for conditions under which the simulations are expected to be consistent with real ground motions: 1) $6 \leq M \leq 8$, 2) $1 \leq R_{rup} \leq 100km$, 3) $220 \leq V_{S30} \leq 760m/s$, 4) $0.01 \leq T \leq 3s$, and 5) vertical strike-slip rupture mechanism.

The upper bound of 3 seconds on the realistic periods is due to the excessive variability of $\ln S_a$ at longer periods, especially for small-magnitude motions. This is inherent to the wavelet transform approach used here, where limited period resolution at long periods is a consequence of the finite time-domain resolution of this method. This might not be a significant practical problem in some cases, however, because the problem arises at long periods and for small-magnitude earthquakes, and under that combination of conditions the spectral accelerations are generally low enough that they are not of engineering interest.

8.2.2 Modeling issues

While the simulated ground motions were observed to be reasonable over the range of conditions described above, there are some remaining unresolved modeling issues that could potentially increase the circumstances under which the simulations could be viewed as realistic.

The proposed stochastic model currently randomizes the signs of the wavelet packets used in the wavelet transform (i.e., the model specifies only the amplitudes of these wavelet packets and not their signs). The signs of the wavelet packets do not appear to have a significant effect on spectral accelerations or other ground motion properties that were studied, but they may have some other as-yet-unidentified effect and so thus could be studied further in the future.

The proposed regression model has only four predictors: moment magnitude, hypocentral distance, rupture distance, and V_{S30}. For future improvement, we could consider including additional predictors such as rupture mechanism and depth to the bedrock. Initial regression models considered did not indicate a statistically significant trend with any of these parameters, but their effectiveness in other ground motion prediction models suggests that they may be useful predictors.

The functional form used for regression was also kept relatively simple for practical purposes. For example, the parameter h employed in the proposed regression model controls saturation of each parameter in the near fault because of the area of the fault. In the current model, h is a constant for a given model parameter, but the model could be modified so h is a function of magnitude (since h is related to the area of the fault).

The database for regression analysis could also be improved in the future as strong ground motion libraries continue to improve. New ground motions recorded on modern instruments have better quality signals at long periods, which may potentially help with the inaccuracies present at long period in the proposed model. The proposed model could also be extended to simulate subduction and other non-crustal earthquake motions if appropriate ground motion libraries were available to develop the needed regression models.

8.2.3 Sensitivity analysis for structural behavior against 13 model parameters

The proposed model requires 13 model parameters to simulate a ground motion. Since these parameters are related to characteristics of the time series, we can examine the influence of each parameter on structural behavior using nonlinear dynamic structural analysis. By varying the model parameters, one can have any kind of simulated ground motions.

Three parameters are of particular interest for structural behavior: 1) duration, 2) dominant period, 3) time-frequency nonstationarity. In Chapter 7, we observed that the duration and dominant period of the simulated motions were related to the MIDR and PFA values observed in structural analysis. The time-frequency nonstationarity is not a significant parameter from the deaggregation of the hazard curves of MIDR and PFA because we used only the short distance ($R_{rup} = 10km$) in the probabilistic seismic demand analysis in Chapter 7. However, it can affect results of nonlinear dynamic structural analysis (Conte 1992b) because the stiffness of structures decreases and the resulting natural periods increase in general as a structure is driven to nonlinear response over the duration of shaking. These relationships could be studied more carefully in the future using the proposed simulation approach, and the results could provide insights for selecting recorded ground motions.

8.2.4 Probabilistic assessment for a portfolio of structures

For the probabilistic assessment of the performance of a portfolio of structures, ground motion simulations with appropriate coherence are needed. Currently, simulated ground motions generated by the proposed stochastic model are independent of each other even at close stations, contrary to real-world observations.

Several coherency models have been proposed in the past research (Vanmarcke 1983, Zerva 1992). For stationary process, Harichandran et al. (1986), Hao (1986), and Abrahamson et al. (1991) proposed the empirical lagged coherency. Der Kiureghian (1996) proposed a theoretical model for the coherency function, including incoherence, wave passage, attenuation, and site effects. In this theoretical model, only site effects has been validated with observations (Der Kiureghian and Keshishian 1996). Deodatis (1996) and Cacciola and Deodatis (2011) proposed coherency models for fully nonstationary and spectrum-compatible ground motion time histories. Also a program (SIMQKE-II, Vanmarcke et al. 1997) can generate fully nonstationary spatially correlated ground motions.

To account for coherency in the proposed ground motion model, the following two types of coherency would need to be considered. First, coherency of the 13 model parameters would need to be defined. In the current regression model, the 13 regression equations are correlated through the correlation of intra- and inter-event residuals. The spatial correlation of intra-event residuals of each regression equation and cross correlation of 13 regression equations need to be defined.

Second, spatial correlation between the other model random variables would need to be considered. Four types of the random variables are used in the proposed stochastic model: 1) random variation of wavelet packets in the minor group around their predicted mean amplitudes, 2) random time-frequency location of the wavelet packets in the major group, 3) random amplitudes of wavelet packets in major group, and 4) the random signs of the of wavelet packets. Spatial correlation of those random variables would be needed in addition to spatial correlation of the 13 model parameters mentioned above. Since the proposed model uses four types of random variables, the existing coherency models cannot be applied directly.

Once both types of coherency are defined, we could potentially produce spatially varying ground motions for probabilistic assessment of portfolio performance.

8.2.5 Three dimensional structural analysis using multi-component simulated ground motions

The current proposed stochastic ground motion model only produces single-component motions in the fault-normal direction (because fault-normal recordings were used to calibrate the model). While the proposed approach demonstrates a general procedure that could be extended to fault-parallel components also in order to obtain multi-component models, one change in the procedure may be needed.

The fault parallel ground motions in near field may have another effect called fling step. The fling step is the permanent residual displacement of the site due to fault deformation. To account for the fling step in the proposed model, we need to employ the wavelet packets in the lowest frequency in velocity. This lowest level of wavelet packets has a functional form that can produce residual displacements and so would be needed to capture this effect (currently this level is omitted from calibration and simulations because no residual displacements are needed). Vertical components also can be modeled by the same procedure of the fault normal and the fault parallel components.

In addition to calibrating additional models for each ground motion component, correlation between parameters for each component would need to be considered. So in addition to correlations between the 13 parameters for a given component, it would be necessary to compute the cross-correlations between the fault-normal and fault-parallel parameters. Such a model has been developed by Rezaeian (2010).

8.2.6 Vector-valued structural response hazard analysis

In this dissertation, the joint structural response hazard analysis was computed for a two-parameter vector MIDR and PFA. Using the simulation-based PSDA, we can increase the dimension of this type of analysis. For example, we can compute the joint hazard for inter-story drift ratio and peak floor acceleration at each story, and ductility of each element of interest. Also we can compute the deaggregation for any characteristics of the time series. In particular, we can explore the spectral shape of ground motions causing a given set of structural responses. These types of calculations may provide interesting insights into the characteristics of input ground motions that are most important to the response of structures. Only preliminary results of this type were considered here, and much more could presumably be learned by performing more in depth analyses of this type.

8.3 Concluding remarks

This dissertation documented the construction of a stochastic ground motion model with time-frequency nonstationarity using the wavelet packet transform. The time- and frequency-varying properties of real ground motions are modeled using wavelet packets, and the proposed model requires only 13 model parameters to describe a given ground motion. These 13 model parameters are then related to seismological variables such as earthquake magnitude and distance, through regression analysis that captures trends in mean values, variabilities and correlations of these parameters observed in a large database of recorded strong ground motions.

Using the simulated ground motions obtained using this approach, hazard curves for ground motions (elastic and inelastic spectral displacement) and structural responses (maximum inter-story drift ratio (MIDR) and peak floor acceleration (PFA)) and hazard deaggregation are computed (simulation-based probabilistic seismic hazard analysis (PSHA) and simulation-based probabilistic seismic demand analysis (PSDA)). Further, hazard analysis for joint exceedances of multiple engineering demand parameters is computed for MIDR and PFA. These results lead us to discussion of the relationship between the ground motion parameters and multiple EDPs since they all are directly connected though the simulated ground motions. These types of calculations are readily performed using this simulation-based PSDA approach, facilitating the study of questions such as this that are difficult to consider when using limited sets of recorded ground motions that require scaling.

The approach can be extended beyond traditional hazard results as well, to consider deaggregation of non-standard ground motion parameters and computation of vector-valued hazard. Future research appears warranted to refine the proposed model, investigate the relationship between the parameters of the simulated motions and nonlinear dynamic structural analysis results, compute and evaluate advanced hazard results, and extend the model to simulate multi-component and spatially coherent motions.

Appendix A

Relationship between wavelet packets in major group, minor group, and total

Here the relationship of the wavelet packets between in major group and minor group is described. Since 70% of energy goes to the major group, the total energy is defined as follows:

$$\begin{aligned} E_{acc} &= E_{acc,maj} + E_{acc,min} \\ E(t) &= 0.7E(t)_{maj} + 0.3E(t)_{min} \\ E(f) &= 0.7E(f)_{maj} + 0.3E(f)_{min} \end{aligned}$$

$$\begin{aligned} S^2(t) &= E(t^2) - \{E(t)\}^2 \\ &= 0.7S^2(t)_{maj} + 0.3S^2(t)_{min} \\ &\quad +0.7 \cdot 0.3 \left\{E(t)_{maj} - E(t)_{min}\right\}^2 \\ S^2(f) &= 0.7S^2(f)_{maj} + 0.3S^2(f)_{min} \\ &\quad +0.7 \cdot 0.3 \left\{E(f)_{maj} - E(f)_{min}\right\}^2 \end{aligned}$$

$$
\begin{aligned}
Cov(t,f) &= E(t,f) - E(t)E(f) \\
&= 0.7Cov(t,f)_{maj} + 0.3Cov(t,f)_{min} \\
&\quad +0.7 \cdot 0.3 \left\{ E(t)_{maj} - E(t)_{min} \right\} \\
&\quad \times \left\{ E(f)_{maj} - E(f)_{min} \right\} \\
R(t,f) &= \frac{Cov(t,f)}{S(t)S(f)}.
\end{aligned}
$$

Since we assume that time and frequency positions of wavelet packets in major group are independent of amplitudes ,mean time, mean frequency, variance of time, variance of frequency, and covariance of time and frequency only from the time frequency location of the wavelet packets are unbiased from those parameters with the time and frequency location and amplitudes of the wavelet packets. Therefore we can control the wavelet packets in the major group by using the time and frequency locations, and the amplitudes of the wavelet packets, which are independent each other.

$$
\begin{aligned}
E[E(t)_{maj}] &= \frac{\sum_{i,k} E[t_k \left| c^i_{j,k,maj} \right|^2]}{E_{acc,maj}} \\
&= \frac{\sum_{i,k} E[t_k a^i_{j,k,maj}]}{\sum_{i,k} a^i_{j,k,maj}} \\
&= \frac{\sum_{i,k} E[t_k] E[a^i_{j,k,maj}]}{\sum_{i,k} a^i_{j,k,maj}} \\
&= \frac{\sum_{i,k} E[t_k]}{n_{maj}} \\
&= E[\frac{\sum_{i,k} t_k}{n_{maj}}] \\
&= E(E(t_{k,maj}))
\end{aligned}
$$

$$
\begin{aligned}
E[Var(t)_{maj}] &= \frac{\sum_{i,k} E[\left\{t_k - E(t_{k,maj})\right\}^2 \left|c^i_{j,k,maj}\right|^2]}{E_{acc,maj}} \\
&= \frac{\sum_{i,k} E[\left\{t_k - E(t_{k,maj})\right\}^2 a^i_{j,k,maj}]}{\sum_{i,k} a^i_{j,k,maj}} \\
&= \frac{\sum_{i,k} E[\left\{t_k - E(t_{k,maj})\right\}^2] E[a^i_{j,k,maj}]}{\sum_{i,k} a^i_{j,k,maj}} \\
&= \frac{\sum_{i,k} E[\left\{t_k - E(t_{k,maj})\right\}^2]}{n_{maj}} \\
&= E[\frac{\sum_{i,k} \left\{t_k - E(t_{k,maj})\right\}^2}{n_{maj}}] \\
&= E[S^2(t_{k,maj})]
\end{aligned}
$$

$$
\begin{aligned}
E[Cov(t,f)_{maj}] &= \frac{\sum_{i,k} E[\left\{t_k - E(t_{k,maj})\right\}\left\{f_i - E(f_{i,maj})\right\} \left|c^i_{j,k,maj}\right|^2]}{E_{acc,maj}} \\
&= \frac{\sum_{i,k} E[\left\{t_k - E(t_{k,maj})\right\}\left\{f_i - E(f_{i,maj})\right\} a^i_{j,k,maj}]}{\sum_{i,k} a^i_{j,k,maj}} \\
&= \frac{\sum_{i,k} E[\left\{t_k - E(t_{k,maj})\right\}\left\{f_i - E(f_{i,maj})\right\}] E[a^i_{j,k,maj}]}{\sum_{i,k} a^i_{j,k,maj}} \\
&= \frac{\sum_{i,k} E[\left\{t_k - E(t_{k,maj})\right\}\left\{f_i - E(f_{i,maj})\right\}]}{n_{maj}} \\
&= E[\frac{\sum_{i,k} \left\{t_k - E(t_{k,maj})\right\}\left\{f_i - E(f_{i,maj})\right\}}{n_{maj}}] \\
&= E[Q(t_{k,maj}, f_{i,maj})]
\end{aligned}
$$

Appendix B

Maximum likelihood estimation of the model parameters

If the X_i are assumed to be i.i.d., their joint density is the product of the marginal densities, and the likelihood is

$$\mathrm{lik}(\theta) = \prod_{i=1}^{n} f(X_i|\theta)$$

Rather than maximizing the likelihood itself, it is usually easier to maximize its natural logarithm. For an i.i.d. sample, the log likelihood is

$$l(\theta) = \sum_{i=1}^{n} \log[f(X_i|\theta)]$$

The wavelet packets in the minor group can be defined as following equations:

$$X_k = \ln(t_k), \;\; Y_i = \ln(f_i) \tag{B.1}$$

$$C_{min}(i,k) = \frac{1}{2\pi S(X)S(Y)\sqrt{(1-R(X,Y)^2)}} \times \frac{1}{X_k Y_i} \exp\left[-\frac{A^2 - 2R(X,Y)AB + B^2}{2\{1-R^2(X,Y)\}}\right] \times \varepsilon_{k,i} \tag{B.2}$$

$$A = \frac{X_k - E(X)}{S(X)}, \quad B = \frac{Y_i - E(Y)}{S(Y)} \tag{B.3}$$

$C_{min}(i,k)$ obeys bivariate normal distribution of X and Y. Therefore we need to estimate $E(X), E(Y), S(X), S(Y)$, and $R(X,Y)$.

First, we estimate $E(X)$ and $S(X)$ by using marginal distribution of $C_{min}(i,k)$ about i.

$$CX(k) = \sum_{i=1}^{2^j} C_{min}(i,k) \tag{B.4}$$

Since $CX(k)$ is equivalent to frequency of each time and frequency, log likelihood of $E(X)$ and $S(X)$ is

$$\begin{aligned} l[E(X),S(X)|X] &= \sum_{i=1}^{n} \log[f(X_k|E(X),S(X))] \\ &= \sum_{k=1}^{2^{N-j}} CX(k) \log\left[\frac{1}{\sqrt{2\pi S^2(X)} \exp\left\{-\frac{X_k - E(X)}{2S^2(X)}\right\}}\right] \end{aligned}$$

$$[E(X),S(X)]_{MLE} = \underset{E(X),S(X)}{\text{argmax}}\, l[E(X),S(X)|X]$$

Then, we estimate $E(Y)$ and $S(Y)$ by using marginal distribution of $C_{min}(i,k)$ about k.

$$CY(i) = \sum_{k=1}^{2^{N-j}} C_{min}(i,k) \tag{B.5}$$

Since the time series are truncated by the bandpass filters in the frequency domain to remove noise, and the filter frequencies differ ground motion to ground motion, we define α as the highest usable frequency and β as the lowest usable frequency. Then log likelihood of $E(X)$ and $S(X)$ is

$$\begin{aligned} l(E(Y),S(Y)|Y) &= \sum_{i=1}^{n} \log[f(Y_i|E(Y),S(Y))] \\ &= \sum_{i=1}^{2^j} CY(i) \log \left[\frac{\frac{1}{\sqrt{2\pi S^2(Y)} \exp\left\{-\frac{Y_i - E(Y)}{2S^2(Y)}\right\}}}{\Phi\left(\frac{\beta - E(Y)}{S(Y)}\right) - \Phi\left(\frac{\alpha - E(Y)}{S(Y)}\right)} \right] \end{aligned}$$

$$[E(Y),S(Y)]_{MLE} = \underset{E(Y),S(Y)}{\operatorname{argmax}}\, l[E(Y),S(Y)|Y]$$

Finally, we estimate $R(X,Y)$. Then log likelihood of $R(X,Y)$ is

$$\begin{aligned} l(R(X,Y)|X,Y) &= \sum_{i=1}^{n} \log[f(Y_i|R(X,Y))] \\ &= \sum_{i=1}^{2^j} CY(i) \log \left[\frac{\frac{1}{2\pi S(X)S(Y)\sqrt{(1-R(X,Y)^2)}} \frac{1}{X_k Y_i} \exp\left\{-\frac{A^2 - 2R(X,Y)AB + B^2}{2\left\{1-R^2(X,Y)\right\}}\right\}}{\Phi\left(\frac{\beta - E(Y)}{S(Y)}\right) - \Phi\left(\frac{\alpha - E(Y)}{S(Y)}\right)} \right] \end{aligned}$$

$$[R(X,Y)]_{MLE} = \underset{R(X,Y)}{\operatorname{argmax}} l[R(X,Y)|Y]$$

Appendix C

Simulated ground motions for the Chi-Chi earthquake

Using our stochastic ground motion model, 378 ground motion recordings from the 1999 Chi-Chi earthquake ($M = 7.6$) are considered. We estimated the 13 model parameters for each of these recordings using the Maximum Likelihood Method (appendix B).

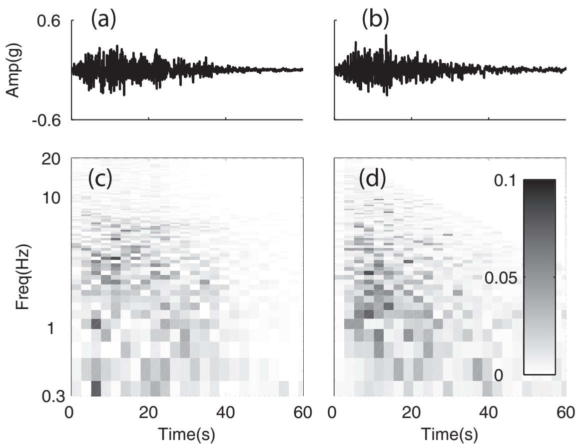

Figure C.1: Simulation of recorded ground motion of the Chi-Chi earthquake at TCU076 [$R_{hyp} = 17.91km, V_{S30} = 615m/s$] (a) acceleration time series of recorded ground motion, (b) simulated time series, (c) wavelet packets of recorded ground motion, and (d) wavelet packets of simulated time series

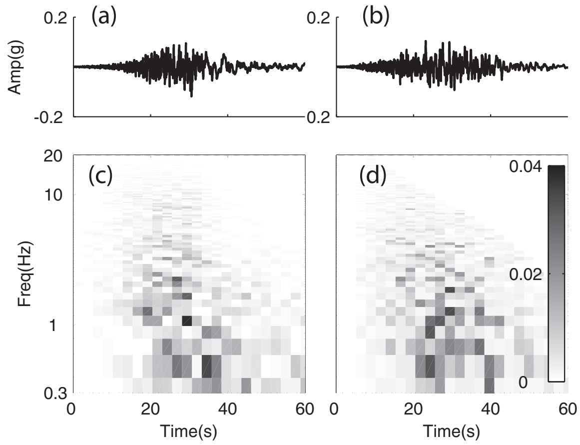

Figure C.2: Simulation of recorded ground motion of the Chi-Chi earthquake at TCU015 [$R_{hyp} = 101.93km$, $V_{S30} = 473.9m/s$] (a) acceleration time series of recorded ground motion, (b) simulated time series, (c) wavelet packets of recorded ground motion, and (d) wavelet packets of simulated time series

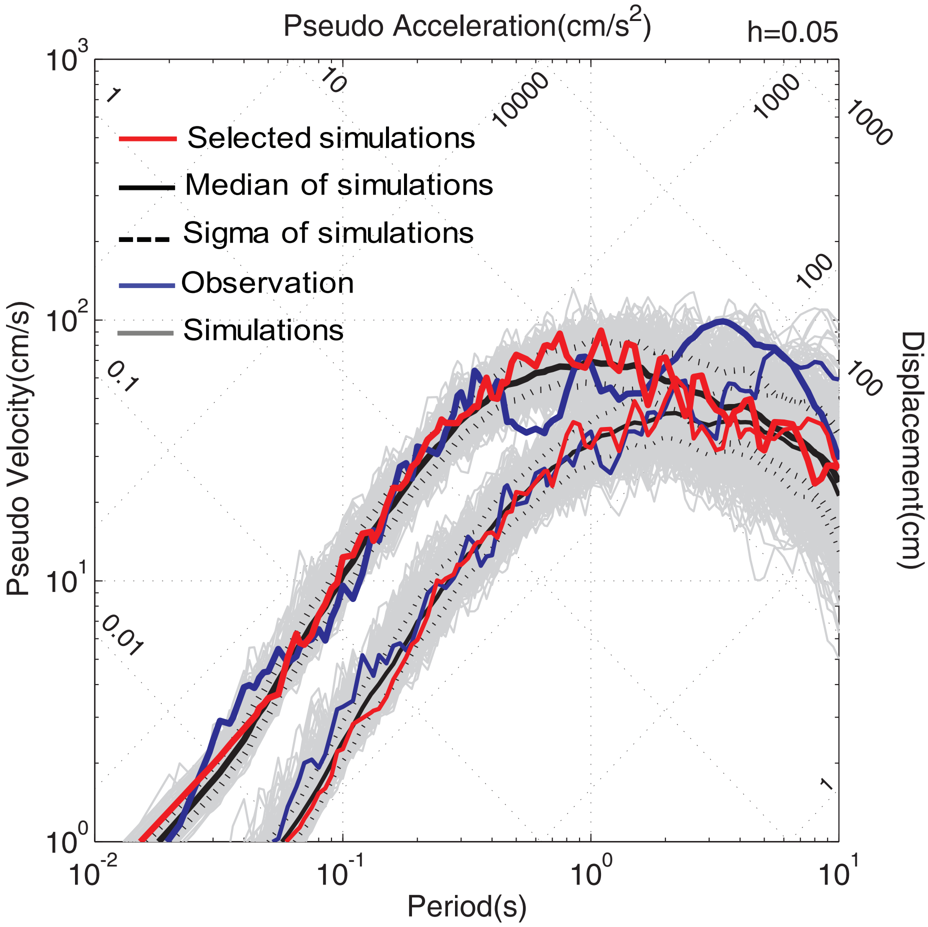

Figure C.3: S_a of simulated ground motion at near field and far field.

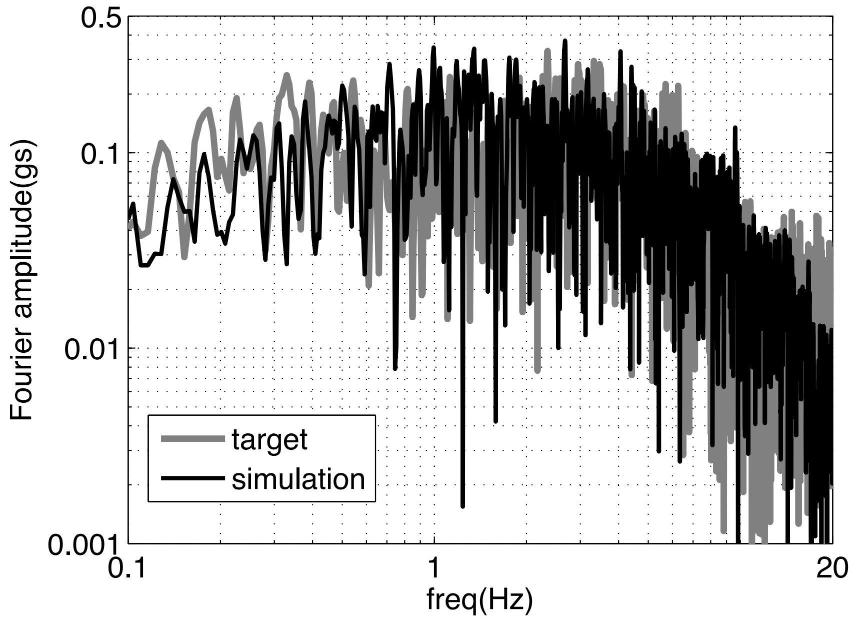

Figure C.4: Fourier spectra of simulated and recorded ground motion of the Chi-Chi earthquake at TCU076 [$R_{hyp} = 17.91km, V_{S30} = 615m/s$]

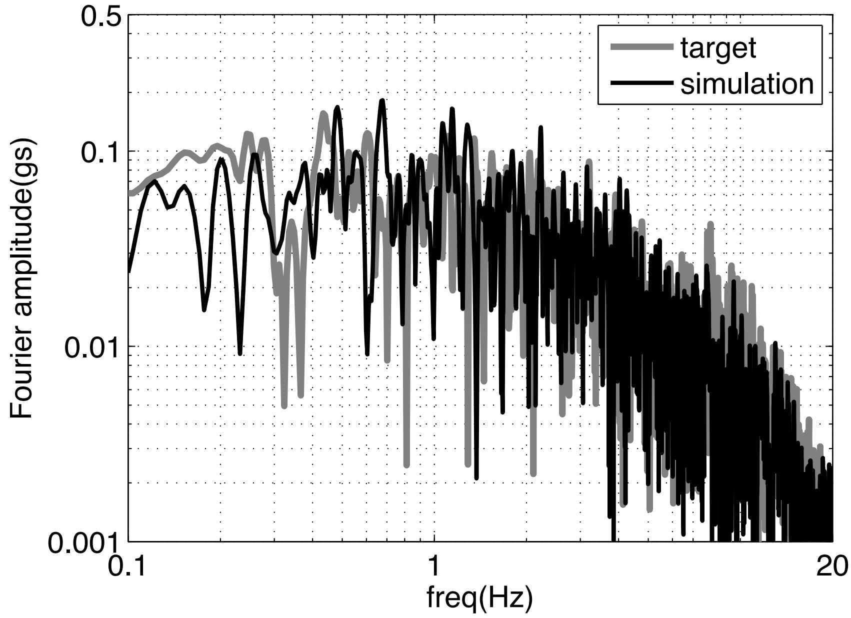

Figure C.5: Fourier spectra of simulated and recorded ground motion of the Chi-Chi earthquake at TCU015 [$R_{hyp} = 101.93km, V_{S30} = 473.9m/s$]

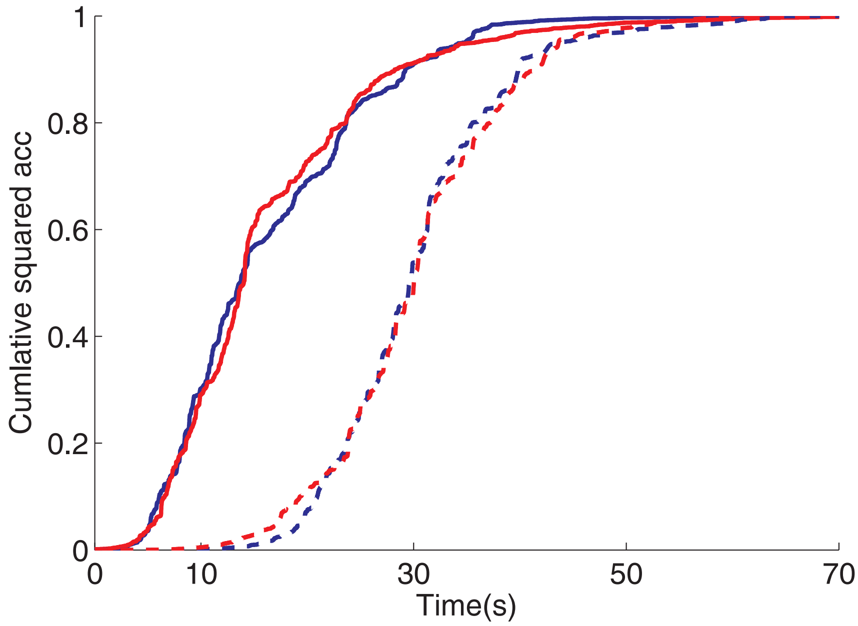

Figure C.6: Cumulative squared acceleration.

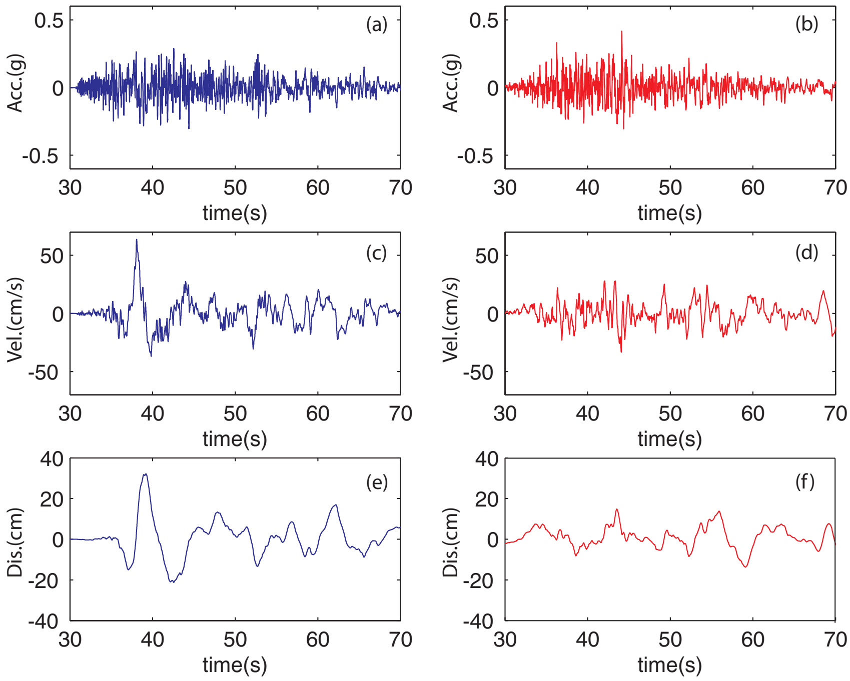

Figure C.7: Simulated and recorded ground motion of the Chi-Chi earthquake at TCU076 [$R_{hyp} = 17.91km$, $V_{S30} = 615m/s$] (a) and (b) acceleration(g), (c) and (d) velocity (cm/s), and (e) and (f) displacement (cm) for recorded and simulated ground motion, respectively.

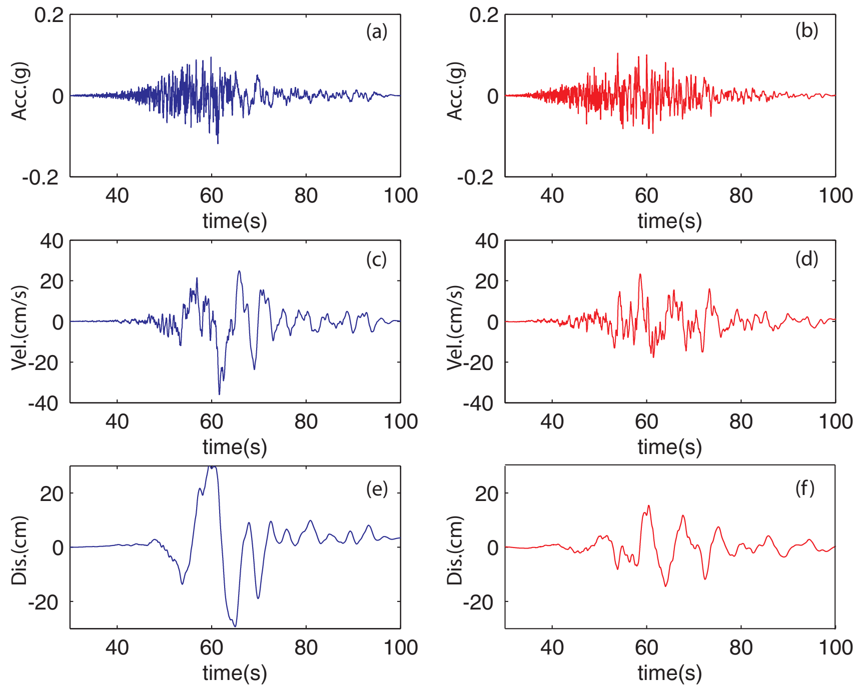

Figure C.8: Simulated and recorded ground motion of the Chi-Chi earthquake at TCU015 [$R_{hyp} = 101.93km$, $V_{S30} = 473.9m/s$] (a) and (b) acceleration(g), (c) and (d) velocity (cm/s), and (e) and (f) displacement (cm) for recorded and simulated ground motion, respectively.

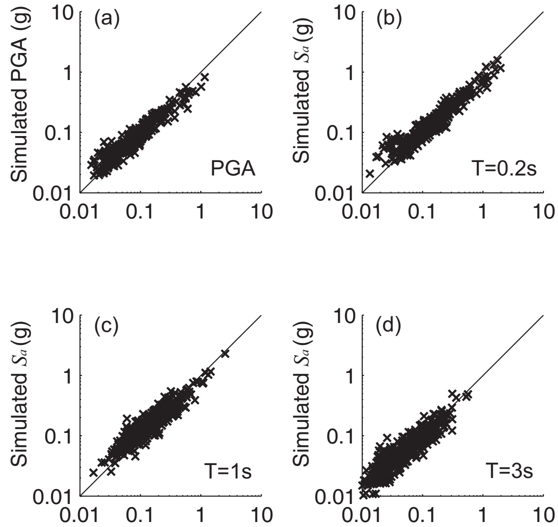

Figure C.9: PGA and S_a from target time series versus median of corresponding value from simulations. (a) PGA, (b) S_a at $T = 0.2s$, (c) S_a at $T = 1s$, and (d) S_a at $T = 3s$.

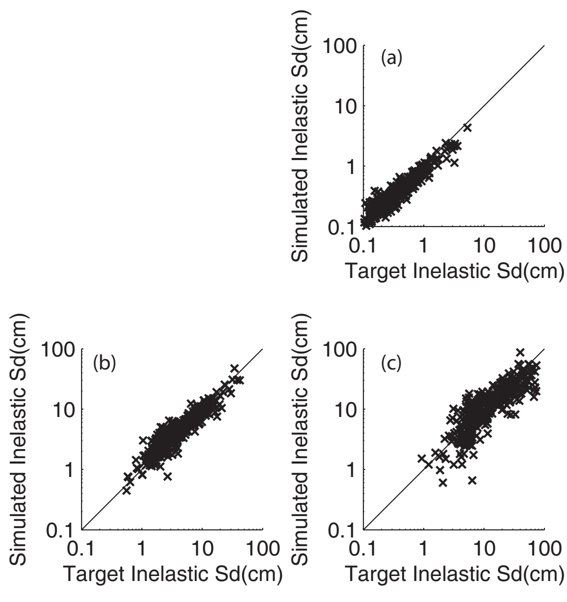

Figure C.10: Median of Pinelastic S_d with ductility $\mu = 8$ between target time series and simulations. (a) S_a at $T = 0.2s$, (b) S_a at $T = 1s$, and (c) S_a at $T = 3s$.

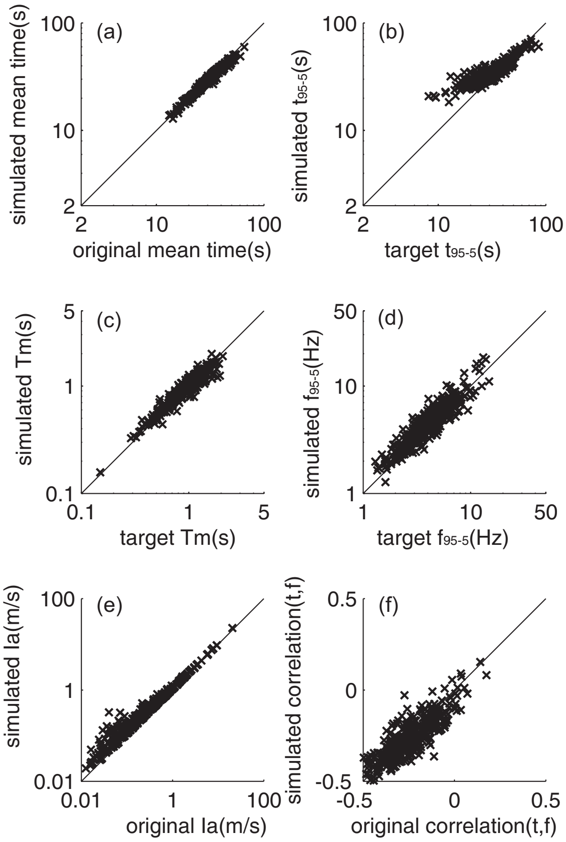

Figure C.11: Model parameters between from the target time series versus the median of the corresponding parameter from 300 simulations. (a) temporal centroid, $E(t)$, (b) significant duration, t_{95-5}, (c) mean period, T_m, (d) significant bandwidth, f_{95-5}, (e) Arias intensity (I_a), and (f) correlation of wavelet packets between time and frequency, $\rho(t,f)$.

Appendix D

Comparison of simulation results with ground motion prediction models for rock site

D.1 Comparison with NGA GMPM

Here the median and logarithmic standard deviation of the spectral acceleration for rock site ($V_{S30} = 760m/s$) from the simulated ground motions are compared with those from NGA GMPM.

D.1.1 Distance scaling

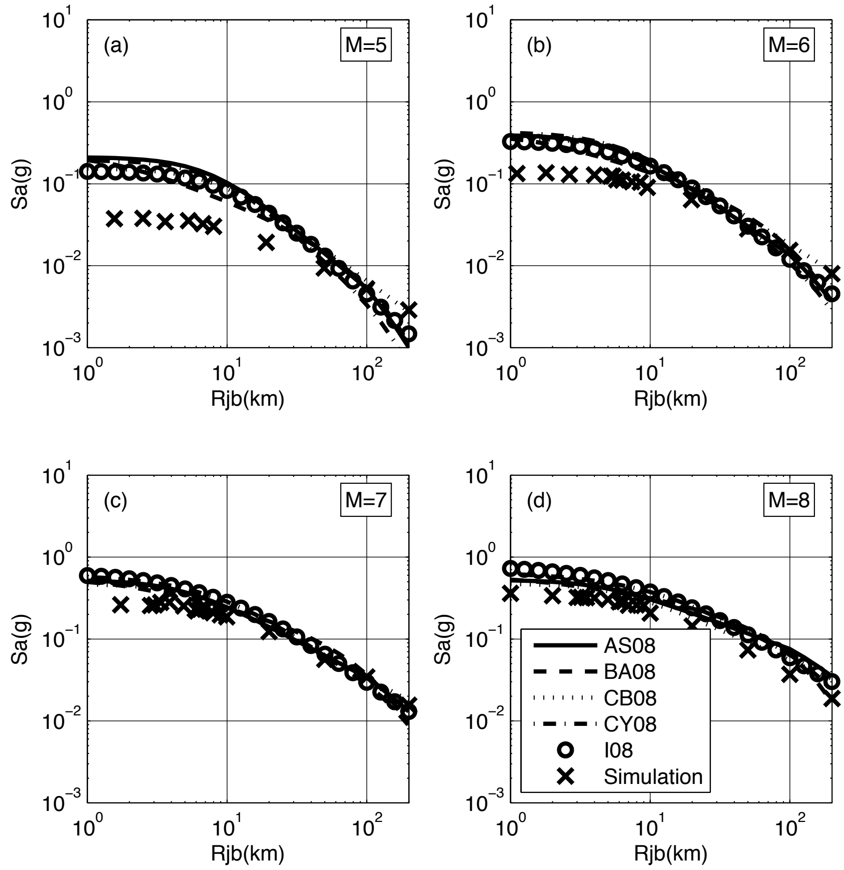

Figure D.1: Median of PGA computed from the NGA GMPM and simulations ($1 \leq R_{JB} \leq 200km, V_{S30} = 760m/s$). (a) $M = 5$, (b) $M = 6$, (c) $M = 7$, and (d) $M = 8$.

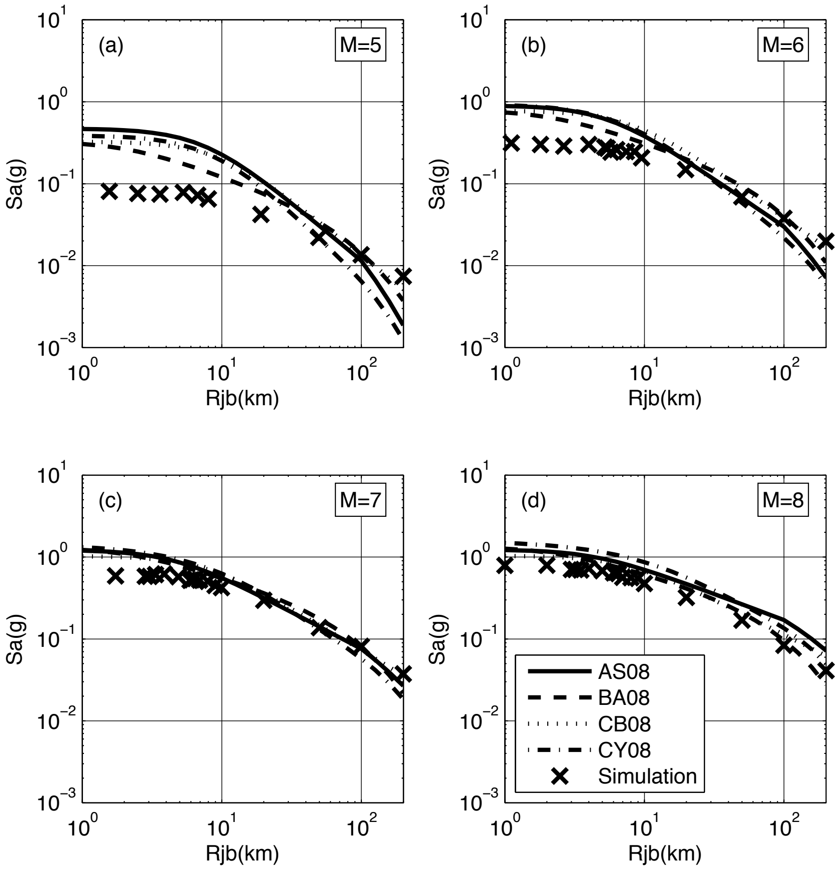

Figure D.2: Median of elastic S_a at $T = 0.2s$ computed from the NGA GMPM and simulations ($1 \leq R_{JB} \leq 200km$, $V_{S30} = 760m/s$). (a) $M = 5$, (b) $M = 6$, (c) $M = 7$, and (d) $M = 8$.

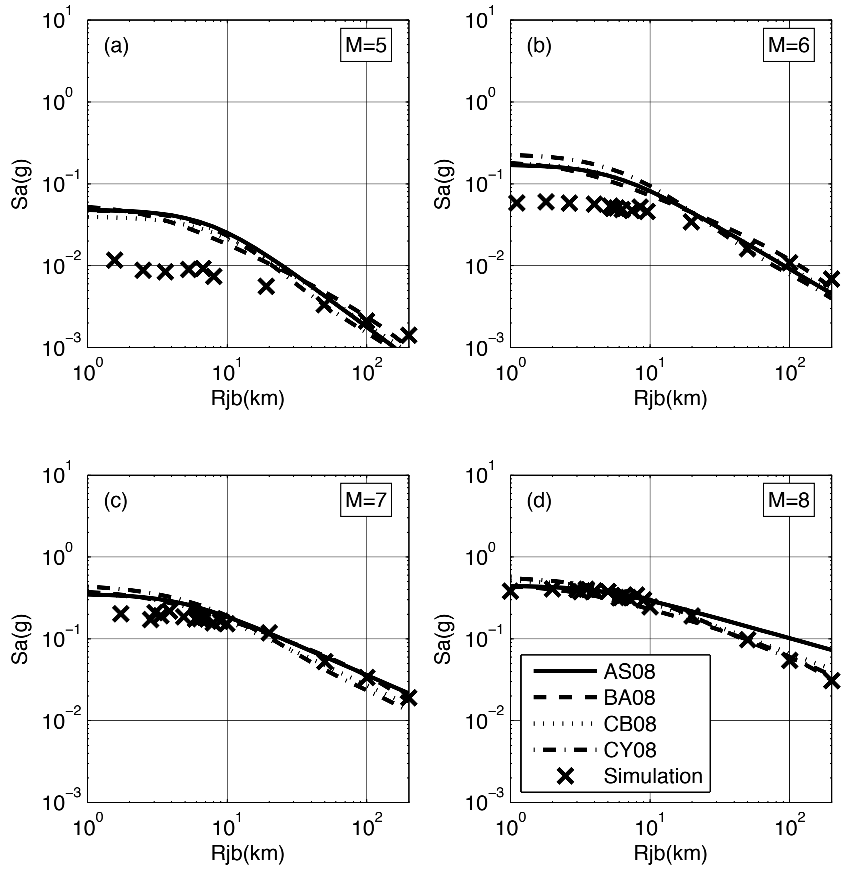

Figure D.3: Median of elastic S_a at $T = 1s$ computed from the NGA GMPM and simulations ($1 \leq R_{JB} \leq 200km$, $V_{S30} = 760m/s$). (a) $M = 5$, (b) $M = 6$, (c) $M = 7$, and (d) $M = 8$.

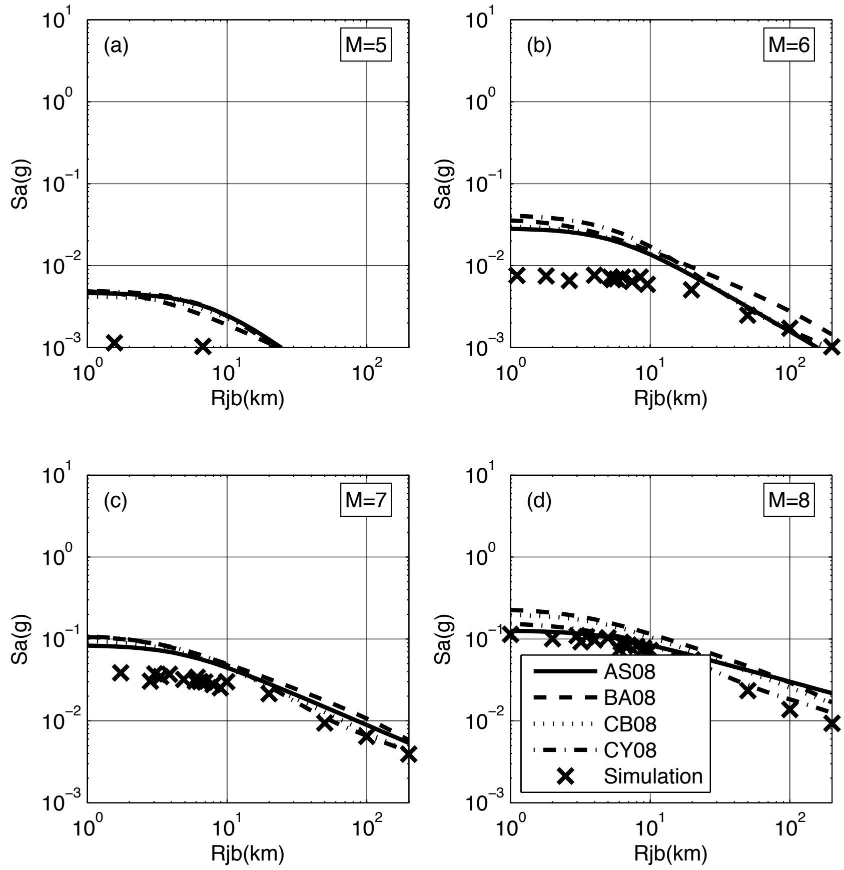

Figure D.4: Median of elastic S_a at $T = 3s$ computed from the NGA GMPM and simulations ($V_{S30} = 760m/s$). (a) $M = 5$, (b) $M = 6$, (c) $M = 7$, and (d) $M = 8$.

D.1.2 Magnitude scaling

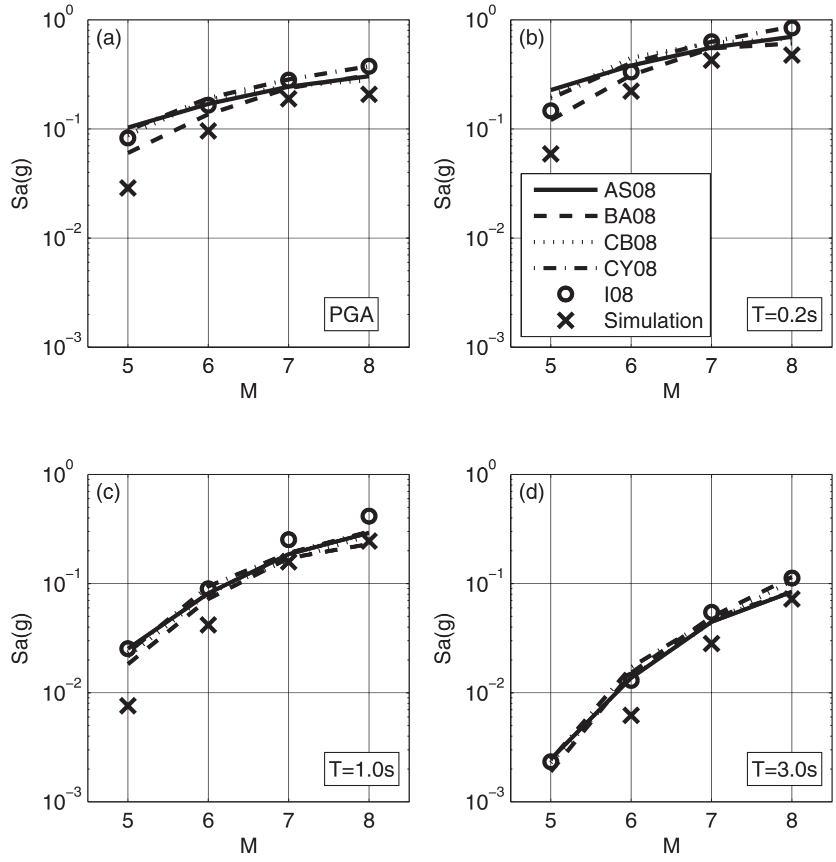

Figure D.5: Median of PGA and elastic S_a computed from the NGA GMPM and simulations ($5 \leq M \leq 8$, $R_{JB} = 10km$ $V_{S30} = 760m/s$). (a) PGA, (b) S_a at $T = 0.2s$, (c) S_a at $T = 1s$, and (d) S_a at $T = 3s$.

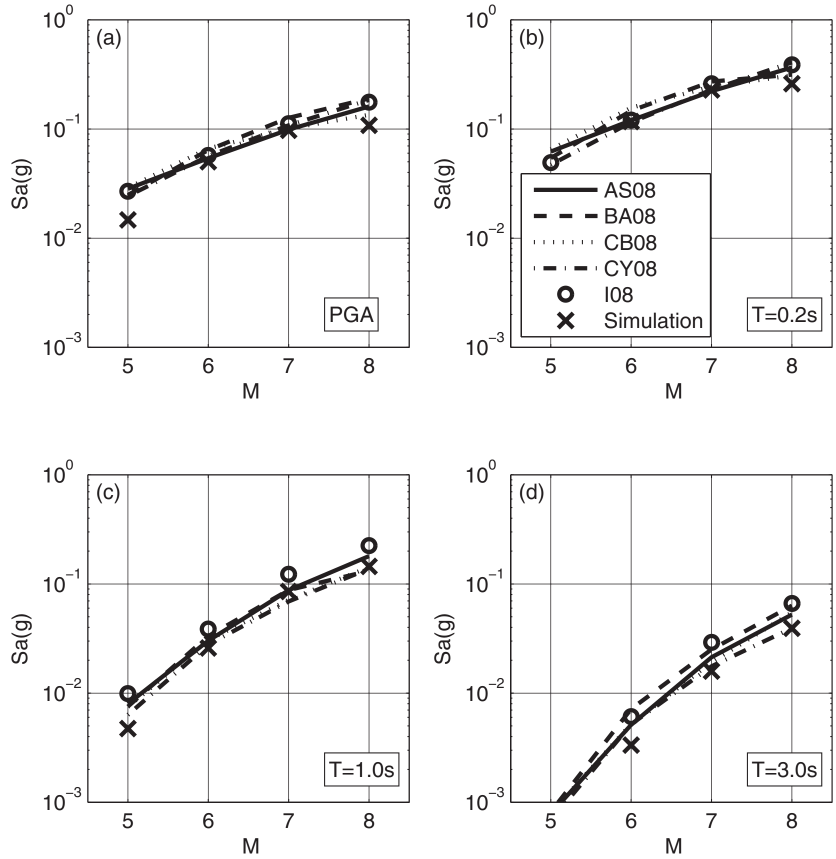

Figure D.6: Median of PGA and elastic S_a computed from the NGA GMPM and simulations ($5 \leq M \leq 8$, $R_{JB} = 30km$ $V_{S30} = 760m/s$). (a) PGA, (b) S_a at $T = 0.2s$, (c) S_a at $T = 1s$, and (d) S_a at $T = 3s$.

D.1.3 Response spectra on period axis

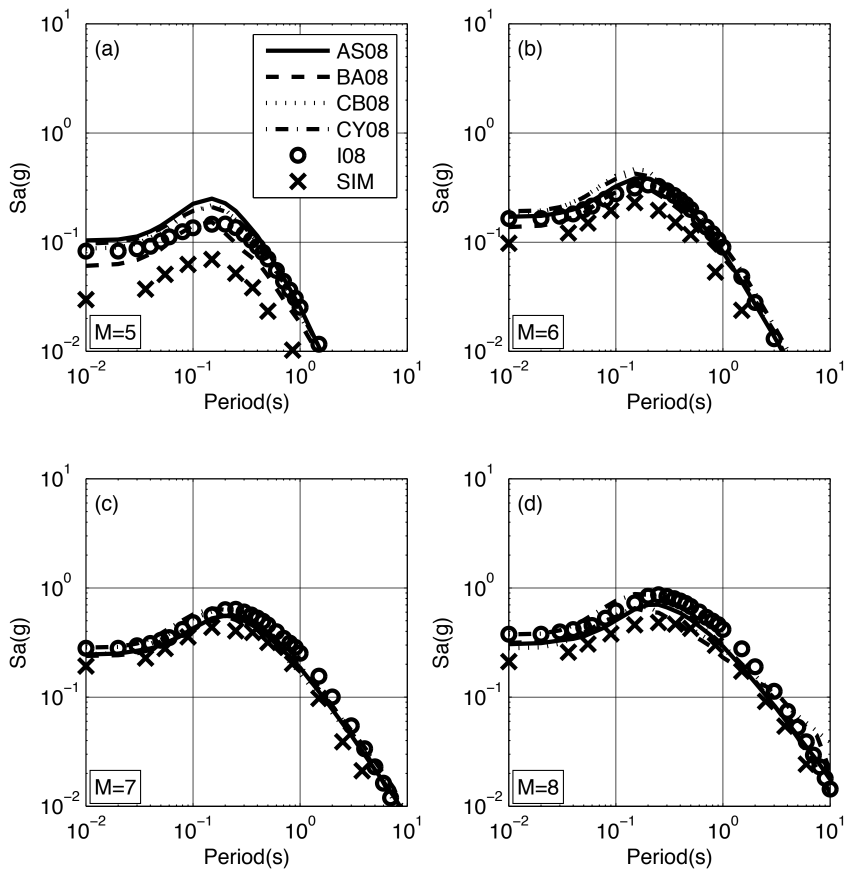

Figure D.7: Median of elastic S_a computed from the NGA GMPM and simulations ($R_{JB} = 10km, V_{S30} = 760m/s$). (a) $M = 5$, (b) $M = 6$, (c) $M = 7$, and (d) $M = 8$.

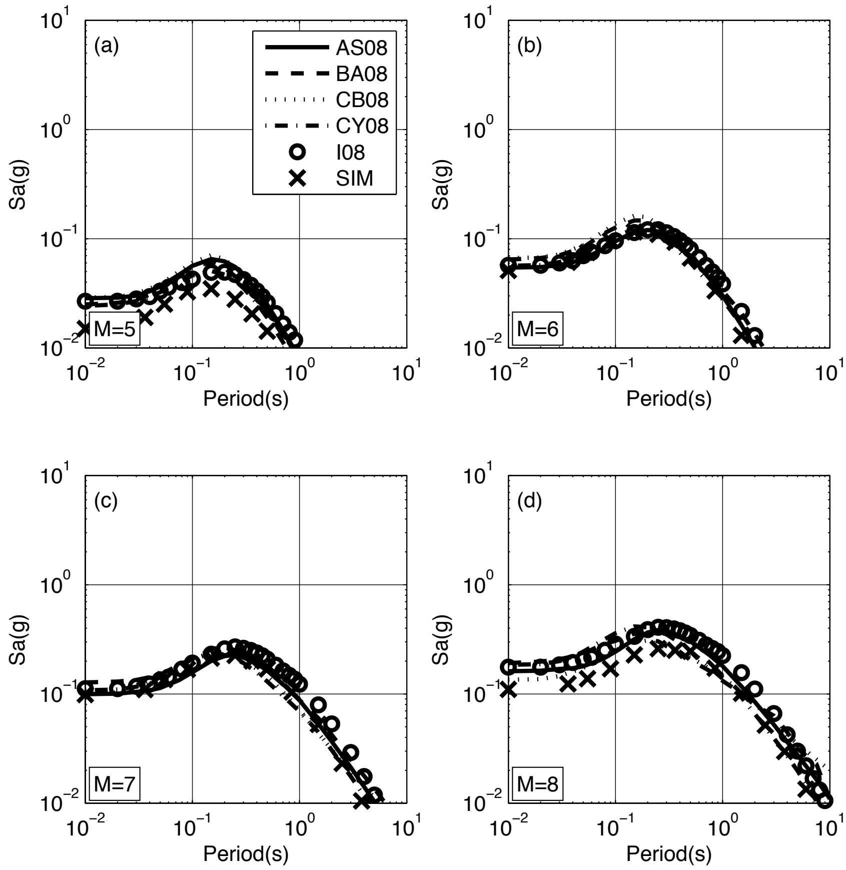

Figure D.8: Median of elastic S_a computed from the NGA GMPM and simulations ($R_{JB} = 30km, V_{S30} = 760m/s$). (a) $M = 5$, (b) $M = 6$, (c) $M = 7$, and (d) $M = 8$.

D.1.4 Comparison of the standard deviation

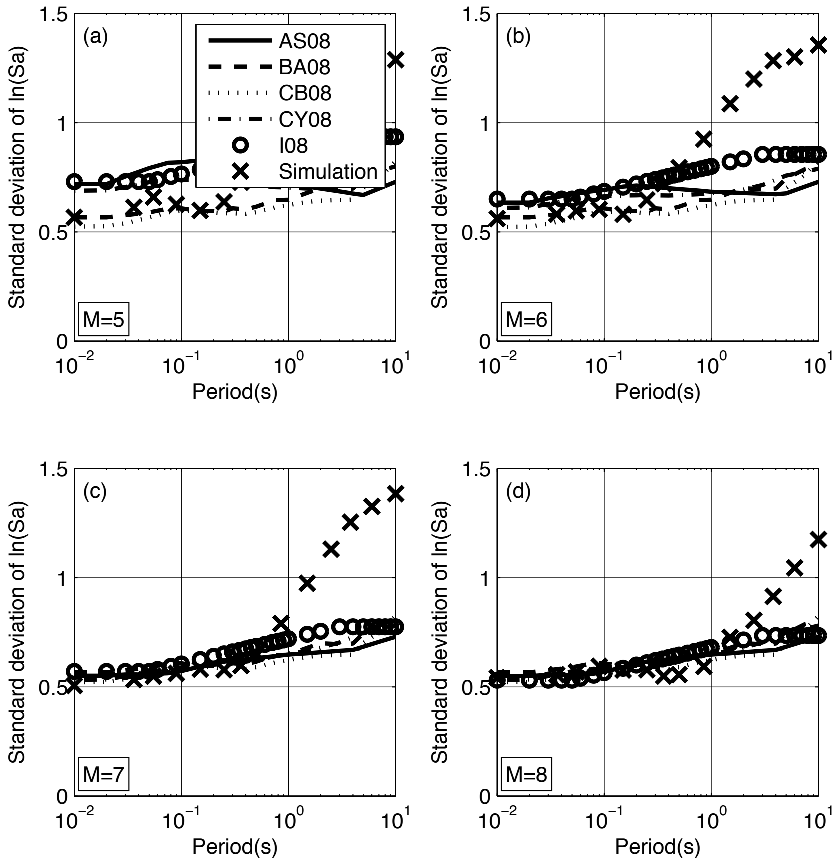

Figure D.9: Logarithmic standard deviation of elastic S_a computed from the NGA GMPM and simulations ($R_{JB} = 10km$, $V_{S30} = 760m/s$). (a) $M = 5$, (b) $M = 6$, (c) $M = 7$, and (d) $M = 8$.

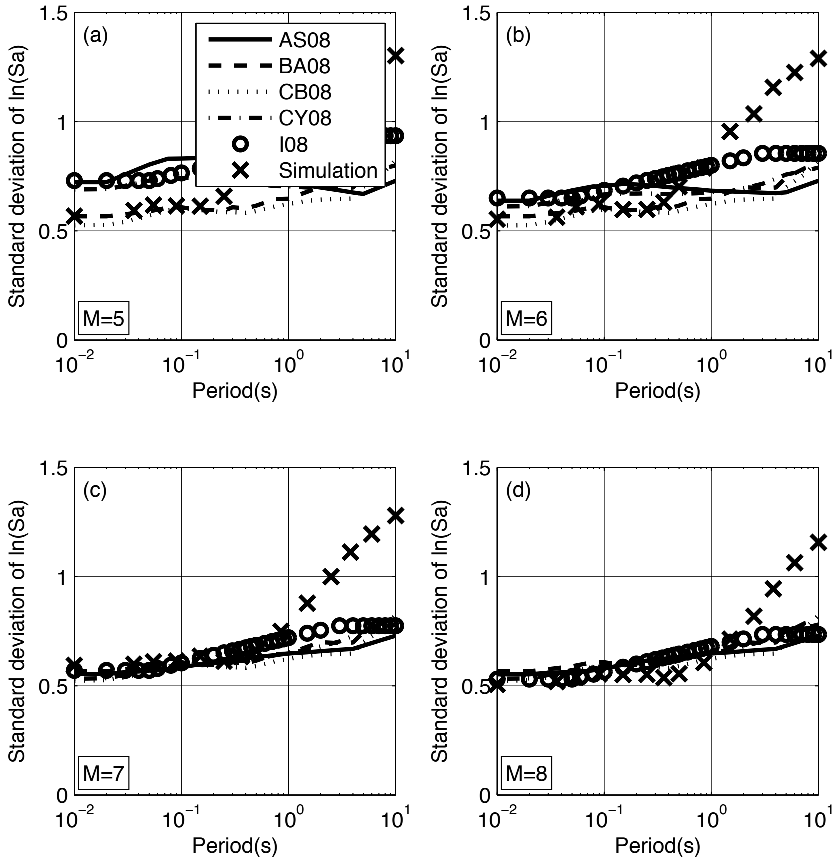

Figure D.10: Logarithmic standard deviation of elastic S_a computed from the NGA GMPM and simulations ($R_{JB} = 30km$, $V_{S30} = 760m/s$). (a) $M = 5$, (b) $M = 6$, (c) $M = 7$, and (d) $M = 8$.

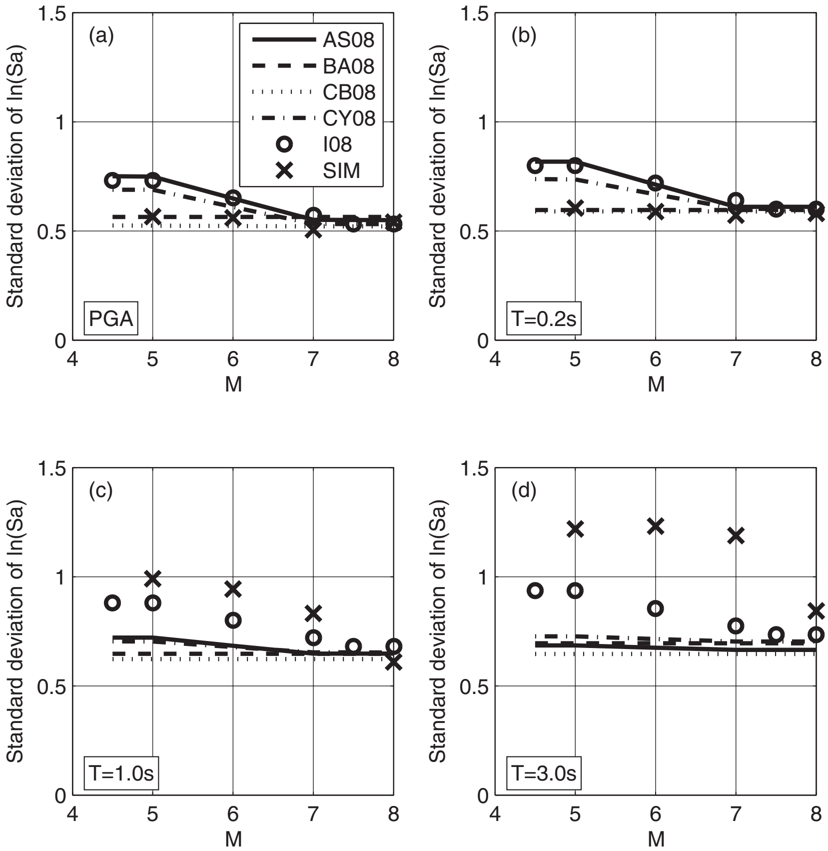

Figure D.11: Logarithmic standard deviation of elastic S_a computed from the NGA GMPM and simulations ($R_{JB} = 10km$, $V_{S30} = 760m/s$). (a) $M = 5$, (b) $M = 6$, (c) $M = 7$, and (d) $M = 8$.

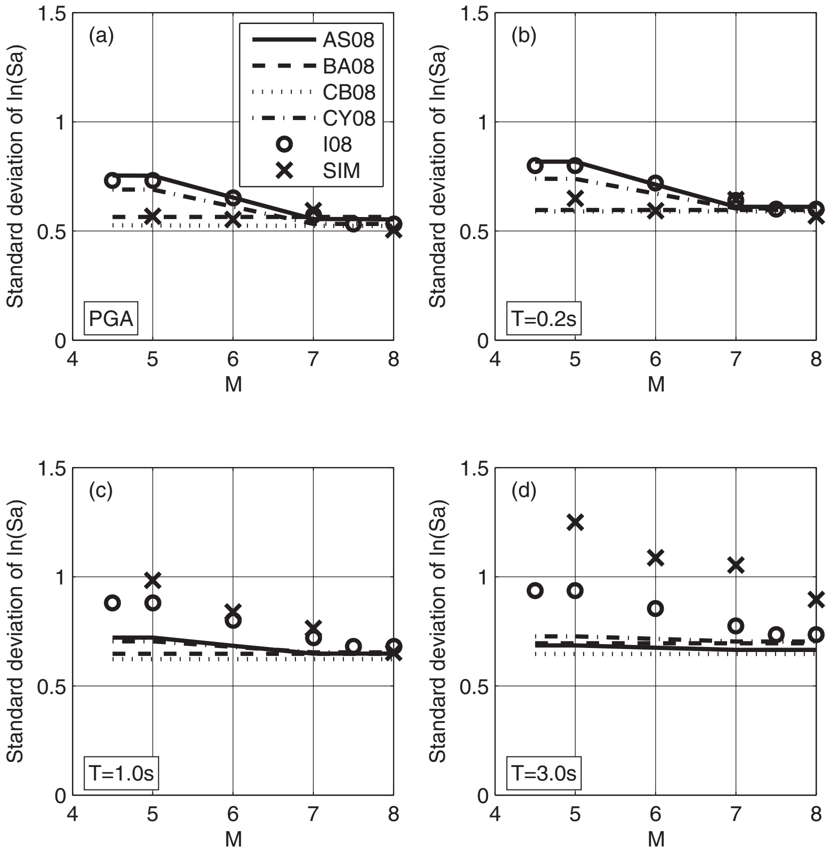

Figure D.12: Logarithmic standard deviation of elastic S_a computed from the NGA GMPM and simulations ($R_{JB} = 30km$, $V_{S30} = 760m/s$). (a) $M = 5$, (b) $M = 6$, (c) $M = 7$, and (d) $M = 8$.

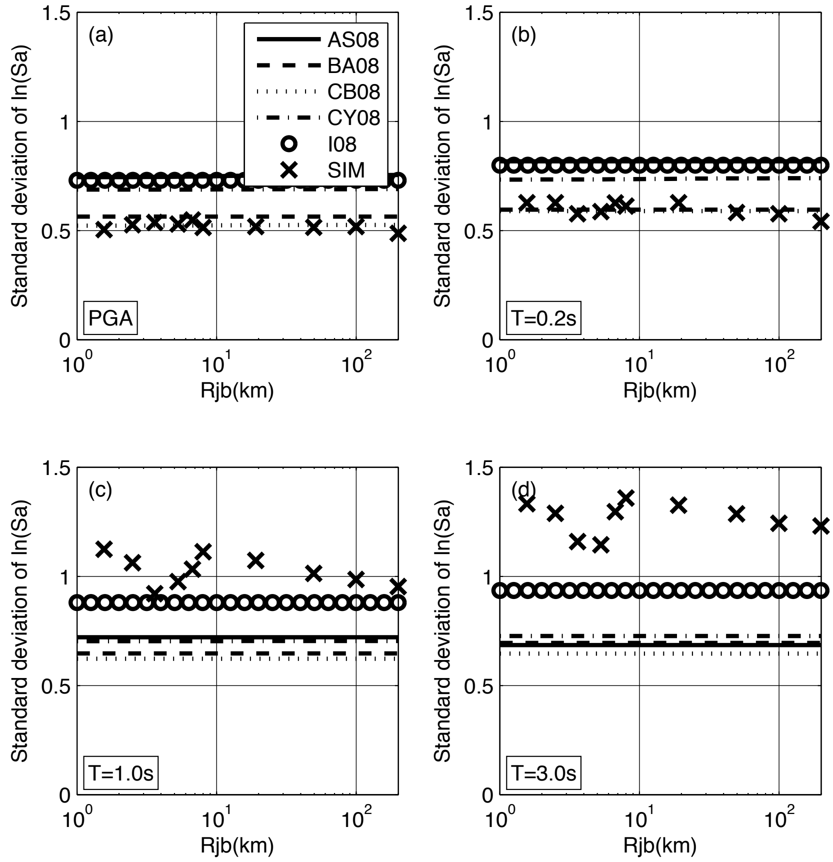

Figure D.13: Logarithmic standard deviation of elastic S_a computed from the NGA GMPM and simulations ($M = 5, V_{S30} = 760m/s$). (a) PGA, (b) $T = 0.2s$, (c) $T = 1s$, and (d) $T = 3s$.

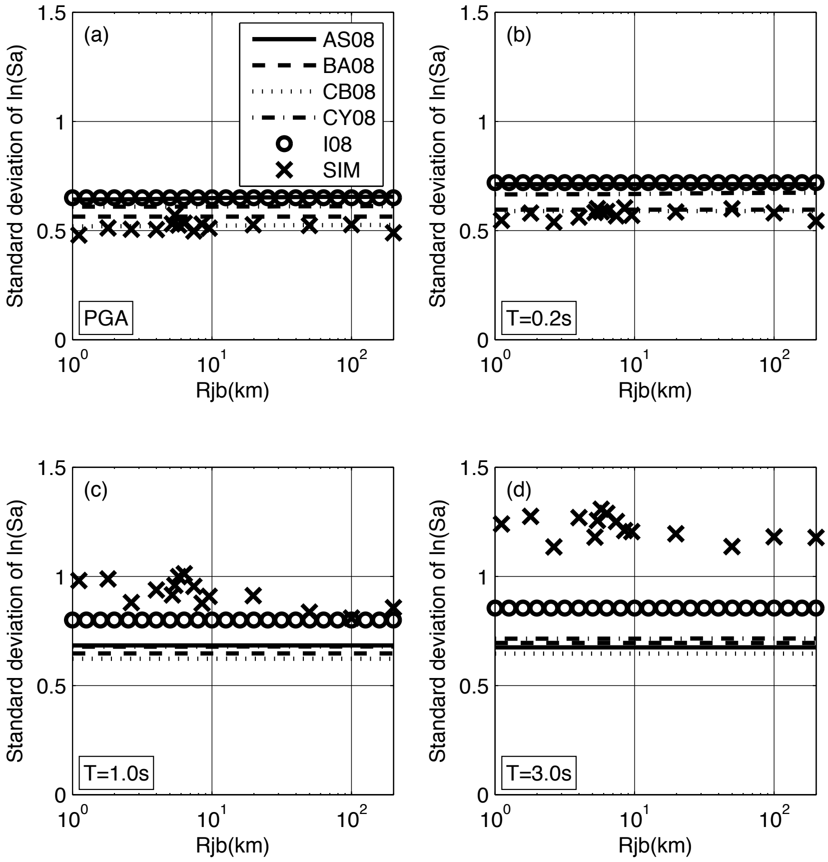

Figure D.14: Logarithmic standard deviation of elastic S_a computed from the NGA GMPM and simulations ($M = 6, V_{S30} = 760m/s$). (a) PGA, (b) $T = 0.2s$, (c) $T = 1s$, and (d) $T = 3s$.

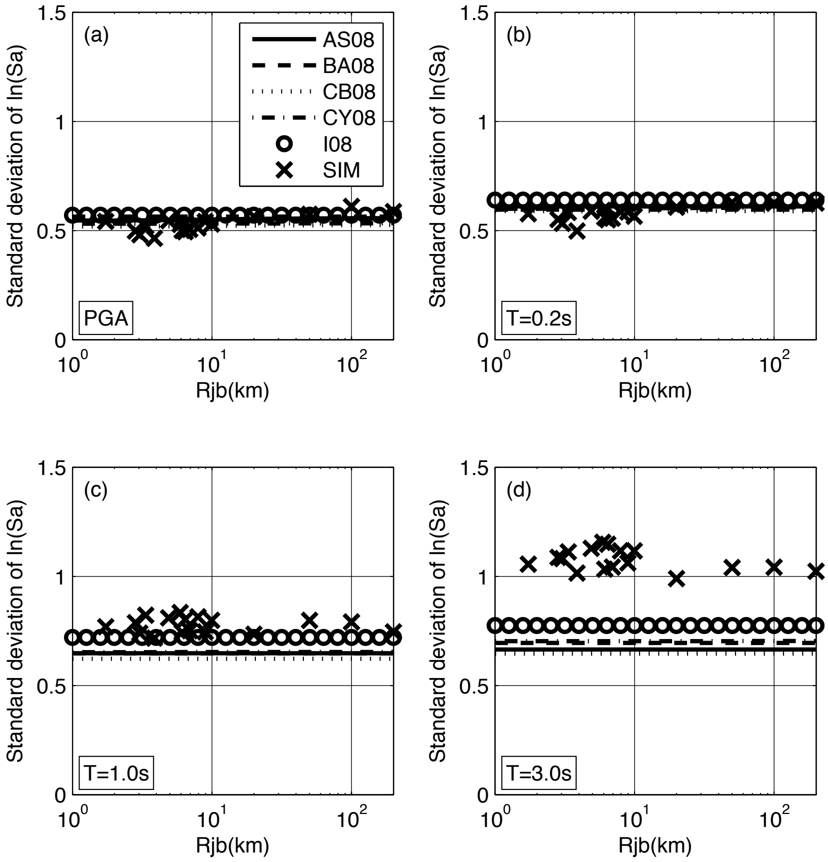

Figure D.15: Logarithmic standard deviation of elastic S_a computed from the NGA GMPM and simulations ($M = 7, V_{S30} = 760m/s$). (a) PGA, (b) $T = 0.2s$, (c) $T = 1s$, and (d) $T = 3s$.

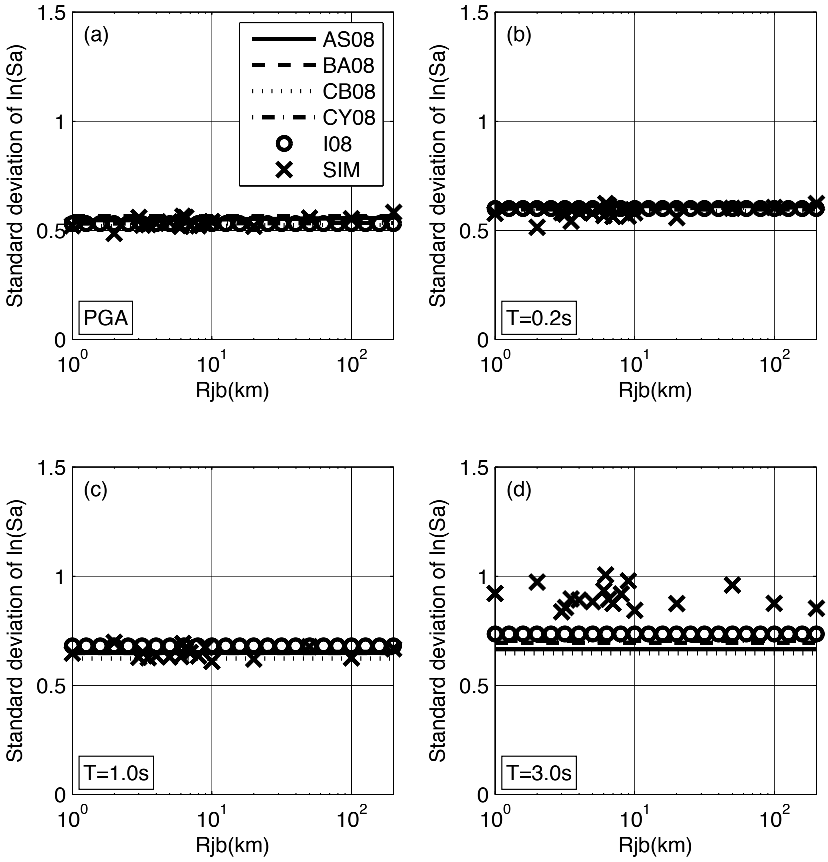

Figure D.16: Logarithmic standard deviation of elastic S_a computed from the NGA GMPM and simulations ($M = 8, V_{S30} = 760m/s$). (a) PGA, (b) $T = 0.2s$, (c) $T = 1s$, and (d) $T = 3s$.

D.2 Inelastic response spectra

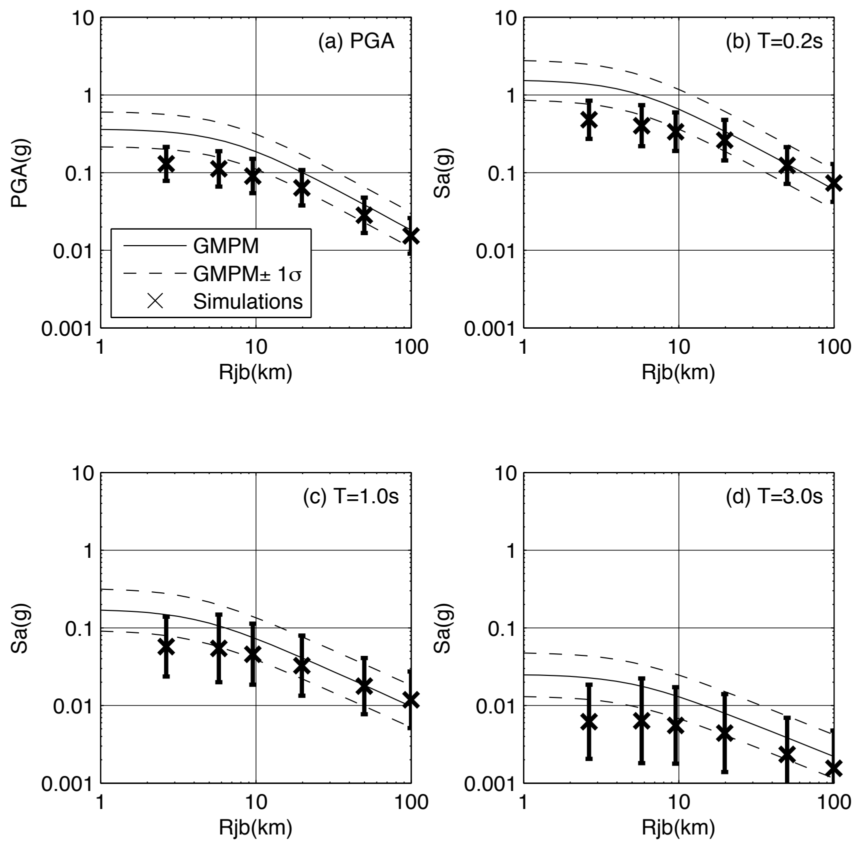

Figure D.17: Median and logarithmic standard deviation of inelastic response spectra F_y/W computed from the GMPM and simulations ($M = 6, V_{S30} = 760m/s$, $\mu = 8$). (a) $T = 0.2s$, (b) $T = 1s$, and (c) $T = 3s$.

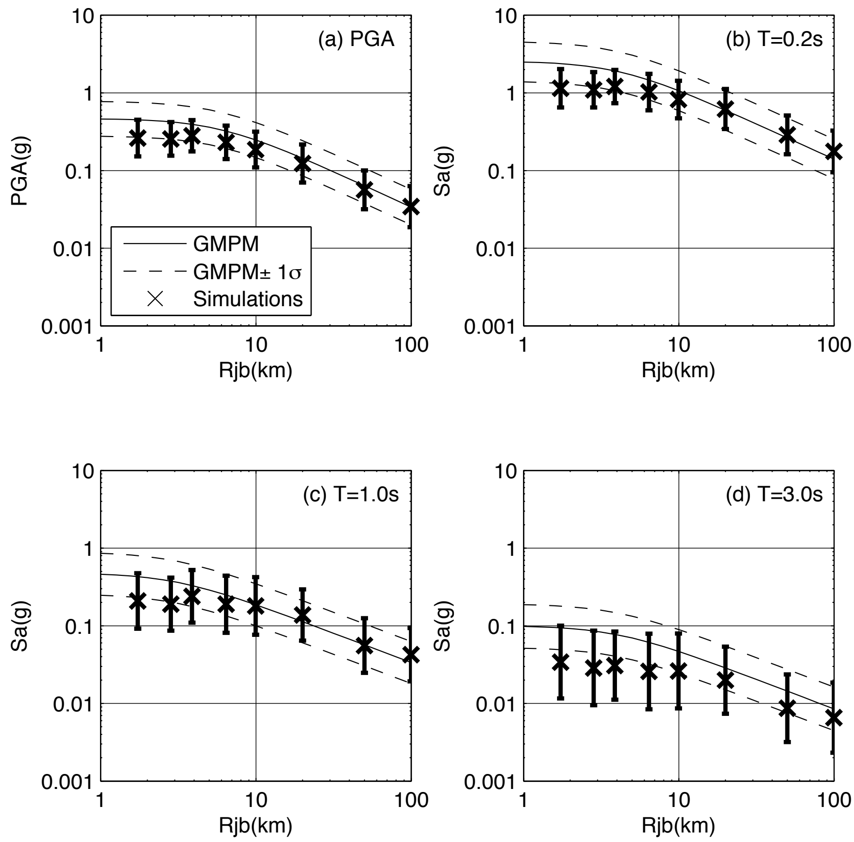

Figure D.18: Median and logarithmic standard deviation of inelastic response spectra F_y/W computed from the GMPM and simulations ($M = 7, V_{S30} = 760m/s$, $\mu = 8$). (a) $T = 0.2s$, (b) $T = 1s$, and (c) $T = 3s$.

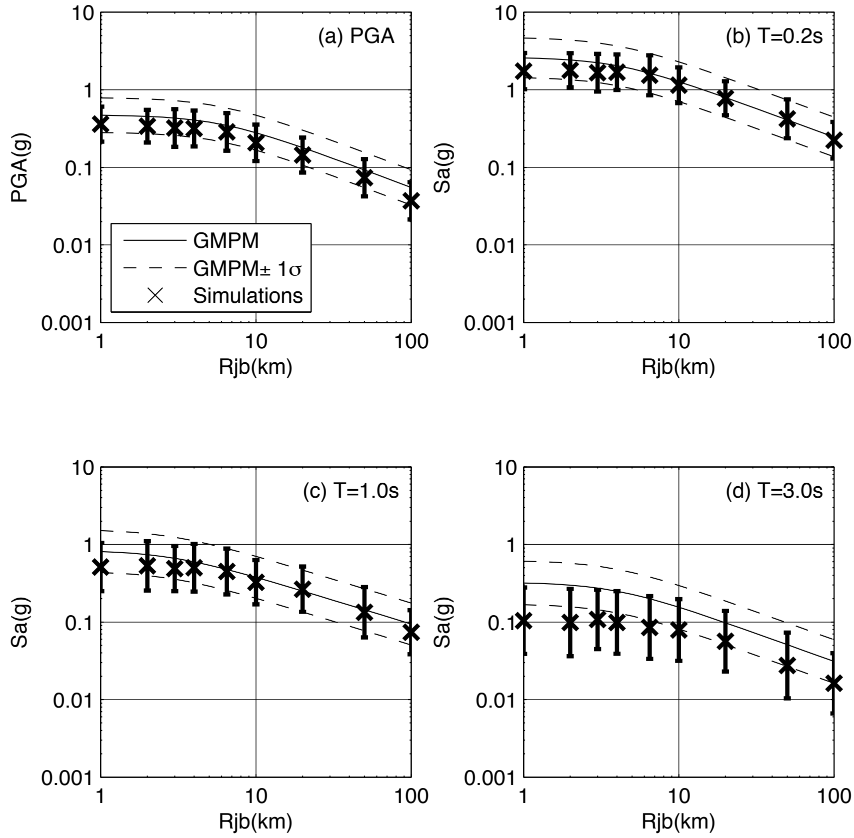

Figure D.19: Median and logarithmic standard deviation of inelastic response spectra F_y/W computed from the GMPM and simulations ($M = 8, V_{S30} = 760m/s$, $\mu = 8$). (a) $T = 0.2s$, (b) $T = 1s$, and (c) $T = 3s$.

D.3 Arias intensity

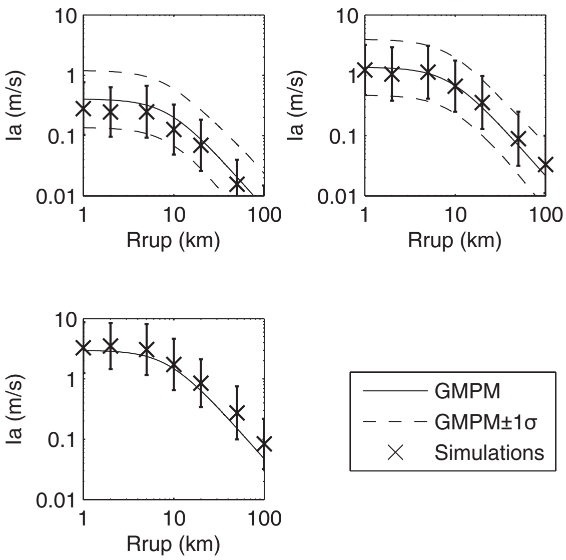

Figure D.20: Median and logarithmic standard deviation of I_A computed from the NGA GMPM and simulations ($V_{S30} = 760 m/s$). (a) $M = 6$, (b) $M = 7$, and (c) $M = 8$.

D.4 Significant duration

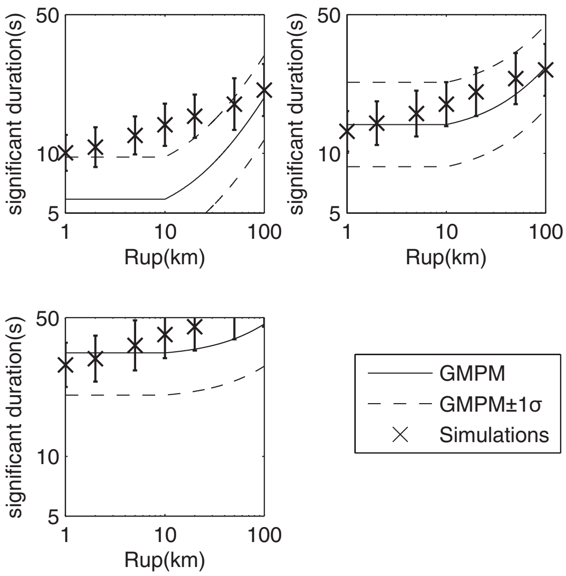

Figure D.21: Median and logarithmic standard deviation of significant duration computed from the NGA GMPM and simulations ($V_{S30} = 760m/s$). (a) $M = 6$, (b) $M = 7$, and (c) $M = 8$.

D.5 Mean period

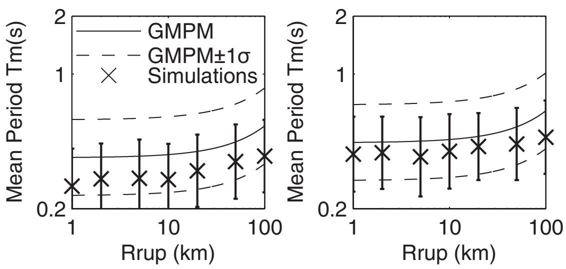

Figure D.22: Median and logarithmic standard deviation of significant duration computed from the NGA GMPM and simulations ($V_{S30} = 760m/s$). (a) $M = 6$, (b) $M = 7$.

Bibliography

Abrahamson, N., G. Atkinson, D. Boore, Y. Bozorgnia, K. Campbell, B. Chiou, I. M. Idriss, W. Silva, & R. Youngs (2008). Comparisons of the NGA ground-motion relations. *Earthquake Spectra 24*(1), 45–66.

Abrahamson, N. & W. Silva (2008). Summary of the Abrahamson & Silva NGA ground-motion relations. *Earthquake Spectra 24*(1), 67–97.

Abrahamson, N. A., J. F. Schneider, & J. C. Stepp (1991). Empirical spatial coherency functions for application to soil-structure interacton analyses. *Earthquake Spectra 7*(1), 1–27.

Abrahamson, N. A. & W. J. Silva (1996). Empirical ground motion models, Section 5: Empirical model for duration of strong ground motion. Report. *Brookhaven National Laboratory*.

Abrahamson, N. A. & R. R. Youngs (1992). A stable algorithm for regression analysis using the random effects model. *Bulletin of the Seismological Society of America 82*(1), 505–510.

Ahmadi, G. (1979). Generation of artificial time-histories compatible with given response spectra - a review. *Solid Mechanics Archives 4*(7), 207–239.

Al Atik, L. & N. Abrahamson (2010). An improved method for nonstationary spectral matching. *Earthquake Spectra 26*(3), 601–617.

Alamilla, J., L. Esteva, J. Garcia-Perez, & O. Diaz-Lopes (2001). Evolutionary properties of stochastic models of earthquake accelerograms : Their dependence on magnitude and distance. *Journal of Seismology 5*, 1–21.

Amin, M. & A. Ang (1968). Nonstationary stochastic model of earthquake motions. *Engineering Mechanics Division (ASCE) 94*, 556–583.

Amiri, G. G., A. Bagheri, & S. A. S. Razaghi (2009). Generation of multiple earthquake accelerations compatible with spectrum via the wavelet packet transform and stochastic neural networks. *Journal of Earthquake Engineering 13*, 899–915.

Amiri, G. G., A. Shahjouei, S. Saadat, & M. Ajallooeian (2011). Hybrid evolutionary-neural network approach in generation of artificial accelerograms using principal component analysis and wavelet-packet transform. *Journal of Earthquake Engineering 15*(1), 50–76.

Arias, A. (1970). *A measure of earthquake intensity* (Hansen RJ ed.)., pp. 438–483. Cambridge, MA: MIT Press.

Aslani, H. & E. Miranda (2005). Probability-based seismic response analysis. *Engineering Structures 27*, 1151–1163.

Baker, J. W. (2011). The conditional mean spectrum: Tool for ground motion selection. *Journal of Structural Engineering 137*(3), 322–331.

Baker, J. W. & C. A. Cornell (2005). A vector-valued ground motion intensity measure consisting of spectral acceleration and epsilon. *Earthquake Engineering and Structural Dynamics 34*(10), 1193–1217.

Baker, J. W. & N. Jayaram (2008). Correlation of spectral acceleration values from NGA ground motion models. *Earthquake Spectra 24*(1), 299–317.

Bazzurro, P. (1998). *Probabilistic seismic demand analysis*. Ph. D. thesis, Department of Civil and Environmental Engineering, Stanford University, CA.

Bazzurro, P. & C. A. Cornell (1999). Disaggregation of seismic hazard. *Bulletin of the Seismological Society of America 89*(2), 501–520.

Bazzurro, P. & N. Luco (2006). Do scaled and spectrum-matched near-source records produce biased nonlinear structural responses? In *Proc. the 8th U.S. National Conference on Earthquake Engineering*.

Boatwright, J. & D. M. Boore (1982). Analysis of the ground accelerations radiated by the 1980 Livermore valley earthquakes for directivity and dynamic source characteristics. *Bulletin of the Seismological Society of America 72*(6), 1843–1865.

Bolotin, V. V. (1960). Statistical theory of the aseismic design of structures. In *Proc. the 2nd World Conference on Earthquake Engineering*, Tokyo and Kyoto, Japan, pp. 1365–1374.

Boore, D. M. (1973). The effect of simple topography on seismic waves: Implications for the accelerations recorded at Pacoima dam, San Fernando valley, California. *Bulletin of the Seismological Society of America 63*(5), 1603–1609.

Boore, D. M. (1983). Stochastic simulation of high-frequency ground motions based on seismological models of the radiated spectra. *Bulletin of the Seismological Society of America 73*(6), 1865–1894.

Boore, D. M. (2003). Simulation of ground motion using the stochastic method. *Pure and Applied Geophysics 160*(3), 635–676.

Boore, D. M. & G. M. Atkinson (2007). Boore-Atkinson NGA ground motion relations for the geometric mean horizontal component of peak and spectral ground motion parameters. *Report No. PEER 2007/01, Pacific Earthquake Engineering Research Center, University of California at Berkeley*.

Boore, D. M. & G. M. Atkinson (2008). Ground-motion prediction equations for the average horizontal component of PGA, PGV, and 5%-damped PSA at spectral periods between 0.01 s and 10.0s. *Earthquake Spectra 24*(1), 99.

Boore, D. M., W. B. Joyner, & T. E. Fumal (1997). Equations for estimating horizontal response spectra and peak acceleration from western north American earthquakes: A summary of recent work. *Seismological Research Letter 68*(1), 128–153.

Bozorgnia, Y. & K. W. Campbell (2004). *Engineering characterization of ground motion, in earthquake engineering: From engineering seismology to performance-based engineering*. Boca Raton, Florida: CRC Press.

Bozorgnia, Y., M. M. Hachem, & K. W. Campbell (2010). Ground motion prediction equation (attenuation relationship) for inelastic response spectra. *Earthquake Spectra 26*(1), 1.

Brune, J. N. (1970). Tectonic stress and the spectra of seismic shear waves from earthquakes. *Journal of Geophysical Research Letters 75*(26), 4997–5009.

Cacciola, P. & G. Deodatis (2011). A method for generating fully non-stationary and spectrum-compatible ground motion vector processes. *Soil Dynamics and Earthquake Engineering 31*(3), 351–360.

Campbell, K. W. & Y. Bozorgnia (2008). NGA ground motion model for the geometric mean horizontal component of PGA, PGV, PGD and 5% damped linear elastic response spectra for periods ranging from 0.01 to 10s. *Earthquake Spectra 24*(1), 139.

Chakravorty, M. K. & E. H. Vanmarck (1973). Probabilistic seismic analysis of light equipment within buildings. *Proc. of 5th World Conference on Earthquake Engineering, Rome, Italy*, 2822–2828.

Chang, M., J. Kwiatkowski, R. Nau, R. Oliver, & K. Pister (1982). ARMA models for earthquake ground motions. *Earthquake Engineering and Structural Dynamics 10*, 651–662.

Chiou, B., R. Darragh, N. Gregor, & W. Silva (2008). NGA project strong-motion database. *Earthquake Spectra 24*(1), 23.

Chiou, B. S.-J. & R. R. Youngs (2008). An NGA model for the average horizontal component of peak ground motion and response spectra. *Earthquake Spectra 24*(1), 173.

Chopra, A. K. (2007). *Dynamics of structures*. Upper Saddle River, NJ.: Prentice Hall.

Cohen, L. (1995). *Time-frequency analysis*. Upper Saddle River, NJ.: Prentice Hall.

Conte, J. (1992a). Nonstationary ARMA modeling of seismic motions. *Soil Dynamics and Earthquake Engineering 11*(7), 411–426.

Conte, J. P. (1992b). Effect of earthquake frequency nonstationarity on inelastic structural response. In *Earthquake Engineering, Tenth World Conference*.

Conte, J. P. & B. F. Peng (1997). Fully nonstationarity analytical earthquake ground-motion model. *Journal of Engineering Mechanics 12*(1), 15–24.

Cornell, C. (1964). *Stochastic process models in structural engineering*. Ph. D. thesis, Department of Civil and Environmental Engineering, Stanford University, CA.

Cui, Y., K. B. Olsen, T. H. Jordan, K. Lee, J. Zhou, P. Small, D. Roten, G. Ely, D. K. Panda, A. Chourasia, J. Levesque, S. M. Day, & P. Maechling (2010). Scalable earthquake simulation on petascale supercomputers. *High Performance Computing, Networking, Storage and Analysis (SC), 2010 International Conference for*, 1–20.

Deodatis, G. (1996). Non-stationary stochastic vector processes: Seismic ground motion applications. *Probabilistic Engineering Mechanics 11*(3), 149–167.

Der Kiureghian, A. (1996). A coherency model for spatially varying ground motions. *Earthquake Engineering & Structural Dynamics 25*, 99–111.

Der Kiureghian, A. & J. Crempien (1989). An evolutionary model for earthquake ground motion. *Structural Safety 6*, 235–246.

Der Kiureghian, A. & P. Keshishian (1996). Effect of site response on spatial variability of ground motion. *Proc. of 11th World Conference on Earthquake Engineering*, 705.

Douglas, J. & H. Aochi (2008). A survey of techniques for predicting earthquake ground motions for engineering purposes. *Surveys in Geophysics 29*(3), 187–220.

Giaralis, A. & P. Spanos (2009). Wavelet-based response spectrum compatible synthesis of accelerograms Eurocode application (EC8). *Soil Dynamics and Earthquake Engineering 29*(1), 219–235.

Graves, R., T. H. Jordan, S. Callaghan, E. Deelman, E. Field, G. Juve, C. Kesselman, P. Maechling, G. Mehta, K. Milner, D. Okaya, P. Small, & K. Vahi (2010). CyberShake: A physics-based seismic hazard model for southern California. *Pure and Applied Geophysics*.

Graves, R. W. & A. Pitarka (2010). Broadband ground-motion simulation using a hybrid approach. *Bulletin of the Seismological Society of America 100*(5A), 2095–2123.

Haar, A. (1910). Zur theorie der orthogonalen funktionensysteme. *Math. Annual. 69*, 331–371.

Haase, J. S., E. Hauksson, F. Vernon, & A. Edelman (1996). Modeling of ground motion from a 1994 Northridge aftershock using a tomographic velocity model of the Los Angeles basin. *Bulletin of the Seismological Society of America 86*(1), 156–167.

Hancock, J., J. Watson-Lamprey, N. A. Abrahamson, J. J. Bommer, A. Markatis, & R. Mendis (2006). An improved method of matching response spectra of recorded earthquake ground motion using wavelets. *Journal of Earthquake Engineering 10*(1), 67–89.

Hao, H. (1986). Effects of spatial variation of ground motion on large multiply-supported structures. *Report No. UCB/EERC-89/06, Earthquake Engineering Research Center, University of California, Berkeley, CA, USA.*.

Harichandran, B. R. S., Vanmarcke, & E. H (1986). Stochastic variation of earthquake ground motion in space and time. *Journal of Engineering Mechanics ASCE 112*(2), 154–174.

Hartzell, S., S. Harmsen, A. Frankel, & S. Larsen (1999). Calculation of broadband time histories of ground motion : Comparison of methods and validation using strong-ground motion from the 1994 Northridge earthquake. *Bulletin of the Seismological Society of America 89*(6), 1484–1504.

Hartzell, S. H. (1978). Earthquake aftershocks as green's functions. *Geophysical Research Letters* (1), 1–4.

Haselton, C. B., J. W. Baker, Y. Bozorgnia, C. A. Goulet, E. Kalkan, N. Luco, T. Shantz, N. Shome, J. P. Stewart, P. Tothong, J. Watson-Lamprey, & F. Zareian (2009). Evaluation of ground motion selection and modification methods: Predicting median inter-story drift response of buildings. *Pacific Earthquake Engineering Research Center, University of California at Berkeley*.

Haselton, C. B. & G. G. Deierlein (2008). Assessing seismic collapse safety of modern reinforced concrete moment-frame buildings. *Report No. PEER 2007/08, Pacific Earthquake Engineering Research Center, University of California at Berkeley*.

Hoshiya, M. & Z. Hasgur (1978). AR and MA models of nonstationary ground motion. *Bulletin of the International Institute of Seismology and Earthquake Engineering 16*, 55–68.

Idriss, I. M. (2008). An NGA empirical model for estimating the horizontal spectral values generated by shallow crustal earthquakes. *Earthquake Spectra 24*(1), 217.

Irikura, K. (1983). Semi-empirical estimation of strong ground motions during large earthquakes. *Bull. Disas. Prev. Res. Inst., Kyoto Univ. 33*(298).

Iyama, J. & H. Kuwamura (1999). Application of wavelets to analysis and simulation of earthquake motions. *Earthquake Engineering & Structural Dynamics 28*(3), 255–272.

Iyengar, R. N. & K. T. S. R. Iyengar (1969). A nonstationary random process model for earthquake acceleration. *Bulletin of the Seismological Society of America 59*(3), 1163–1188.

Jayaram, N. & J. W. Baker (2008). Statistical tests of the joint distribution of spectral acceleration values. *Bulletin of the Seismological Society of America 98*(5), 2231–2243.

Jayaram, N., T. Lin, & J. W. Baker (2011). A computationally efficient ground motion selection algorithm for matching a target response spectrum mean and variance. *Earthquake Spectra, in press*.

Joyner, W. B. & D. M. Boore (1993). Methods for regression analysis of strong-motion data. *Bulletin of the Seismological Society of America 83*(2), 469–487.

Joyner, W. B. & D. M. Boore (1994). Errata, Methods for regression analysis of strong-motion data. *Bulletin of the Seismological Society of America 84*(3), 955–956.

Jurkevics, A. & T. J. Ulrych (1978). Representing and simulating strong ground motion. *Bulletin of the Seismological Society of America 68*(3), 781–801.

Kameda, H. (1975). Evolutionary spectra of seismogram by multifilter. *Journal of Engineering Mechanics ASCE 101*(6), 787–801.

Kanamori, H. (1977). The energy release in great earthquake. *Journal of Geophysical Research 82*(20), 2981–2987.

Kozin, F. (1988). Autoregressive moving average models of earthquake record. *Probabilistic Engineering Mechanics 3*(2).

Kramer, S. L. (1996). *Geotechnical earthquake engineering*. Upper Saddle River, NJ.: Prentice Hall.

Kumar, M., J. M. Castro, P. J. Stafford, & A. Y. Elghazouli (2011). Influence of the mean period of ground motion on the inelastic dynamic response of single and multi degree of freedom systems. *Earthquake Engineering and Structural Dynamics 40*, 237–256.

Lin, Y. K. (1965). Nonstationary excitation and response in linear systems treated as sequences of random pulses. *Journal of the Acoustical Society of America 38*, 453–460.

Lin, Y. K. (1986). On random pulse train and its evolutionary spectral representation. *Probabilistic Engineering Mechanics 1*(4), 219–223.

Liu, S. C. (1970a). Evolutionary power spectral density of strong-motion earthquakes. *Bulletin of the Seismological Society of America 60*(3), 891–900.

Liu, S. C. (1970b). Synthesis of stochastic reprentations of ground motions. *The Bell Systems Technical Journal 49*, 521–541.

Luco, N. & P. Bazzurro (2007). Does amplitude scaling of ground motion records result in biased nonlinear structural drift responses? *Earthquake Engineering and Structural Dynamics 36*, 1813–1835.

Mallat, S. (1999). *A wavelet tour of signal processing* (Second ed.). 525 B Street, Suite 1900, San Diego, California: Academic Press.

Martin Mai, P. & G. C. Beroza (2003). A hybrid method for calculating near-source, broadband seismograms: Application to strong motion prediction. *Physics of The Earth and Planetary Interiors 137*, 183–199.

Masuda, A. & A. Sone (2002). Generation of spectrum-compatible earthquake motion using wavelet transform. In *ASME 2002 Pressure Vessels and Piping Conference*, Vancouver, BC, Canada, pp. 175–180.

Mavroeidis, G. P. & A. S. Papageorgiou (2003). A mathematical representation of near-fault ground motions. *Bulletin of the Seismological Society of America 93*(3), 1099–1131.

McGuire, R. K. (1995). Probabilistic seismic hazard analysis and design earthquakes: Closing the loop. *Bulletin of the Seismological Society of America 33*(7), A294.

McGuire, R. K. (2004). *Seismic hazard and risk analysis* (Monograph ed.). Oakland, CA: Earthquake Engineering Research Institute.

Meyer, Y. (1986). Principe d'incertitude, bases hilbertiennes et algebres d'operateurs. *Séminaire N. Bourbaki 662*, 209–223.

Mobarakeh, A., F. Rofooei, & G. Ahmadi (2002). Simulation of earthquake records using time-varying Arma (2,1) model. *Probabilistic Engineering Mechanics 17*(1), 15–34.

Moczo, P., J. Kristek, M. Galis, P. Pazak, & M. Balazovjech (2007). The finite-difference and finite-element modeling of seismic wave propagation and earthquake motion. *acta physica slovaca 57*(2), 177 – 406.

Moczo, P., J. O. A. Robertsson, & L. Eisner (2007). The finite-difference time-domain method for modeling seismic wave propagation. *Advances in Geophysics 48*(06), 421–516.

Montaldo, V., A. S. Kiremidjian, H. Thráinsson, & G. Zonno (2003). Simulation of the Fourier phase spectrum for the generating of synthetic accelerograms. *Journal of Earthquake Engineering 7*(3), 427–445.

Mukherjee, S. & V. K. Gupta (2002). Wavelet-based generation of spectrum-compatible time-histories. *Soil Dynamics and Earthquake Engineering 22*, 799–804.

Nakamura, M., F. Sasaki, K. Yokoyama, & T. Tamaoki (2008). Generation of artificial earthquake motion using observed earthquake motions. *Proc. the 14th World Conference on Earthquake*.

Okano, H., H. Ishida, & K. Kato (2010). Theoretical study on inter period correlation of residuals of ground motion prediction equation - Cause of reverse increase of correlation in short period side - (in Japanese). *J. Struct. Constr. Eng., AIJ 75*(655), 1617–1624.

Page, C. H. (1952). Instantaneous power spectra. *Journal of applied physics 23*(1), 103–106.

Papadimitrios, K. (1990). Stochastic characterization of strong ground motion and applications to structural response. *Report NO. EERL 90-03, Earthquake Engineering Research Laboratory, California Institute of Technology, Pasadena, CA.*.

Papageorgiou, A. S. & K. Aki (1983a). A specific barrier model for the quantitative description of in homogeneous faulting and the prediction of strong ground motion. I. Description of the model. *Bulletin of the Seismological Society of America 73*(3), 693–722.

Papageorgiou, A. S. & K. Aki (1983b). A specific barrier model for the quantitative description of in homogeneous faulting and the prediction of strong ground motion. part II. Applications of the model. *Bulletin of the Seismological Society of America 73*(4), 953–978.

Pitarka, A., K. Irikura, T. Iwata, & H. Sekiguchi (1998). Three-dimensional simulation of the near-fault ground motion for the 1995 Hyogo-ken Nanbu (Kobe), Japan , Earthquake. *Bulletin of the Seismological Society of America 88*(2), 428–440.

Polhemus, N. & A. Cakmak (1981). Simulation of earthquake ground motions using autoregressive moving averate (ARMA) models. *Earthquake Engineering and Structural Dynamics 9*, 343–354.

Pousse, G., L. F. Bonilla, F. Cotton, & L. Margerin (2006). Nonstationary stochastic simulation of strong ground motion time histories including natural variability: Application to the K-net Japanese database. *Bulletin of the Seismological Society of America 96*(6), 2103–2117.

Priestley, M. B. (1965). Evolutionary spectra and non-stationary processes. *Journal of the Royal Statistical Society. Series B (Methodological) 27*(2), 204–237.

Priestley, M. B. (1996). Wavelets and time-dependent spectral analysis. *Journal of Time Series Analysis 17*(1), 85–103.

Rathje, E. M., F. Faraj, S. Russell, & J. D. Bray (2004). Empirical relationships for frequency content parameters of earthquake ground motions. *Earthquake Spectra 20*(1), 119.

Rezaeian, S. (2010). *Stochastic modeling and simulation of ground motions for performance-based earthquake engineering*. Ph. D. thesis, Department of Civil and Environmental Engineering, University of California, Berkeley, CA.

Ruiz, P. & J. Penzien (1971). Stochastic seismic response of structures. *Journal of Engineering Mechanics ASCE 97*, 441–456.

Ruiz, P. T. & J. Penzien (1969). PSEQGN: Artificial generation of earthquake accelerograms.

Sabetta, F. & A. Pugliese (1996). Estimation of response spectra and simulation of nonstationary earthquake ground motions. *Bulletin of the Seismological Society of America 86*(2), 337–352.

Saragoni, G. R. & G. C. Hart (1974). Simulation of artificial earthquakes. *Earthquake Engineering and Structural Dynamics 2*, 249–267.

Sasaki, F., T. Maeda, & Y. Yamamoto (2003). Artificial ground motion with nonstationarity generated using the wavelet analysis. In *Proc. the 17th Structural Mechanics In Reactor Tecnology(SMiRT17)*.

Scherer, R. J., J. D. Riera, & G. I. Schueller (1982). Estimation of the time-dependent frequency content of earthquake accelerations. *Nuclear Engineering and Design 71*, 301–310.

Shinozuka, M. & G. Deodatis (1988). Stochastic process models for earthquake ground motion. *Probabilistic Engineering Mechanics 3*(3), 114–123.

Shinozuka, M. & Y. Sato (1967). Simulation of nonstationary random process. *Journal of Engineering Mechanics ASCE 93*, 11–40.

Shome, N., C. A. Cornell, P. Bazzurro, & J. E. Carballo (1998). Earthquakes, records, and nonlinear responses. *Earthquake Spectra 14*(3), 469–500.

Silva, W. J. & K. Lee (1987). State-of-the-art for assessing earthquake hazards in the united states, Report 24, WES RASCAL code for synthesizing earthquake ground motions. *Pacific Engineering and Analysis, ElCerrito, CA 94530*.

Spanos, P., a. Giaralis, & N. Politis (2007). Time-frequency representation of earthquake accelerograms and inelastic structural response records using the adaptive chirplet decomposition and empirical mode decomposition. *Soil Dynamics and Earthquake Engineering 27*(7), 675–689.

Spanos, P. D. & G. Failla (2004). Evolutionary spectra estimation using wavelets. *Journal of Engineering Mechanics 130*(8), 952.

Spanos, P. D., A. Giaralis, N. P. Politis, & J. M. Roesset (2007). Numerical treatment of seismic accelerograms and of inelastic seismic structural responses using harmonic wavelets. *Computer-Aided Civil and Infrastructure Engineering 22*(4), 254–264.

Stewart, J. P., S.-J. Chiou, J. D. Bray, R. W. Graves, & P. G. Somerville (2001). Ground motion evaluation procedures for performance-based design ground motion evaluation procedures for performance-based design. *Report No. PEER 2001/09, Pacific Earthquake Engineering Research Center, University of California at Berkeley*.

Suarez, L. & L. Montejo (2005). Generation of artificial earthquakes via the wavelet transform. *International Journal of Solids and Structures 42*, 5905–5919.

Sugihara, M. (1997). Sinc approximation using double exponential transformations (in Japanese). *Kokyuroku, Research Institute for Mathematical Sciences, Kyoto University 990*, 125–134.

Taghavi, S. & E. Miranda (2003). Probabilistic study of peak floor acceleration demands in linear structures. *Proceedings of the 9th international conference on applications of statistics and probability in civil engineering*, 1565–1572.

Thomson, D. J. (1982). Spectrum estimation and harmonic analysis. *Proceedings of the IEEE 70*(9), 1055–1096.

Thráinsson, H. & A. S. Kiremidjian (2002). Simulation of digital earthquake accelerograms using the inverse discrete Fourier transform. *Earthquake Engineering and Structural Dynamics 31*(12), 2023–2048.

Tothong, P. & C. a. Cornell (2006). An empirical ground-motion attenuation relation for inelastic spectral displacement. *Bulletin of the Seismological Society of America 96*(6), 2146–2164.

Travasarou, T., J. D. Bray, & N. A. Abrahamson (2003). Empirical attenuation relationship for Arias intensity. *Earthquake Engineering and Structural Dynamics 32*(7), 1133–1155.

Trifunac, M. D. & A. G. Brady (1975). A study on the duration of strong earthquake ground motion. *Bulletin of the Seismological Society of America 65*(3), 581–626.

Vanmarcke, E. H. (1983). *Random fields*. Cambridge, MA: MIT Press.

Vanmarcke, E. H., C. A. Cornell, D. A. Gasparini, & S.-n. Hou (1976). SIMQKE-I: Simulation of earthquake ground motions.

Vanmarcke, E. H., G. A. Fenton, & E. Heredia-Zavoni (1997). SIMQKE-II: Conditioned earthquake ground motion simulator.

Vanmarcke, E. H. & D. A. Gasparini (1976). Simulated earthquake motions compatible with prescribed response spectra. *R76-4, Dept. of Civil Engineering, Massachusetts Inst. of Technology Cambridge*.

Wald, D. J., D. V. Helmberger, & T. H. Heaton (1991). Rupture model of the 1989 Loma Prieta earthquake from the inversion of strong-motion and broadband teleseismic data. *Bulletin of the Seismological Society of America 81*(5), 1540–1572.

Wang, J., L. Fan, S. Qian, & J. Zhou (2002). Simulations of non-stationary frequency content and its importance to seismic assessment of structures. *Earthquake Engineering & Structural Dynamics 31*(4), 993–1005.

Wen, Y. K. & P. Gu (2004). Description and simulation of nonstationary processes based on hilbert spectra. *Journal of Engineering Mechanics 130*(8), 942.

Yazdani, A. & T. Takada (2009). Wavelet-based generation of energy- and spectrum-compatible earthquake time histories. *Computer-Aided Civil and Infrastructure Engineering 24*(8), 623–630.

Yeh, C. & Y. Wen (1990). Modeling of nonstationary ground motion and analysis of inelastic structural response. *Structural Safety 8*(1-4), 281–298.

Youngs, R. R. & K. J. Coppersmith (1985). Implications of fault slip rates and earthquake recurrence models to probabilistic seismic hazard estimates. *Bulletin of the Seismological Society of America 75*(4), 939–964.

Zeng, Y., J. G. Anderson, & G. Yu (1994). A composite source model for computing realistic synthetic strong ground motions. *Geophysical Research Letters 21*(8), 725–728.

Zerva, A. (1988). Seismic source mechanism and ground motion models. *Probabilistic Engineering Mechanics 3*(2), 64–73.

Zerva, A. (1992). Seismic ground motion simulations from a class of spatial variability models. *Earthquake Engineering & Structural Dynamics 21*(4), 351–365.